UNIVERSITÉ DE LORRAINE | BIBLIOTHÈQUES UNIVERSITAIRES

AVERTISSEMENT
DROIT D'AUTEUR

Ce document est le fruit d'un long travail approuvé par le jury de soutenance et mis à disposition de l'ensemble de la communauté universitaire élargie.

Il est soumis à la propriété intellectuelle de l'auteur. Ceci implique une obligation de citation et de référencement lors de l'utilisation de ce document. Toute contrefaçon, plagiat ou reproduction illicite encourt une poursuite pénale.

Contact bibliothèque : ddoc-theses-contact@univ-lorraine.fr
(Cette adresse ne permet pas de contacter les auteurs)

Code de la Propriété Intellectuelle. articles L 122. 4
Code de la Propriété Intellectuelle. articles L 335.2- L 335.10

UNIVERSITÉ DE LORRAINE
34 COURS LÉOPOLD — CS 25233
54052 NANCY CEDEX
TÉL : 03 54 50 54 00
CONTACT@UNIV-LORRAINE.FR
WWW.UNIV-LORRAINE.FR

Thèse

Présentée et soutenue publiquement pour l'obtention du titre de

DOCTEUR DE l'UNIVERSITE DE LORRAINE
Mention : Science des Matériaux

Par Antoine Marsigny
Sous la direction d'Olivier Mirgaux et Fabrice Patisson

Experimental and modeling study of the iron ore direct reduction by a H2-rich gas

Réduction directe du minerai de fer par un gaz riche en hydrogène : étude expérimentale et modélisation

Présentée et soutenue publiquement le 12 novembre 2025

Membres du jury :

Présidente du jury :	**Mme Sabine Denis**	**Professeur émérite, IJL, Nancy**
Directeur(s) de thèse :	**Mr Olivier Mirgaux**	**Maître de Conférences, IJL, Nancy**
	Mr Fabrice Patisson	**Professeur émérite, IJL, Nancy**
Rapporteurs :	**Mr Aras Ahmadi**	**Maître de Conférences, TBI, Toulouse**
	Mr Loïc Favergeon	**Professeur, Centre SPIN, Saint-Étienne**
Examinatrice :	**Mme Valentine Weber-Zollinger**	**Ingénieur-Docteur, ArcelorMittal Maizières, Maizières-lès-Metz**
Membres invités :	**Mr Thorsten Hauck**	**Docteur, Betriebsforschungs institut, Düsseldorf**

Remerciements

Ce travail n'aurait pas été possible sans le soutien constant de mes deux directeurs de thèse, que je tiens d'abord à remercier ici. Je remercie Olivier Mirgaux, pour qui rien n'était impossible dans cette période de doctorat, et qui m'a toujours encouragé à porter plus loin nos ambitions de recherche, avec beaucoup de bienveillance. Je remercie également Fabrice Patisson, dont la sérénité m'a permis d'appréhender les épreuves parfois compliquées de ce projet. Je retiens votre compétence scientifique, votre engagement pour mon orientation future, et toutes les qualités humaines qui vous sont propres.

J'exprime ma pleine gratitude à Aras Ahmadi et Loïc Favergeon qui ont accepté d'être les rapporteurs de ma thèse, ainsi qu'à l'ensemble des autres membres du jury, Sabine Denis, Valentine Weber-Zollinger et Thorsten Hauck.

Je remercie grandement l'ensemble des partenaires du projet européen MaxH2DR, dont la collaboration a permis aux différentes équipes d'avancer à un rythme soutenu, notamment les chercheurs des universités RUB et ÂBO et de l'institut BFI.

Je tiens également à remercier Thibault Quatravaux pour l'intérêt qu'il a toujours porté à mon travail et pour son aide régulière au cours de mon doctorat.

Je suis très reconnaissant envers Jean-Baptiste Letz, sans qui le corpus de résultats expérimentaux présenté ici aurait été bien maigre. Merci pour ton aide avec la mise en place, la maintenance et l'utilisation des nombreuses machines dont je me suis servi.

Je tiens à remercier Rabeb Ben Hassine pour nos échanges mutuels et pour l'aide précieuse qu'elle m'a apporté dans la caractérisation de mes échantillons.

Je remercie les membres de mon CSI, Éric Schaer et Silvère Barrat, qui m'ont guidé certes ponctuellement, mais avec beaucoup de rigueur et de bienveillance.

Je suis reconnaissant envers tous les autres membres du laboratoire qui ont permis à ce travail d'aboutir, notamment Jean-Sébastien Kroll-Rabotin, Sébastien Fontana et Stéphane Kiener.

J'adresse enfin mes remerciements à la Commission Européenne, qui finance ce travail à travers le projet MaxH2DR.

Je dédie ce travail de thèse à mes parents : ce travail est avant tout le leur, celui de leur éducation rigoureuse, de leur soutien constant et de leur inlassable écoute lors des moments difficiles. J'espère pouvoir vous rendre un jour ce que vous m'avez apporté pendant ces trois ans. Aujourd'hui plus que toujours, je sais à quel point je veux profiter du temps que je passe avec vous.

Je dédie également ce travail à mes camarades de lutte, Kacim, Roméo et Thomas. Un jour le drapeau rouge resplendira, etc, etc. Vous avez été présents pour moi du début à la fin de ma thèse et je ne saurai jamais vous le rendre aussi bien. Tant pis. Sachez quand même que votre tour viendra, les premiers seront les derniers, …

Je dédie aussi cette thèse aux nouvelles rencontres, à nos discussions au café de Nat, aux containers aménagés, à notre version aménagée de GTA.

J'adresse une immense gratitude à ceux de Nancy qui m'ont accueilli pendant les premières années, car je reste sans voix des moments passés avec vous. Chloé, Julien, Alma, Thomas, Valentin, vous avez réussi à me faire adorer cette ville. Merci pour tout ce que vous m'avez apporté pendant ces trois ans.

Et à toi, je ne peux t'offrir que quelques mots ingrats, qui seront bien vite oubliés. Je ne m'en veux pas, car autant qu'ils sont, ils ne sauront jamais réunir assez de passion.

Summary

Abbreviations and Nomenclature **7**

Résumé en Français **11**

General Introduction **19**

I. The kinetics of reduction of iron ore pellets by hydrogen-rich gas mixtures **25**

I.1. Introduction 25

I.1.1. The reduction of iron oxides 25

I.1.2. The different reactions in the Fe-O-H-C system 27

I.1.3. Thermodynamical considerations 28

I.1.4. Kinetics of the reduction with H_2-CO gas mixtures 30

I.2. Kinetic Modeling 33

I.2.1. Physical and mathematical framework of SCM and GM 33

I.2.2. An analytical grain model for the reduction of iron ore pellets 38

I.3. Article 1: Kinetics of the reduction of iron ore pellets with hydrogen: a parametric experimental and modeling study, by A. Marsigny, J.B. Letz, O. Mirgaux, F. Patisson (under review) 43

I.4. Additional results on the reduction of iron oxides with hydrogen 66

I.4.1. Reproducibility of the reduction experiments 66

I.4.2. Effect of pellet type on the reduction 67

I.4.3. Investigation of the kinetic slowdowns of hydrogen reduction 69

I.4.4. High temperature reduction experiments 72

I.5. Conclusion 73

II. Transformations of the pore structure in iron ore pellets during reduction by hydrogen **75**

II.1. Article 2: A macroscopic investigation of the pore structure of iron ore pellets reduced with hydrogen, by A. Marsigny, J.B. Letz, O. Mirgaux, F. Patisson 75

III. The thermochemical behavior of a hydrogen-enriched shaft furnace **89**

III.1. Introduction 89

III.2. The behavior of a pure hydrogen shaft furnace 95

III.2.1. Article 3: Operating Solutions to Improve the Direct Reduction of Iron Ore by Hydrogen in a Shaft Furnace 95

III.2.2. The role of kinetics and geometry on a pure hydrogen shaft furnace 111

III.3. Hydrogen enrichment of a NG shaft furnace 120

III.3.1. H_2-enrichment of a shaft furnace in the standard geometry 120

III.3.2. Benefits of the Christmas tree 122

III.3.3. Energy demand and CO_2 emissions of H_2- and NG-based shaft furnaces 124

III.4. Conclusion 126

IV. Solid flow patterns in a direct reduction shaft furnace **129**

IV.1. Introduction 129

IV.2. State of the art on the continuum modeling of granular flow in moving bed systems 132

IV.2.1. Analytical aspects of the silo discharge 132
IV.2.2. Continuum mechanics approaches 138
IV.3. A continuum model for the solid flow of pellets in a shaft furnace 146
IV.4. Results of the continuum model 151
IV.5. Conclusion and outlook 155
General conclusion and outlook 157
References 159

Abbreviations and Nomenclature

Abbreviations

The following abbreviations are used in this manuscript:

BF	Blast furnace
BOF	Basic oxygen furnace
CFD	Computational fluid dynamics
DEM	Discrete element method
DMR	Dry methane reforming
DR	Direct reduction
DRI	Directly reduced iron
DRSF	Direct reduction shaft furnace
EAF	Electric arc furnace
GHG	Greenhouse gases
GM	Grain model
GPM	Grainy pellet model
GUD	Gas utilization degree
HBI	Hot briquetted iron
H_2-DR	Hydrogen direct reduction of iron ore
H_2-DRSF	Hydrogen direct reduction shaft furnace
IPCC	Intergovernmental panel on climate change
KS	Kinetic slowdown
LART	Law of additive reaction times
MaxH2DR	Maximize hydrogen enrichment in direct reduction shaft furnaces
MGPM	Modified grainy pellet model
NG-DRSF	Natural gas direct reduction shaft furnace
Nlpm	Normo liters per minute
NTU	Number of transfer units
SCM	Shrinking core model
SEM	Scanning electron microscopy
SMR	Steam methane reforming
TGA	Thermogravimetry analysis
TGR	Top gas recycling
TTT	Time-temperature-transformation
ULCOS	Ultra-low CO_2 steelmaking
VALORCO	Valorisation et Réduction des émissions de CO_2 dans l'industrie
WGSR	Water gas shift reaction

Nomenclature

The following notations are used in this manuscript:

Latin

a_b	Specific surface area of the pellets per unit bed volume, $m^2\ m^{-3}$
a_c	Carbon activity
a_{sp}	Specific surface area of pellets, $m^2\ kg^{-1}$
a_{sp,Fe_2O_3}	Initial specific surface area of the hematite pellets, $m^2\ kg^{-1}$
B	Constant of Mullins' model, m
C	Ratio of carbon atoms to iron atoms
$c_{p,g}$	Molar specific heat of the gas, $J\ mol^{-1}\ K^{-1}$
$c_{p,s}$	Mass specific heat of the solid, $J\ kg^{-1}\ K^{-1}$
c_t	Gas concentration, $mol\ m^{-3}$
c_i	Gas concentration in gas species i, $mol\ m^{-3}$
d_{Christ}	Diameter of the Christmas tree, m
d_{0cryst}	Diameter of the crystallites at the wustite stage, m
d_{cryst}	Diameter of the crystallites at the iron stage, m
$d_{furnace}$	Furnace diameter, m
d_{grain}	Diameter of the grains of the pellet, m
d_p	Diameter of the pellet, m
d_{pores}	Average diameter of the pores of the pellet, m
d_s	Iron oxide characteristic diameter, m
dV	Differential intruded volume, $mL\ g^{-1}$
D	Solid outlet diameter, m
D_{ijkl}	Component of the elasticity tensor, $Pa\ m^{-1}$
$\mathcal{D}_{ij}$	Binary diffusion coefficient between gas i and j, $m^2\ s^{-1}$
D_{eff}	Effective diffusion coefficient of the gas inside the pores, $m^2\ s^{-1}$
D_{Kn}	Knudsen diffusion coefficient of the gas inside the pores, $m^2\ s^{-1}$
D_{mix}	Molecular diffusion coefficient of the gas in the gas mix, $m^2\ s^{-1}$
e_i	Unit vector for the axis i
E_a	Activation energy related to a chemical kinetic constant, $J\ mol^{-1}$
$f,\ g,\ h$	Conversion functions (Table A1)
F_g	Gas flowrate, $m^3\ s^{-1}$
f_m	Reaction driving force, $mol\ m^{-3}$
h	Height above the solid outlet, m
h_d	Mass transfer coefficient, $m\ s^{-1}$
h_T	Heat transfer coefficient, $W\ m^{-2}\ K^{-1}$
I	Inertial parameter
k	Kinetic factor associated to a characteristic time, $m\ s^{-1}$
k_i	Intrinsic kinetic constant associated with reaction i
k_0	Frequency factor associated to a chemical kinetic constant, $m\ s^{-1}$
K	Permeability coefficient in the Ergun equation, $kg\ m^{-3}\ s^{-1}$
K_{eq}	Equilibrium constant
m	Pellet mass, kg
m_p	Stress growth parameter
M	Metallization degree
M_i	Molecular mass of species i, $kg\ mol^{-1}$
P	Pressure, Pa
Q_0	Vertical stress at the transition between the upper and the lower sections of the shaft, Pa
R	Ideal gas constant, $J\ mol^{-1}\ K^{-1}$
R_h	Radius or equivalent hydraulic radius of a silo, m
r	Radius, m
r_n	Reaction rate of reaction number n, $mol\ s^{-1}\ m^{-3}$
S_i	Source term associated with gas species i, $mol\ m^{-3}\ s^{-1}$
t	Time, s
t_X	Time to reach a specific conversion degree, s
T	Temperature, K
$u_{r,\varphi}, u_{z,\varphi}$	Radial (axial) velocity of phase φ (solid or gas), $m\ s^{-1}$
v_X	Reaction rate, s^{-1}
V	Pellet volume, m
w_j	Pellet mass fraction of species j
W	Inlet solid flow rate, $kg\ s^{-1}$
W_{out}	Outlet solid flow rate, $kg\ s^{-1}$

X_j	Gas molar fraction of species *j*
X	Conversion degree
z	Vertical coordinate, m
Z_i	Vertical position of slice *i*

Greek

α	Hopper half angle (°)
β	Stoichiometric factor associated to a characteristic time
$\dot{\gamma}_{ij}$	i-th and j-th component of the strain rate tensor, s^{-1}
$\dot{\gamma}$	One-dimensional strain rate, s^{-1}
Γ	Pellet tortuosity
Γ_g	Gas thermal conductivity, W m^{-1} K^{-1}
$\Gamma_{r,e}$, $\Gamma_{z,e}$	Radial (axial) effective thermal conductivity of the pellet bed, W m^{-1} K^{-1}
$\Delta_r H$	Heat of reaction, J mol^{-1}
$\Delta_r H^0$	Heat of reaction at 25°C, J mol^{-1}
ϵ	Pellet porosity
ε_{bed}	Porosity of the pellet bed
ϵ_{ij}	Component of the strain tensor, m
η	Dynamic viscosity, kg m^{-1} s^{-1}
θ	Polar angle, °
λ	Stress transmission coefficient
λ_r	Regularization parameter
μ	Friction coefficient
μ_s	Coulomb's friction coefficient
$\nu_{i,n}$	Stoichiometric coefficient of species i associated with reaction n
ρ_b	Apparent mass density of the pellet bed, kg m^{-3}
ρ_g	Mass density of the gas, kg.m^{-3}
ρ_p	Apparent mass density of the pellet, kg.m^{-3}
$\tilde{\rho}_s$	Iron oxide molar density, mol.m^{-3}
σ_{ij}	Component of the stress tensor, Pa
σ_v	Vertical normal stress, Pa
σ_w	Horizontal normal stress at the wall, Pa
τ	Characteristic time, s
τ_s	One-dimensional shear stress, Pa
τ_w	Shearing stress at the wall, Pa
τ_{ij}	i-th and j-th component of the stress deviator tensor, Pa
τ_0	Yield stress, Pa
Φ_s	Solid internal friction angle, °
Φ_w	Wall-solid friction angle, °

Subscripts

app	Apparent
chem	Local chemical reaction
diff	Gas diffusion in the pores
e	Effective
eq	Equilibrium
ext	Gas external diffusion
g	Gas
grav	gravity
ini	initial
interc, intrac	intercrystallite or intracrystallite
interg, intrag	intergrain or intragrain
mod	modified
pyc	pycnometry
r	radial coordinate
s	solid
tot	total
v	vertical
w	wall
X	oxide conversion degree
z	Axial coordinate
z_0	Stress saturation depth, m

Résumé en Français

Contexte et enjeux

L'intensification des activités humaines exerce une pression croissante sur la biosphère, que ce soit par l'artificialisation des terres, le rejet dans la nature de substances chimiques et plastiques, ou l'émission de gaz à effet de serre (GES). En conséquence, des phénomènes comme le réchauffement climatique bouleversent les sociétés humaines. Les rapports du GIEC[1] montrent que l'augmentation rapide de la concentration de GES est due principalement aux activités humaines, et qu'elle résultera en une augmentation de la température moyenne de la planète estimée entre +1,4 °C et +4,4 °C d'ici la fin du XXIe siècle [1].

Entre 1990 et 2023, les émissions globales de GES ont augmenté de 62 % tandis que celles associées à la combustion et aux procédés industriels ont augmenté de 91 % sur la même période [2]. L'industrie sidérurgique est particulièrement émettrice de GES: la production d'acier a émis 3,6 Gt de CO_2 en 2023, soit près de 7 % des émissions anthropiques annuelles mondiales [3]. La sidérurgie repose historiquement sur la filière haut-fourneau-convertisseur à oxygène (BF-BOF), dans laquelle s'opère successivement la réduction des oxydes de fer présents dans le minerai par du monoxyde de carbone, issu de la combustion du coke, puis la conversion du métal liquide en acier. A chacune de ces étapes d'importantes quantités de CO_2 sont émises dans l'atmosphère.

Une filière alternative, développée depuis les années 1970, consiste en la réduction directe du minerai de fer (DR) à l'état solide par un gaz réducteur, associée à un four à arc électrique (EAF) pour convertir le fer ainsi obtenu en acier. Le gaz réducteur employé est un mélange H_2-CO, issu du gaz naturel ou du charbon, appelé syngaz. Les émissions de cette filière sont moindres que celles de la filière BF-BOF (1,4 t_{CO_2}/t_{acier} au lieu de 2,2 t_{CO_2}/t_{acier}, [4]), mais elle reste tributaire des énergies fossiles. Pour finir, la production d'acier peut également se faire par recyclage de ferrailles dans les EAF, ce qui est bien moins émetteur (0,3 t_{CO_2}/t_{acier}[5]), mais ne peut malheureusement pas suffire à couvrir la demande mondiale en acier, en raison du manque de disponibilité de ferrailles de haute qualité.

Dans ce contexte, la réduction directe des minerais de fer dans un four à cuve (DRSF) utilisant de l'hydrogène pur, plutôt que du syngas, apparaît comme une solution de premier choix pour décarboner l'industrie sidérurgique. En effet, la réduction des oxydes de fer par de l'hydrogène ne rejette que de l'eau. Sous réserve que cet hydrogène soit produit de façon décarbonée, c'est-à-dire qu'il soit issu par exemple de l'électrolyse de l'eau en employant de l'électricité renouvelable ou nucléaire, les émissions associées à la fabrication d'acier peuvent alors être limitées à environ 0,3 t_{CO_2}/t_{acier} [5], soit un niveau d'émissions comparable à celui du recyclage. De nombreux projets industriels européens se sont engagés dans cette voie : SALCOS en Allemagne ainsi que HYBRIT et STEGRA en Suède développent ainsi des pilotes et des unités de grande capacité à horizon 2027.

Cette bascule technologique s'appuie sur une succession de travaux de recherche, parmi lesquels le projet européen ULCOS et le projet français VALORCO, qui ont permis de mieux comprendre les

[1] Le Groupe International d'Experts du Climat (GIEC) est un organisme des Nations Unies qui réunit des experts chargés de comprendre et de prédire l'évolution du climat, dictée en partie par les activités humaines.

mécanismes fondamentaux de la réduction à l'hydrogène ainsi que le fonctionnement des fours à cuve à hydrogène (H_2-DRSF). La présente thèse s'inscrit dans la continuité de ces études antérieures et elle est conduite dans le cadre du projet européen, MaxH2DR, dont l'objectif est l'étude de la réduction directe du minerai de fer en four à cuve, sous atmosphère riche en hydrogène (>85% en composition), depuis l'échelle d'une boulette de minerai de fer jusqu'à l'échelle d'une usine de fabrication de DRI.

Ce manuscrit est structuré en quatre chapitres. Tout d'abord, nous présentons nos résultats sur la cinétique de réduction des boulettes de minerai de fer par H_2 dans le Chapitre I. L'évolution de la microstructure des boulettes en cours de réduction est ensuite abordée dans le Chapitre II. Le procédé de réduction à l'échelle du four fait l'objet du Chapitre III et, pour terminer, un modèle de rhéologie permettant de mieux décrire l'écoulement des boulettes dans le DRSF est présenté dans le Chapitre IV.

Chapitre 1 : Cinétique de réduction de boulettes de minerai de fer par un gaz riche en hydrogène

La réduction des oxydes de fer par H_2 ou CO se déroule en 3 étapes au-dessus de 570°C ($Fe_2O_3 \rightarrow Fe_3O_4 \rightarrow FeO \rightarrow Fe$). L'hématite est réduite quasi-immédiatement, alors que la réduction de la magnétite et de la wüstite est plus lente. D'autres réactions peuvent entrer en jeu, notamment la réaction du gaz à l'eau (WGSR), le dépôt de carbone par CO ou CH_4, et le reformage de CH_4 par H_2O ou CO_2.

La réduction par H_2 est fortement endothermique alors que celle par CO est légèrement exothermique. Ainsi, de hautes températures favorisent la réduction par H_2, et de basses températures favorisent la réduction par CO. En conditions de réduction isotherme, plus le rapport H_2:CO est élevé, plus la réduction est rapide. En conditions de réduction non-isotherme, l'énergie libérée par les réactions de réduction par CO apporte l'énergie nécessaire aux réactions par H_2. De manière générale, la réaction du gaz à l'eau a peu d'effet sur la cinétique, alors que le dépôt de carbone par CO peut fortement réduire la vitesse de réduction.

La vitesse de réduction des boulettes de minerai de fer peut être contrôlée par différents processus physicochimiques : la diffusion de H_2 dans le gaz externe, la diffusion de H_2 dans les pores de la boulette et les réactions chimiques proprement dites. Chacun de ces processus physiques est associé à un temps caractéristique τ_k. Pour décrire la réduction des boulettes, l'étude des courbes de réduction ainsi que l'observation de boulettes réduites nous ont menés à développer un modèle de grains couplé à la loi des temps caractéristiques additifs (GM-LART). Ce modèle considère la réduction à l'échelle des grains d'oxyde, qui réagissent selon le schéma du cœur rétrécissant (SCM). A l'étape de la wüstite, les grains se subdivisent en cristallites avant d'être finalement convertis en fer dense (Figure 1). Pour chaque réaction de réduction, la vitesse de réduction prend alors la forme suivante :

$$v_X = \frac{1}{\sum_k \tau_k f_k(X)} \qquad (1)$$

où f_k est une fonction associée à chacun des processus.

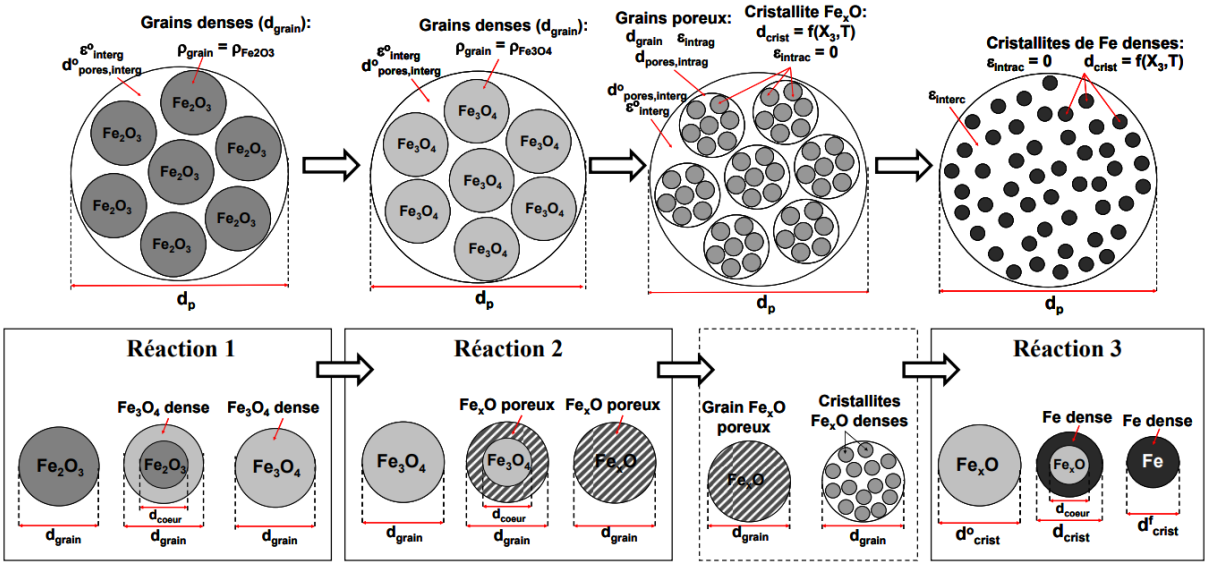

Figure 1: Schéma représentant les étapes successives de réduction d'une boulette de minerai de fer, à l'échelle de la boulette (en haut) et à l'échelle des grains puis des cristallites (en bas).

Les travaux présentés dans l'Article 1 (reproduit en section I.3) étendent le domaine d'application de ce modèle en prenant en considération l'appauvrissement de l'atmosphère réductrice en H_2 (ou CO) lors d'expériences de thermogravimétrie. Au travers d'expériences de réduction de boulettes de taille standard (d_p = 13 mm) entre 600°C et 900°C, nous montrons que la cinétique de réduction est fortement influencée par la température, la taille des boulettes, la pression du gaz ainsi que son débit et sa composition. Un modèle de grains modifié est proposé (MGPM), où la thermobalance et la boulette sont discrétisées en 1D pour prendre en compte l'approvisionnement du four en H_2 ainsi que sa consommation par les réactions de réduction. Ce modèle se montre pertinent et robuste pour simuler aussi bien la réduction de boulettes dans une thermobalance que dans un lit fixe de laboratoire. Les constantes cinétiques de chaque sous-réaction sont obtenues par calibrage du modèle avec les courbes expérimentales à l'aide d'un algorithme de recherche aléatoire. Ce modèle se montre ainsi capable de simuler la réduction de boulettes dans une large gamme de conditions opératoires (température, pression, débit de gaz, composition du gaz, etc.). Une étude numérique montre ensuite que la cinétique de réduction est également sensible aux caractéristiques du réseau poreux interne des boulettes, comme la tortuosité, l'aire spécifique et, dans une moindre mesure, la porosité des boulettes.

En complément de l'Article 1, d'autres expériences de réduction ont permis l'étude des phénomènes de ralentissement cinétique observés à différentes températures. En effet, si la vitesse de réduction des boulettes augmente globalement avec la température, les vitesses de réduction mesurées à 700°C et 950°C en fin de réduction sont particulièrement lentes. Des explications liées à la faible porosité intragranulaire du fer à 700°C ainsi qu'à la lente diffusion de l'oxygène dans le fer gamma formé au-dessus de 912°C sont proposées. Par ailleurs, les vitesses de réduction mesurées au-delà de 1000°C sont anormalement élevées, ce qui est vraisemblablement en lien avec la formation de fissures lors de la réduction à haute température.

Chapitre 2 : Évolution de la microstructure de boulettes de minerai de fer lors de la réduction par H_2

Comme démontré dans l'Article 1 (section I.3), la cinétique de réduction est fortement tributaire de la microstructure poreuse des boulettes de minerai de fer. Dans ce chapitre, nous explorons cette problématique à travers un deuxième article qui traite de la caractérisation de boulettes réduites à différentes températures (600°C – 900°C) après des expériences de réduction complète (X = 100%) ainsi que des expériences dites « interrompues » (X = 15%, 30%, et 50%). Pour ce faire, nous avons effectué des mesures de porosité, d'aire spécifique et de distribution de taille de pores par des méthodes de porosimétrie au mercure (MIP) et d'adsorption gazeuse au Krypton.

Ces mesures indiquent que nos boulettes présentent initialement une seule population de pores de taille micrométrique (P1). La réduction des oxydes de fer par H_2 transforme profondément la microstructure des boulettes : l'aire spécifique a_{sp} augmente fortement au début de la réduction, en lien avec la formation de pores fins (P2). Ceux-ci disparaissent ensuite (X = 30-50%) au profit d'une troisième population de pores caractéristique de la phase fer (P3), qui apparaît d'abord à la surface de la boulette, puis se propage vers le cœur. A la fin de la réduction, seules les populations (P1) et (P3) subsistent, ce qui indique des phénomènes de coalescence de pores ou de frittage des pores (P2). Par ailleurs, les pores (P2) et (P3) formés en cours de réduction sont bien plus larges aux températures plus élevées, en accord avec les observations au microscope électronique présentées dans la littérature, cf. par exemple [6].

Le retrait progressif de l'oxygène initialement présent dans la boulette conduit à une augmentation de la porosité au cours de la réduction. Les valeurs de porosité mesurées et calculées théoriquement diffèrent car l'évolution de la porosité calculée ne prend pas en compte le gonflement de la boulette à haute température, la potentielle ouverture ou fermeture des pores en cours de réduction, ainsi que la formation de fer en surface aux faibles degrés de conversion.

Cette caractérisation macroscopique offre néanmoins diverses pistes à approfondir pour mieux comprendre l'évolution de la structure poreuse des boulettes en cours de réduction par H_2. Des observations à l'échelle microscopique seraient cependant nécessaires pour être mesure de valider ou d'invalider les hypothèses présentées ici.

Chapitre 3 : Comportement thermochimique d'un four à cuve fonctionnant sous atmosphère enrichie en hydrogène

Dans ce chapitre, les mécanismes fondamentaux de la réduction des boulettes à l'hydrogène étudiés dans les 2 premiers chapitres sont exploités pour la modélisation d'un four à cuve industriel. L'outil central de cette approche est le code REDUCTOR, développé au sein de notre équipe depuis une vingtaine d'années et adapté ici pour représenter au mieux les conditions d'enrichissement en hydrogène.

REDUCTOR est basé sur un modèle stationnaire en deux dimensions (r,z) discrétisé par la méthode des volumes finis et conçu pour décrire le fonctionnement de fours à cuve de type HYL/MIDREX avec un gaz réducteur H_2-CO. Le code résout des bilans de matière, de quantité de mouvement et d'énergie pour les espèces solides présentes dans le minerai (Fe_2O_3, Fe_3O_4, $Fe_{0.95}O$, Fe, gangue) et pour les espèces gazeuses (H_2, H_2O, CO, CO_2, CH_4, N_2). Un sous-modèle basé sur le MGPM présenté précédemment (section I.3) permet de calculer la vitesse des réactions de réduction ainsi que la vitesse des réactions secondaires. Par ailleurs, l'implémentation dans le cadre de cette étude d'un algorithme de type SIMPLE pour la résolution couplée des bilans de

matière et de quantité de mouvement pour le gaz a conduit à un bien meilleur bouclage des bilans globaux de masse et d'énergie.

Dans l'Article 3 (section III.2.1), des solutions innovantes sont présentées pour réduire la consommation énergétique d'un four à cuve 100% H_2, qui est particulièrement importante en raison de l'endothermicité des réactions de réduction par H_2,. Cette endothermicité est en outre à l'origine de la formation d'une zone centrale de basse température et pauvre en hydrogène qui n'est pas favorable au bon fonctionnement du réacteur. Pour pallier ce problème, il est ainsi proposé de :

- rediriger une partie du gaz réducteur vers une seconde injection de gaz froid située dans la partie inférieure du four ;
- ajouter une quantité importante de N_2 chaud au mélange gazeux ;
- introduire les boulettes chaudes dans le four.

Ces trois solutions conduisent à une baisse substantielle de la demande énergétique du procédé. Il est également montré que pour un four 100% H_2, passer de 94% à 100% de métallisation des boulettes en sortie est possible au prix d'un coût énergétique additionnel relativement faible.

En complément de cet article, d'autres simulations sont présentées. On montre tout d'abord que l'augmentation du débit solide d'un four 100% H_2 conduit à une baisse importante de la métallisation causée par le manque d'énergie thermique évoqué plus haut. Une solution très efficace pour augmenter la performance d'un four à cuve de ce type est alors d'injecter une partie du gaz réducteur dans un dispositif appelé « Christmas tree », placé au centre du four dans la partie inférieure de la zone cylindrique (Figure 2). En uniformisant l'apport d'énergie thermique et de gaz réducteur au sein de la cuve, ce dispositif permet des gains importants en termes de métallisation sans augmenter la demande énergétique.

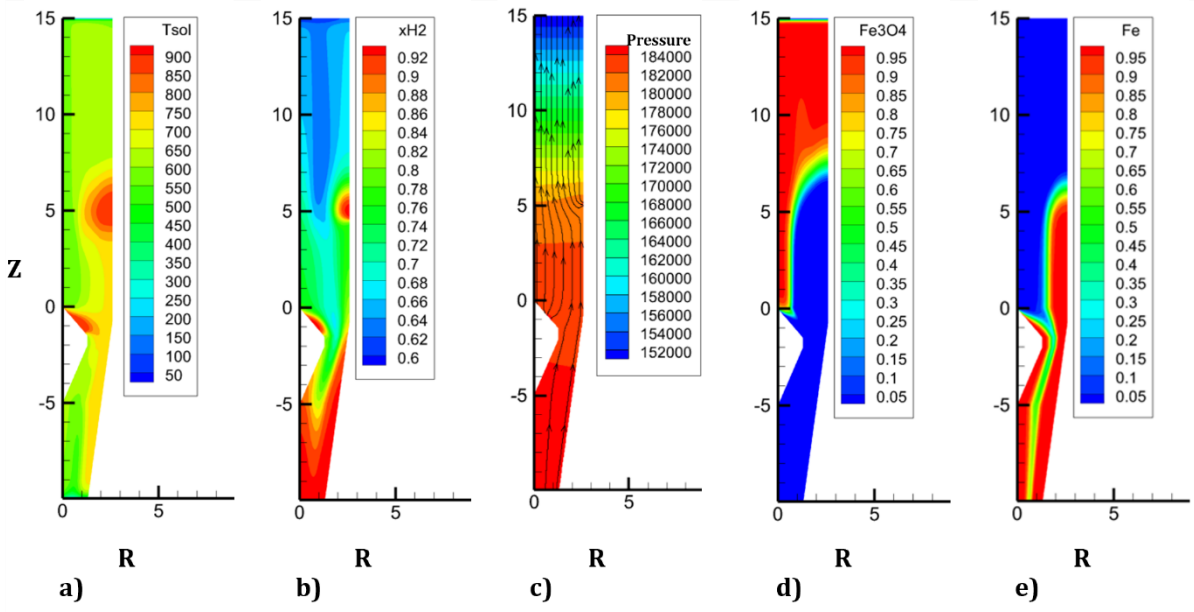

Figure 2: Variables de procédé pour l'opération d'un four à cuve 100% H_2 équipé d'un Christmas tree et d'une injection de gaz centrale. W = 50 kg/s, M = 96%.

L'opération d'un four à cuve avec des niveaux d'enrichissement en H_2 moindre est ensuite étudiée pour deux cas distincts :

- un cas d'enrichissement modéré où le gaz contient 55% H_2 et 45% CO. Ces conditions opératoires autorisent une production supérieure qui s'explique par une excellente distribution de température au sein de la cuve aidée par l'apport énergétique de la réduction par CO ;
- un cas d'enrichissement élevé où le gaz contient 80% H_2 et 20% CO. Dans ce cas, la production est à mi-chemin entre les cas 100% H_2 et 55% H_2 et la présence du Christmas tree conduit à une meilleure distribution de température, qui améliore grandement la métallisation.

L'utilisation de CO se fait cependant au prix d'une forte augmentation des émissions de CO_2. Par ailleurs, plus le taux d'hydrogène est élevé, plus l'homogénéisation des températures par la présence d'un dispositif de type Christmas tree est efficace.

Chapitre 4 : Écoulement de boulettes dans un four à cuve

L'écoulement des boulettes dans un four à cuve a été relativement peu étudié. En revanche, une riche littérature existe dans un domaine analogue, qui est l'écoulement d'un solide granulaire dense dans un silo. Un tour d'horizon de cette littérature permet de classer les différentes approches couramment utilisées dans ce domaine en trois catégories :

- les approches analytiques développées au cours du XXe siècle, qui se basent le plus souvent sur une discrétisation du four en tranches horizontales infinitésimales. Un bilan de forces appliqué à ces tranches permet d'obtenir une distribution des contraintes dans le four. D'autres approches analytiques cherchent à déterminer les distributions de vitesse par des considérations stochastiques ou énergétiques, ou à prédire le débit de vidange par une loi empirique, comme la loi de Beverloo ;
- les approches continues, qui se basent sur une discrétisation plus poussée en éléments ou en volumes finis. Le milieu granulaire est souvent modélisé par un fluide non-Newtonien dont l'écoulement est prédit par les équations de Navier-Stokes. En parallèle, d'autres approches de mécanique des sols assimilent le milieu granulaire à un solide qui subirait une déformation plastique ininterrompue, caractérisée par des états critiques de déformation. Les deux approches (fluide et solide) donnent des résultats très satisfaisants pour la simulation de la vidange de silos ;
- les approches discrètes (DEM), qui considèrent les interactions entre des particules individuelles à travers des modèles de force et de couples.

Les trop nombreuses hypothèses simplificatrices sur lesquelles se basent les modèles analytiques les limitent à une analyse qualitative des distributions de contraintes et de vitesse. Par ailleurs, le coût de simulation trop élevé des méthodes DEM les disqualifie également. L'approche retenue ici se base sur un modèle de fluide non-Newtonien doté d'une rhéologie $\mu(I)$, qui attribue au milieu granulaire une friction variable selon la pression et le taux de cisaillement local. Cette approche donne des résultats très satisfaisants pour l'écoulement de solides granulaires dans les silos [7].

La résolution numérique de l'écoulement avec un tel modèle présente des difficultés en raison du haut degré de non-linéarité des équations, particulièrement en état stationnaire. Pour assurer la convergence du code, le calcul de la pression induit par le poids du lit s'appuie ici sur des modèles analytiques. Par ailleurs, l'équation de comportement du fluide est régularisée suivant le modèle

de Papanastasiou [8, 9], et un deuxième algorithme SIMPLE permet d'assurer de bons bilans de matière et de quantité de mouvement.

En choisissant minutieusement les paramètres du modèle, des profils de vitesse proches de ceux observés en DEM sont obtenus. Les performances de ce modèle paraissent dépasser les modèles utilisés précédemment dans REDUCTOR, comme le modèle piston ou le modèle cinématique. Cependant, ce modèle reste exploratoire : la résolution complète du champ de pression ainsi que la prise en compte des systèmes de vidange des fours à cuve industriels (à vis, à roue, etc.) sont nécessaires pour passer de résultats qualitatifs à des résultats quantitatifs.

Conclusion générale et perspectives

Ce travail explore divers aspects de la réduction de boulettes de minerai de fer par H_2 dans un four à cuve, de l'échelle des grains d'oxyde de fer jusqu'à l'échelle du four. L'objectif principal est d'identifier les changements de comportement des fours à cuve lorsqu'on augmente la teneur en H_2 du gaz réducteur et de proposer des solutions innovantes lorsque ces changements de comportement sont négatifs.

La cinétique de réduction des boulettes par H_2 est fortement influencée par la température, la pression, la composition du gaz, son débit et la taille des boulettes. Les résultats des expériences de réduction isotherme réalisées en thermobalance ont servi pour développer un modèle robuste de prédiction de la vitesse de réaction aux différents stades de la réduction. Par ailleurs, la caractérisation de boulettes partiellement ou complètement réduites nous a permis de mieux comprendre l'évolution de la microstructure en cours de réduction. Des pores fins apparaissent en début de réduction avant de disparaître, et leur taille croît de manière importante avec la température. Tous ces résultats, plus des modifications numériques, ont été réutilisés pour perfectionner le modèle de four à cuve REDUCTOR développé précédemment. De l'exploitation de ce modèle découle qu'en dépit de la forte demande énergétique du four 100% H_2, de nombreuses voies d'amélioration existent, principalement en augmentant ou en uniformisant l'apport d'énergie thermique et de gaz réducteur. Enfin, la base d'un modèle rhéologique pour la simulation de l'écoulement des boulettes dans le four a été posée. Ce modèle tient compte des contraintes locales de pression et de cisaillement de la matière granulaire. Tous ces résultats contribuent à mieux appréhender le comportement d'un futur four à cuve 100% H_2, encore inexistant à l'échelle industrielle.

Plusieurs pistes restent encore à explorer pour l'optimisation du procédé de réduction directe. La fissuration et le gonflement des boulettes aux hautes températures est encore difficile à modéliser, ainsi que l'évolution de la structure des boulettes les plus grosses. A plus long terme, la comparaison du modèle avec des expériences de réduction non-isotherme et la caractérisation de boulettes réduites dans ces conditions est cruciale pour pouvoir prédire le comportement de boulettes dans un four à cuve. D'ailleurs, les données industrielles de fours à cuve 100% H_2 sont grandement attendues afin de pouvoir valider le modèle REDUCTOR pour ces conditions opératoires. Parmi les pistes d'optimisation du procédé, le rôle prépondérant de la localisation des injections de gaz (centrales, latérales) est encore à explorer. Enfin, en lien avec la déplétion des ressources d'hématite mondiale, la cinétique de réduction de minerais de fer alternatifs (magnétite, goethite, etc.) devrait être étudiée.

General Introduction

The intensification of human activity worldwide puts the equilibrium of the biosphere into question. Lesser land is left for wildlife to flourish while more and more waste is discharged into untouched environments: chemicals, plastics and greenhouse gases (GHG) that disrupt ecosystems globally. In turn, this disruption of the biosphere poses a threat to the stability of human societies. The most dramatic example among these issues is the global warming. It was shown by IPCC[2] that the human activities have undoubtedly had a major impact on the climate, mostly due to the emission of greenhouse gases. The accumulation of these gases in the atmosphere leads to a global increase in temperature, which is projected between +1.4°C and +4.4°C by the end of the 21th century [1].

The global anthropogenic GHG emissions increased by 62% between 1990 and 2023, and the sole emissions of the industrial combustion and process sector increased by 91% in the same duration [2]. This sector includes most heavy industries, such as cement, alumina, chemicals and steel industries. In 2023, the production of crude steel led to the release of the equivalent of 3.6 Gt of CO_2 in the atmosphere. This accounts for almost 7% of the total anthropogenic GHG emissions this year [2, 4, 10]. The steelmaking industry and the origin of its associated GHG emissions (mostly CO_2) are presented below.

Iron is present in the nature in its oxidized form, mostly as hematite (Fe_2O_3) or magnetite (Fe_3O_4). To be suitable for most uses, oxygen has to be removed from these minerals. This chemical transformation of iron oxides is called reduction and it converts iron oxides into pure iron. It is often coupled with iron carburization, that is the incorporation of carbon into the iron matrix to increase its strength and produce casts or steels. Both reduction and carburization are usually done with carbon monoxide (CO), obtained from the partial combustion of coal, and this results in huge emissions of CO_2.

The main process route of the steelmaking industry revolves around the operation of the blast furnace (BF), which has been the historical way to reduce iron oxides at industrial scale since 1875. The base materials used in a BF are iron oxides, coal and fluxes. Prior to its introduction in the furnace, most of the iron oxide feedstock is processed into sinter or pellets to increase its porosity and strength. The rest is added as lump ore that helps with gas permeability, see Figure 3. In the same way, most of the coal is processed into coke, which presents an excellent mechanical strength in the BF. Some pulverized coal is also injected at the tuyeres of the furnace with the so-called blast (mostly hot air). Iron oxides and coke are loaded alternatively at the top of the furnace, forming a succession of stacked layers. Finally, fluxes are added to the burden to promote the formation of the slag, which is a mixture of melted impurities surrounding the hot liquid metal.

[2]The Intergovernmental Panel on Climate Change (IPCC) brings together groups of scientists who share expertise on climate change. It is a body of the United Nations.

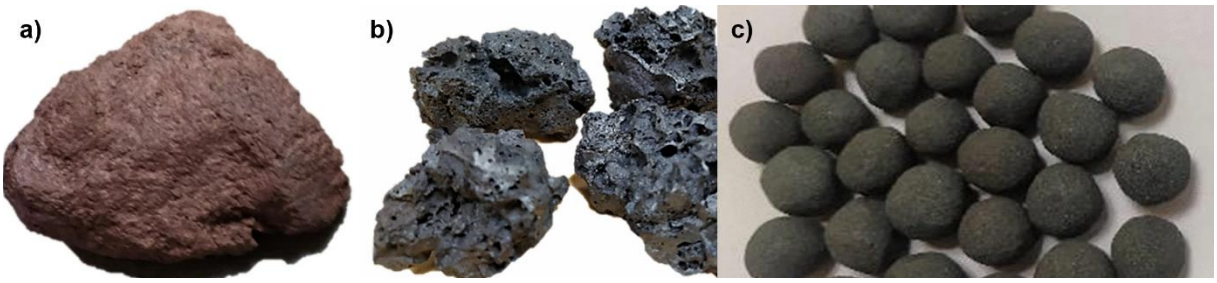

Figure 3: Iron oxide feedstock used in blast furnaces, **a)** lump ore **b)** sinter and **c)** pellets [11] with approximate size d_p ~ 12 mm.

The descending burden starts melting before reaching the bottom of the furnace, at which point the slag separates itself from the hot liquid metal, see Figure 4. The heat and reducing gas are produced by the partial combustion of the coke and pulverized coal by the hot blast, which provides oxygen. The hot metal is then sent to a converter to produce steel, while the slag can be valorized elsewhere. The most common type of converter is the basic oxygen furnace (BOF), which transforms the hot liquid cast into steel by lowering its carbon content under 1.5% in weight. This is done by injecting high temperature oxygen into the bath of the converter, which oxidizes part of the dissolved carbon and releases CO and CO_2.

Though this route is known for centuries and industrially developed since the first industrial revolution, the BF-BOF is not the only process route available for the production of cast and steel. The abundance of cheap natural gas (NG) and the development of the electric arc furnace technology (EAF) in the 70's paved the way for a second route for steel production based on direct reduced iron (DRI-EAF)[12]. Contrarily to the BF, the direct reduction (DR) processes reduce the iron ore directly at the solid state (hence the name direct reduction) in dedicated reactors such as shaft furnaces or rotary kilns. For these processes, the iron oxide feedstock is mainly constituted of pellets that present a great flowability, with a possible addition of lump ore. The reducing gas is a mixture of the two reducing agents CO and H_2, which is called syngas. This syngas is produced either by coal gasification in rotary kilns or NG reforming in shaft furnaces. When using natural gas, the reforming may take place in a reformer reactor prior to the gas injection inside the shaft or directly inside the shaft furnace, depending on the technology. Additionally, fluxes are added to the iron oxide feedstock to prevent the pellets from sticking together and obstruct the solid outlet.

In a direct reduction shaft furnace (DRSF), the iron oxides are introduced at the top of the furnace (Figure 5), while the hot reducing gas is injected sideways in the reduction zone. Additionally, room temperature NG is introduced in the cooling zone to cool down and carburize the pellets. The DRI produced is usually transferred to an EAF where it is melted with additives (lime, carbon, coke…) to produce steel.

The BF-BOF and DRI-EAF routes respectively share 70% and 5% of the global steel production [3, 4]. The rest of the production is ensured by the recycling of steel scraps in EAF. In this case, no prior reduction step is needed.

In the recent years, the steelmaking Industry has been looking for alternative processes to mitigate its massive CO_2 emissions. Indeed, the CO_2 emission intensities of the main production routes reach 2.2 $t_{CO_2}/t_{\text{crude steel}}$ for the BF-BOF route and 1.4 $t_{CO_2}/t_{\text{crude steel}}$ for the DRSF-EAF route [4]. Scrap-based EAF generates much less CO_2, 0.3 $t_{CO_2}/t_{\text{crude steel}}$, since most emissions in the other processes derive from the reduction step, which is avoided here. However, the

availability of high-quality scraps is not sufficient to meet the global steel demand, which is expected to continue to grow, and steel production from ore will remain necessary.

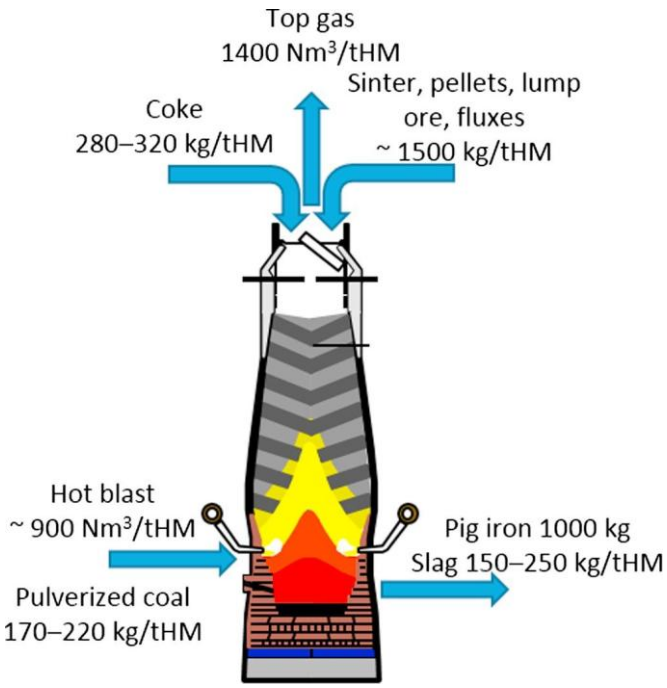

Figure 4: Simplified flowchart of a blast furnace [13].

In this context, the use of pure H_2 instead of syngas as reducing agent in DRSF is seen as a great opportunity to mitigate the CO_2 emissions of the iron and steelmaking industries. Indeed, the reduction process with pure hydrogen only releases H_2O. If H_2 is produced in a decarbonized manner, so called green H_2 produced from water electrolysis and renewable electricity, the CO_2 emissions of the whole process could be dramatically reduced down to 0.3 $t_{CO_2}/t_{\text{crude steel}}$ [14]. The injection of H_2 in the BF is also possible but with limited effect, as coke is needed for maintaining the structure of the burden inside the reactor: the potential for reducing the CO_2 emissions is thus limited to 20% [5] in the BF route.

This promising technology incited the industry to start innovative projects in the early 2020s. Those projects rely on the production of green hydrogen from water electrolysis, which is then heated electrically and used as a reducing agent in a DRSF. The resulting DRI is next melted in an EAF to produce steel. These projects are now moving from pilot scale to industrial scale. In Germany, high-temperature electrolysis and wind energy were used to power a small-scale DRSF in the SALCOS project, which produces 0.876 kt_{DRI}/year. In Sweden, the abundance of decarbonized electricity encouraged the construction and operation of a pilot plant with a production capacity of 15 kt_{DRI}/year in the HYBRIT project. For the same reasons, a greenfield plant is currently under construction by STEGRA in Boden, with a planned capacity of 5000 kt_{DRI}/year in 2027.

Prior to these industrial projects, a series of international projects had already considered the operation of a H_2-DRSF. The European ULCOS project (2004-2010) was pioneer in designing novel C-lean processes for steel production. In this context, the first work on the reduction of iron ore by H_2 in our team at Université de Lorraine (UL) was that of D. Wagner. He determined the kinetics and mechanisms that govern the H_2 reduction of small hematite cubes (5 mm in edge). Wagner

modeled the reduction zone of a shaft furnace in a 2D finite-volume framework and programed this model as an in-house computer code called REDUCTOR [17]. This study was later pursued by A. Ranzani Da Costa (UL), who perfectioned the kinetic model and the computer code after an in-depth experimental study of the reduction of industrial pellets [18]. These works relied heavily on the characterization of DRI with X-ray diffraction, porosity measurements and scanning electron microscopy. Further work was presented by H. Hamadeh (UL) in the French project VALORCO. Hamadeh improved the kinetic model by considering the CO reduction as well as multiple side reactions that can occur in a shaft furnace e.g., carburization or gas reforming. The operation of a DRSF with both reduction and cooling zones was modeled successfully compared with some plant data [16].

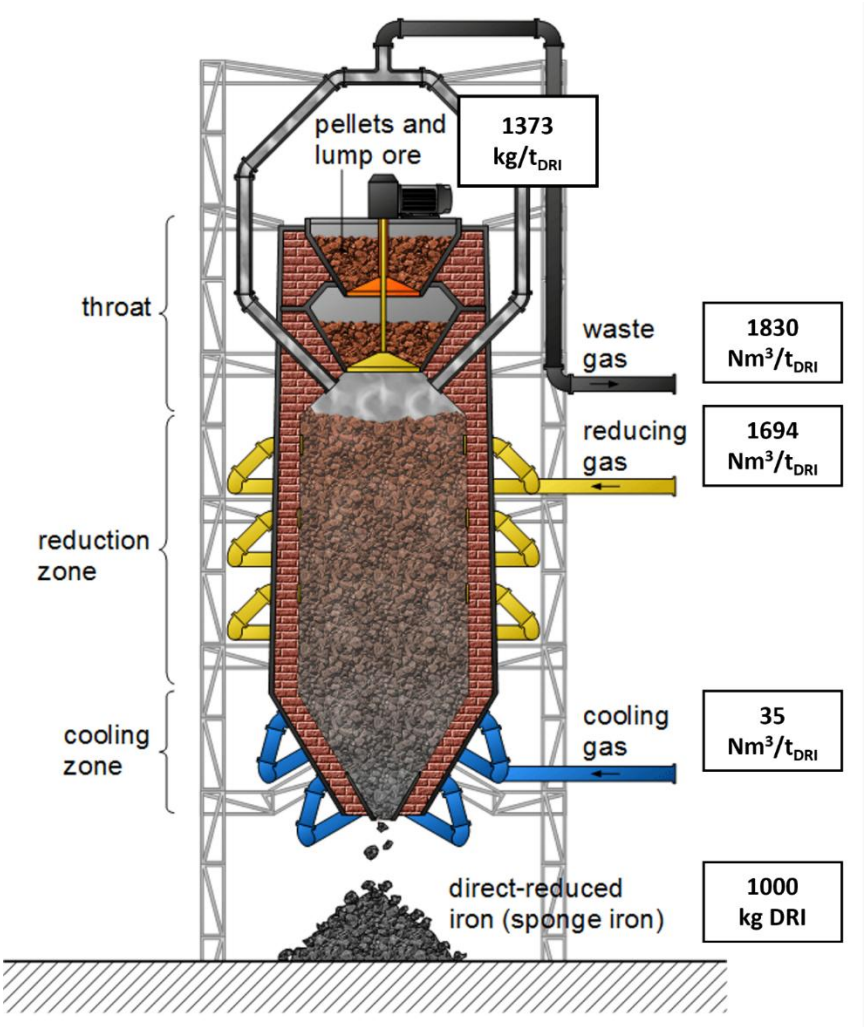

Figure 5: Simplified flowchart of a direct reduction shaft furnace (DRSF) [15]. The figures added are those of a HYL III type furnace [16].

The present work is part of the ongoing European project MaxH2DR (**Max**imize **H**ydrogen Enrichment in **D**irect **R**eduction Shaft Furnaces) funded by the European Commission in the frame of Horizon Europe programme [19]. This project aims at filling the knowledge gap in the reduction of iron ore with H_2-rich gas and to incorporate this knowledge into appropriate models for process simulation purposes. UL contributes to two work packages inside this project and brings state-of-the-art knowledge and skills. The first work package is devoted to the study of properties and

reduction kinetics of single pellets. The second work package addresses process simulation of the shaft furnace with the REDUCTOR code.

New reduction experiments at the pellet scale were led to offer an improved version of our kinetic model, which was then shared with partners of the MaxH2DR project. The results of these investigations are presented in chapter 1. The mechanisms of H_2 reduction were assessed by a macroscopic characterization of the reduced pellets, and the results are presented in chapter 2. The REDUCTOR code was upgraded in several ways to improve the accuracy of the energy and mass balances, and an exploratory study of some operating solutions for a H_2-DRSF is presented in Chapter 3. This Chapter was complemented by studying the central question of the MaxH2DR project, that is the reducing gas enrichment with H_2. Finally, with the intent to improve the modeling of the solid flow in a DRSF, a continuum model based on a non-Newtonian rheology was implemented in REDUCTOR. The flow patterns of the pellets inside a DRSF were explored, considering different geometries of the shaft, and the results are presented in Chapter 4.

Several papers were prepared in the wake of these investigations, and they were incorporated into this manuscript. Papers 1 and 3 have already been published and are fully reproduced in Chapters 1 and 3, respectively. An unpublished version of Paper 2 is also presented; it is planned for publication after the submission of the present manuscript.

I. The kinetics of reduction of iron ore pellets by hydrogen-rich gas mixtures

I.1. Introduction

As addressed in the general introduction, one objective of the MaxH2DR project is to accurately model the reduction of iron ore pellets with hydrogen. In this chapter, the fundamental phenomena that govern the kinetics and thermodynamics of the reduction are investigated. A mathematical framework for gas-solid reactions and a new robust kinetic model are then presented. This model and the associated experimental results were the object of a paper (Article 1) submitted to Metals and reproduced in section 3. A number of additional results on the reduction of iron oxides are given in the last section of this chapter.

I.1.1. The reduction of iron oxides

Mined iron ores come under a variety of forms to the iron and steel industry: iron ore fines in fluidized bed reactors (d_p = 0.1-0.5 mm), sinter agglomerates in blast furnaces (d_p = 12-35 mm), porous pellets in blast furnaces and shaft furnaces (d_p = 10-15 mm), and dense lump ore (d_p = 6-30 mm). This variety of forms corresponds to a variety of properties in use: fines show excellent heat transfer properties, sinter has considerable mechanical strength, and both are cheap. On the other hand, lump ore maintains good gas permeability of the burden and pellets show great flowability in blast furnaces and direct reduction shaft furnaces (DRSF). In the following, we will take interest only in the reduction of iron oxides processed under the form of spherical pellets.

The reduction of iron oxides refers to the conversion of Fe_2O_3 or Fe_3O_4 oxides to Fe by a reductant, in our case a gas, usually H_2 or CO. The reduction from Fe_2O_3 to Fe with H_2 is rather fast but strongly endothermic ($\Delta_r H^0 = 50$ kJ $\mathrm{mol}_{\mathrm{Fe}}^{-1}$), while the reduction with CO is slower and moderately exothermic ($\Delta_r H^0 \sim -12$ kJ $\mathrm{mol}_{\mathrm{Fe}}^{-1}$), as shown in numerous experimental studies [15, 20, 21, 22]. In an industrial shaft furnace, the reducing gas is usually a hot mixture (850–1050°C) of CO and H_2 called syngas, obtained from the reforming of methane. The injection of this hot syngas both ensures the heating of the ore pellets loaded in the shaft and the heat required for the different reactions [23]. The overall reduction reaction can be written as follows:

$$\begin{aligned} Fe_2O_3 + 3H_2 &= 2Fe + 3H_2O \\ Fe_2O_3 + 3CO &= 2Fe + 3CO_2 \end{aligned} \qquad (2)$$

At the microscopical scale, the reduction proceeds in multiple steps: each oxide is successively reduced to a lower oxide until iron is formed. Due to wustite being metastable below 570°C, it is generally considered that the reduction pathway below this temperature is different than at higher temperatures. Reduction pathways below and above 570°C are given in Table 1. Moreover, the reduction subreactions are given in

Table **2**, along with their enthalpy of reaction [24].

Table 1: Reduction pathways of hematite depending on the reduction temperature.

	Successive oxides	Reactions
Below 570°C (CO and H_2)	$Fe_2O_3 \rightarrow Fe_3O_4 \rightarrow Fe$	1-2bis /4-5bis
Above 570°C (CO and H_2)	$Fe_2O_3 \rightarrow Fe_3O_4 \rightarrow Fe_{0.95}O \rightarrow Fe$	1-2-3 / 4-5-6

Table 2: Subreactions for the reduction of iron oxides with H_2 or CO. The heat of reactions are given at 25°C and are taken from [24].

Reaction 1	$3Fe_2O_3 + H_2 = 2Fe_3O_4 + H_2O$	$\Delta_r H^0 \sim 0$ kJ mol_{Fe}^{-1}
Reaction 2	$Fe_3O_4 + \frac{16}{19}H_2 = \frac{60}{19}Fe_{0.95}O + \frac{16}{19}H_2O$	$\Delta_r H^0 = 26$ kJ mol_{Fe}^{-1}
Reaction 2bis	$Fe_3O_4 + 4H_2 = 3Fe + 4H_2O$	$\Delta_r H^0 = 50$ kJ mol_{Fe}^{-1}
Reaction 3	$Fe_{0.95}O + H_2 = 0.95Fe + H_2O$	$\Delta_r H^0 = 24$ kJ mol_{Fe}^{-1}
Reaction 4	$3Fe_2O_3 + CO = 2Fe_3O_4 + CO_2$	$\Delta_r H^0 = -7$ kJ mol_{Fe}^{-1}
Reaction 5	$Fe_3O_4 + \frac{16}{19}CO = \frac{60}{19}Fe_{0.95}O + \frac{16}{19}CO_2$	$\Delta_r H^0 = 12$ kJ mol_{Fe}^{-1}
Reaction 5bis	$Fe_3O_4 + 4CO = 3Fe + 4CO_2$	$\Delta_r H^0 = -17$ kJ mol_{Fe}^{-1}
Reaction 6	$Fe_{0.95}O + CO = 0.95Fe + CO_2$	$\Delta_r H^0 = -5$ kJ mol_{Fe}^{-1}

This separation of the global reduction reaction in multiple subreactions can be noticed when plotting the reduction rate against the conversion degree, as seen in Figure 6. In this plot derived from one of our thermogravimetry experiments, the reaction rate initially increases very rapidly due to the introduction of the reducing gas inside the furnace of the thermobalance (a presentation of thermobalance devices is available in Article 1). The reduction rate is kept very high until hematite is fully converted into magnetite; a monotonic decrease in reaction rate is then associated with the conversion of magnetite into wustite, and another monotonic decrease in reaction rate is eventually associated with the slow reduction of wustite into iron.

The reduction curves shown in Figure 6 were obtained for conditions in which the subreactions take place uniformly across the porous pellet. However, in most cases, due to the limited gas diffusion in the pores of the pellet, the reduction does not proceed uniformly throughout the pellet. This implies that the different steps of the reaction occur simultaneously at different locations inside the pellet. For this reason, appropriate modeling of the pellet structure is needed to correctly assess the kinetics of the reduction – this point will be largely discussed in sections I.2 and I.3 (Article 1).

Aside from the main reduction reactions, a series of side reactions take place when multiple gas components are present around the iron phase. A brief description of these reactions is given in the next subsection.

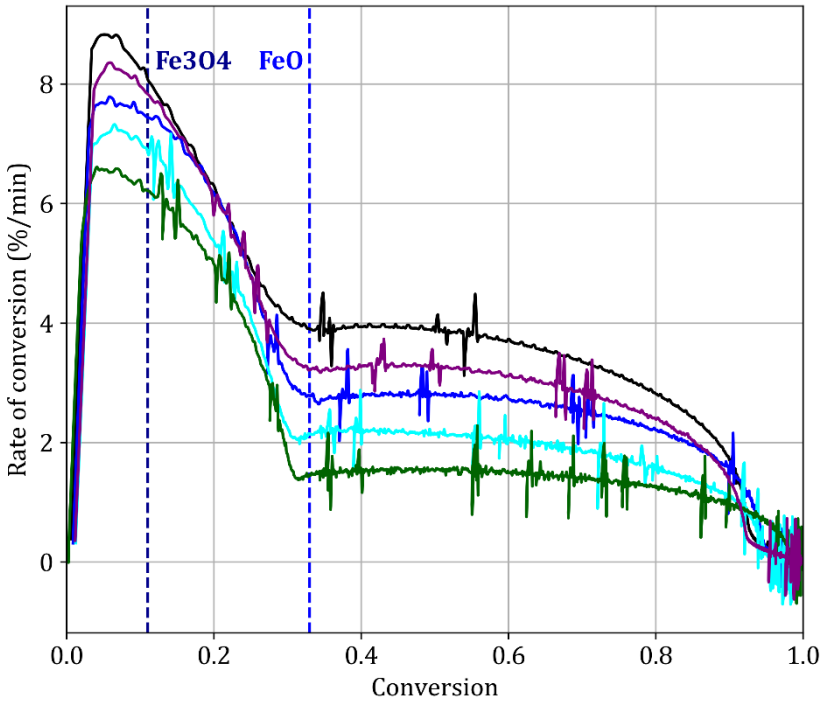

Figure 6: Rate of reduction against conversion for the reduction of iron ore pellets in H_2-H_2O conditions. T = 900°C, d_p = 13 mm, F_g = 0.25 Nlpm. The vertical dashed lines correspond to the theoretical compositions Fe_3O_4 and FeO.

I.1.2. The different reactions in the Fe-O-H-C system

The presence of multiple iron oxides and multiple gas species in industrial reduction units (H_2, H_2O, CO, CO_2, CH_4) brings about a number of reactions that take place simultaneously together with the reduction reactions. The presence of the two redox couples (H_2, H_2O) and (CO, CO_2) leads to the establishment of a redox equilibrium, commonly known as the Water Gas Shift Reaction (WGSR):

Reaction 7 $\quad \mathrm{CO + H_2O = CO_2 + H_2} \quad \Delta_r H^0 = -41 \text{ kJ mol}^{-1}$

Depending on the local equilibrium conditions, this highly reversible reaction can either increase or decrease the H_2:CO ratio of the gas. Its effect on the reduction of pellets in a lab-scale furnace is limited, but it may influence the composition of the gas mixture in a direct reduction shaft furnace (DRSF) [25, 26].

Moreover, the presence of carbon monoxide in the gas may lead to carbon deposition onto the pellets. As pointed out by [27], carbon deposition can only occur if carbon activity is superior to one, and if metallic iron is present (these conditions are addressed in the next subsection). If these conditions are met, carbon deposition can proceed according to the inverse Boudouard reaction:

Reaction 8 $\quad \mathrm{2CO = C + CO_2} \quad \Delta_r H^0 = -86 \text{ kJ mol}^{-1}$

This reaction is favored at low temperatures, high CO contents and high pressures. Small molar fraction of H_2 favor the kinetics of the carbon deposition reactions [28]. This reaction can lead to impressive formation of amorphous carbon under the form of soot, which is considered

detrimental to the DRSF process. To be of industrial interest, the carbon is preferred deposited under the form of metastable cementite Fe_3C [16] in the reduced pellet (Direct Reduced Iron - DRI):

Reaction 8bis $\quad 3Fe + C = Fe_3C \quad \Delta_r H^0 = 8 \text{ kJ mol}^{-1}$

A carburized DRI lowers the energy consumption of the EAF, and helps with the formation of a foaming slag. The conditions for obtaining cementite rather than carbon soot are still unclear.

Another common way to bring carbon in the DRI is to add methane to the gas mix. In industrial DRSF technology, methane is used to cool and carburize the burden in the cooling section. The decomposition of methane proceeds as:

Reaction 9 $\quad CH_4 = C + 2H_2 \quad \Delta_r H^0 = 75 \text{ kJ mol}^{-1}$

Natural gas is also used as the primary source of hydrogen and carbon monoxide in DRSF process to create the so-called syngas. The steam methane reforming reaction (SMR) creates a syngas with high reduction potential:

Reaction 10 $\quad CH_4 + H_2O = CO + 3H_2 \quad \Delta_r H^0 = 206 \text{ kJ mol}^{-1}$

Under appropriate gas conditions and sufficient energy supply, this reaction can happen inside a DRSF. While dry methane reforming (with CO_2 instead of H_2O) is also possible (the syngas is formed that way in the MIDREX reformer), that reaction was not further considered here as its rate is negligible compared to the one of SMR [29].

The result of all these reactions can only be predicted with a robust thermodynamic and kinetic framework. These are introduced in the next two subsections.

I.1.3. Thermodynamical considerations

With a first glance at the reaction enthalpies, it follows from Le Chatelier's principle that reduction reactions 1-3, 2bis and 5 should be favored by higher temperatures, while reactions 4, 5bis and 6 should be favored by lower temperatures. This is in agreement with the equilibria domains drawn on the Chaudron diagram for the (Fe-C-O) and (Fe-H-O) systems, see Figure 7. The equilibria lines were determined based on the temperature and the reducing power of the gas, *i.e.*

$$\frac{x_{H_2}}{x_{H_2} + x_{H_2O}} \text{ or } \frac{x_{CO}}{x_{CO} + x_{CO_2}} \quad (3)$$

It can be seen in Figure 7 that the equilibria domains of each iron oxide are strongly dependent on the gas composition – the lower the concentration of the reducing species (H_2 and CO), the more difficult the reduction reactions. First, under the equilibrium lines in the diagram, the higher oxides are stable. Second, the reaction rates of each subreaction are proportional to the difference between the concentration of the reductant gas and its equilibrium concentration (*e.g.*, $c_{H_2} - c_{H_2,eq}$), which is called the reaction driving force. This point will be further discussed in section I.2.

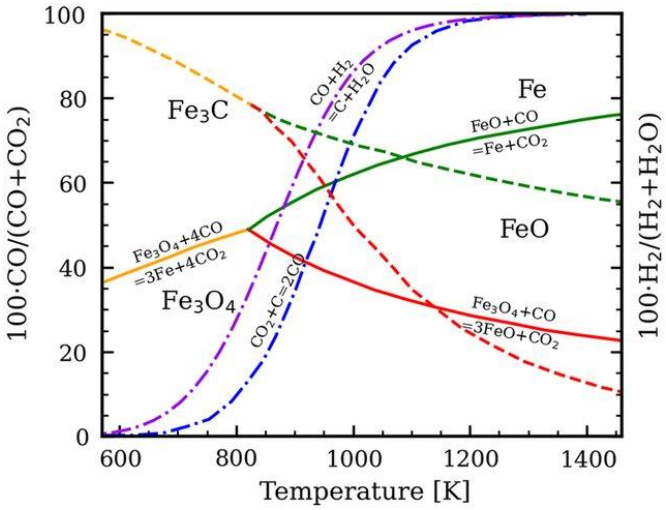

Figure 7: Chaudron thermodynamic diagram for the reduction of iron oxides with H_2 or CO [30]. The solid and dashed lines respectively represent the equilibrium lines of the reduction reactions with CO and H_2. The dash dotted lines represent the equilibria of carbon side reactions. Note: The Fe_2O_3 stability domain is very close to the *x*-axis.

When carbon is present in the system, the Boudouard reaction (represented by the blue dash dotted line in Figure 7) has to be considered. The inverse Boudouard reaction is quite an exothermic carbon deposition reaction. The equilibrium of this reaction and other carbon deposition reactions (reactions 8 and 10) depends on the gas composition and on the carbon activity (a_C), given by the formula of Chipman [31]:

$$\log(a_C) = \frac{2300}{T} - 0.92 + \left(\frac{3860}{T}\right) C + \log\left(\frac{C}{1-C}\right) \tag{4}$$

$$K_{eq,8} = \left(\frac{a_C x_{CO_2}}{x_{CO}^2}\right)_{eq} \tag{5}$$

where C is the ratio of carbon atoms to iron atoms in the solid.

If both carbon and hydrogen are present in the system, the reversible WGSR (reaction 7) will take place. Its equilibrium constant is expressed as:

$$K_{eq,7} = \left(\frac{x_{H_2} x_{CO_2}}{x_{CO} x_{H_2O}}\right)_{eq} \tag{6}$$

The direct reaction is exothermic and favored at low temperatures, which is why it can be of particular importance in the top part of a DRSF [29].

If methane is present in the gas mix, the methane decomposition and SMR reactions presented earlier should also be considered (reactions 9-10). Both of these are considerably endothermic.

$$K_{eq,9} = \left(\frac{a_C x_{H_2}^2}{x_{CH_4}}\right)_{eq} \tag{7}$$

$$K_{eq,10} = \left(\frac{x_{H_2}^3 x_{CO}}{x_{CH_4} x_{H_2O}} \right)_{eq} \quad (8)$$

DRSF processes usually require the carburization and SMR reactions to happen at separate places in the furnace, as they are concurrent of each other. Actually, these can be separated by simple thermodynamic considerations. As methane decomposition is highly favored over SMR in standard DRSF conditions [32], the H_2O content in the gas should be sufficiently increased so that SMR is favored and methane decomposition is not.

I.1.4. Kinetics of the reduction with H_2-CO gas mixtures

Numerous studies have paved the way for determining the kinetics of reduction of iron ore depending on the ratio between H_2 and CO in the reducing gas. A first set of studies presented here takes interest only in the reduction phenomenon under operating conditions which do not allow carbon deposition. A second set of studies explores the interactions between reduction and carbon deposition phenomena, as well as the influence of WGSR and CH_4 content in the gas. The effects of each of these phenomena are presented in the following paragraphs.

I.1.4.1. Kinetics of the reduction with no carbon deposition

Influence of thermodynamics on the kinetics

From purely thermodynamic considerations, since the reduction with H_2 is endothermic, the global reaction is favored at higher temperatures. Indeed, increasing the temperature increases the driving force of the reaction, which in turns fastens the kinetics of H_2 reduction.

Conversely, the CO reduction is exothermic: the driving force of the reduction decreases when temperature is increased, so the reduction kinetics are hindered. However, as the temperature increases, kinetics of both diffusion and local chemical reaction are greatly enhanced. Actually, in the case of CO reduction, the increase in pure kinetics is greater than the decrease in the driving force, so that CO reduction is improved at higher temperatures see, e.g., [21].

Isothermal reduction conditions

In isothermal conditions, the reduction of an iron ore pellet is systematically faster with pure H_2 than with pure CO, even when no carbon deposition takes place [33]. In comparison with CO, H_2 has a higher reactivity, is smaller in size, and has a higher diffusivity [34]. For a mixture of H_2 and CO, reduction reactions for each reductant are generally assumed to proceed as additive parallel reactions, even if a strong non-linear relationship between the reaction rate and the molar fractions of both gas exists [34, 35].

Since H_2 is a better reductant than CO, increasing the H_2:CO ratio of the gas leads to faster reduction. A H_2:CO ratio of 3:1 signifies that 3 moles of H_2 are present in the gas for 1 mole of CO. It was shown that increasing the H_2:CO ratio up to 1.6:1 equally increases the reduction rate in the temperature range 850-1050°C [36]. Above this threshold, the reduction rate was not improved when replacing CO with H_2; only a minor improvement in reduction rate was observed for H_2:CO = 2.6:1 at 1050°C.

These results are not in agreement with those presented in [22]. These authors show that the reduction with pure H_2 is much faster than the reduction with a H_2–CO gas mixture, which is itself much faster than the reduction with pure CO (see Figure 8). Indeed, only a minor substitution of H_2 by CO in the gas drastically decreases the initial reduction rate at the wustite stage; conversely,

only a minor addition of H_2 to a pure CO gas greatly increases the reduction rate [34]. This is because the addition of CO in the gas poisons the reaction sites of wustite and slows down the formation of iron nuclei [34]. Moreover, the effective diffusion coefficient of H_2 decreases quite considerably even when a little amount of CO is added to the gas mix [22].

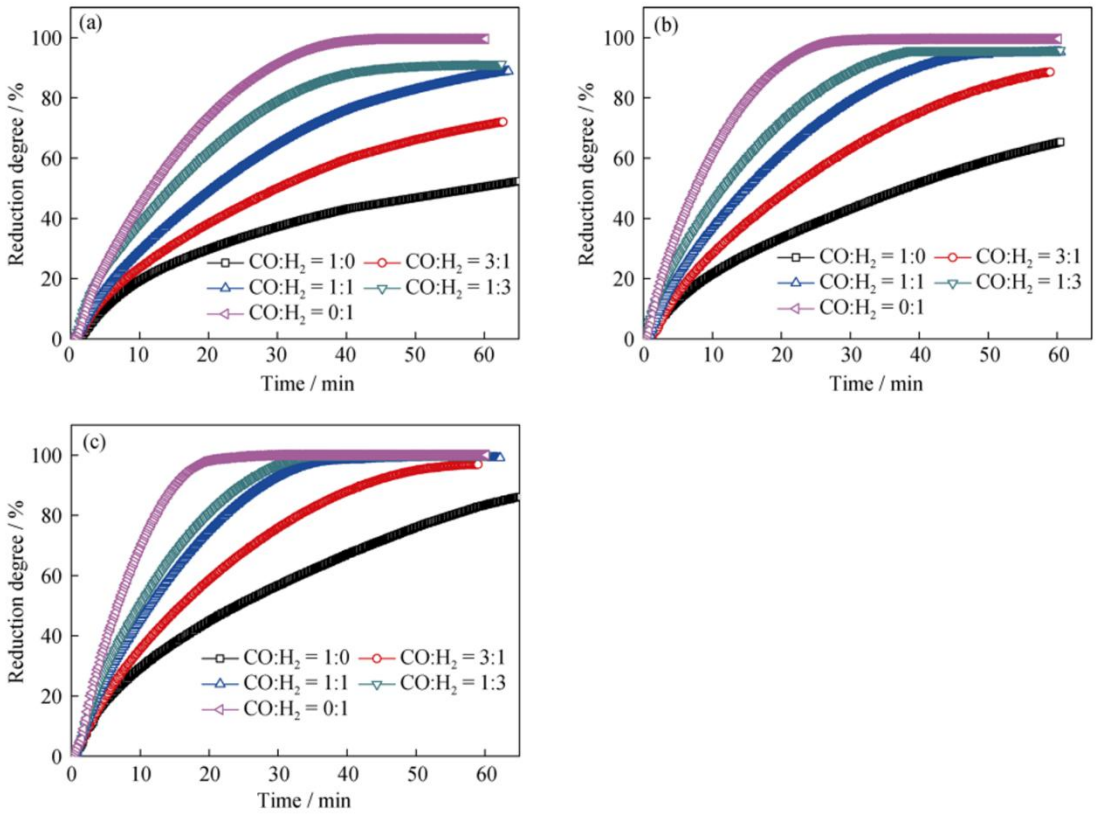

Figure 8: Experimental results of the H_2-CO reduction of iron ore pellets with different gas compositions and **(a)** T = 1073 K, **(b)** T = 1173 K, **(c)** T = 1273 K. $d_p = 12$ mm, $F_g = 5$ Nlpm [22].

Non-isothermal reduction conditions

In non-isothermal conditions, the endothermicity of the H_2 reduction causes the temperature to decrease, which in turns hinders the kinetics of the reduction. In this case, replacing H_2 with CO is beneficial to the reduction rate. In a study of the limiting effects of heat transfer, it was found that the reduction of pellets at low flowrate was faster when the H_2:CO ratio was 4:1 at 850°C. This was attributed to a positive contribution of CO which provided extra energy for the reduction with H_2 [37].

Effect of pellet type

The reducibility of iron ore pellets depends on their origin and the way they are manufactured. In a previous work of our team [18], the reducibility of three different types of pellets were studied with pure hydrogen: two were DR-grade[3] (CVRD, LKAB) and one was BF-grade[4] (CVRD). The main

[3] Pellets dedicated to shaft furnace use
[4] Pellets dedicated to blast furnace use

physical properties of these pellets are recalled in Table 3. The reducibility of DR-grade pellets with different chemical compositions was found to be very similar, except at high temperature (1000°C). The reduction of denser BF-grade pellets was systematically slower than the reduction of DR-grade pellets. Similarly, in another study [38], the hydrogen reduction of pellets at 800°C and 850°C was found to be faster for high porosity pellets (34%) than for regular porosity pellets (26%).

Table 3: Measured structural parameters of industrial DR grade and BF grade pellets [18].

Pellet type	a_{sp,Fe_2O_3} ($m^2\ kg^{-1}$)	ρ_p ($kg\ m^{-3}$)	ϵ	d_{grain}(µm)
CVRD-BF	21.0	4750	0.10	54.2
CVRD-DR	60.4	3528	0.33	18.9
LKAB-KPRS	56.3			20.2

The effect of the chemical composition of the gangue on the H_2 reduction of iron oxides has yet to be widely studied. In their review, Zakeri et al. conclude that Al_2O_3 and CaO additions have beneficial effects on the reduction rate by facilitating gas diffusion. On the contrary, SiO_2 is shown to hinder reduction by facilitating the formation of fayalite (Fe_2SiO_4) [39].

The effect of key parameters such as the initial porosity or specific surface area on hydrogen reduction is further discussed in Article 1 (section I.3).

I.1.4.2. Kinetics of the reduction with carbon deposition

Influence of the carbon deposition reactions

In the previously mentioned studies for the reduction of single pellets, conditions were met so that little to no carbon deposition would occur. However, when a pellet is reduced by a H_2-CO gas mixtures in other conditions (e.g., lower temperature), carbon deposition can drastically affect the reduction rate and even lead to an increase in the mass of the pellets above a certain conversion degree of the iron ores, as shown in [16]. In this study, Hamadeh led a series of reduction experiments at 850-950°C for H_2-CO-He gas mixtures containing 40% He and a given ratio of H_2:CO. It was found that severe carbon deposition happened even with a 30% H_2 – 30% CO – 40% He gas mix. A methodology was then proposed to separate the contribution of reduction and carbon deposition regarding the mass variation of the pellets, with great success. Compared with pure CO cases, Hamadeh showed that H_2 promoted the carbon deposition.

The fact that a small fraction of hydrogen helps to achieve better carbon deposition and carburization of the pellets is widely observed in the literature [15, 21, 27, 28]. Generally, carburization of the pellets is found to be the highest at low temperatures (650-750°C) [27, 40]. At higher temperatures, the carbon is either deposited as amorphous carbon, or the cementite is decomposed into iron and amorphous carbon [27]. Other factors than temperature should be taken into account to gain knowledge on cementite decomposition: for instance, the presence of additives in the gas such as H_2S is known to greatly slow down the decomposition of cementite [40], while CO_2 is detrimental to both carbon deposition and carburization [28].

It has to be noted that Towhidi et al. conducted reduction experiments of 7-mm porous pellets with different ratios of H_2–CO at various temperatures and they found that no carbon deposition occurred above 900°C and below a certain reduction degree [21].

Influence of the SMR

In a DRSF, the introduction of CH_4 in a gas mixture containing H_2O can lead to in-situ SMR. Actually, this reaction only happens when metallic iron, which acts as a catalyst, is present at the surface of the pellets (Takahashi et al., 1986). A kinetic model was developed by Münster and Grabke and confronted with recent catalytic reforming experiments with great success [32, 41, 42].

It was found that steam decomposition left adsorbed oxygen atoms on the reactive sites of the pellets, which hindered the reaction rate of SMR. As a consequence, higher conversion degrees of methane were obtained with lower H_2O content in the gas, which means in other words higher H_2/H_2O ratios. It was also shown that as the temperature increased, the kinetics of SMR were improved [42].

I.2. Kinetic Modeling

The gaseous reduction of iron ore pellets is a complex phenomenon which involves gaseous diffusion, diffusion inside the pores of the pellet and proper chemical reduction of the oxides. Here, the popular shrinking core model (SCM), grain model (GM) and law of additive reaction times (LART) are presented, along with considerations regarding the determination of the physical parameters that these models are based upon.

I.2.1. Physical and mathematical framework of SCM and GM

A complete introduction to gas-solid reactions is given in [43]. In the following subsections, we recall the basics of the modeling of gas-solid reactions. A generic gas-solid reaction can be written as:

$$aA_{(g)} + bB_{(s)} = cC_{(g)} + dD_{(s)} \quad (9)$$

At the microscopic level, a reaction between a gas and a solid involves several consecutive steps:

1. External gas mass transfer (bulk diffusion): the gas reactant diffuses through the boundary layer of the solid reactant.
2. Gas diffusion in the pores: the gas reactant diffuses in the pores of the solid, which is either partially or completely reacted. If the product layer is dense, this step is replaced by solid-state diffusion of reactants and products.
3. Local chemical reaction: gas and solid reactants react according to eq. (9).

To determine the kinetics of a gas-solid reaction, one needs to assess the rate of each of these phenomena, their interplay, and the influence of various chemical variables. In each case where one of these phenomena comes to be rate-limiting, a simple rate equation can be derived. These rate equations will be helpful when building the complete kinetic model.

I.2.1.1. Mass transfer of reactant gas

To evaluate the mass transfer of gas reactant, the following quantities are defined (index A and C relate to eq. (9)):

- the flow of gas reactant through the solid boundary layer N_A;
- the concentration of gas reactant C_A. It equals bulk concentration C_{A0} at the exterior of pellet and local concentration C_{As} at the solid reactant surface;
- the mass transfer coefficient h_d, which relates to the Sherwood number N_{Sh}.

The diffusion of gas reactant through the solid boundary layer, from the bulk of the gas to the solid outer surface, obeys a simple transport equation including convection and diffusion phenomena. The mass transfer equation gives, in its integral form:

$$N_A = h_d(C_{As} - C_{A0}) + X_{As}(N_A + N_C) \tag{10}$$

where X_{As} is the molar fraction of A at the solid surface. In the case of iron ore reduction, all reduction reactions ($i = 1 - 6$) consume and produce an equal number of moles of gas ($S_{H_2,i} = -S_{H_2O,i}$). This situation, called equimolar counterdiffusion, allows to write the equation in a simpler form:

$$N_A = h_d(C_{As} - C_{A0}) \tag{11}$$

h_d can be determined fairly reasonably with empirical correlations. The correlation of Ranz and Marshall can be used to determine h_d in the case of the reduction of a spherical pellet [44]. This correlation involves the Schmidt and Reynolds numbers (N_{Sc} *and* N_{Re}, resp.):

$$N_{Sh} = 2.0 + 0.6N_{Re}^{\frac{1}{2}}N_{Sc}^{\frac{1}{3}} \tag{12}$$

$$N_{Sh} = h_d \frac{d_p}{\mathcal{D}_{AC}} \tag{13}$$

$$N_{Re} = \frac{\rho_g u_g d_p}{\eta_g} \tag{14}$$

where ρ_g, u_g are the gas mass density and velocity, respectively, and where $\mathcal{D}_{AC}$ is the binary diffusion coefficient which can be calculated from the Chapman-Enskog theory. The viscosity of the gas mix η_g can be evaluated by the formula of Wilke [45]:

$$\eta_g = \sum_{i\ gas} x_i \frac{\eta_i}{\zeta_i} \tag{15}$$

$$\zeta_i = \sum_{j\ gas} x_j \phi_{ij} \tag{16}$$

$$\phi_{ij} = \frac{1}{\sqrt{8\left(1 + \frac{M_i}{M_j}\right)}}\left[1 + \left(\frac{\phi_i}{\phi_j}\right)^{\frac{1}{2}}\left(\frac{M_j}{M_i}\right)^{\frac{1}{4}}\right]^2 \tag{17}$$

I.2.2.2. Gas diffusion in the pores

A gas-solid reaction does not systematically involve gas diffusion in the pores. When the solid reactant *B* is gasified or the solid product *D* is completely dense, no pore diffusion occurs and no characterization of the porosity is needed. The reaction of a porous pellet however requires the correct assessment of the gas diffusion in the pores. Compared with molecular diffusion, the phenomenon of pore diffusion includes complicating factors, such as the presence of non-straight solid pores (described with a tortuosity factor Γ), a shift in the diffusion regime depending on the pore width (transition from molecular to Knudsen diffusion), and potential pressure gradients within the pores. To account for these phenomena, both molecular and Knudsen diffusion can be modelled as parallel resistances in a pellet with porosity ϵ:

$$D_{A,eff} = \frac{\epsilon}{\Gamma}\left(\frac{1}{D_{A,Kn}} + \frac{1}{D_{A,mix}}\right) \quad (18)$$

where $D_{A,mix}$ is the molecular diffusion of A in the gas mix. It is usually expressed as

$$D_{A,mix} = \frac{1 - x_A}{\sum_{j \neq A} \frac{x_j}{\mathcal{D}_{Aj}}} \quad (19)$$

The Knudsen diffusion coefficient can be readily calculated from:

$$D_{A,Kn} = \frac{d_{pores}}{3}\sqrt{\frac{8RT}{\pi M_A}} \quad (20)$$

where d_{pores} is the mean diameter of the pores, R is the ideal gas coefficient and M_A is the molecular mass of gas A.

I.2.2.3. Local chemical reaction

The chemical reaction itself is not a single process. The heterogeneous reaction (eq. 12) is preceded by the adsorption of A onto the reaction site and followed by the desorption of C. The reaction site can be located on the outer surface of B or on the B/D internal interface. The reaction rate per unit of reaction surface r_s (in mol s^{-1} m^{-2}) is usually written:

$$r_s = k_c\left[c_{As}^n - \left(\frac{c_{Cs}^m}{K_{\text{eq}}}\right)\right] \quad (21)$$

where k_c is the reaction rate constant, n and m the reaction orders relative to A and C, respectively, and $K_{\text{eq}}$the equilibrium constant. The rate constant follows the Arrhenius equation:

$$k_c(T) = k_0\, exp\left(-\frac{E_a}{RT}\right) \quad (22)$$

I.2.2.4. Rate-limiting equations

As explained earlier, a single rate equation can be derived when one of the above-mentioned phenomena is rate-limiting. In each case, this equation is obtained by a molar balance between disappearance of solid and gas reactant species, see Table 4:

Table 4: Rate equation related to each potential rate-limiting phenomenon [43]. ρ_B is the apparent molar density of the solid reactant B, r_C is the radius of the reacting interface, r_0 is the initial radius of the sample.

Rate limiting phenomenon	Rate equation
Local chemical reaction	$\rho_B \frac{dr_c}{dt} = k_c\left[C_{As}^n - \left(\frac{C_{Cs}^m}{K_{\text{eq}}}\right)\right]$

Gas reactant mass transfer	$\rho_B \frac{dr_c}{dt} = h_d \left[C_{A0} - \left(\frac{C_{C0}}{K_{\text{eq}}} \right) \right] \left[\left(\frac{K_{eq}}{1 + K_{\text{eq}}} \right) \right]$
Gas reactant diffusion through the pores	$-4\pi r_c^2 \rho_B \frac{dr_c}{dt} = \frac{4\pi b D_{eff}}{\frac{1}{r_c} - \frac{1}{r_0}} \left[C_{A0} - \left(\frac{C_{C0}}{K_{\text{eq}}} \right) \right] \left[\left(\frac{K_{eq}}{1 + K_{\text{eq}}} \right) \right]$

From Table 4, whatever the rate-limiting phenomenon, the reaction rates can be written in the same framework. Thus, we can define a generic characteristic time constant τ, which is the time needed to reach full conversion under a specific control regime:

$$\tau = \beta \frac{\rho_B d_s}{k f_m} \tag{23}$$

Here, α is a stoichiometric factor, d_s is a characteristic diameter, k is a kinetic factor depending on the control regime, and f_m is the driving force of the reaction. The time needed to reach a certain conversion X can then be written:

$$t(X) = \tau f(X) \tag{24}$$

where f is a conversion function depending on the solid shape factor (if it is a flat plate, a cylinder, a sphere) and the control regime. The rate of conversion is finally obtained as:

$$v_X = \frac{dX}{dt} = \frac{1}{\tau f'(X)} \tag{25}$$

In the previous example, only one kinetic process was assumed rate-limiting. In the general case (mixed regime) the various kinetic processes have to be coupled, and several approaches are possible. Two models are very popular in the literature, the shrinking core model (SCM) and the grain model (GM). These are quickly described below.

I.2.2.5. The shrinking core model (SCM)

If the reaction proceeds topochemically with a sharp interface between the solid product and reactant layers, we can consider the rate-limiting phenomena in a series combination [46]. This particular configuration is described by the so-called shrinking core model (SCM), which is very efficient at describing the reaction of dense solids [43]. In this model, the gas reactant must first travel through the bulk of the gas, then in the pores of the solid product, and finally react at the reaction interface. The external part of the solid will react first, and the interface of the reaction will progressively move toward the center of the solid (Figure 9). The time needed to reach a certain conversion is then expressed as:

$$t(X) = \tau_{chem} f(X) + \tau_{diff} g(X) + \tau_{ext} h(X) \tag{26}$$

where f, g, h are specific conversion functions related to each phenomenon, and the subscripts chem, diff, ext respectively relate to local chemical reaction, pore diffusion and mass transfer phenomena.

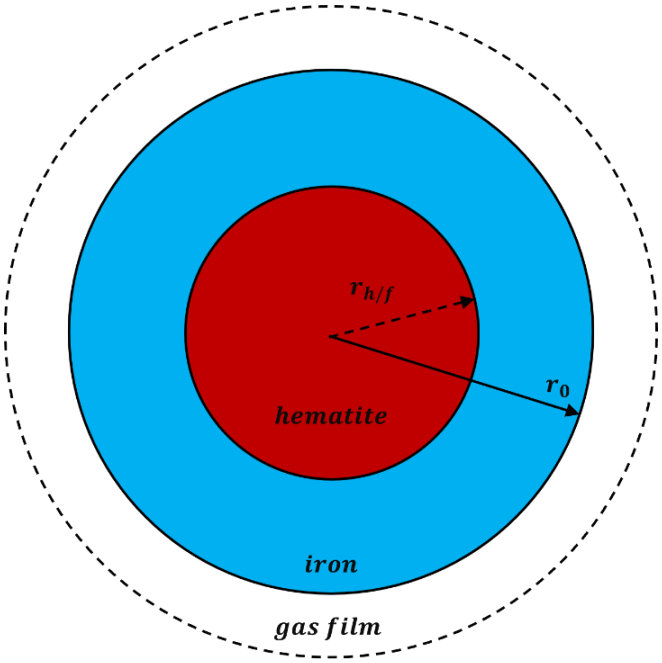

Figure 9: Topochemical reduction of a spherical pellet according to the SCM.

In the case of porous solids however, this approximation is not reasonable anymore: indeed, the reaction interface is not sharp but rather diffuse, so that a finer characterization of the pellet is needed [33, 43].

I.2.2.6. The grain model (GM) and the law of additive reaction times (LART)

A straightforward option to describe the reaction of a porous pellet is to model it as a cluster of dense grains separated by pores (Figure 10). Grain arrangement is described through the properties of the pore network, i.e. intergrain porosity ϵ, mean pore diameter d_{pores} or pore diameter distribution, pore tortuosity Γ (ratio between the length of a pore between and the length of a straight line joining its extremities). It is also described through grain diameter d_{grain} or grain diameter distribution, and grain shape factor F_p. This framework, called the grain model (GM), allows to derive new characteristic time constants. In the case of local chemical reaction control, diffusion is fast compared to chemical reaction, and the reaction is homogeneous at the scale of the pellet: the time needed to reduce the pellet becomes equal to the time needed to reduce a single grain. Any model can then be applied to the reduction of a grain: in most cases, the reaction can be considered topochemical at the scale of the grain.

In the grain model, the characteristic times for bulk and pore diffusion are unchanged. Although the series combination is not as natural as in the previous situation, one can use the law of additive reaction times (LART) developed by [47]. The combination of GM and LART (GM-LART) results in a grain model based on an analytical calculation. Care is needed before using this mathematical approximation, as its validity is limited to the reaction of an isothermal solid with a reaction order close to 1. However, GM-LART is quite robust even in multiparticle reactor systems, in which temperature and gas composition evolve depending on time and position. In these situations, the law should be used in its differential form. This approximate solution of the grain model allows for a considerable gain of time during calculation.

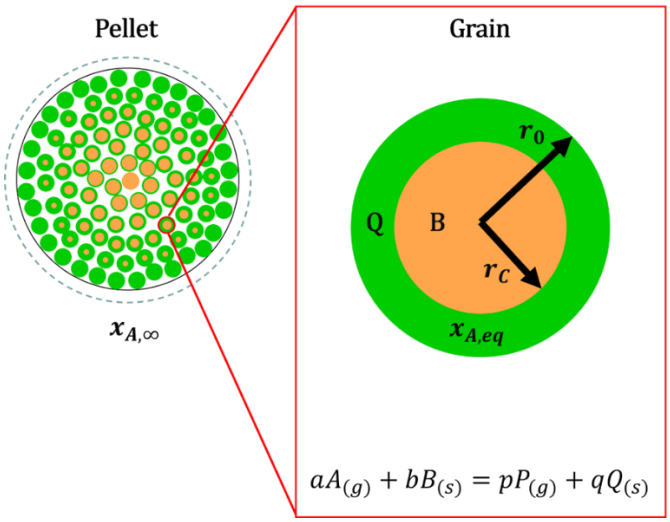

Figure 10: Reduction of a spherical pellet according to the GM.

I.2.2. An analytical grain model for the reduction of iron ore pellets

The SCM and GM models have been extensively applied to the reduction of iron ore pellets with both hydrogen and carbon monoxide. It has been shown that the GM and GM-LART can properly predict the reduction of iron ore pellets [33, 48, 49, 50]. This subsection presents the key assumptions and parameters of the GM-LART presented in [18] and [16], which is the basis for the new model presented in Article 1.

I.2.2.1. Modeling assumptions

The GM-LART describes the reduction of iron ore pellets at T>570°C. In this case, the reduction takes place in three consecutive steps (reactions 1-6, except 2bis and 5bis). The following reduction pathway is proposed below (Figure 11), supported by numerous experimental investigations [18, 33, 51]. The main hypotheses of the model are the following:

- a spherical pellet (diameter d_p) is made of dense spherical grains of hematite (diameter d_{grain}) separated by pores (porosity ϵ). For the sake of simplicity, the diameter of the pellet is considered constant. To account for the molar volume mismatch between successive oxides, the intergrain porosity continuously evolves during reduction;
- the hematite grains react topochemically to form dense grains of magnetite;
- the magnetite grains react topochemically to form porous grains of wustite (ϵ_{grain}). These grains are made of so-called crystallites ($d_{0,cryst}$), which are spherical dense particles. A strong positive correlation was found between the reduction temperature and the diameter of the crystallites;
- the wustite crystallites react topochemically to form dense iron crystallites (d_{cryst});
- for each reduction step, a characteristic time constant is defined for bulk gas diffusion, intergrain gas diffusion and local chemical reaction. For the second reaction (magnetite→ wustite), another characteristic time constant related to intragrain diffusion through the product layer (i.e., porous FeO) was considered. For the third reaction (wustite→iron), another characteristic time constant related to solid diffusion of oxygen through the product layer (dense Fe) was added. The latter is of particular importance when considering the reduction of wustite for temperatures above 912°C [20];

- the temperature is supposed constant inside the pellet and the reaction order for each step is 1.

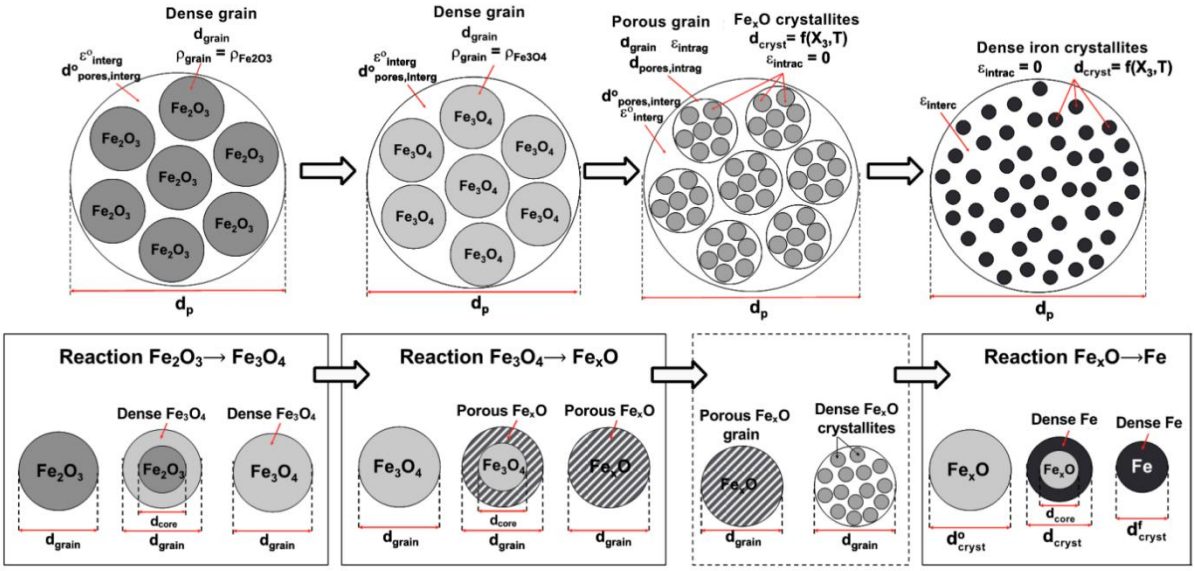

Figure 11: Assumed reduction pathway of an iron ore pellet. Top row represents the evolution at the pellet scale, while bottom row represents the evolution at the grain and crystallite scales.

I.2.2.2. Determination of structural parameters

The bulk density of the pellets was measured with sand pycnometry at TSE Ijmuiden, in the context of the MaxH2DR project, see Table 5. Additionally, the true density was measured through helium pycnometry with the gas displacement method. The initial interparticle porosity is directly derived from bulk and true density, as:

$$\epsilon = 1 - \frac{\rho_{bulk}}{\rho_{true}} \tag{27}$$

The evolution of porosity during reduction is based on a molar balance between successive oxides. As the first reaction produces dense grains of magnetite, the little volume mismatch leads to a moderate increase in interparticle porosity. On the contrary, a large volume mismatch between magnetite and wustite (with a constant grain diameter) leads to the formation of pores within the layer of wustite; the estimated intraparticle porosity is $\epsilon_{intrag} = 0.18$. The final volume mismatch between wustite cristallites and iron cristallites increases the interparticle porosity.

The initial grain diameter is calculated based on the measured specific surface area (SSA) of the sample:

$$d_{grain,ini} = \frac{6}{\rho_{true} a_{sp,ini}} \tag{28}$$

This diameter is supposed to be constant until the separation of the wustite grains into crystallites. SSA was measured again after reduction at different reduction temperatures, and it was found that the final crystallite diameter greatly increases when temperature is increased:

$$d_{cryst}(T) = (1.67 \times 10^{-9}) exp(T \times 6.08 \times 10^{-3}) \tag{29}$$

Table 5: Properties of pellets from different manufacturers (A, B, C, D) indexed according to their size. Index 1 refers to small pellets, $d_p = 10 - 13mm$, while index 2 refers to bigger pellets, $d_p = 13 - 15mm$.

Pellet type	Bulk density (kg m^{-3})	True density (kg m^{-3})	Porosity (%)
A1	3570	4920	27.4
A2	3530	4920	28.3
B1	3550	5040	29.7
B2	3490	5010	30.3
C1	3680	5190	29.2
C2	3610	5150	29.9
D1	3630	5170	29.7
D2	3610	5130	29.7

The initial diameter of wustite crystallites was calculated based on a molar volume balance:

$$d_{cryst} = 1.225\, d_{0,cryst} \tag{30}$$

The initial pore diameter was estimated based on SEM observations. The measured mean diameters are $d_{pores,interg} = 6 \times 10^{-6}$ m and $d_{pores,intrag} = 10^{-6}$ m. The final diameter of the pores was measured by mercury porosimetry after complete conversion. A significant positive linear correlation was found between the mean diameter of the pores in the DRI and the reduction temperature:

$$d_{pores,Fe}(T) = 7.75 \times 10^{-9}\,(T - 273) - 2.05 \times 10^{-6} \tag{31}$$

The pore tortuosity was set as $\Gamma = 2$, as a reasonable value of tortuosity should be between 1 and 3 [18].

I.2.2.3. Calculation of the characteristic time constants and reaction rates of reduction

Each characteristic time constant is derived from the rate equations presented in Table 4 (details of the calculation are available in [17], while each time constant used in the model is given in Article 1). Some important remarks regarding these time constants are given here. They address both H_2 and CO reduction:

1- The expression of the driving force presented earlier is different whether it is associated with chemical control or not. In the case of chemical control, we have:

$$f_{\mathrm{H_2},chem,i} = c_t \left(x_{\mathrm{H_2}} - \frac{x_{\mathrm{H_2O}}}{K_i} \right), i = 1,2,3 \tag{32}$$

In the case of mass transfer or pore diffusion control, we have:

$$f_{\mathrm{H_2},i} = c_t \left(x_{\mathrm{H_2}} - x_{H_2,eq,i} \right), i = 1,2,3 \tag{33}$$

$$x_{\mathrm{H_2},eq,i} = \frac{x_{\mathrm{H_2}} + x_{H_2O}}{\left(1 + K_i^{\frac{1}{\nu_{\mathrm{H_2},i}}} \right)} \tag{34}$$

2- The characteristic densities and diameters are chosen according to the limiting phenomenon at hand. For pellet-scale phenomena (e.g. bulk diffusion, intergranular diffusion), the time constant is calculated based on the apparent density and the pellet diameter; on the other hand, for grain-scale or crystallite-scale chemical control, the calculation is based on the density and diameter of the grains/crystallites.
3- The characteristic time associated with solid state diffusion of oxygen has been derived from the literature [52].
4- The intrinsic kinetic constant associated with each local chemical reaction follows the Arrhenius law, that is:

$$k_i = k_{0,i} \exp\left(-\frac{E_{a,i}}{RT}\right) \tag{35}$$

where $k_{0,i}$ and $E_{a,i}$ are the frequency factor and activation energy of the reaction. As the exact mechanism of iron oxide reduction is unclear, these constants have to be mathematically determined. This is done through curve-fitting of these parameters between simulations and experiments. A specific procedure for this purpose is presented in Article 1.

Upon calculating the time constants, the time needed to reach a certain conversion can be readily calculated through specific conversion functions. For each rate-limiting phenomenon, this time is expressed as:

$$t(X) = \begin{cases} \tau_{ext} X & \text{for bulk diffusion control} \\ \tau_{diff}\left[1 - 3(1-X)^{\frac{2}{3}} + 2(1-X)\right] & \text{for pore diffusion control} \\ \tau_{chem}\left[1 - (1-X)^{\frac{1}{3}}\right] & \text{for chemical control} \end{cases} \tag{36}$$

Finally, the instantaneous rate of reaction for each reaction (i = 1,…,6) is given by:

$$v_X = \frac{1}{\sum_k \tau_k f_k(X)} \tag{37}$$

I.2.2.4. Kinetics of the side reactions

The rate equations for all side reactions except SMR were taken from a previous work [16] inspired by the literature [25, 29, 53]. A proper rate equation for SMR (reaction 10) was found in [41, 42]. These rate equations are presented below (eqs. 38-41), and their rate constants are given in Table 6.

$$r_{7,Fe_3O_4} = k_{7,\mathrm{Fe_3O_4}} \rho_{\mathrm{Fe_3O_4}} \left(1 - \epsilon_{interg}\right)\left(P_{\mathrm{CO}} P_{\mathrm{H_2O}} - \frac{P_{\mathrm{CO_2}} P_{\mathrm{H_2}}}{K_{eq,7}}\right) \quad (\mathrm{mol\ m^{-3}\ s^{-1}}) \tag{38}$$

$$r_8 = \left(k_8 P_{\mathrm{H_2}}^{0.5} + k_8'\right)\left(P_{\mathrm{CO}}^2 - \frac{P_{\mathrm{CO_2}} a_C}{K_{eq,8}}\right) \quad (\mathrm{mol\ m^{-3}\ s^{-1}}) \tag{39}$$

$$r_9 = \frac{k_9}{P_{\mathrm{H_2}}}\left(1 - \epsilon_{interg}\right)\left(P_{\mathrm{CH_4}} - \frac{P_{\mathrm{H_2}}^2 a_C}{K_{eq,9}}\right) \quad (\mathrm{mol\ m^{-3}\ s^{-1}}) \tag{40}$$

$$r_{10} = k_{10}\rho_{\mathrm{Fe}}(1-\epsilon_{interg})\left(\frac{1}{\left(1+K_{eq,10}\frac{P_{\mathrm{H_2O}}}{P_{\mathrm{H_2}}}\right)}\right)\left(\frac{P_{\mathrm{CH_4}}}{P_{\mathrm{H_2}}^{0.5}}\right) \quad (\mathrm{mol\ m^{-3}\ s^{-1}}) \tag{41}$$

The WGSR is catalyzed by iron and iron oxides, except for hematite [54]. As both methane decomposition and SMR are catalyzed by iron, these reactions take place only when an iron layer is formed at the exterior of the pellet (X > 50%) [25].

In this section, different frameworks for kinetic modeling were presented. Particular attention was given to the analytical grain mode previously developed in our team, as it is the basis for our new model. The latter is thoroughly presented in Article 1, which is fully reproduced in the next section.

Table 6: Rate constants for each considered side reaction (7,8,9,10) and for each catalyzer.

Reaction	Catalyzer	Rate constant k_i	Reference
7	Fe_3O_4	$k_7 = 2.683372\times10^5\times\exp\left(-\frac{112000}{RT}\right)$ $(mol.kg_{cat}^{-1}.s^{-1})$	[53]
	$Fe_{0.95}O$	$k_7 = 1.83\times10^{-5}\times\exp\left(\frac{7.84}{RT}\right)$ $(mol.cm^{-3}.s^{-1})$	[25]
	Fe	$k_7 = 93.3\times\exp\left(-\frac{7320}{RT}\right)$ $(mol.cm^{-3}.s^{-1})$	[25]
8		$k_8 = 1.8\times\exp\left(-\frac{27200}{RT}\right)$ $(mol.m^{-3}.s^{-1})$ $k_8' = 2.2\times\exp\left(-\frac{8800}{RT}\right)$ $(mol.m^{-3}.s^{-1})$	[29]
9	Fe	$k_9 = 16250\times\exp\left(-\frac{55000}{RT}\right)$ $(mol.m^{-3}.s^{-1})$	[29]
10	Fe	$k_{10} = 2.285841\times10^9\times\exp\left(-\frac{258000}{RT}\right)$ $(mol.g_{cat}^{-1}.s^{-1})$	[42]

I.3. Article 1: Kinetics of the reduction of iron ore pellets with hydrogen: a parametric experimental and modeling study, by A. Marsigny, J.B. Letz, O. Mirgaux, F. Patisson (under review)

Article 1 – **Abstract**

The direct reduction of iron ore by hydrogen is a serious candidate for reducing greenhouse gas emissions in the iron- and steelmaking industry by replacing traditional blast furnace technology. The reduction kinetics are key to this process. The present paper reports an extensive parametric study of the reduction of iron ore pellets with hydrogen that combines both experiments and modeling. A new model (modified grainy pellet model) was developed on the basis of the grainy pellet concept, the law of additive reaction times and the evolution of gas composition. The chemical kinetic constants of the three-step reduction reaction were determined from isothermal thermogravimetry experiments in the 600–900 °C temperature range. The model was then validated against laboratory-scale fixed-bed experimental results. A comparison with the experimental thermogravimetry results for a broad range of operating parameters shows the robustness of the model. The effects of temperature, gas dilution, gas flow rate, water content, pellet size, pressure, porosity, tortuosity, and specific surface area were investigated. The temperature, pellet size, pressure, gas composition and, particularly, the water content and gas flow rate have major influences on the reaction rate, in contrast to the initial porosity and specific surface area.

Article 1 – **1. Introduction**

Hydrogen direct reduction of iron ore (H_2-DR) is a promising technology for decreasing the high carbon emissions of the iron and steel industry. It relies on hydrogen rather than carbon monoxide, and it emits water vapor instead of CO_2. In the H_2-DR process, iron oxides are successively converted to metallic iron. The reaction proceeds in two steps below 570 °C (eqs. 1 and 2bis) and three steps above 570 °C (eqs. 1, 2 and 3). Overall, it is a highly endothermic reaction, but it presents excellent kinetics compared with CO reduction [33].

$$3Fe_2O_3 + H_2 = 2Fe_3O_4 + H_2O \quad (1)$$

$$Fe_3O_4 + 4H_2 = 3Fe + 4H_2O \quad (2bis)$$

$$Fe_3O_4 + \frac{16}{19}H_2 = \frac{60}{19}Fe_{0.95}O + \frac{16}{19}H_2O \quad (2)$$

$$Fe_{0.95}O + H_2 = 0.95Fe + H_2O \quad (3)$$

These features make the hydrogen direct reduction shaft furnace (H_2-DRSF) a great competitor to replace the traditional syngas shaft furnace and the blast furnace, and they explain the recent surge of interest in this technology (see, for instance, the reviews [5, 26]) and the many R&D projects launched. The present work is part of the European MaxH2DR project, which intends to maximize the use of hydrogen in DR and its integration in steelmaking plants [55].

The kinetics of the reduction of iron ore pellets (10–15 mm) have been extensively studied, mostly using isothermal thermogravimetry analysis (TGA) [38, 49, 50, 56, 57, 58, 59, 60, 61, 62]. The main findings concerning the kinetics are as follows:

- The rate of reduction of a pellet is limited by different "resistances", namely, the external mass transfer of the reactant gas from the bulk gas to the pellet surface, the diffusion of the reactant gas through the pores of the pellet, and the chemical reaction itself [43]. Oxygen solid-state diffusion in the iron layer is sometimes seen as a supplementary resistance, especially in the late stage of the reaction [20]. High temperatures and large pellet diameters promote gas diffusion control, whereas low temperatures and small pellet diameters lead to chemical control [62]. Likewise, high pressures and high temperatures also promote gas diffusion control [63].
- The operating parameters have a major influence on the pellet reduction kinetics. Higher temperatures and pressures lead to faster reduction [49, 64]. A higher gas flow rate, lower proportion of inert and lower proportion of water vapor in the gas mixture lead to faster reduction [65].
- Suitable properties can greatly enhance the reducibility of the pellet. Smaller pellets are reduced faster because of the shorter diffusion distances [66]. Pellets with high porosity and low tortuosity are reduced faster [50], and the impact of porosity is more pronounced at higher temperatures [57]. In addition, natural hematite is more suitable than natural magnetite is for reduction since the former is porous and the latter is dense [67]. The reduction is facilitated in pellets with microstructures that feature small grains and a high density of defects [68, 69].
- Models that can simulate the reduction of single pellets for a broad range of operating parameters and pellet properties are crucial for the optimization of the H_2-DR process. Tsay applied a three-interface shrinking core model (3SCM) to simulate hydrogen reduction experiments with great success [70]. The three interfaces separate shells of Fe, Fe_xO, Fe_3O_4, and Fe_2O_3. This model serves as a basis for most of the integrated models that simulate the behavior of the H_2-DRSF [26]. However, SEM observations revealed that the oxides are reduced in a diffuse zone and not at sharp interfaces, as assumed in the 3SCM [26, 33]. A more sophisticated model that better reflects the actual pellet structure (a porous pellet made up of small grains) is the grain model (GM) [43, 71]. In principle, the GM requires numerical integration over the pellet radius. However, an approximation of the GM, which is based on the law of additive reaction times (LART), was proposed by Sohn [47]. The concept of additive reaction times is similar to the sum of mass transfer resistances in series. With a constant reduction temperature (isothermal conditions) and constant molar fractions of gas (static gas conditions), the GM–LART calculation is analytical, which considerably reduces the computation time when it is incorporated into multiparticle reactor models. Under nonisothermal and dynamic gas conditions, the GM–LART can still be applied in differential form, and the approximation made by applying the LART remains very satisfactory [47, 72].

The traditional SCM, GM and GM–LART approaches cannot describe the effect of the gas flow rate on the reduction rate. Indeed, if the reactant gas flow rate is not sufficiently high compared with the quantity of oxides to be reduced, gas reactant depletion occurs in the furnace [62]. New studies tend to integrate hydrogen consumption and transport within a computational fluid dynamics (CFD) framework. This allows us to model the distribution of hydrogen and water vapor in a lab-scale reactor such as a TGA furnace [38, 56, 57, 59] and thus to better calculate the reaction rate at each time step. However, to the best of our knowledge, no systematic study of the effects of reduction parameters, such as the gas flow rate, on the hydrogen reduction of iron ore pellets has been performed.

In this article, we report an extensive parametric study of the reduction of iron ore pellets with hydrogen on the basis of both experiments and modeling. The effects of reducing parameters such as temperature, gas dilution, gas flow rate, water content, pellet size, pressure, porosity, tortuosity, and specific surface area were investigated. The new model extends GM–LART to variable external gas conditions without resorting to CFD calculations. The kinetic constants were obtained by fitting the model to the experimental results in the range of 600–900 °C. Comparisons with the results of in-house TGA experiments, which were performed using two different devices, and partner lab-scale fixed-bed experiments show that the model can describe the reduction of pellets in a broad range of experimental conditions.

Article 1 – **2. Materials and Methods**

Article 1 – **2.1. Raw materials**

Commercial DR-grade pellets from Vale, Brazil, were used. The pellets were carefully chosen to have a spherical shape and no surface cracks. Sampling and characterization of the pellets were performed by our partner Tata Steel from the Netherlands within the MaxH2DR project, and the results of the chemical analysis are given in Table 7. The initial porosity was measured by mercury intrusion ($\varepsilon = 0.295$) and the initial specific surface area by krypton adsorption ($a_{sp} = 60.4\ \mathrm{m^2\ kg^{-1}}$).

Table 7. Chemical composition of the pellets [73].

Pellet	Fe	SiO_2	CaO	Al_2O_3	FeO	B2	MnO	MgO	TiO_2	P_2O_5
D1 (d_p < 13 mm)	66.4	2.3	1.0	0.73	0.71	0.41	0.15	0.12	0.09	0.06
D2 (d_p > 13 mm)	67.1	2.0	0.9	0.56	<0.1	0.47	0.14	0.12	0.08	0.06

An arbitrary diameter of 13 mm (approximately 4 g in mass) was chosen to separate the sets into small pellets D1 and large pellets D2.

Hydrogen was produced on site using a lab-scale water electrolyzer, LNI Swissgas model HG PRO 4000 LN, with a purity >99.99999%.

Article 1 – **2.2. TGA devices**

Iron ore pellet reduction experiments were carried out using two different TGA devices under isothermal conditions (Figure 12).

The main TGA device used in this study was a SETARAM thermobalance, model TG96. It can carry large pellets of up to 10 g. For each experiment, the sample (one pellet) was placed in a wired platinum basket and preheated to the desired temperature under a given helium flow rate. For reduction experiments in pure H_2, the helium valve was then closed, and pure hydrogen was injected at the same flow rate. For reduction experiments in H_2–He mixtures, the helium valve was kept open, and hydrogen was added at a given flow rate. Cooling was performed under a helium atmosphere.

A second TGA device was used to add water vapor to the gas mixture (Netzsch Jupiter, Figure 12b). As with the TG96 device, preheating and cooling were performed under a helium atmosphere. Then, the helium valve was closed, and reduction proceeded under H_2/H_2O. In contrast to the TG96 device, the pellet was placed on a dense alumina pan and not in a permeable basket: during reduction, the bottom part of the pellet was more difficult to access for the reducing gas. On the

reduction curves, this translated into a brutal slowdown of the reduction at approximately 95 % conversion; thus, when comparing the experimental and simulated curves for this device, conversion degrees greater than 95 % were not considered.

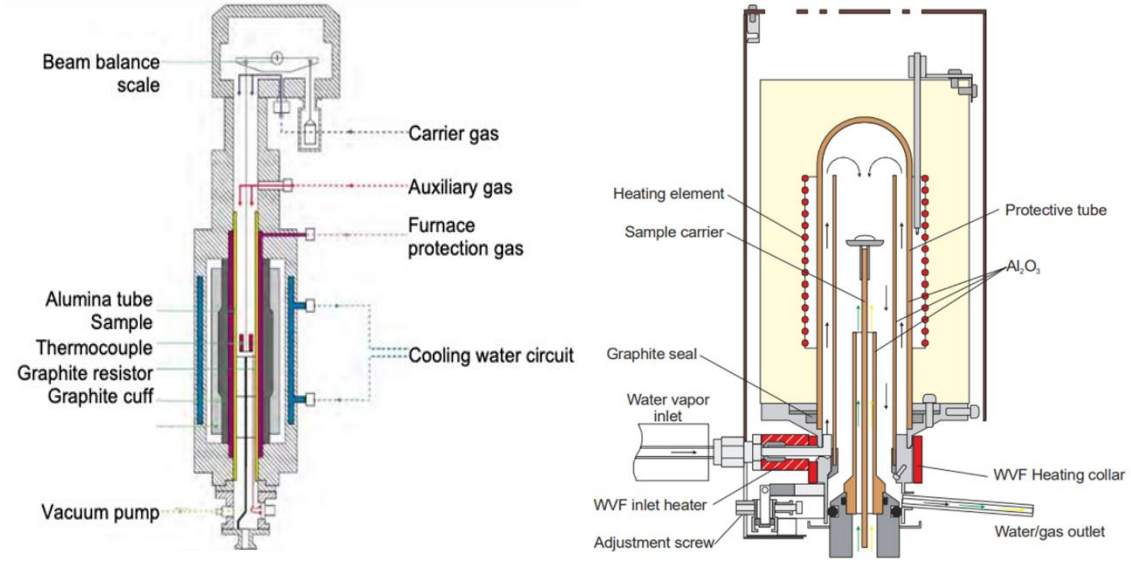

a) **b)**

Figure 12: a) Blueprint of the TG96 thermobalance (Setaram, France). In our setup, the carrier gas was He, the protection gas Ar, and the auxiliary gas H_2. **b)** Blueprint of the Jupiter thermobalance (Netzsch, Switzerland). In our setup, the carrier was He, the protection gas Ar, and the auxiliary gas a mix of H_2 and H_2O.

The reproducibility of the reduction of pellets was assessed for the TG96 device, the Jupiter device, and both devices. In the latter case, reduction proceeded in the same manner until a conversion degree of 95% was reached for the reasons mentioned above. The repeatability was also checked, e.g. for a series of 5 identical runs at 900°C with TG96, the times to reach 50% of conversion were 6.03±0.55 min and to 90% of conversion 16.86±1.19 min, which means a relative standard deviation below 10%.

Article 1 – **2.3. Limits of isothermal and static gas TGA**

An isothermal TGA setup is used to provide a controlled atmosphere for the reduction of the samples, that is, isothermal and static gas conditions. However, previous studies have shown that the reduction of iron ore pellets could lead to the depletion of the gas reactant at low flow rates [38, 62, 74]. On the one hand, reduction is greatly hindered by reactant depletion, and the determination of the reaction kinetics from the experiment is biased; on the other hand, the mechanism of the reaction itself may change, e.g., the kinetics of the first and third subreactions become limited by nucleation and growth mechanisms [75]. Moreover, temperature gradients may appear in the pellet [76], especially for large diameters and low flow rates. However, the difference in terms of reduction efficiency is not as sensitive as it is for the evolution of the gas composition and was thus neglected in the model presented below, which considers the isothermal reduction of the pellets in a changing gas atmosphere (dynamic conditions).

Article 1 – **2.4. Modified grainy pellet model (MGPM)**

On the basis of a previous GM–LART model from our research group [77], we developed a new model, the modified grainy pellet model (MGPM), which simulates the reduction of a single iron ore pellet in an atmosphere with a dynamic bulk gas composition. To this end, the TGA furnace was discretized in time and space. The corresponding in-house code was written in Python. The core features of the model are as follows:

- The model describes the reduction of a spherical iron ore pellet in a gas mixture (H_2, H_2O, He, and N_2) at T > 570 °C.
- A pellet of constant size (usually in the range of 10–15 mm) is considered to be made up of monosized grains (Figure 13). The initial hematite grain diameter is derived from the known initial specific area of the pellet.
- As in [77], the dense grains of hematite are converted to dense grains of magnetite, which are then converted to porous grains of wustite. These wustite grains are made of smaller dense particles called crystallites, which are converted to dense iron during the last reduction stage.

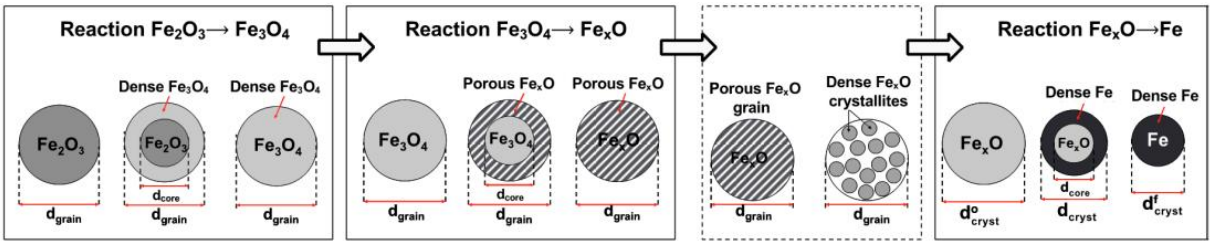

Figure 13: Modeled representation of the evolution of the pellet (top row) and grains (bottom row) during the reduction. Reproduced and modified with permission from [33].

- The TGA furnace is axially discretized. A time-dependent 1-D finite-volume method is implemented, and the numerical resolution is achieved through a Gauss-Seidel algorithm using an upwind scheme. We retained a 1-D model as a simplification able to consider the vertical gradients of gas composition resulting from the reactant gas consumption and product gas production. Horizontally, the average gas composition is considered; the radial gradients, if any, are not described.
- The pellet is discretized into slices, as shown in Figure 14, to match the axial discretization of the furnace. This enables us to relate the local bulk gas composition to the local reaction rate. The gas contained in the volume between the axial indices i and i+1 is considered to reduce the grains of the pellet located between the polar angles θ and $\theta + d\theta$.
- Unlike other models in the literature, e.g. [57], the gas velocity is not calculated inside the pellet: it is assumed—for modeling—that the gas that reacts in a given slice enters and exits in the same slice. This leads to a much simpler calculation.

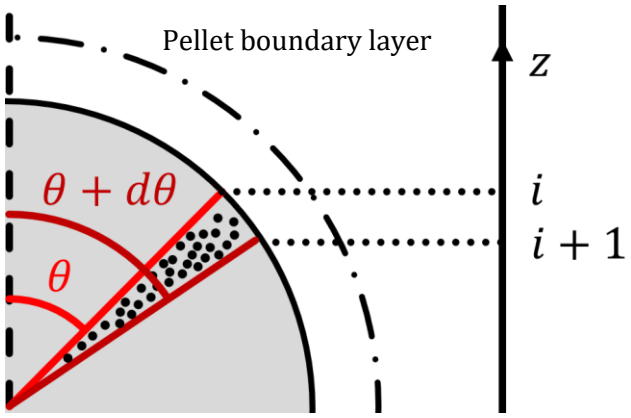

Figure 14: Discretization diagram. The gas present in the axial slice $(i,\ i+1)$ reduces the grains of the polar slice $(\theta, \theta + d\theta)$.

- At each time step, the grains in the slice $(\theta, \theta + d\theta)$ react according to the GM–LART model [18]. Characteristic time constants are calculated for each solid slice and each subreaction on the basis of the local temperature and gas composition. Each of these time constants accounts for the influence of a potential rate-limiting phenomenon (namely, mass transfer of the reactant gas, pore diffusion, solid-state diffusion and local chemical reactions). All time constants used in the model are given in the Appendix. The instantaneous rate of each subreaction is obtained from the law of additive reaction times in its differential form [47]:

- $$v_X = \frac{1}{\tau_{\text{chem}}\, f'(\text{X}) + \tau_{\text{diff}}\, g'(\text{X}) + \tau_{\text{ext}}\, h'(X)} \tag{4}$$

  where the functions f', g', and h' are the time derivatives of the conversion functions related to each phenomenon (Table A1). Solid conversion is then readily obtained from first-order Euler integration.

- Additionally, the gas composition is also calculated for each axial slice $(i, i+1)$ at each time step. x_{H_2} is obtained from a simplified mass balance:

$$c_t \frac{dx_{\text{H}_2,i}}{dt} = -c_t u_z \frac{dx_{\text{H}_2,i}}{dz} + S_{\text{H}_2,i} \tag{5}$$

The gas source term is obtained from the initial apparent molar density of hematite, a geometric factor relating the volume of the solid to the height of the axial slice, and the reaction rate of the global reduction reaction:

$$S_{\text{H}_2,i} = -3\, \tilde{\rho}_{\text{Fe}_2\text{O}_3,\text{ini}}\, \frac{Z_i - Z_{i+1}}{d_p}\, r_{X,i} \tag{6}$$

For clarity, a computation flow chart of the new model is given below in Figure 15.

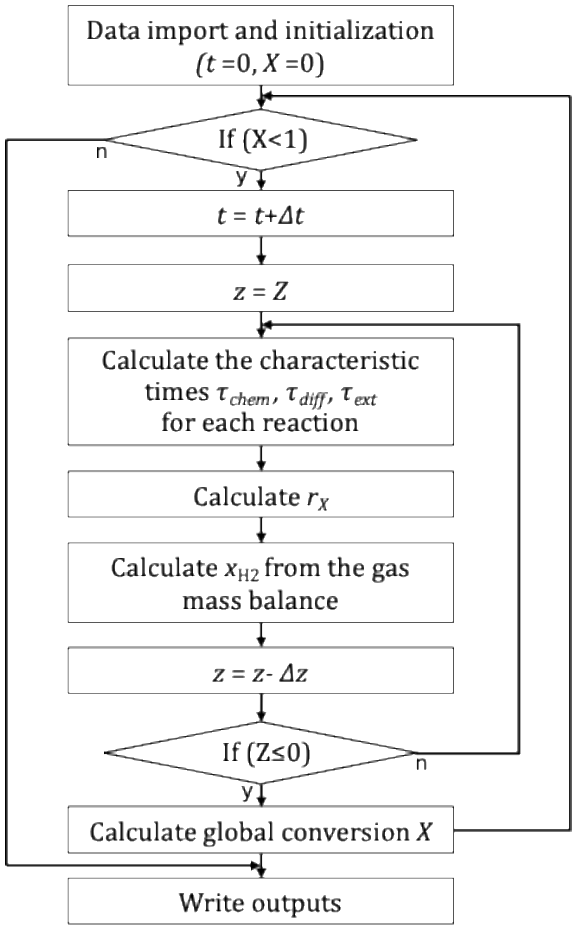

Figure 15: Flowchart of the MGPM computation.

Article 1 – **3. Results**

Article 1 – **3.1. Kinetic parameter estimation**

Since the chemical time constant for each subreaction depends on an Arrhenius equation, the reaction rate is ultimately determined by the kinetic triplets ($k_{0,j}$, $E_{a,j}$) for each subreaction ($j = 1, 2, 3$).

$$k_j = k_{0,j} \exp\left(-\frac{E_{a,j}}{RT}\right) \tag{7}$$

Owing to the intricacy in modeling the reaction of iron ore pellets with hydrogen, values reported in the literature differ quite dramatically among different authors. Figure 16 shows the scattered values of the activation energies most often reported, as well as those obtained in the present work. These factors, together with the associated frequency factors (Table 8), were determined by mathematical optimization on the basis of a comparison between the experimental and calculated kinetic curves.

Table 8: Kinetic parameters obtained by model curve-fitting against TGA experiments

	Hematite → Magnetite	Magnetite → Wustite	Wustite → Iron
Frequency factor	$k_{0,1} = 8.89 \times 10^{-4}$ m s^{-1}	$k_{0,2} = 0.165$ m s^{-1}	$k_{0,3} = 2.29$ m s^{-1}
Activation energy	$E_{a,1} = 30{,}584$ J mol^{-1}	$E_{a,2} = 80{,}721$ J mol^{-1}	$E_{a,3} = 115{,}864$ J mol^{-1}

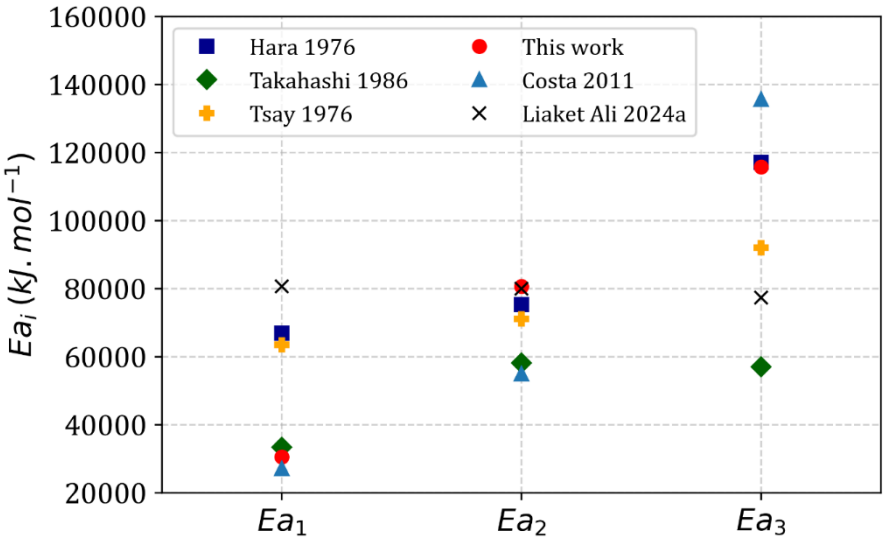

Figure 16: Overview of the activation energies reported in the literature.

More precisely, this kinetic parameter calibration was achieved by fitting the conversion curves calculated using the parameters listed in Table 3 to the experimental conversion curves, for the temperatures from 600 to 900 °C. This kinetic optimization was achieved by comparing to reduction experiments performed at temperatures between 600 °C and 900 °C using the parameters listed in Table 9. The temperature range was kept as broad as possible. However, low temperatures were disregarded because of changes in the kinetic regime due to thermodynamics [71, 78]. High temperatures were also disregarded because cracks were observed in the pellets at these temperatures; these cracks greatly enhanced diffusion and were not considered in the model. The curve fitting was achieved with a pattern search algorithm using the *pymoo* framework in Python 3.11. To avoid overfitting at high conversion degrees, the optimization was limited to X between 0 and 99 %.

Table 9: Base case parameters used in the simulations for the calibration of the kinetic triplets. Unless explicitly mentioned, these are also the parameters of the other experiments and simulations discussed in sections 3 and 4.

Operating parameters	F_g (Nlpm*)	x_{H_2}	x_{He}	P (bar)	$d_{furnace}$ (m)
	1.8	0.55	0.45	1	0.02
Pellet properties	d_p (m)	$w_{Fe_2O_3}$	w_{inert}	ρ_p (kg m^{-3})	a_{sp,Fe_2O_3} (m^2 kg^{-1})
	0.01282	0.963	0.037	3630	60.4

*Nlpm stands for normo (standard)- liter per minute, 1.8 Nlpm =3×10^{-5} m^3_{STP} s^{-1}

The obtained kinetic triplets allow us to simulate experiments with reasonable agreement in the given temperature range of 600–900 °C (Figure 17). The agreement is excellent at lower

conversion degrees, $X < 25\%$. At 700 °C and 750 °C and for $X > 60\%$, the simulation overestimates the reaction rate. This is correlated with the experimental time–temperature–transformation (TTT) diagram (Figure 19), in which kinetic slowdown is observed in this temperature range. This phenomenon has already been reported by previous authors, although no satisfactory explanation was provided [62].

The activation energies found with this method are in global agreement with other values reported in the literature (Figure 16). The short duration of the first reaction and experimental discrepancies related to gas injection explain the wide range of activation energies for this reaction. Most researchers find closer values for the activation energy of the second reaction. Models in which great importance is given to diffusion resistance rely on a relatively low activation energy for the third reaction, as shown in [25, 56, 70]. In the work of Ranzani Da Costa [18]: the activation energy of the third reaction was higher than that in our work: this is mostly due to the narrow temperature range (800–900 °C) that was used for the kinetic parameter evaluation, which resulted in underestimated reaction rates at lower temperatures.

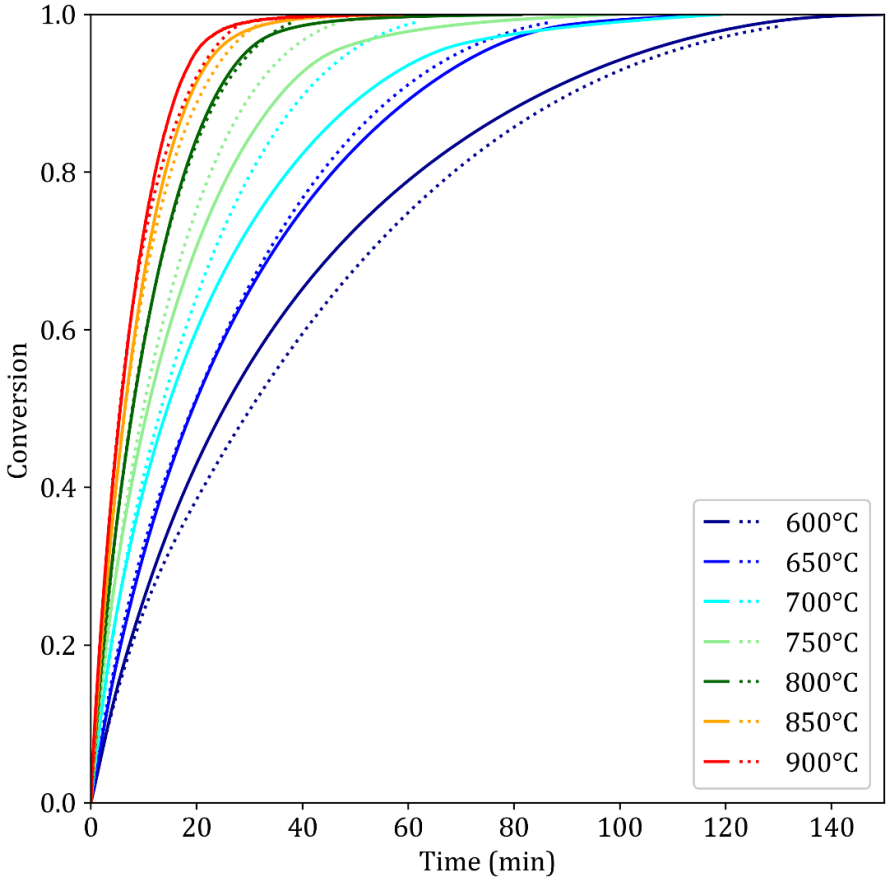

Figure 17: Simulated (dotted lines) and experimental (solid lines) reduction curves for the TG96 reduction experiments. The kinetic triplets were obtained through curve fitting of the experimental results.

Article 1 – **3.2. Validation against fixed bed experimental results**

In addition to the successful simulation of the TGA experiments (Figure 17), the pellet model was further validated at another scale against fixed bed experiments. These lab-scale experiments were performed at Tata Steel IJmuiden, Netherlands, as part of the MaxH2DR project. A 500 g

sample of D1 pellets (10–13 mm) was reduced by a 55% H_2–45% N_2 gas mixture flowing at 18 Nlpm. The objective was to observe any bed effect that could influence the reduction of the pellets. Reduction was performed until the overall conversion reached $X = 0.933$.

The simulations of the fixed-bed experiments were performed with two sets of kinetic triplets: one was obtained from curve fitting of the TGA experiments, as discussed in section 3.1, and the other one was obtained from curve fitting of the fixed-bed experiments. For simplicity, a constant pellet diameter of 12 mm was used for the simulations: it corresponds to the mean diameter of the pellet D1 sample.

Figure 18a shows the experimental and simulated curves of the fixed bed with the "fixed-bed kinetic triplet". The model greatly adapts to this new situation. Figure 18b shows the same results as those of the "TGA kinetic triplet". Here, the simulations are slightly less accurate at the start of the reaction, which could be due to differences in gas injection between TGA and fixed bed devices. Likewise, the simulations are less accurate at the end of the reaction. This is probably due to the nonisothermal behavior of the fixed bed device. Owing to the low hydrogen flow rate and high endothermicity of hydrogen reduction, the furnace temperature slightly decreased during the reduction experiments, which explains why the reaction rate was slightly overestimated by our isothermal model. Overall, the agreement between the TGA experiment and the fixed-bed simulations is very satisfactory, which further shows that the model can adapt to multiple situations and different scales. Additionally, using either He or N_2 as the inert gas only makes a minor difference in the obtained kinetics; all other experiments and simulations presented in section 3 were performed with He as the inert gas.

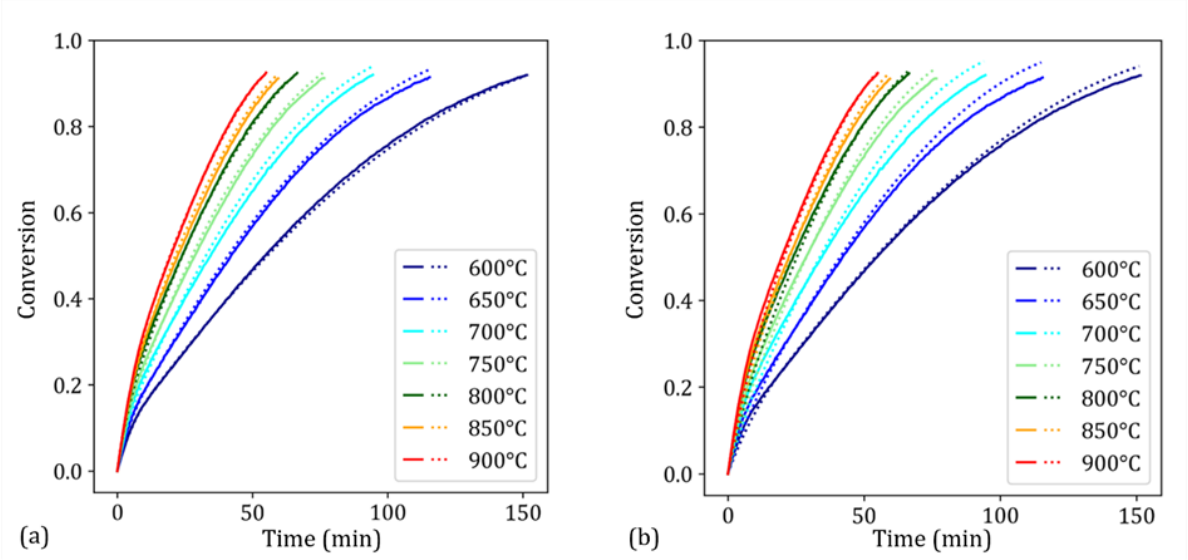

Figure 18: Simulated (dotted lines) and experimental (solid lines) reduction curves for the fixed-bed experiments, with the kinetic triplets obtained through curve fitting achieved on (a) the fixed bed experimental results and (b) the TGA experimental results.

In the next sections, simulations are first compared with experimental results for a broad range of operating parameters, such as temperature, pellet diameter, gas flow rate, water vapor content, and pellet size. To investigate the effects of parameters that could not be tuned during the experiments, a numerical parametric study of the pressure, porosity, tortuosity, and specific

surface area is then presented. Unless explicitly mentioned, the parameters used are those given in Table 9 at 900 °C.

Article 1 – **3.3. Kinetic regime**

Before the effects of these parameters are analyzed in the next sections, it is interesting to report important results from the model, which could be used to determine the type of kinetic regime. As mentioned in the Introduction, with iron ore pellets, the main cited mechanisms are control by the kinetic reaction itself and diffusion through the intergranular pores. A simple way to evaluate their respective resistances is to calculate the *reaction modulus* ϕ, so-called by Szekely et al. [43], which is equivalent to the Thiele modulus in catalysis.

$$\phi = \frac{\tau_{\text{diff}}}{\tau_{\text{chem}}} \tag{8}$$

When ϕ is small, the reaction is under chemical control; when it is large, it is controlled by diffusion; and if $0.1 < \phi < 10$, it is under mixed control. Table 10 lists the values of ϕ calculated under various conditions and at different overall conversion degrees. Globally, this shows that the reaction is in a chemical or mixed regime. In the base case (line 2), hematite and magnetite are reduced in the chemical regime, whereas wustite is reduced in a mixed regime. The results for the other cases are discussed later in their respective sections.

Table 10: Values of the reaction modulus ϕ under various conditions.

$\boldsymbol{\phi = \frac{\tau_{\text{diff}}}{\tau_{\text{chem}}}}$	$\boldsymbol{\phi_1}$ $\boldsymbol{(X = 5\%)}$	$\boldsymbol{\phi_2}$ $\boldsymbol{(X = 25\%)}$	$\boldsymbol{\phi_3}$ $\boldsymbol{(X = 60\%)}$	$\boldsymbol{\phi_4}$ $\boldsymbol{(X = 90\%)}$
Base case	**0.03**	**0.10**	**0.43**	**0.69**
$T = 600$ °C	0.04	0.01	0.11	0.15
$d_p = 10.5$ mm	0.01	0.05	0.24	0.38
$d_p = 16.5$ mm	0.05	0.16	0.60	0.99
$P = 6$ bar	0.21	0.63	2.39	4.12
$\epsilon = 0.15$	0.07	0.16	0.5	0.8
$\Gamma = 5$	0.07	0.24	0.93	1.49
$a_{sp} = 20$ m^2 kg^{-1}	0.006	0.02	0.44	0.60

Base case: T = 900 °C, d_p = 13 mm, P = 1 bar, e = 0.295, G = 2, and a_{sp} = 60.4 m^2 kg^{-1}. Each specific case was studied by varying one parameter at a time. In bold: base case; in blue: chemical control; in black: mixed control; in brown red: diffusion-predominated mixed control.

Article 1 – **3.4. Parametric study – both experimental and numerical**

Article 1 – **3.4.1. Effect of temperature**

A comparison of the experimental and numerical conversion curves for different temperatures is shown and discussed (Figure 17, section 3.1; Figure 18, section 3.2). Note that the curves get closer to each other when the temperature increases. This trend indirectly supports the assumption of

isothermicity since the temperature gradients, if any, were reported sizeable mostly above 800°C [76].

A complementary time–temperature–transformation (TTT) diagram is presented below (Figure 19). It shows that the reduction rate globally increases with increasing temperature in the range of 600–900 °C. This is due to enhanced diffusion and chemical kinetics. One can note that 98% reduction is achieved in 120 minutes at 600 °C and 25 minutes at 900 °C. The kinetic control remains unchanged in this temperature range (Table 10, compare line 3 at 600 °C and line 2 of the base case at 900 °C), with the diffusion resistance slightly increasing with temperature. However, an unusual decrease in the reaction rate is observed at temperatures of 700 °C and 750 °C and above X = 80 %. This anomaly may be due to the effects of temperature on the microstructure and the presence of wustite compared with lower temperatures [62]. This effect is more pronounced for smaller particles [18]. Specific investigations are needed to elucidate this phenomenon.

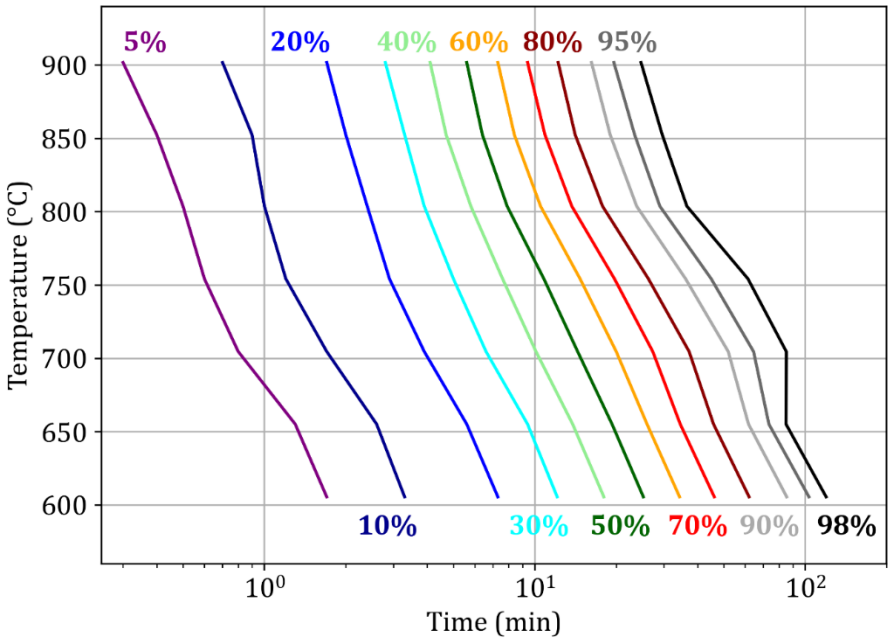

Figure 19: Time–temperature–transformation diagram for the reduction of medium-sized pellets by H_2–He. $d_p = 13\ mm$, TG96 device.

Article 1 – **3.4.2. Effect of dilution in helium**

The presence of inert gas in the mixture slows the reaction, since it reduces the frequency of interactions between hydrogen and iron oxides. As shown in Figure 20, for a constant gas flow rate, a higher helium molar fraction leads to a decreased reaction rate. This experimental behavior is accurately represented by the model. The pressure can drop suddenly in the TGA experiment when shifting from He to H_2–He, which disrupts the electrolyzer: this explains the discrepancies observed at the start of the reaction for the experiments where x_{H_2} = 80 % and x_{H_2} = 100 %.

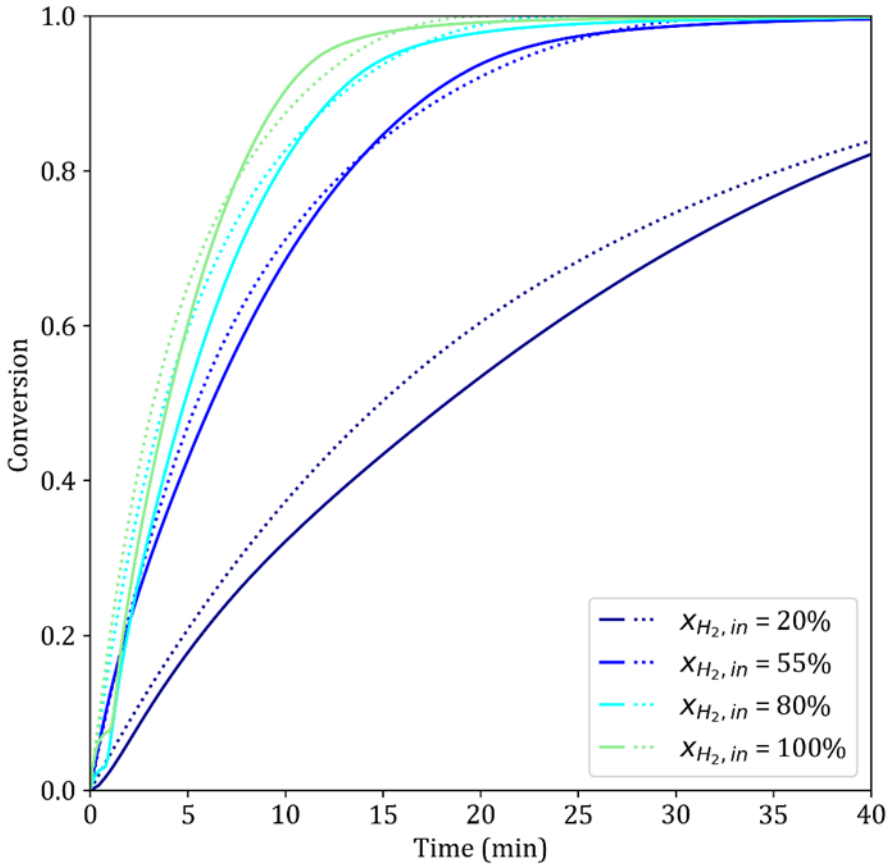

Figure 20: Simulated (dotted lines) and experimental (solid lines) results of the reduction of iron ore pellets by H_2–He at different helium dilution ratios. T = 900 °C, $d_p = 13\ mm$, TG96 device.

Article 1 – **3.4.3. Effect of the gas flow rate**

As discussed in section 2.3, decreasing the gas flow rate can have quite dramatic effects on the reaction rate. First, it decreases the gas velocity, which in turn slows the external mass transfer of hydrogen. Second, it lowers the hydrogen content in the device, which may lead to hydrogen depletion. Very high gas flow rates (10 Nlpm of pure hydrogen for 15 mm pellets) are used to compensate for this effect [62].

The simulation results for pure hydrogen at low gas flow rates agree reasonably well with the experimental results above F_g = 0.15 Nlpm (Figure 21). In fact, there is a critical gas flow rate at which the reduction reaction greatly slows, as documented in [75]. This slowdown is first observed at the very start of the reaction and is linked to difficulties in replacing the helium atmosphere with hydrogen at such low flow rates. A second slowdown is observed at the start of the third step of the reaction, after which the calculated rate of reaction is again equal to the experimental rate at the same degree of conversion. This suggests that the slowdown may be due to a nucleation effect, as mentioned in [75]. In fact, the main consequence of a lower gas flow rate is reactant gas depletion and a high content of product gas [79]. The presence of a high water vapor content in the gas mixture was reported to hinder nucleation by the adsorption of H_2O at reaction sites, thus leading to complicated nucleation before the reaction continues [46, 80]. This change in the kinetic regime is not included in the present model.

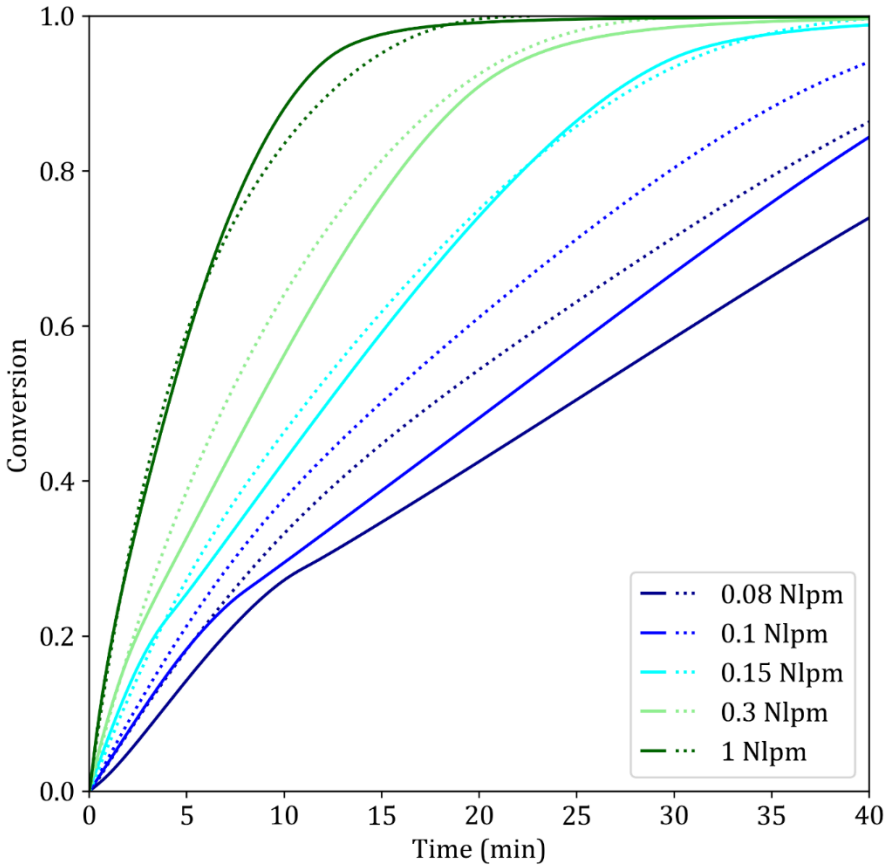

Figure 21: Simulated (dotted lines) and experimental (solid lines) results of the reduction of iron ore pellets by pure H_2 at different gas flow rates. T = 900 °C, $d_p = 13\ mm$, TG96 device.

Article 1 – **3.4.4. Effect of the inlet water vapor content**

The presence of water vapor in the gas mixture greatly slows the reaction (Figure 22). In these experiments using the Jupiter TGA system, the total gas flow rate was 0.25 Nlpm, and the inlet water vapor content was adjusted from 0 to 20 %. A major inflection point in the reduction curve is observed at approximately X = 0.3. The high water vapor inlet content and low gas flow rate saturated the TGA atmosphere with water vapor. These results directly corroborate the experiments with low gas flow rates discussed in the previous section. In both cases, the high water vapor content poisons the reaction sites on the oxides. The nucleation of iron is hindered, leading to a slowdown at the start of the third reaction. As in the previous case, this effect, which was not included in the model, could not be simulated. Finally, the slowdown systematically observed above X =0.9–0.95 reflects the difficulty in accessing the bottom part of the pellet by the gas in the Jupiter device, as explained in section 2.2.

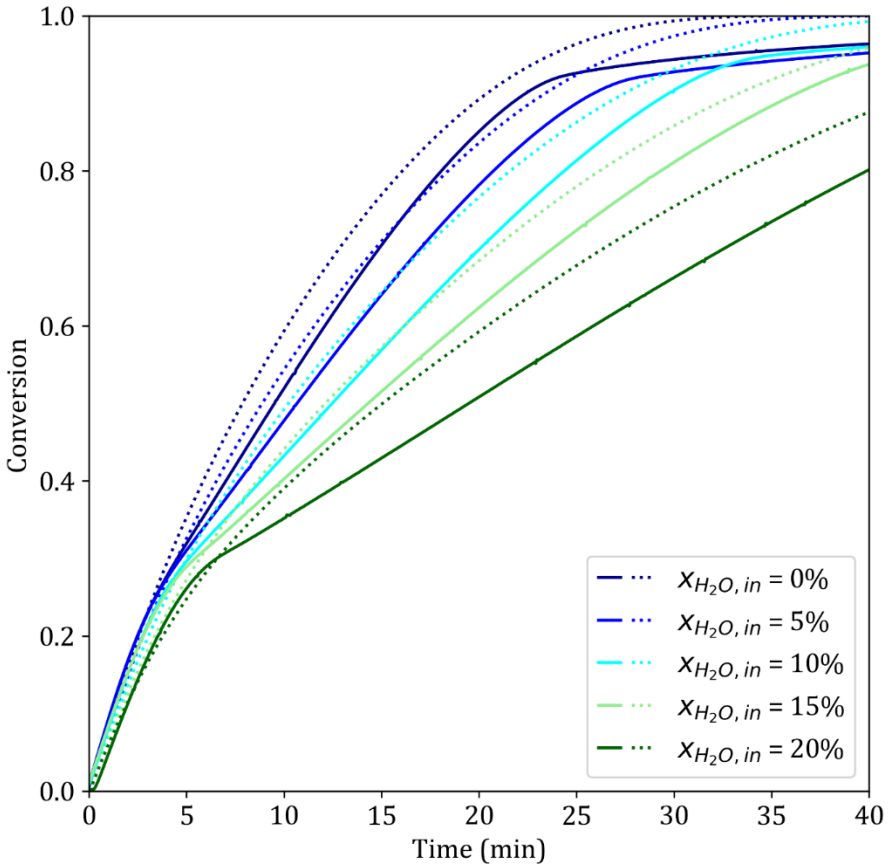

Figure 22: Simulated (dotted lines) and experimental (solid lines) results of the reduction of iron ore pellets by pure H_2 for different water vapor molar fractions. T = 900 °C, $d_p = 13\ mm$, Jupiter device.

Article 1 – **3.4.5. Effect of the pellet size**

As shown in Figure 23, increasing the pellet diameter slows the reduction reaction. First, the characteristic times of external mass transfer and gas diffusion in the pores both increase with increasing pellet size. Second, the consumption of hydrogen during TGA increases with increasing pellet size. At sufficiently large pellet diameters, this leads to hydrogen depletion at the bottom of the pellet, which in turn slows the reduction reaction.

The model correctly simulates the reduction of pellets by pure hydrogen in the 10–13 mm range. However, for larger pellets at both temperatures, the model does not sufficiently reflect the kinetic slowdown. We selected the experimental data of Metolina et al. [49] for comparison to further test the ability of our model to simulate external results. Although the main experimental parameters were available to enable the simulation, the diffusion-related parameters used in our model may not be completely adaptable to the actual samples. The kinetics may thus be more limited by intergrain diffusion than predicted (Table 10, line 5). With the 15-mm and 16.5-mm pellets, a moderate slowdown occurs at the start of the third reaction, likely due to the high water vapor content generated by the reduction reaction, for the reasons mentioned in sections 3.4.3 and 3.4.4.

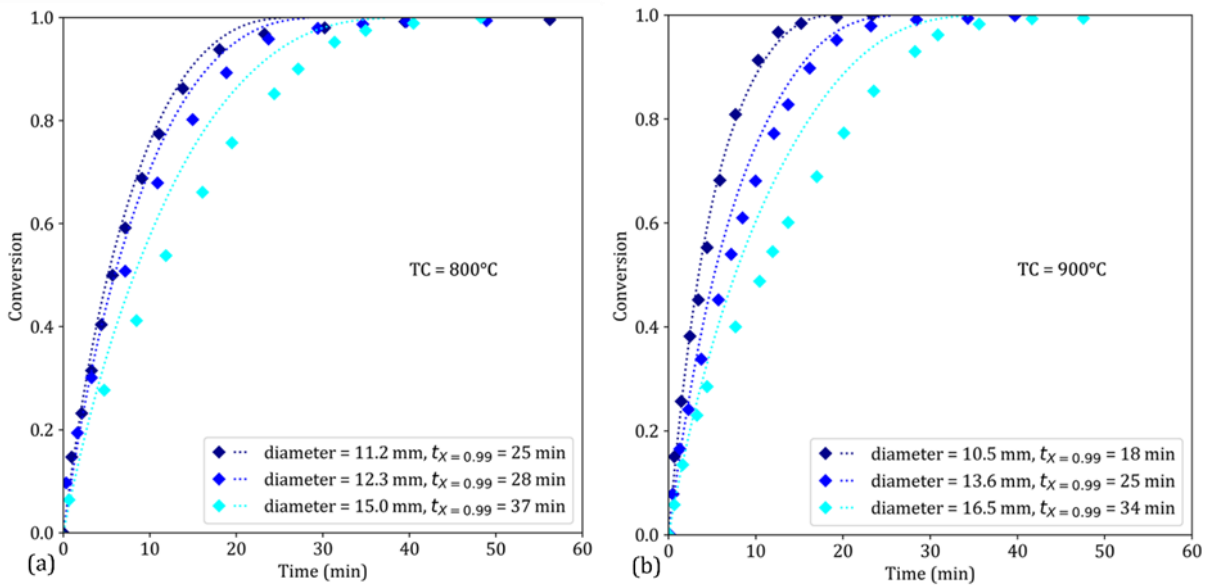

Figure 23: Simulated (dotted lines) and experimental (markers) results of the reduction of iron ore pellets by pure H_2 for different pellet diameters at (a) 800 °C and (b) 900 °C. The experimental points were obtained from [49]. $t_{X=0.99}$ represents the time necessary to reach a conversion degree X = 99 %.

Article 1 – **3.5. Parametric study – numerical**

Article 1 – **3.5.1. Effect of pressure**

According to the literature, increasing the partial pressure of hydrogen greatly decreases the reduction time [80]. In addition, above a certain threshold, increasing the pressure no longer affects the kinetics [20, 64]. In fact, increasing the pressure gradually shifts the kinetic regime from mixed to diffusion controlled, as suggested by [63].

The same conclusions can be drawn from our simulations. Figure 24 shows that increasing the pressure from 1 to 3 bar greatly decreases the reduction time, whereas only a minor improvement is observed when the pressure is further increased from 6 to 9 bar. With more H_2 available when passing from 1 to 3, 6 and 9 bars at constant x_{H_2}, the chemical reaction rates accelerate almost proportionally. Concurrently, the effect of pressure on diffusion remains negligible. As a result, the reaction becomes more limited by diffusion, as confirmed by the clear increase in the reaction modulus values (Table 10, lines 2 and 6). Thus, there is excellent agreement between the literature and our simulation results.

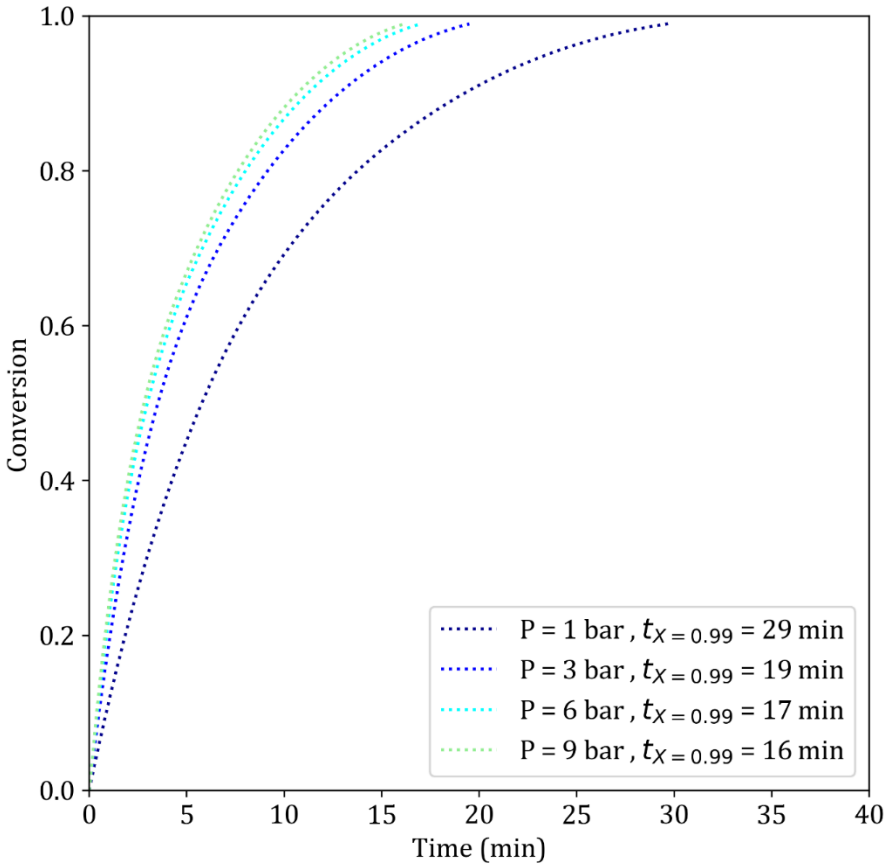

Figure 24: Simulation results of the reduction of iron ore pellets by H_2–He at different gas pressures. T = 900 °C, $d_p = 13\ mm$.

Article 1 – **3.5.2. Effect of the initial porosity**

With a constant pellet mass, increasing the porosity implies increasing the pellet diameter. Since both parameters respectively increase and decrease the reduction rate, no marked effect is observed on the reduction curves (Figure 25a). However, with a constant diameter and a varying mass, the effect of porosity becomes appreciable. An increasing porosity means that there is less hematite to convert and less water vapor generated. Both combined effects led to a slight increase in the reduction rate (Figure 25b).

The effect of porosity remains limited in our simulations. This is due to the chemical control (or chemical-predominated mixed control) of the reaction (Table 10, lines 2 and 7). Therefore, enhanced diffusion only partially increases the overall reduction rate. These results are in good agreement with those presented by [49]. Conversely, the effect of porosity is more sensible in models that give greater importance to diffusion effects (e.g. [50]).

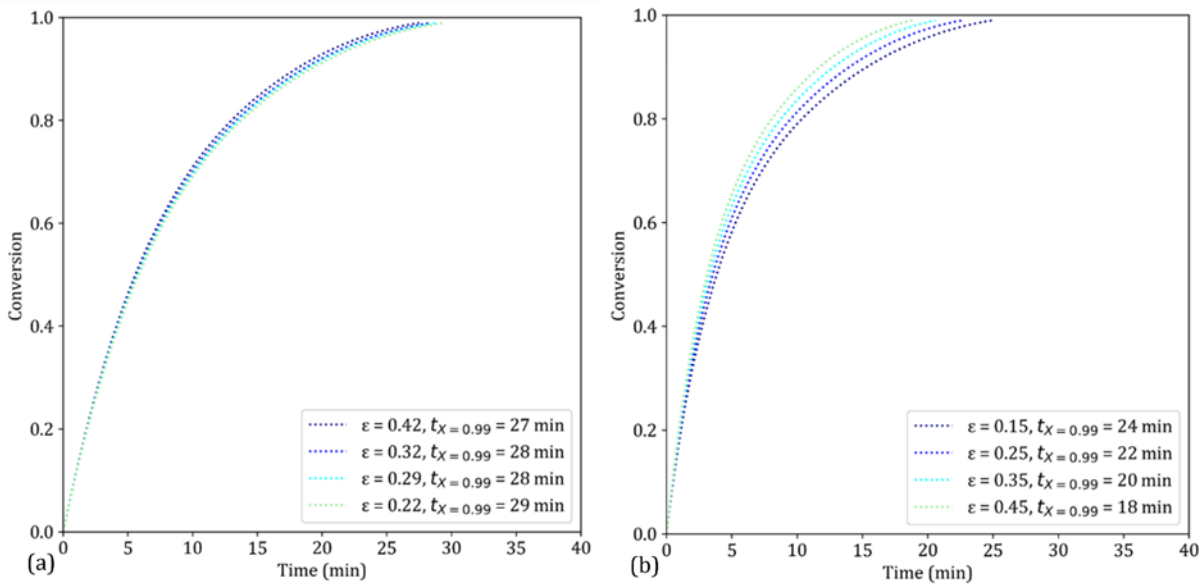

Figure 25: Simulation results of the reduction of iron ore pellets by H_2–He for different initial porosities. T = 900 °C: (a) with constant pellet mass m = 4 g; (b) with constant pellet diameter d_p=13 mm.

Article 1 – **3.5.3. Effect of tortuosity**

Tortuosity is an important parameter in regard to kinetic control since it is inversely proportional to the diffusion coefficient and proportional to the reaction modulus. An increase in tortuosity increases the characteristic time associated with diffusion and makes the kinetic regime more diffusion-controlled (Table 10, lines 2 and 8). As shown in Figure 26, increasing the tortuosity from 2 to 5 results in a 41% increase in the time necessary to reach 99% conversion, from 29 to 41 minutes. Models with greater tortuosity values usually exhibit lower activation energies, especially for the third reaction [81]. In contrast, situations in which chemical control is largely predominant give less importance to tortuosity, as shown in [59]. Physically, tortuosity should be in the range of 1–3 [18]; hence, we chose a moderate value of 2 in this work.

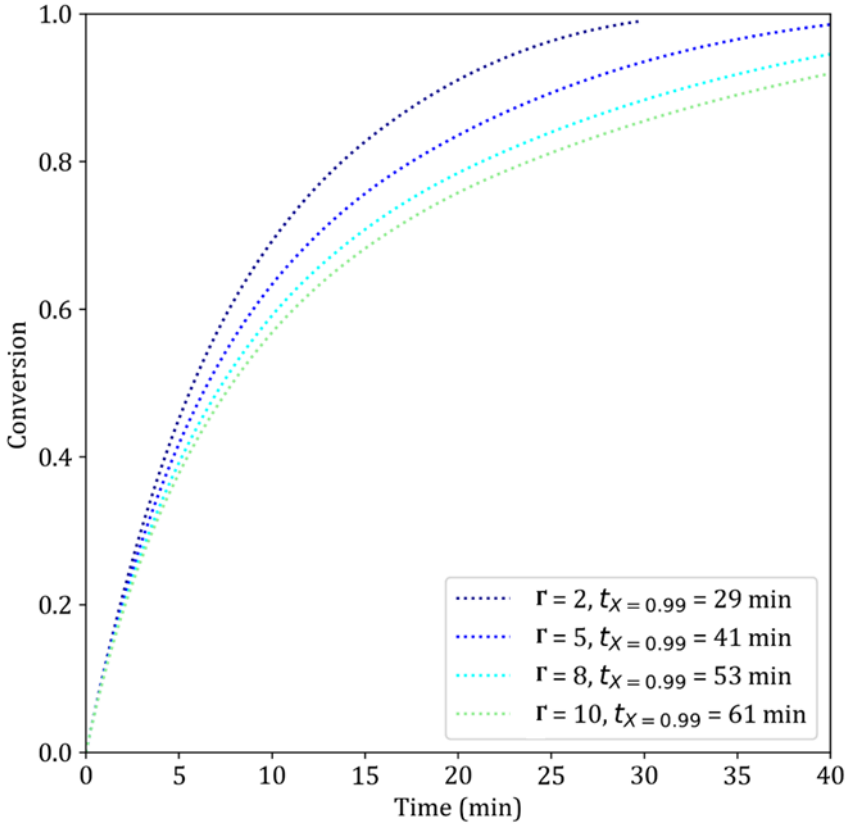

Figure 26: Simulation results of the reduction of iron ore pellets by H_2–He at different tortuosity values. T = 900 °C,$d_p = 13\ mm$.

Article 1 – **3.5.4. Effect of the initial specific surface area**

The specific surface area is highly valuable since it is a macroscopic parameter that can be easily measured. In the model, it is inversely proportional to the grain diameter, as suggested in [18]. Commercial pellets typically exhibit specific surface areas ranging from 20–60 $m^2\ kg^{-1}$ [18]. Our simulations show (Figure 27) that increasing the initial specific surface area within this range has a minor effect on the reduction time. The reaction starts faster since the first two reactions are under chemical control (Table 10, lines 9 and 2). In the third reaction, the specific surface area is determined by the size of the crystallites (Figure 13), which is independent of the size of the initial grains and thus of the initial specific surface area.

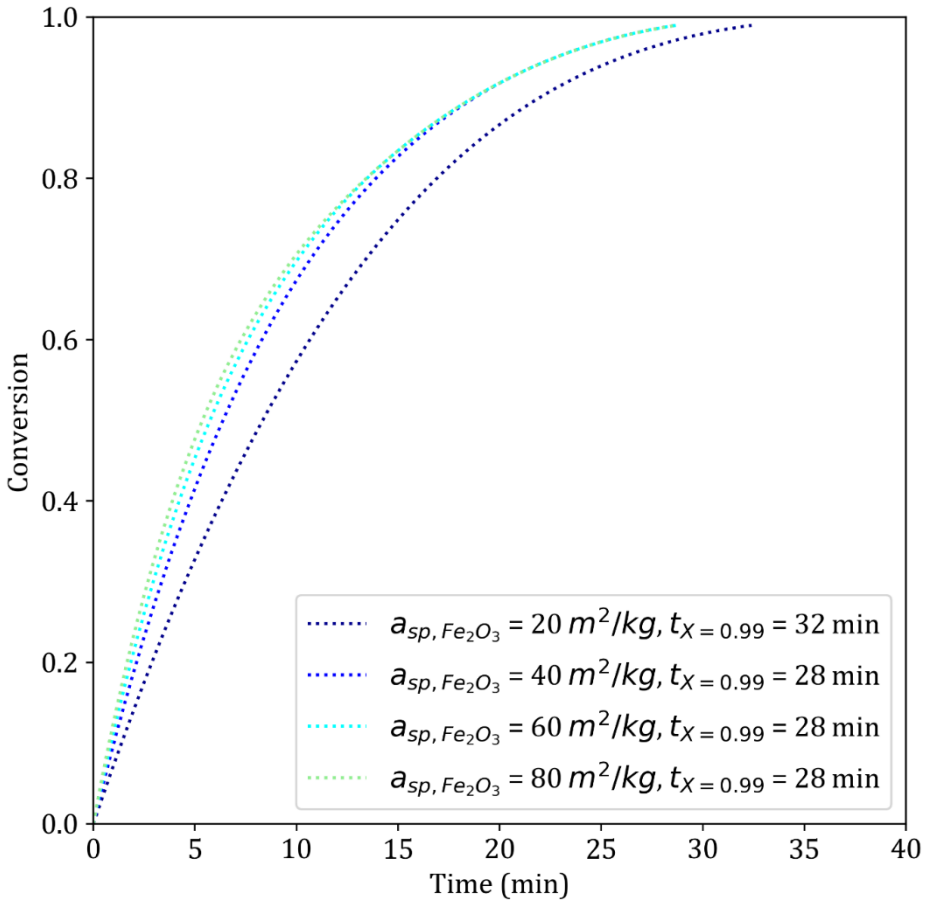

Figure 27: Simulated results of the reduction of iron ore pellets by H_2–He for different initial specific surface areas of hematite. T = 900 °C, $d_p = 13\ mm$.

Article 1 – **3.6. General Discussion**

Conclusions were drawn from the study of the hydrogen reduction of pellets with various single parameters. At this point, a few more general observations can be made:

- the reduction of iron oxides with hydrogen is limited mainly by the local chemical reactions, also called phase-boundary control [80]. The numerical parametric study conducted with the model shows that decreasing the diffusion resistance, *e.g.,* increasing the porosity, has quite limited effects on the reduction rate;
- the results indicate that the major parameters to be tuned for the reduction of iron ore pellets are the reduction temperature and the pellet diameter, which agrees with [49]. The molar fraction of hydrogen also plays a great role (if it is diluted or not), as do the molar fraction of water vapor, the initial amount of oxides and the gas flow rate, as corroborated by [65]. Conversely, the initial porosity does not seem to play such an important role in the reduction reaction, as previously observed by [49];
- for moderate flow rates (*e.g.*, 1 Nlpm H_2), a high reaction rate leads to substantial hydrogen depletion in the furnace. The atmosphere is partially replaced with water vapor, so assuming a static gas atmosphere is not reasonable. Thus, traditional single pellet reduction models (SCM and GM) cannot correctly describe the reduction reaction at low to medium flow rates in a laboratory furnace. More recent studies [38, 59, 81] tend to incorporate this evolution of the gas mixture during reduction using more complex

models than the present model does. Note that industrial blast or shaft furnaces are not likely concerned by local hydrogen depletion in view of the high gas flowrates used;
- in situations of high water vapor content and hydrogen depletion, discrepancies appear between the simulation and experimental results. This is the case for situations with low flow rates, large pellet diameters and high inlet water vapor contents. According to the literature, this is probably due to the poisoning effect of water vapor, which is adsorbed at reaction sites [46, 80]. The decrease in the number of reaction sites available for hydrogen reduction hinders nucleation, which leads to a major slowdown at the start of the third reaction;
- most operating parameters are directly related to one another in such a way that the analysis is quite intricate. For example, increasing the size of the pellet also increases the amount of oxides to be reduced, which can lead to hydrogen depletion in the furnace and complicate the analysis;
- one possible way to separate the contributions of gas diffusion and local chemical reactions is to study the reduction under specific operating conditions. The high temperature, large diameter and high pressure make the diffusion rate-limiting [62, 63]. Conversely, low temperatures, small diameters and low pressures make the local chemical reaction rate-limiting.

Article 1 – **4. Conclusions**

An extensive parametric study of the reduction of iron ore pellets by hydrogen was carried out via both laboratory experiments and modeling.

A new single pellet kinetic model was developed to describe the reduction of an iron ore pellet with hydrogen under dynamic gas conditions. This model is based on the grainy pellet model, in which we incorporate the law of additive reaction times and the evolution of gas composition due to reactant consumption. This model was validated against results from both TGA and fixed bed devices. Kinetic parameters were obtained through curve fitting; the values of activation energies obtained are close to those reported in the literature. The main conclusions of this work are as follows:

- the model can qualitatively and quantitatively describe the reduction of an iron ore pellet across a wide range of operating conditions, especially under dynamic gas conditions.
- For the temperature range considered (600–900 °C), there is a direct link between the reduction of a pellet in a TGA system and the reduction of iron ore pellets in a small fixed bed. No particular effect of the bed on the reduction rate was observed;
- the most decisive parameters for increasing the reaction rate are the temperature, pellet diameter, pressure, gas flow rate and gas composition. The initial porosity of a sample does not seem to have a major influence on the reaction rate. The graphical abstract schematically illustrates these results;
- the measured rate of reduction of iron oxides in the presence of a high water vapor content is lower than what is simulated. The same is observed in situations where the pellet is large or the gas flow rate is very low. This is attributed to the poisoning effect of water vapor, which adsorbs on reaction sites instead of hydrogen.

In addition to the cases studied, this approach allows us to predict the behavior of pellets during reduction and can help to identify suitable pellet properties. The MGPM can be implemented in multiparticle reactor models, such as shaft furnace simulation models. The above-mentioned current limitations of the model could be lifted as follows: introducing

nucleation kinetics in connection with the water vapor poisoning effect, modeling the formation of cracks at high temperature that enhance gas diffusion, further characterizing the pore and grain evolution to better describe the influence of the pellet diameter and the slowdown at 700–750 °C. The extension of the model to non-isothermal conditions) would also deserve to be considered.

Article 1 – **Appendix: Characteristic time constants**

Please refer to the main text for the notation and the reference.

The kinetic parameters $k_{1,A}$… are discussed in the main text. Note that the expressions of the chemical reaction times correspond to reactions that are first order with respect to hydrogen, as evidenced by many authors, e. g. [20].

The diffusion parameters are determined as follows. The effective diffusion coefficients (D_{interg}, D_{intrag}, etc.) consider the complex gas diffusion through the pores of the pellet. For a gas species A, these are as follows:

$$D_{A,\text{eff}} = \frac{\epsilon}{\Gamma}\left(\frac{1}{D_{A,\text{mix}}} + \frac{1}{D_{A,\text{Kn}}}\right) \quad (A1)$$

where ε is the porosity of the ash layer, which is the layer through which the reactant gas diffuses to reach the oxide phase undergoing reduction; Γ is the tortuosity factor accounting for nonstraight pores; $D_{A,mix}$ is the molecular coefficient of diffusion of A in the gas mixture; and $D_{A,\text{Kn}}$ is the Knuden coefficient of diffusion, which must be considered in the case of small pores. Their respective expressions are as follows:

$$D_{A,\text{mix}} = \frac{1 - x_A}{\sum_{i \neq A} \frac{x_i}{\mathcal{D}_{Ai}}} \quad (A2)$$

where x_i is the molar fraction of each gas i and where $\mathcal{D}_{Ai}$ is the binary diffusion coefficient of gas A and gas i; the latter is derived from the Chapman–Enskog theory, e.g., [82];and

$$D_{A,\text{Kn}} = \frac{d_{\text{pores}}}{3}\sqrt{\frac{8RT}{\pi M_A}} \quad (A3)$$

where d_{pores} is the mean diameter of the pores and where M_A is the molecular mass of gas A.

Table A1: Characteristic times and conversion functions used in the model.

	Hematite → Magnetite	Magnetite → Wustite	Wustite → Iron
External mass transfer	$\tau_{\text{ext1},A} = \frac{\tilde{\rho}_{Fe_2O_3} d_p}{18 k_g c_t (x_{A,\infty} - x_{A,\text{eq1}})}$	$\tau_{\text{ext2},A} = \frac{8\tilde{\rho}_{Fe_3O_4} d_p}{57 k_g c_t (x_{A,\infty} - x_{A,\text{eq2}})}$	$\tau_{\text{ext3},A} = \frac{\tilde{\rho}_{Fe_{0.95}O} d_p}{6 k_g c_t (x_{A,\infty} - x_{A,\text{eq3}})}$
Intergrain diffusion	$\tau_{\text{diff1interg},A} = \frac{\tilde{\rho}_{Fe_2O_3} (d_p)^2}{72 D_{\text{interg1},A} c_t (x_{A,\infty} - x_{A,\text{eq1}})}$	$\tau_{\text{diff2interg},A} = \frac{2\tilde{\rho}_{Fe_3O_4} (d_p)^2}{57 D_{\text{interg2},A} c_t (x_{A,\infty} - x_{A,\text{eq2}})}$	/
Intragrain diffusion	/	$\tau_{\text{diff2intrag},A} = \frac{2\tilde{\rho}_{Fe_3O_4} (d_{\text{grain}})^2}{57 D_{\text{intrag2},A} c_t (x_{A,\infty} - x_{A,\text{eq2}})}$	/
Intercrystallite diffusion	/	/	$\tau_{\text{diff3interc},A} = \frac{2\tilde{\rho}_{Fe_{0.95}O} (d_p)^2}{24 D_{\text{interc3},A} c_t (x_{A,\infty} - x_{A,\text{eq3}})}$
Solid–state diffusion	/	/	$\tau_{\text{diff3intrac},A} = \frac{\tilde{\rho}_{Fe_{0.95}O} (d_{\text{crist,ini}})^2}{24 D_{\text{sol}} (c_{Ox,eq} - c_{Ox,\infty})}$
Local chemical reaction	$\tau_{\text{chem1},A} = \frac{\tilde{\rho}_{Fe_2O_3} d_{\text{grain}}}{6 k_{1,A} c_t (x_{A,\infty} - \frac{x_{C,\infty}}{K_{\text{eq},1}})}$	$\tau_{\text{chem2},A} = \frac{\tilde{\rho}_{Fe_3O_4} d_{\text{grain}}}{2 k_{2,A} c_t (x_{A,\infty} - \frac{x_{C,\infty}}{K_{\text{eq},2}})}$	$\tau_{\text{chem1},A} = \frac{\tilde{\rho}_{Fe_{0.95}O} d_{\text{crist,ini}}}{2 k_{3,A} c_t (x_{A,\infty} - \frac{x_{C,\infty}}{K_{\text{eq},3}})}$
The conversion functions below are the same for the three subreactions			
Chemical conversion function	$f(X) = 1 - (1 - X)^{\frac{1}{3}}$		
Diffusion conversion function	$g(X) = 1 - 3(1 - X)^{\frac{2}{3}} + 2(1 - X)$		
External transfer conversion function	$h(X) = X$		

I.4. Additional results on the reduction of iron oxides with hydrogen

A thorough experimental and numerical study on the hydrogen reduction of iron ore pellets was presented in Article 1. A versatile modified grainy pellet model (MGPM) was developed with the intent to simulate the reduction of iron ore pellets in a reducing atmosphere, the gas composition of which evolves over time. The model was validated against lab-scale TGA devices and lab-scale fixed bed experiments. It was notably shown that the most decisive parameters in improving the reaction rate were the temperature, the pellet diameter, the pressure, the gas flowrate and the gas composition.

In this section, we present additional results, not given in the publication. The reproducibility of the reduction experiments was assessed. Investigations were led to determine the influence of pellet type, but also to get a clearer understanding of the kinetic slowdowns and of the high temperature reduction behavior.

I.4.1. Reproducibility of the reduction experiments

The reproducibility of the reduction experiments was assessed by repeating certain experiments multiple times in our laboratory in University of Lorraine (UL) and in TSE Ijmuiden. This was done to evaluate the uncertainty margins for further analysis. The reproducibility was evaluated for three different sets of experimental conditions:

- 4.0 g CVRD pellets (type D) reduced by 1 Nlpm H_2/1 Nlpm He at 900°C;
- 4.0 g QCM pellets (type C) reduced by 1 Nlpm H_2/1 Nlpm He at 900°C;
- 6.6 g CVRD pellets (type D) reduced by 1 Nlpm H_2/1 Nlpm He at 800°C.

As seen in Figure 28 and Figure 29, little deviation is observed between the conversion curves of pellets (type D) reduced in the same experimental conditions – the maximum difference in reduction time is approximately 15% for conversion of 98%. A deviation of the same order of magnitude was observed for QCM pellets, while no deviation was observed for heavier pellets (6.6 g). Further reproducibility experiments were led at TSE Ijmuiden, and minor deviation was found for type C and type D pellets. This was attributed to batch-to-batch variation. As a conclusion, the reproducibility of our reduction experiments is quite satisfying.

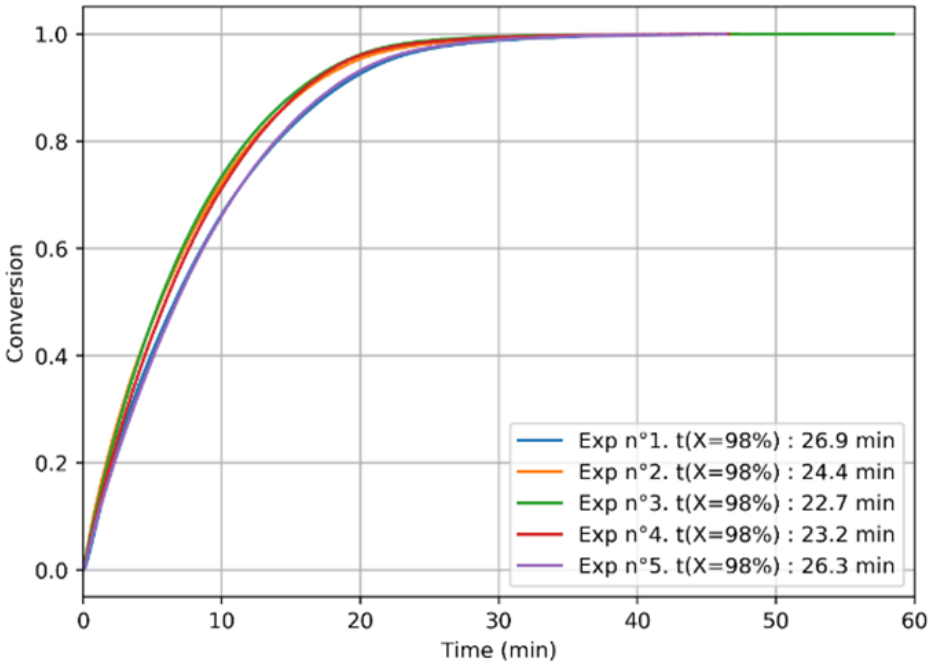

Figure 28: Assessment of the reproducibility of the reduction of D type pellets. Reduction of single pellets in a TGA at 900°C (experiments done at UL).

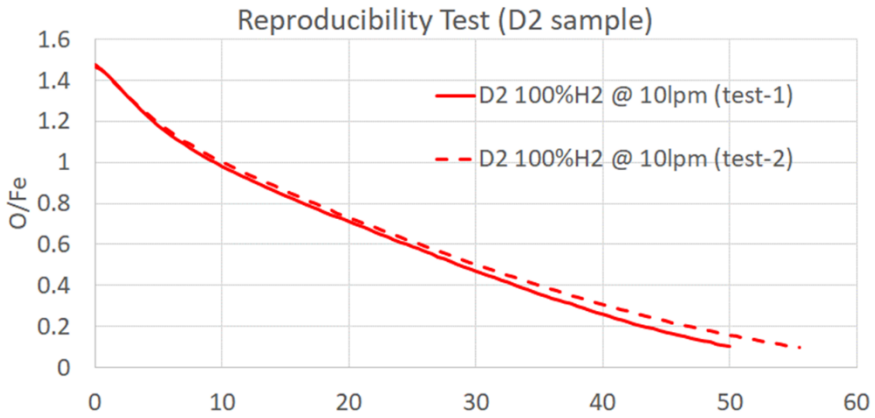

Figure 29: Assessment of the reproducibility of the reduction of D2 pellets (type D, d_p = 13-15 mm). Reduction of a 500-g batch pellet at 800°C (experiments realized by TSE, in the context of the MaxH2DR project).

I.4.2. Effect of pellet type on the reduction

Joint experiments performed at UL (Figure 30 and Figure 31) and TSE (Figure 32and Figure 33) help to understand the reduction behavior of the pellets considered. The chemistry of each type of pellet is given in Table 11. In most cases, it was observed that pellets B and C are respectively the fastest and slowest to reduce. This effect could be attributed to the high content in beneficial additives (CaO and Al_2O_3) in pellet B, as these were reported to promote a porous structure during reduction [39]. However, no direct cause could be attributed to the slow reduction of type C pellets.

Generally speaking, these results show a dispersion of the curves more pronounced at low temperatures, where the reduction rates are only controlled by chemical kinetics. For higher

temperatures the reduction rates shift to more diffusion control, and similar reduction paths were observed for all the considered pellets. From these observations, we can suppose that the difference in behavior at low temperatures is due to chemical effects associated to the composition of the gangue. This is in contradiction with the literature, which suggests that the gangue composition mostly influences the diffusion properties of pellets [39].

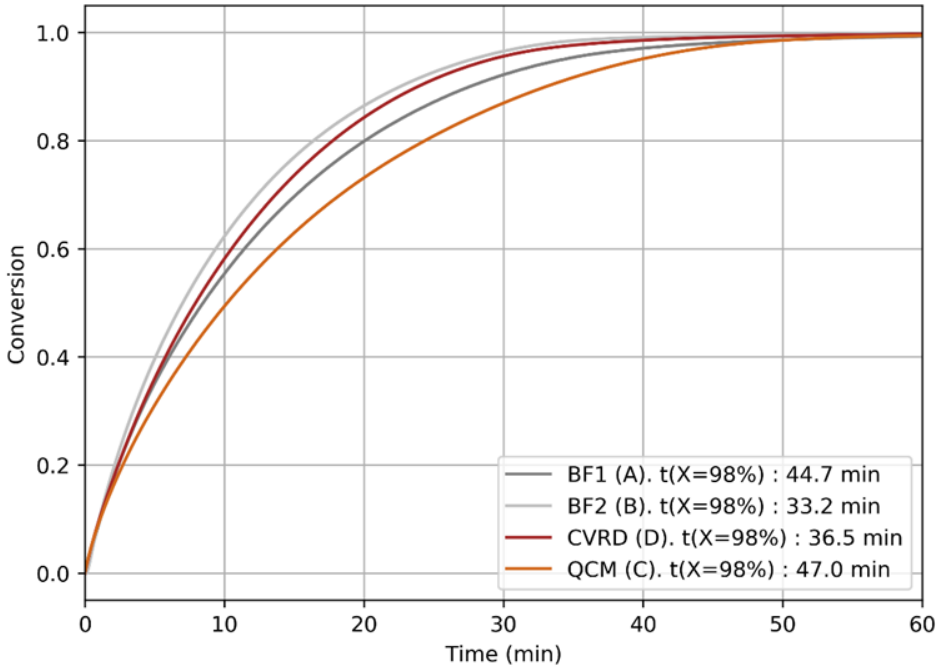

Figure 30: Reduction of different types of pellets in a TGA with a 55% H_2 45% He gas mix at T = 800°C. $d_p = 13$ mm, $F_g = 1.8$ Nlpm (experiments done at UL).

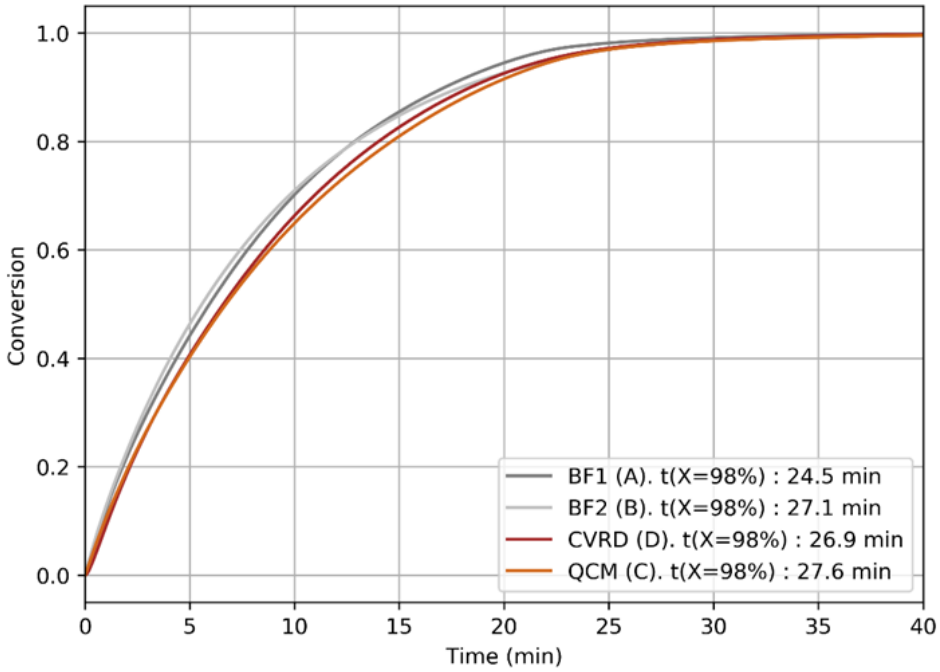

Figure 31: Reduction of different types of pellets in a TGA with a 55% H_2 45% He gas mix at T = 900°C. $d_p = 13$ mm, $F_g = 1.8$ Nlpm (experiments done at UL).

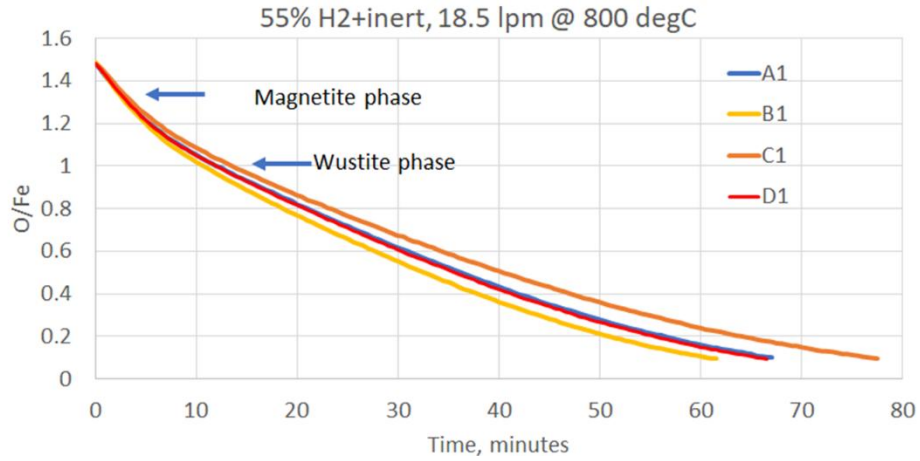

Figure 32: Reduction of different types of pellets in a batch furnace with a 55% H_2 45% He gas mix at T = 800°C. $m = 500$ g, $d_p = 10 - 13$ mm, $F_g = 18.5$ Nlpm (experiments done at TSE Ijmuiden).

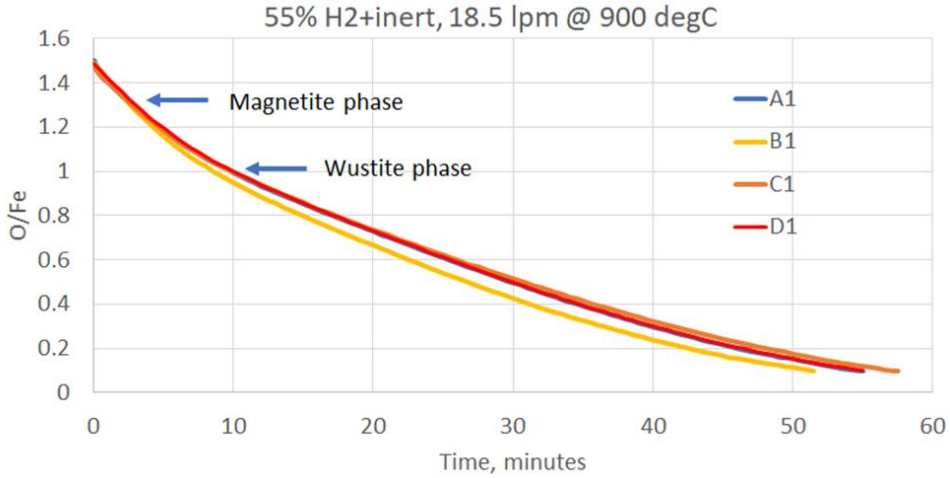

Figure 33: Reduction of different types of pellets in a batch furnace with a 55% H_2 45% He gas mix at T = 900°C. $m = 500$ g, $d_p = 10 - 13$ mm, $F_g = 18.5$ Nlpm (experiments done at TSE Ijmuiden).

I.4.3. Investigation of the kinetic slowdowns of hydrogen reduction

Generally speaking, the rate of reduction increases at higher temperatures owing to the enhancement of diffusion and chemical kinetics. However, a series of discrepancies in the temperature dependency of the reduction rate is systematically observed and is reported in the literature under the appellation of kinetic slowdowns (KS). For iron oxide samples in general, these slowdowns are observed in the 650–750°C temperature range (KS1), and around 920°C (KS2) [46]. For pellets in particular, these are usually observed in the vicinity of 700°C and in the temperature range 950–1000°C [18, 20, 62, 74, 83, 84].

KS1 is generally attributed to difficulties in intraparticle gaseous diffusion related to the formation of wustite [46, 62]. At the grain scale, the sintering of a dense layer of FeO or metallic Fe leads to entrapped oxides, which are difficult to reduce. This phenomenon leads to a drastic drop in the

reduction rate [46]. This kinetic slowdown is much more marked for small particles than for large pellets [18, 62, 83].

Table 11: Chemistry of the pellets studied in this work and in the MaxH2DR project. XRD measurements were realized at TSE IJmuiden.

Name	Size (mm)	Al2O3	CaO	Fe	FeO	MgO	MnO	P2O5	SiO2	TiO2
A1	10-13	0.34	1.04	64.9	0.15	0.39	0.15	0.017	5.0	0.047
A2	13-15	0.35	1.05	64.9	0.16	0.38	0.16	0.016	5.1	0.042
B1	10-13	0.64	2.08	64.6	<0.1	1.34	0.27	0.057	2.76	0.21
B2	13-15	0.64	2.12	64.6	0.15	1.33	0.27	0.058	2.75	0.21
C1	10-13	0.43	0.99	66.9	0.69	0.28	0.053	0.027	1.73	0.21
C2	13-15	0.4	0.9	67.0	0.73	0.29	0.0	0.0	1.69	0.2
D1	10-13	0.73	0.95	66.4	0.71	0.12	0.15	0.057	2.33	0.094
D2	13-15	0.72	0.93	67.7	1.79	0.12	0.14	0.056	2.27	0.092

This observation may be linked to the heterogeneity of the reduction process at the scale of the pellet. In smaller pellets, the diffusion of the gas in the pellet is quite fast, so the gas composition and temperature inside the pellet are quite homogeneous [62]. Consequently, if a kinetic slowdown is observed, it refers to a global slowdown, at the scale of the whole pellet. For large pellets however, the extent of the reduction is much more heterogeneous at the scale of the pellet, especially between the outer part of the pellet and its center. Indeed, as diffusion inside the pores is coupled with chemical reaction, the composition of the reducing gas at the center of the pellet is different from the composition at the periphery of the pellet. At the periphery of the pellets the gas is highly reducing, while it is loaded with H_2O and poorly reducing at the center. Consequently, this poorly reducing gas may not be able to promote the formation of dense layers of FeO/Fe, which could prevent the kinetic slowdown in the innermost regions of the pellet. On the reduction curves, this would result in a smoothed kinetic slowdown for large pellets, as observed in the above-mentioned studies.

This interpretation fits well to a set of experiments with no water vapor in the inlet gas, which clearly exhibited a kinetic slowdown around 700°C (Figure 34).

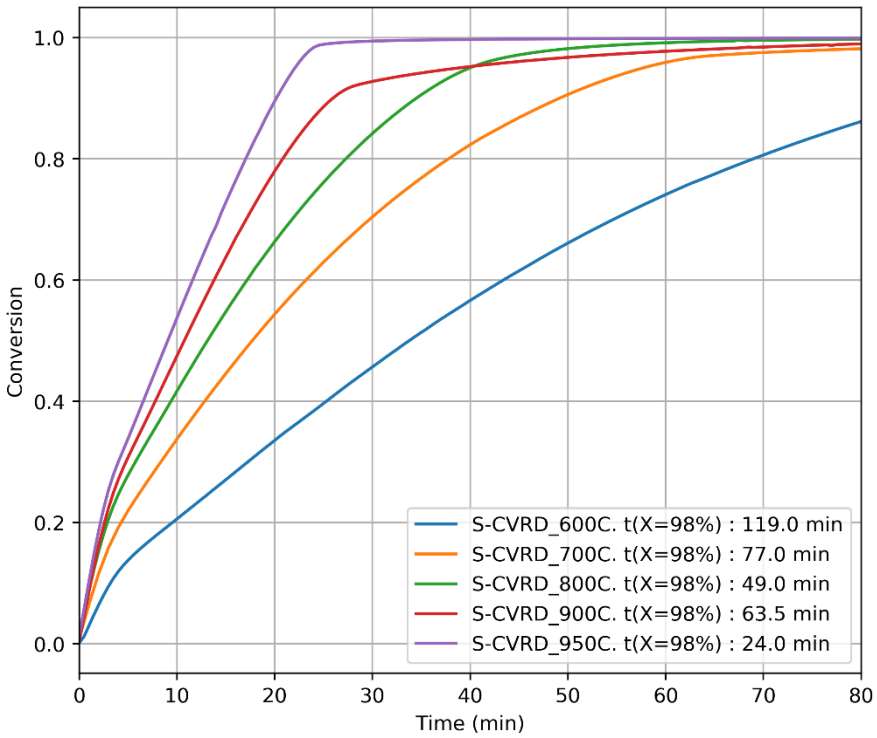

Figure 34: Reduction of 13mm D-type pellets between 600°C and 950°C in atmosphere containing water vapor ($x_{\mathrm{H_2O},inlet} = 5\%, F_{g,H_2} = 0.2375$ Nlpm).

This explanation also sheds light on some results presented in [51], which did not exhibited the kinetic slowdown around 700°C. In these experiments, the sample to be reduced was a powder (very small particles) and the flowrate was very low. The reducing gas being only poorly renewed in H_2, the composition of the gas surrounding the powder varied with time and could contained a significant amount of H_2O, resulting from the reduction of oxides. This presence of H_2O in the gas drastically lowered its reducing power and may have prevented the sintering of the Feo/Fe phases, which in turns would have avoided a kinetic slowdown at this stage of the reduction.

The second known kinetic slowdown, KS2, is usually considered to be caused by the allotropic transformation of alpha iron to gamma iron above 912°C [20]. Indeed, at high temperatures, solid-state diffusion of oxygen influences the reduction rate. This solid-state diffusion is much slower in gamma iron phase than in alpha iron phase, which causes the reduction to slow down when temperature is raised above 912°C. In [18], three different types of pellets were reduced (see Table 3 in section I.1.4.1.). For each type of pellet, KS2 was observed between 900°C and 950°C. Furthermore, these experiments showed that the conversion degree at which the kinetic slowdown started was higher for smaller pellets. Indeed, KS2 was observed at X = 70% for 18.5-mm CVRD-DR pellets, and at X = 90% for 11-mm CVRD-DR pellets. This indicates a diffusion control of the reaction, which is usual at high temperatures. As the allotropic transformation of alpha to gamma iron is dependent on impurities in the iron, the exact temperature of transformation can vary and KS2 is often observed at 1000°C [74]; sometimes it is not observed at all [62].

In our experiments, KS2 was observed at T = 950°C for A-type and D-type pellets (Figure 35 and Figure 36). Actually, the reduction rate at 950°C was faster than the one at 900°C until X = 0.9, before drastically decreasing. On the other hand, KS2 was not observed at low flowrates or high H_2O inlet content.

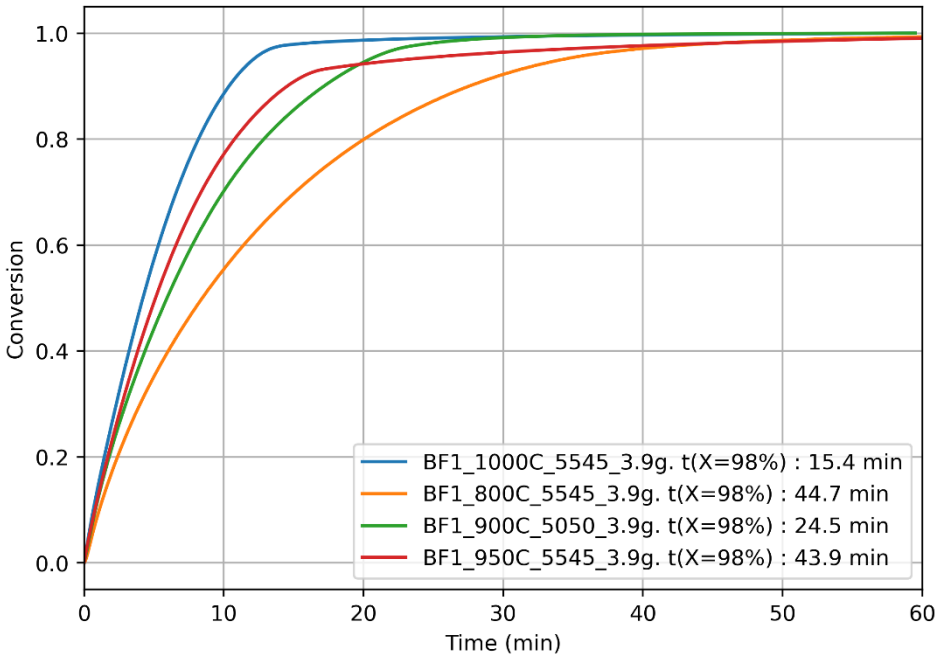

Figure 35: Reduction of 13 mm A-type pellets between 600°C and 1100°C with a 55% H_2 45% He gas mix. $F_g = 1.8$ Nlpm.

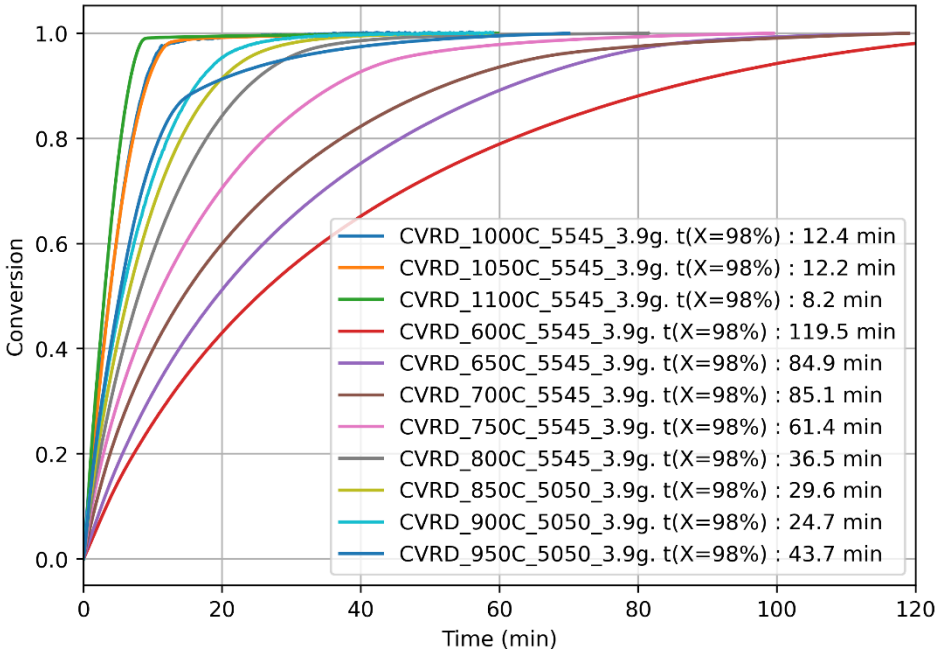

Figure 36: Reduction of 13mm D-type pellets between 600°C and 1100°C with a 55% H_2 45% He gas mix. $F_g = 1.8$ Nlpm.

I.4.4. High temperature reduction experiments

Our model is not designed to work at very low temperatures since the reduction pathway changes below $T < 570$°C. However, it can theoretically predict the reduction behavior of pellets above 900°C. Simulation results for the reduction of pellets at high temperature ($T > 1000$°C) are presented in Figure 37. We can see that the model greatly underestimates the reduction rate for

conversion $X > 50\%$. One possible explanation lies in the formation of wide-open radial cracks during reduction above 1000°C [18]. These cracks are probably caused by internal stresses due to the volume mismatch between wustite and iron [18, 85]. If these cracks indeed appear during reduction, they would highly enhance gas diffusion inside the pellet. Since gas diffusion becomes the rate-limiting mechanism at high temperatures, bypassing it can lead to much higher experimental reaction rates than the simulated ones.

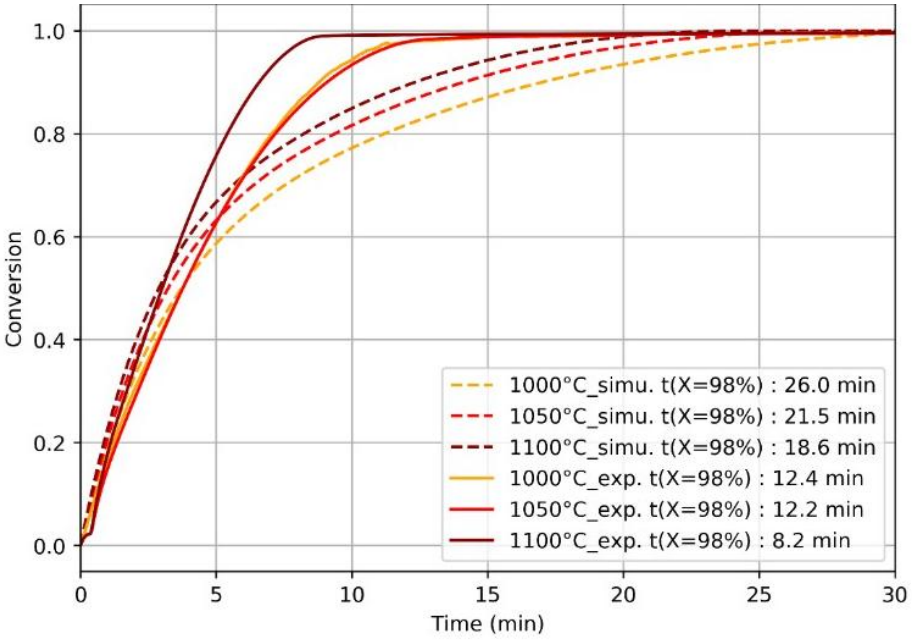

Figure 37: Reduction experiments (solid lines) and simulations (dashed lines) of 13mm D-type pellets between 1000°C and 1100°C by a 55% H_2 45% He gas mix. $d_p = 13$ mm, $F_g = 1.8$ Nlpm.

I.5. Conclusion

The reduction of iron oxides is a multi-step process that involves chemical reaction and gas diffusion phenomena. These features make the task of reaction modeling uneasy. A proper modified grainy pellet model (MGPM), proposed in Article 1, was designed to simulate the reduction of iron ore pellets with hydrogen and with gas compositions that evolve over time. It proved robust in most simulation situations in the temperature range studied (600–900°C). However, observations of kinetic slowdowns and high-temperature reduction behavior show that both further experimental investigations and model improvement are still required to fully understand and simulate the reduction mechanisms over a wider temperature range.

As seen in this chapter, the operating conditions can either enhance or hinder the transport phenomena associated to the reduction. To get a clearer idea of the diffusion mechanisms inside the pores of the pellets, further physical characterization is needed. In the next chapter, characterization devices are used to determine the relevant properties of partially or completely reduced pellets, such as porosity, surface area, pore size distribution... This will give us clearer insight on the interplay between the reduction kinetics and the evolution of the pellet microstructure.

II. Transformations of the pore structure in iron ore pellets during reduction by hydrogen

Hematite pellets used in the direct reduction industry are aggregates of dense grains separated by a massive pore network. These pores enable transport of reductant and product gas within the samples which is crucial for ensuring great reduction kinetics, particularly for large samples such as iron ore pellets [18, 62]. The shape of these pores evolves drastically during reduction by hydrogen. The phase transformations result in volume shrinkage associated with the removal of oxygen, which in turn promotes the formation of new pores [68]. Later in the reduction, the grains disintegrate to give birth to smaller entities called crystallites [17], leading to a major modification of the pore characteristics. The extent of these transformations highly depend on the reduction temperature and the reduction rate [86]. The intricated interplay between the reduction rate and the transformation of the pore network is a major subject of investigation, which must rely on a systematic characterization of reduced pellets. An efficient way to reconstruct the reduction path is to achieve interrupted experiments, that is to artificially stop reduction experiments in order to reach arbitrary conversion degrees. In this chapter, the results of investigations of the pore properties of pellets reduced by hydrogen between 600°C and 900°C are presented in the following paper (Article 2). The results presented in this article offer a macroscopic view of the evolution of the pore properties of pellets, based on Hg porosimetry and Kr adsorption experiments. The Article is written but was not submitted yet, as future SEM observations are planned in order to complement the abovementioned measurements.

II.1. Article 2: A macroscopic investigation of the pore structure of iron ore pellets reduced with hydrogen, by A. Marsigny, R. Ben Hassine, J.B. Letz, O. Mirgaux, F. Patisson

Article 2 – **Abstract**

The hydrogen direct reduction of iron ore pellets is a promising technology to mitigate the massive carbon emissions of the steelmaking industry. To optimize the reduction process, understanding the interplay between the reduction kinetics and the evolution of the pellet microstructure is a crucial issue. The rate of reduction of an iron ore pellet depends on its adsorption and pore diffusion properties, which require the knowledge of the pore distribution and specific surface area in the course of reduction. These were measured using mercury intrusion porosimetry and krypton adsorption. Both methods gave concordant results. The porosity of pellets reduced with hydrogen increase with the conversion degree and temperature, and a dip in the curve is observed above 800°C. Additionally, the specific surface area greatly increases from the start of the reduction before reaching a maximum value, which is considerably higher after reduction at low temperatures. The results on pore size distributions reveal that small pores generated at the start of the reduction coalesce as the reduction progresses, hinting at possible sintering of the freshly formed iron grains. These results clearly show different reduction pathways as the reduction temperature is increased and major microstructural rearrangements above 800°C.

Article 2 – **1. Introduction**

The iron and steelmaking industry is responsible for 7-8% of the global CO_2 emissions [87]**.** 70% of these emissions are due to the conversion of iron ores in the blast furnace unit, which converts iron ore and coke into pig iron and CO_2. A competing, C-lean technology is the hydrogen direct reduction shaft furnace, which reduces the iron ore with hydrogen, producing pure iron at solid state and water vapor. In a recent paper, we showed that the most crucial parameters to improve the kinetics of reduction is the tuning of operational parameters at the process scale, such as the temperature of reduction and the reducing gas flowrate [88]. However, the kinetics of reduction also highly depend on the physical properties of the pellets, such as their porosity and their specific surface area.

Hematite pellets used in the direct reduction industry are porous aggregates of dense grains of Fe_2O_3, with traces of impurities called gangue (SiO_2, CaO, MgO…). They are designed to present a high intergranular porosity and a high specific surface area a_{sp}. The former facilitates the gas diffusion inside the pellet while the latter increases the area of contact between the reductant gas and the iron oxides, resulting in improved kinetics. This porous microstructure considerably evolves during reduction with hydrogen, as oxygen is removed from the iron oxides and new phases are formed following the reduction reactions (1-3) above 570°C:

Reaction 1 $$3Fe_2O_3 + H_2 = 2Fe_3O_4 + H_2O \quad (42)$$

Reaction 2 $$Fe_3O_4 + \frac{16}{19}H_2 = \frac{60}{19}Fe_{0.95}O + \frac{16}{19}H_2O \quad (43)$$

Reaction 3 $$Fe_{0.95}O + H_2 = 0.95Fe + H_2O \quad (44)$$

Firstly, the overall volume of the pellet can increase substantially during the reduction by H_2 or CO, and this is called pellet swelling. This phenomenon is rarely observed at temperatures below 750°C, but it gains in importance with increasing temperatures [18, 89, 90, 91]. It is usually attributed to the formation of iron whiskers during CO reduction and to the phase transformations during CO and H_2 reduction [84, 89, 90, 92]. The swelling index (relative change in volume) reaches a maximum value for a reduction degree between 20 and 40% and steadily decreases afterwards, until the end of reduction [84, 89, 90, 91]. Some pellets present negligible swelling up to 900°C [18, 86], which is usually attributed to differences in gangue composition [92].

Inside the pellet, the gradual removal of oxygen leads to a large increase in porosity, which can double in the course of complete reduction [18]. Mercury intrusion porosimetry (MIP) measurements have shown that the pore network after reduction can be highly interconnected [86] but that the pores may also act as closed cavities unavailable for gas diffusion [18, 68, 93]. An increased reduction temperature generally results in an increased measured porosity of the reduced pellets, i.e. a more interconnected pore network [94]. The pore network is made of the initial porosity inherited from the pelletizing process [68] and new pores formed during reduction; the latter being finer at low temperatures and coarser at high temperatures. This results in a lower specific surface area at high temperatures [18, 86, 93]. Lower reduction rates, higher water vapor content in the gas and low H_2:CO ratios also favor coarser pores [58, 93, 95, 96] but the influence of these parameters is considerably weaker than that of temperature [46, 95, 97]. The reason behind the pore coarsening at high temperatures is linked to an evolution of the grains, referred to as sintering, when neighboring grains join and merge to minimize the overall surface energy [18, 86, 98, 99]. This is corroborated by scanning electron microscopy

(SEM) observations, which shows that grains become larger, rounder and smoother at high temperatures [18, 58, 84].

SEM micrographs of pellets in the course of reduction by H_2 show a major gradient of oxide phases at the scale of the pellet, between the more oxidized core and the more reduced shell regions [69, 84, 93]. This global gradient is itself highly dependent on the local microstructure, so that oxide islands still exist in regions closed to hydrogen penetration [33, 68, 69]. At the microscopic scale, the iron oxide grains generally keep their initial shape until the reduction of wustite [33], [100]. Signs of grain disintegration are present during and after wustite reduction especially at high temperatures. This grain disintegration is attributed to the high molar volume mismatch between wustite and iron [33, 101]. The newly formed dense particles resulting from the disintegration of wustite grains were referred to as "crystallites" [33], and they are initially dense iron layers covering encapsulated wustite islands [18, 69]. After the formation of these crystallites, the reduction of wustite proceeds via the outbound diffusion of oxygen through the freshly formed dense iron layers [33, 68]. The size of these crystallites was observed to increase with temperature [18], in agreement with the decrease in the specific surface area at increased temperatures.

A major challenge for the pellet producers is to provide the ironmaking industry with iron ore pellets which maintain easy gas diffusion towards the oxide cores, especially at the stage of wustite. Actually, the initial pore structure of the industrial iron ore pellets is often heterogeneous, which is not ideal to ensure good reducibility [84, 93, 102]. A series of studies showed that an highly porous iron microstructure could be obtained in extreme reduction conditions, such as very high or very low reduction temperatures and high H_2:H_2O ratios [58, 103, 104]. Similarly, extremely high pressures (50-100 bar) allow to form very fine microporous iron structure that increases the reduction rate [105]. While these diffusion-enhancing microstructures cannot be obtained from the actual industrial conditions, these works offer clear pathways for understanding the microscopic mechanisms that govern the nucleation of iron, the apparition of pores, and the formation of specific morphologies [95, 99, 103, 106, 107, 108].

In the present paper, we investigate the macroscopic evolution of the porous structure of iron ore pellets during their reduction by hydrogen in the 600–900°C temperature range. Complete and interrupted reduction experiments were performed, and the reduced pellets were subsequently characterized by means of MIP and gas adsorption methods. A general discussion with the literature is then proposed, with a specific emphasis on studies that rely on microscopical examination of reduced pellets.

Article 2 – **2. Materials and methods**

Article 2 – **2.1. Raw materials**

Commercial DR-grade pellets from CVRD, Vale, Brazil, were used. Spherical pellets of 13–15 mm diameters were selected as representative of the pellet batch size distribution. A chemical analysis of these pellets was performed by our partner Tata Steel Netherlands in the framework of the MaxH2DR project. Its results are given in Table 12 [73].

Table 12 : Chemical composition of the pellets (wt%)

Fe	SiO_2	CaO	Al_2O_3	FeO	B2	MnO	MgO	TiO_2	P_2O_5
67.1	2.0	0.9	0.56	<0.1	0.47	0.14	0.12	0.08	0.06

Article 2 – **2.2. Reduction experiments**

Reduction experiments were conducted in isothermal conditions in the temperature range 600-900°C (by intervals of 100°C) with a SETARAM TG96 TGA device. Details on this device were presented in a previous paper [88]. For each experiment, a single pellet was placed in a wired platinum basket hung to one end of a weighing scale. The pellet was then preheated by the furnace by injecting helium at 1 bar with a flowrate of 0.81 Nlpm (Normo-liter per minute). When the working temperature was reached and stabilized, the hydrogen valve was opened and the H_2 gas flowrate was set to 0.99 Nlpm so that the gas composition reached 55% H_2 and 45 % He in volume. The reduction experiment was carried out until reaching a desired conversion degree ($15\% < X < 100\%$). To reach a conversion degree lower than 100%, the hydrogen valve was manually shut off, after what the reduction kept going for 30 to 40 seconds before completely stopping. Each pellet was then cooled down in He atmosphere.

Article 2 – **2.3. Porosity characterization methods**

Two different methods were used to evaluate the porosity of the iron ore pellets. The first method relies on the direct measurement of the open porosity ϵ_{MIP} with a mercury intrusion porosimeter (MIP), model Autopore 9500 from Micromeritics. This type of device thrusts Hg into the pores of a sample at increasing pressures. Each pressure increment allows to intrude an additional volume dV into finer pores, so that the cumulative intruded volume can be plotted as a function of pressure, or of the pore diameter using the Laplace–Washburn law. The open porosity of the sample and its pore size distribution are then readily obtained. The limited size of our penetrometer made it possible to characterize only pellets up to 4 g of initial mass (d_p~13 mm). The second method derived porosity from calculation and measurements of density. First, the apparent or bulk density of the pellets ρ_{bulk} was determined by a displacement method with dry sand, which did not penetrate into the pores of the pellets. A blank volume of packed sand was measured, and another measurement was made after introducing previously weighed pellets in the sand and packing it again. This bulk density was then compared to the theoretical true density of the pellets ρ_{true}. The latter was directly calculated from the composition of the pellets (Table 12) and the known value of the true densities of its components:

$$\rho_{true} = \frac{1}{\sum_{i\ elements} \frac{w_i}{\rho_i}} \tag{45}$$

$$\epsilon_{tot} = 1 - \frac{\rho_{bulk}}{\rho_{true}} \tag{46}$$

where w_i is the mass fraction of the element i in the pellet. The density of the pellets was evaluated in a third manner by means of a pycnometry method based on helium displacement (ρ_{pyc}). In these experiments, a blank volume of helium is measured, and another measurement is made after introducing a pellet in the chamber. This method leads to a higher measured density in comparison to the one measured with the dry sand method, since it accounts for the open pores of the pellets in which the gas can penetrate. Moreover, compared with the MIP method, He can penetrate into finer pores than Hg, which is limited to pore diameters above 4 nm. Overall, He displacement measurements allow to evaluate the presence of closed pores in the pellets, since these are the only ones that He cannot access:

$$\epsilon_{closed} = \frac{\rho_{pyc} - \rho_{bulk}}{\rho_{true}} \quad (47)$$

The dry sand and He displacement measurements were performed by TATA Steel Netherlands Europe [73].

Article 2 – **2.4. Specific surface area characterization methods**

The specific surface area of pellets was determined with two different methods. The first method derives a_{sp} from the abovementioned MIP measurements. Indeed, if we consider that a_{sp} equals the total area of open pores (per unit mass), and under the assumption that these pores are cylindrical, we find that:

$$a_{sp} = \sum_{r} \frac{2dV(r)}{r} \quad (48)$$

where *dV(r)* is the volume of Hg intruded into pores of radius *r*, per unit mass.

For the second characterization technique, pellets were crushed to obtain small particles that could fit into the gas adsorption measuring device, and these samples were subsequently degassed. Krypton adsorption isotherms were plotted according to the BET theory, see e.g. [43]. Nitrogen adsorption proved to be inefficient in this situation owing to the small values obtained for a_{sp}. Moreover, owing to the needs for large surfaces to realize the measurements, pellets with mass of 5 g were chosen in these experiments.

Kr can penetrate pores with a diameter lower than 4 nm, while Hg cannot. This discrepancy between the two methods may result in different measured values of a_{sp}.

Article 2 – **3. Results**

The present paper is devoted to the effect of temperature on the evolution of the pellet microstructure during reduction. The kinetics of the reduction are not presented here, as an extensive investigation on this subject was recently published in [88].

In the following sections, the porosity and specific surface area of unreduced pellets are first reported. Then, for each reduction temperature, the results of 3 experiments interrupted at conversion degrees X = 15%, 30%, 50% and of one experiment completed (X = 100%) are presented and discussed.

Article 2 – **3.1. Characterization of unreduced pellets**

MIP measurements gave an initial pellet porosity of 28.98%. Additionally, the total and closed porosity derived from density measurements were respectively evaluated at 30% and 1.13%, resulting in an open porosity of 28.87%. Clearly then, both methods agree on the value of the initial porosity. Moreover, we found that only a minor fraction of the total porosity (3.7%) is closed, which means that almost all pores in the unreduced pellets are interconnected.

A single pore population was detected from the MIP measurements, ranging from 1 to 10 μm, with an average diameter of 4 μm (see the Hematite curve in Figure 38, which will be commented later).

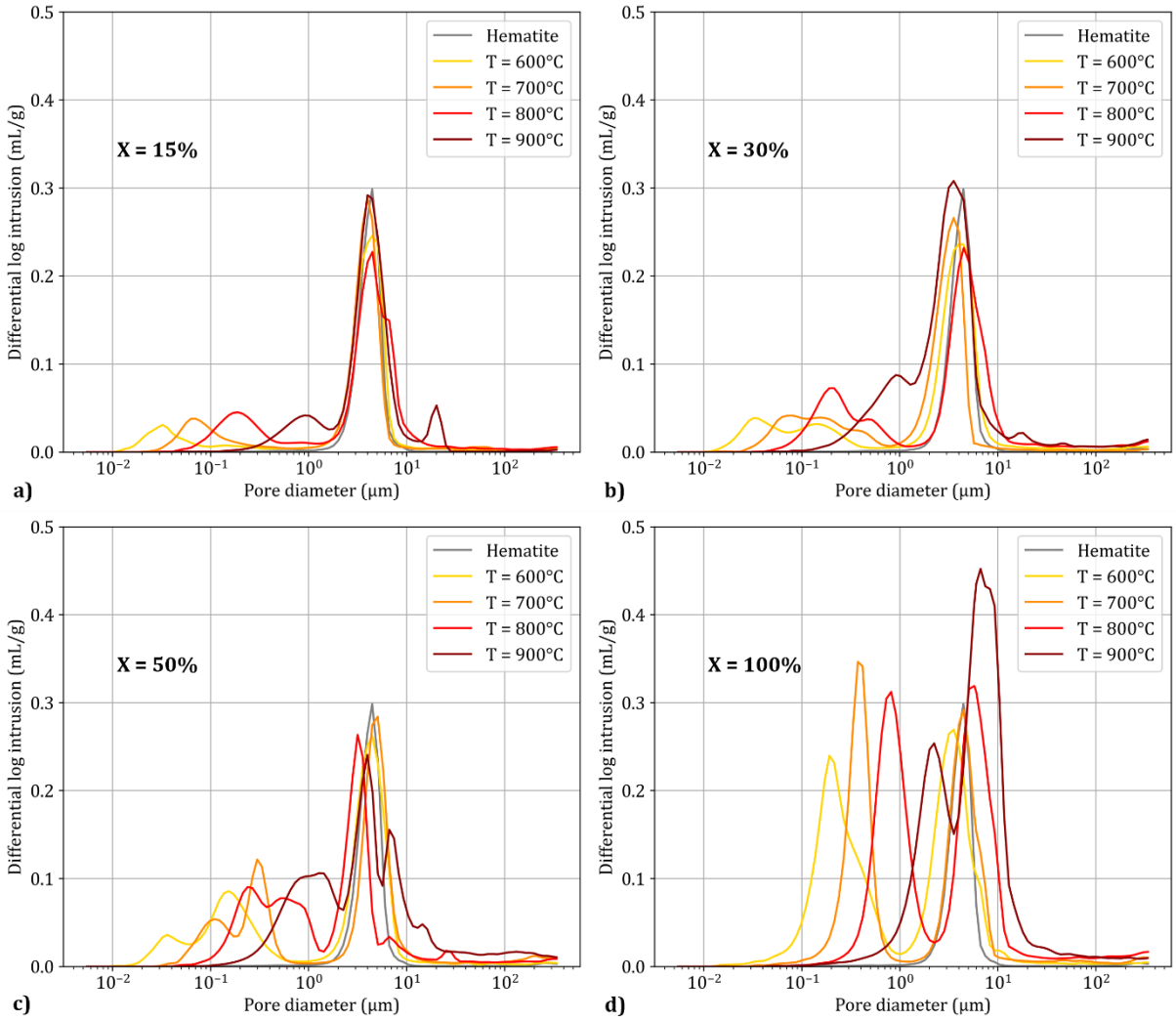

Figure 38: Pore size distributions derived from MIP measurements as a function of temperature and at different final conversion degrees, **a)** X = 15%, **b)** X = 30%, **c)** X = 50%, **d**) X = 100%.

Article 2 – **3.2. Characterization of pellets reduced by hydrogen**

The specific surface area of partly and fully reduced pellets was derived from MIP and adsorption measurements (Figure 39a).

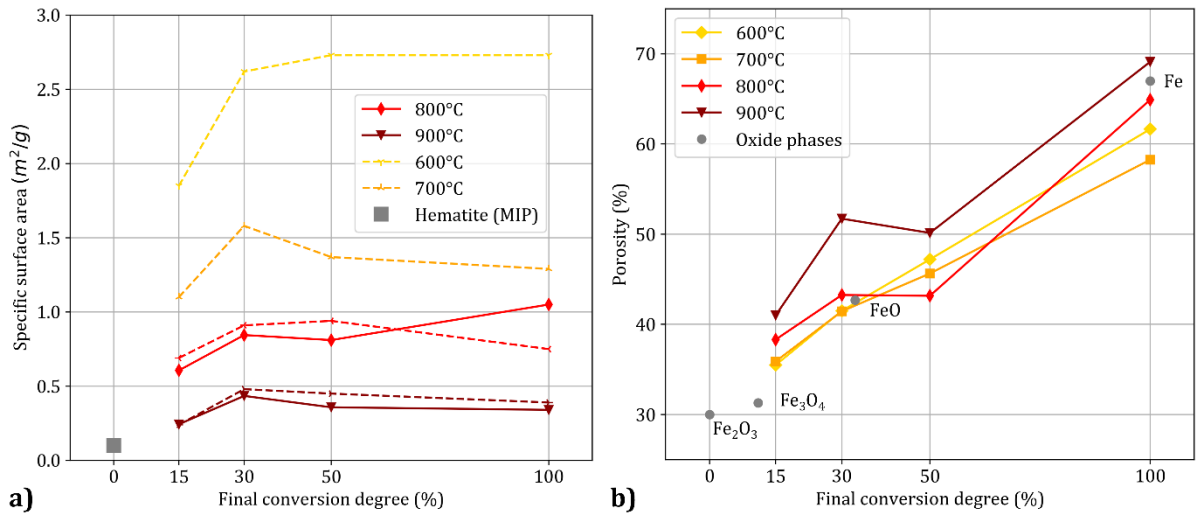

Figure 39: a) Specific surface area obtained from Kr adsorption (solid lines) and MIP (dashed lines) measurements, and **b)** Open (mercury) porosity of reduced pellets as a function of the final conversion degree and temperature. The theoretical total porosity of the successive oxides (hematite, magnetite, wustite) and iron is given for comparison.

The graph shows similar values of a_{sp} from both methods at 800°C and 900°C, which indicates that most pores are larger than 4 nm at these temperatures. For each temperature, a_{sp} greatly increased at the start of the reaction and reached a maximum value between X = 30% and X = 50%. Afterwards, it stabilized or slightly decreased, except at 800°C and X = 100% in the case of Kr adsorption. Moreover, increasing the reduction temperature resulted in drastically lower values of a_{sp}: for a reduction degree of 30%, a_{sp} was evaluated at 0.45 $m^2\ g^{-1}$ at 900°C, and 2.62 $m^2\ g^{-1}$ at 600°C. This suggests that the reduction resulted in many small pores at low temperatures and fewer coarser pores at high temperatures. Actually, the decrease in specific surface area at X = 50% observed above 700°C hints at a possible sintering of the freshly formed iron phase. SEM micrographs from the literature highlight the presence of fine pores in the first stages of reduction (X = 11%) at 700°C which are not found in the dense iron formed in later stages of reduction (X = 50%), see Figure 40.

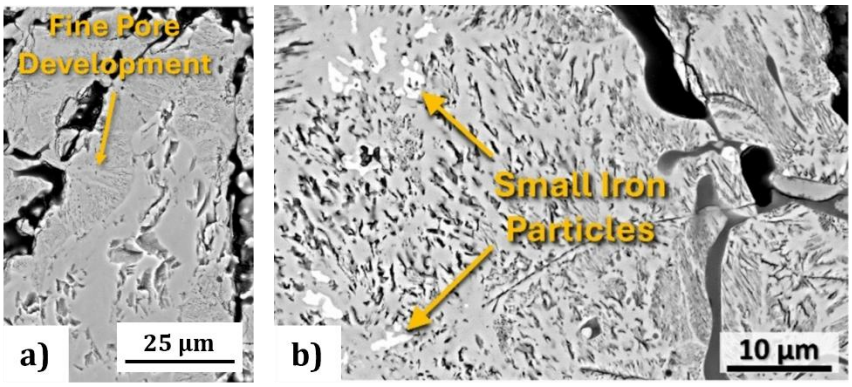

Figure 40: SEM micrographs of pellets reduced at 700°C to different conversion degrees: **a)** X = 11%, **b)** X = 50% [6]. The micrographs were obtained in the so-called "intermediate" region, located halfway between the core and the surface of the pellet (see Figure 41 below).

The open porosity of the reduced pellets was measured with MIP. Figure 39b) shows that the porosity globally increased with the conversion degree and temperature, with some exceptions: the pellets reduced at 700°C presented the lowest porosity, except for X = 50%, and a dip in the curve was observed at 800°C and 900°C for X = 50%.

The theoretical porosities of the successive oxide phases (hematite, magnetite, wustite, iron) were also plotted on the graph, see Figure 39b). These were calculated on the basis of a molar balance detailed in the Appendix. These calculated total porosities show the same trend than and values rather close to the measured open ones, which suggests a mostly open porosity. Nevertheless, some discrepancies are present, which can be explained by multiple factors. Firstly, the calculation of the total porosity is based on the assumption of completely successive reactions at the scale of the pellet, whereas gradients of composition are known to appear as previously mentioned. Actually, the early formation of highly porous iron in the external region of the pellet results in an increased open porosity, as suggested by SEM observations (Figure 41). Moreover, swelling of the pellet also lead to an increase in porosity: if the volume of the pellet expands by 15%, as reported in [109], the porosity of the pellet increases from 30% to 39%. This could explain the abnormally high values of porosity that we observed at 900°C. Finally, pores can close or open during the reduction, leading to a decrease (resp. increase) in the measured porosity.

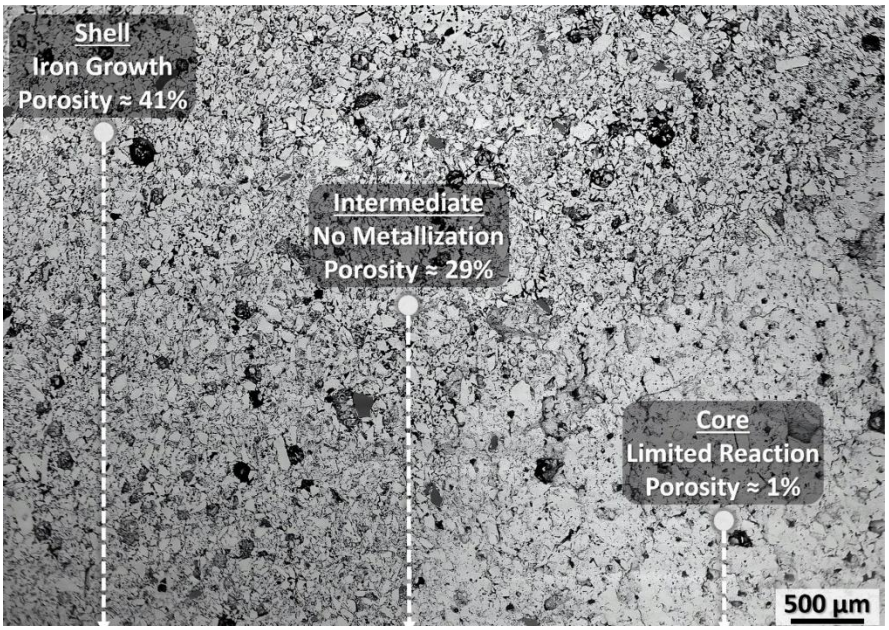

Figure 41: Overview of the porosity of a pellet reduced at 800°C along its radius for X = 33% [6]. The shell and intermediate regions initially present similar porosity (ϵ = 24–29%), which is not the case of the core region which is in this sample initially very dense (ϵ = 1–3%).

The evolution of the pore network during reduction is presented in Figure 38. The initial pore population (P1), centered around 4 µm in diameter (hematite curve) is still present at the end of the reduction at each temperature, with a slight increase of the mean diameter at high temperature (800 and especially 900°C). Along with this inherited porosity, a second population of small pores (P2) appears at X = 15% (Figure 38a), probably first formed at the surface of the magnetite grains [18]. The diameter of these new pores greatly increases with temperature, from 30 nm at 600°C to 1 µm at 900°C. At 900°C, large pores (P1') are also observed, with an average diameter of 20 µm. Between X = 15% and X = 30%, a third population of pores (P3) appears with a diameter intermediate between that of (P2) and (P1) below 900°C. All pore populations become

less distinguishable as the reduction progresses towards X = 50%, especially for high temperatures. The final pore distribution at X =100% systematically results in a bimodal distribution, each mode being of similar amplitude (similar cumulative volume) except for T = 900°C. The first mode results from the inherited population (P1), the diameter of which is increased above 800°C compared with the initial diameter. The second mode is thought to result from the combined coarsening of the small pore population (P2) due to sintering or pore coalescence and from the growth of the third pore population (P3) due to oxygen removal. As this third pore population is present and grows in intensity from X = 30% until X = 100%, we can assume that it is representative of the pores of the iron, which is firstly formed at the pellet surface and then progresses to the center of the pellets. An estimate of the average pore diameter of each population at each temperature and conversion degree is reported in Table 13. We can see that globally, the pores grow in size with increasing temperature and conversion degree. No SEM observations were performed in this study, but the the values of the pore diameters obtained in Figure 38d) are in very good agreement with previous observations (Figure 42).

These porosimetry results can be related to the specific surface area measurements presented earlier. The increase of a_{sp} at the start of the reaction (X < 30%) reflects the formation of the second and third pore populations. At X = 50%, the growth of pores of intermediate size (P3) results in a slight increase in a_{sp} at 600°C. At higher temperatures, the growth of the intermediate pores (P3) is coupled with the disappearance of the smallest pores (P2), resulting in a slight decrease in $a_{sp.}$ The same effect is observed for all temperatures between X = 50% and X = 100%; however, the decrease in a_{sp} due to pore coarsening is mitigated by the growth of the large (P1) and intermediate (P3) pore populations.

The direct comparison between measured porosity values and pore size distributions is however more difficult. Further discussion with the literature is needed to shed light on these results, and particularly with studies that rely on microscopical observations of the reduced pellets.

Table 13: Average diameter of the different pore populations at each temperature and degree of reduction.

	X = 15%	X = 30%	X = 50%	X = 100%
600°C	(P1): 4 µm (P2): 30 nm	(P1): 4 µm (P2): 30 nm (P3): 200 nm	(P1): 4 µm (P2): 30 nm (P3): 200 nm	(P1): 3 µm (P3): 200 nm
700°C	(P1): 4 µm (P2): 70 nm	(P1): 4 µm (P2): 70 nm (P3): 200 nm	(P1): 5 µm (P2): 100 nm (P3): 200 nm	(P1): 4 µm (P3): 400 nm
800°C	(P1): 4 µm (P2): 200 nm	(P1): 4 µm (P2): 200 nm (P3): 600 nm	(P1): 3 µm (P2): 200 nm (P3): 700 nm	(P1): 5 µm (P3): 800 nm
900°C	(P1): 4 µm (P1'): 20 µm (P2): 1 µm	(P1): 4 µm (P1'): 20 µm (P2): 1 µm	(P1): 4 µm (P2): 1 µm	(P1): 7 µm (P2): 2 µm

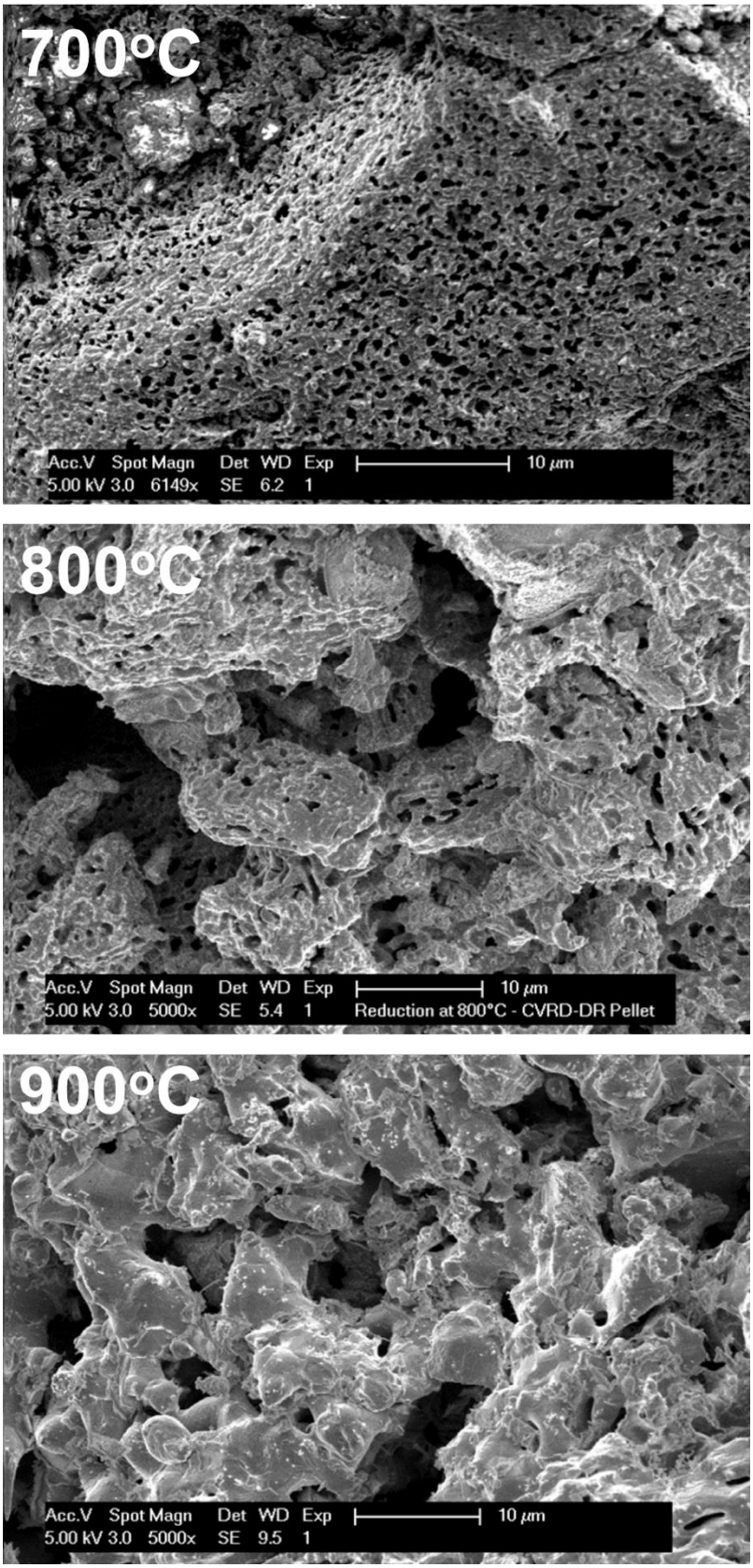

Figure 42: SEM micrographs of pellets after complete reduction by hydrogen at various temperatures, from [18].

The porosity of pellets completely reduced by hydrogen (X = 100%) was frequently observed to increase with temperature [18, 84, 86, 94, 96], while a minimum porosity was often reported at T = 900°C [84, 86, 94]. This was usually attributed to the absence of fine porosity in the iron formed above 800°C due to sintering of this phase [84, 97]. In our case, we obtained a minimum porosity at 700°C which may indicate sintering at this temperature. Note that even lower sintering and recrystallization temperatures were mentioned in the literature: from 650°C in [32] and 550°C in [110]. Additionally, surface pores were observed to close during reduction above 900°C [6], which is in agreement with the dip in the porosity observed in our MIP measurements at X = 50%.

Our results regarding the pore size distribution and the specific surface area of the iron phase are in global agreement with the literature, which shows a clear consensus on the fact that higher temperatures yield coarser pores due to sintering [18, 86, 93]. Pellets initially present an inherited pore population, and a second pore population is formed during reduction [68, 69], the average diameter of which increases with temperature [18, 94]. The disappearance of the smallest pores (under 0.1 µm) in our experiments can result from the disappearance of the associated oxides or from sintering, especially at high temperature. The combined decrease in small pores, decrease in intermediate pores, and increase in (P2) and (P3) peak diameters could correspond to pore coalescence. The fact that the pores from (P3) formed at X = 30% are still present in the iron (X = 100%), while the ones from (P2) are not indicates that the final second mode is characteristic of the iron phase.

In agreement with our results, the specific surface area of completely reduced pellets was systematically found to decrease with increasing temperature [18, 86, 98, 99]. Results regarding the birth of a second pore population at the start of the reduction and the formation of sponge iron at high temperatures were obtained for the reduction of magnetite pellets [101] and dense wustite [103], which suggests that these are related to the nature of iron oxide reduction rather than specific features of the materials studied.

The stabilization of the specific surface area observed above X = 50% in our experiments can be linked to the evolution of the microstructure. It was frequently reported in the literature that the evolution of the grain structure was mainly happening in the first phases of the wustite reduction and resulted in the formation of "crystallites", that are dense grains of iron which are smaller than the initial grains of wustite [6, 17, 18, 69, 69]. After this disintegration stage, the reduction is thought to continue at the scale of these crystallites, which show a dense iron layer surrounding islands of encapsulated wustite. Following this hypothesis, it was found that the size of these crystallites was increasing with the reduction temperature [17, 18, 111].

Our results also shed some light on the mechanism of pore formation. Indeed, the formation of pores during the reduction of hematite and magnetite and during the decomposition of wustite is generally attributed to the diffusion of iron ion vacancies [99, 112]. But the formation of new pores and the corresponding increase in a_{sp} can only last as long as there are iron ion vacancies in the wustite, that is until the wustite becomes saturated with iron ions [99]. This clearly corroborates our findings where a_{sp} only slightly evolves after X = 50%. The further decrease of a_{sp} observed at T > 700°C hints at possible sintering of the freshly formed iron phase, corroborating our findings on porosity. SEM observations of the reduced pellets are still needed to clarify this particular issue.

Article 2 – **5. Conclusion and outlooks**

A macroscopic investigation of the porous properties of pellets reduced by H_2 in the 600-900°C temperature range was presented. This first step in characterizing the evolution of the porous structure of the pellets allows to draw the following conclusions:

- globally, the porosity increases with the reduction degree and temperature, except at 700°C which shows a particularly low final porosity. The high porosity observed above 800°C is attributed to the combined effects of swelling, pore opening and early formation of iron at the edge of the pellet;
- the initial pellet pores result from an inherited monomodal pore network (P1) with a mean diameter determined as 4 µm in this study. A second population of finer pores (P2) is formed at the start of the reduction, the diameter of which is larger than 4 nm, as suggested by the concordant values of a_{sp} derived from Kr adsorption and MIP. A third intermediate pore population (P3) is formed from X = 30%, which is likely linked to the iron phase formation. The small pores (P2) disappear together with the oxides at high conversion indicating mechanisms of sintering at high temperatures and pore coalescence at low temperatures;
- the specific surface area a_{sp} of the reduced pellets is drastically higher at low temperatures. During reduction, a_{sp} greatly increases at the start of the reduction before reaching a slightly decreasing plateau. This supports the view that the new pore formation is related to the migration of iron ion vacancies, after what further evolution of the a_{sp} is dictated by the evolution of the microstructure.

Further investigations should include swelling measurements and microscopical observations of partially reduced pellets. In particular, the heterogeneity of pellets should be investigated to determine the porosity distribution along the pellet radius, as well as the potential presence of a compact core once reported in the literature [6]. The development of X-ray microtomography and in-situ SEM techniques is of great interest to get a clearer view of the mechanisms that govern the formation of pores and the evolution of the grains during reduction. The influence of impurities on the evolution of these features is also of major importance in order to design pellets with great reducibility for the hydrogen direct reduction industry.

Article 2 – **Appendix: Theoretical evolution of the porosity during reduction**

During their reduction by hydrogen, the iron oxides are successively converted from hematite into magnetite, then wustite, and finally iron. With the gradual removal of oxygen, porosity is generated within the iron material. A method is proposed hereafter to calculate the porosity that would be found in the successive phases (magnetite, wustite and iron) shown in Figure 39.

This simple calculation relies on the hypothesis that the freshly formed iron or iron oxide consists of a single phase (i.e., magnetite, wustite or iron) and that the exterior volume of the pellet is constant. When a quantity of hematite $n_{Fe_2O_3}$ is converted into a corresponding quantity of magnetite $n_{Fe_3O_4}$, one has:

$$V_{Fe_3O_4} = \frac{n_{Fe_3O_4}}{\tilde{\rho}_{Fe_3O_4}} = \frac{\nu_{Fe_3O_4}}{\nu_{Fe_2O_3}} \frac{n_{Fe_2O_3}}{\tilde{\rho}_{Fe_3O_4}} = V_{Fe_2O_3} \frac{2}{3} \frac{\tilde{\rho}_{Fe_2O_3}}{\tilde{\rho}_{Fe_3O_4}} \quad (49)$$

where $\nu_{Fe_2O_3}$ and $\nu_{Fe_3O_4}$ are the stoichiometric coefficients in eqn (1), 3 and 2 respectively, and $\tilde{\rho}_{Fe_2O_3}$ and $\tilde{\rho}_{Fe_3O_4}$ are the true molar densities.

Moreover, the total volume of the pellet can be expressed as:

$$V_{pellet} = \left(1 - \epsilon_{Fe_2O_3}\right)V_{Fe_2O_3} = \left(1 - \epsilon_{Fe_3O_4}\right)V_{Fe_3O_4} \tag{50}$$

Rearranging of the equations gives the porosity of the reduced phase:

$$\epsilon_{Fe_3O_4} = 1 - \frac{\nu_{Fe_3O_4}}{\nu_{Fe_2O_3}}\left(1 - \epsilon_{Fe_2O_3}\right)\frac{\tilde{\rho}_{Fe_2O_3}}{\tilde{\rho}_{Fe_3O_4}} \tag{51}$$

The same reasoning can be applied to obtain the porosity of the wustite and iron phases.

III. The thermochemical behavior of a hydrogen-enriched shaft furnace

III.1. Introduction

Direct reduction technologies

The galaxy of technologies that can be labeled as "direct reduction" is quite broad. While shaft furnace processes are currently dominant on the DR market, technologies involving rotary kilns, fluidized beds and reducer-smelter furnaces make up a significant part of the research ongoing in this field. For the sake of completion, a brief overview of these alternative processes is given below. A proper introduction of shaft furnace processes is then presented.

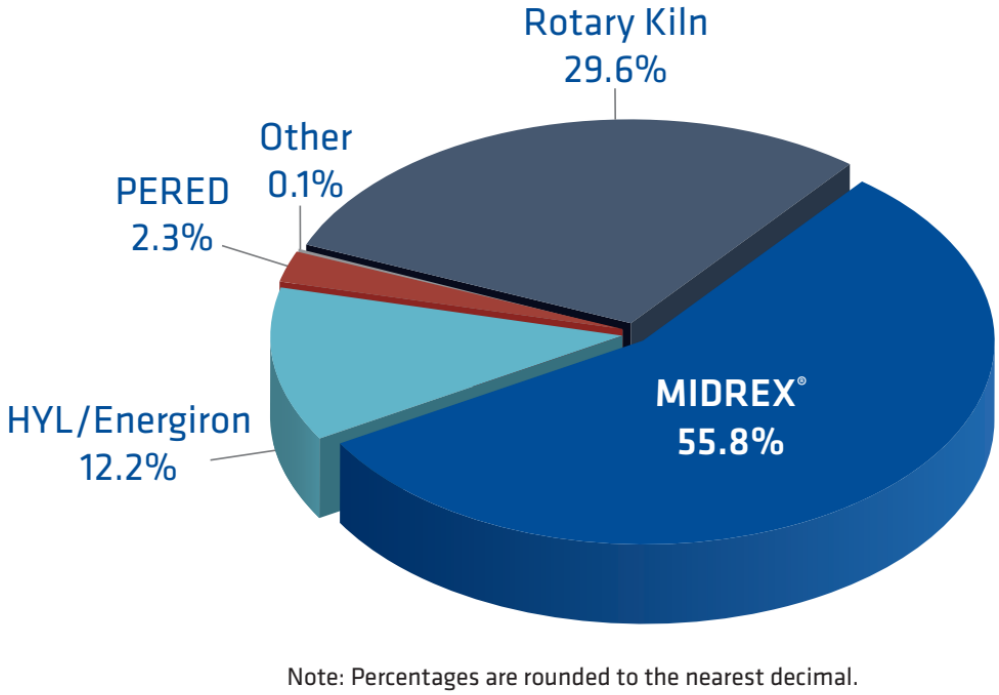

Figure 43: World DRI production by process in 2023 [113].

Indeed, if the vast majority of DRI is produced through HYL and MIDREX processes, around a quarter of DRI is produced in coal-based rotary kilns (see Figure 43 and Figure 44). In fact, the DRI production by rotary kilns has increased by 161% in the last decade [113]. Rotary kiln reactors are a mature and versatile technology used in multiple industries. In the iron and steel industry, these furnaces work both as iron ore reduction and coal gasification units. This versatility makes the rotary kiln a serious alternative to other technologies, especially in regions with cheap coal resources. However, as the syngas produced in a rotary kiln originates from the partial combustion of coal, it yields very high carbon emissions compared to other DR technologies. For this reason, this technology is not eligible for CO_2 mitigation.

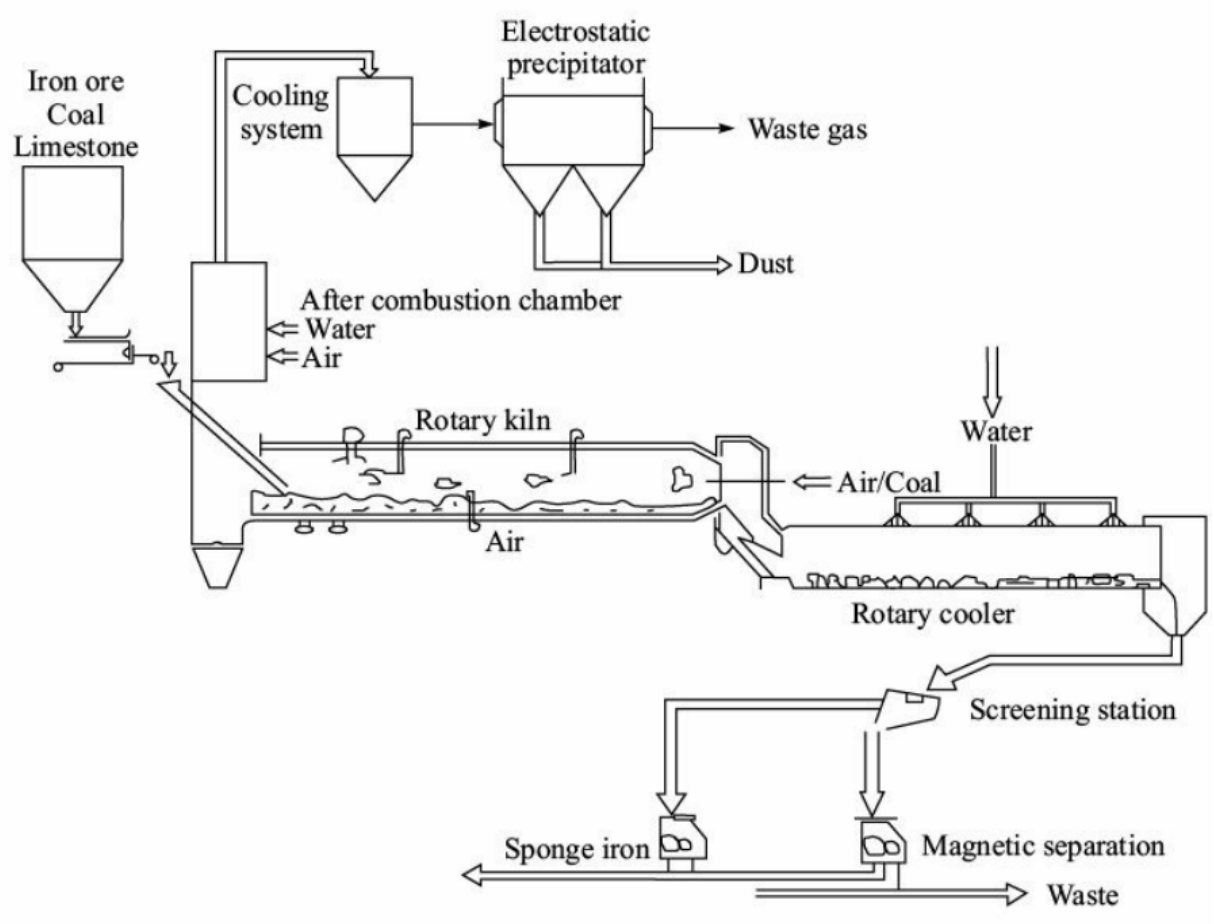

Figure 44: Schematic representation of an iron ore rotary kiln plant. The kiln is slightly inclined and rotates, so that the burden slowly moves inside and reaches the other end. Air and coal are supplied inside the kiln to raise the temperature and reduce the iron ore, usually fed under the form of pellets or lump ore [114].

Another alternative to the main DR processes is the smelter-gasifier furnace developed by COREX (Figure 45). Although the COREX technology is usually categorized as smelting rather than DR, this type of plant actually relies on both a smelter-gasifier and a pre-reduction shaft furnace. The latter is quite similar to MIDREX or HYL shaft furnaces. In such a system, the inlet gas of the pre-reduction SF originates from the gasification of coal in the melter-gasifier. The gasification of coal with O_2 and H_2O produces a syngas with a low H_2:CO ratio, typically 1:3 [115].

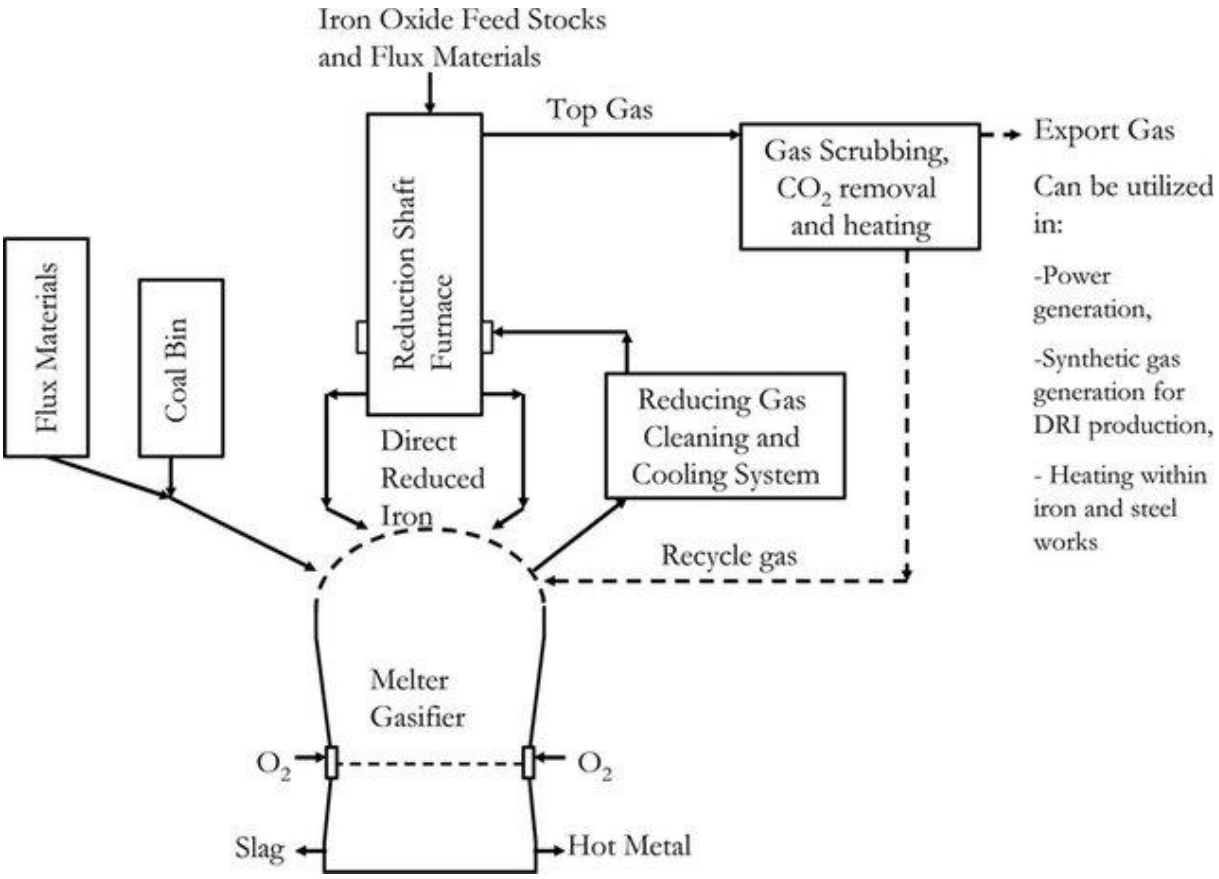

Figure 45: Schematic representation of a COREX plant [116]. Iron ore is introduced as pellets, lump ore or sinter in the reduction shaft and pre-reduced to reach 85% metallization [5]. It is then transferred to a melter gasifier to finish the reduction and to melt into hot liquid metal.

Conversely, a plant running on pure hydrogen was operated in the early 2000's by CIRCORED, and it offers insights on the challenges of H_2-DR, see Figure 46. With a considerable gas flow, the reduction of high-grade iron ore fines in a fluidized bed is possible at low temperatures (630-650°C). This low temperature operation is not possible with CO or syngas due to poor kinetics as well as sticking issues. While the absence of carbon in the final product was seen as a major problem at first, trials showed that the no-carbon DRI had some advantages, including the fact that the produced DRI was pure [114].

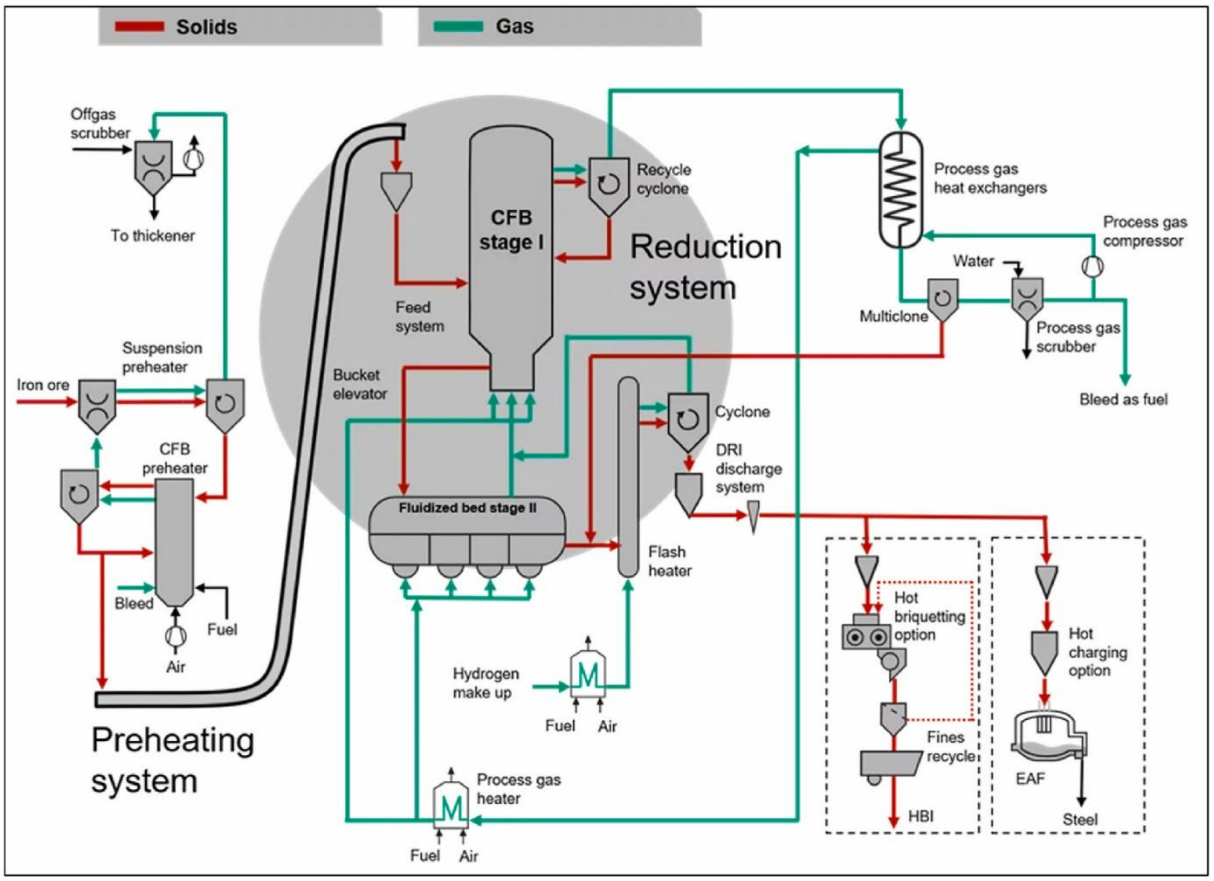

Figure 46: Overview of the CIRCORED Ironmaking process [5]. Iron ore fines (100-200 µm) are pre-reduced into a circulating fluidized bed (stage 1) where they stay for approximately 20 minutes. They are then delivered into a stationary fluidized bed (stage 2) where the retention time is adjusted to reach the desired metallization. Both reduction steps are realized with pure hydrogen and the final metallization degree reaches 95%.

Direct Reduction Shaft Furnaces (DRSF)

The largest part of DRI production is shared between the NG-based DRSF technologies MIDREX, HYL, and Pered. Nowadays, almost all of these furnaces are countercurrent, meaning that the descending iron ore burden is reduced by a hot ascending gas. These furnaces rely on the use of syngas and natural gas in various proportions depending on the process. This syngas is obtained from the catalytic reforming of methane in dedicated units or directly inside the shaft furnace (in-situ reforming). The reforming is done with H_2O or CO_2 and usually Ni or Fe are used as catalyzers (Figure 47). Steam methane reforming (SMR) produces a syngas which yields a high H_2:CO ratio (3:1), while dry methane reforming (DMR) with CO_2 produces a syngas with half H_2 and half CO (1:1, see reactions 10,11). The heat of reactions are given at 25°C and are taken from [24].

Reaction 10 $\quad CH_4 + H_2O = CO + 3H_2 \quad \Delta_r H^0 = 206\ \text{kJ/mol}$

Reaction 11 $\quad CH_4 + CO_2 = 2CO + 2H_2 \quad \Delta_r H^0 = 247\ \text{kJ/mol}$

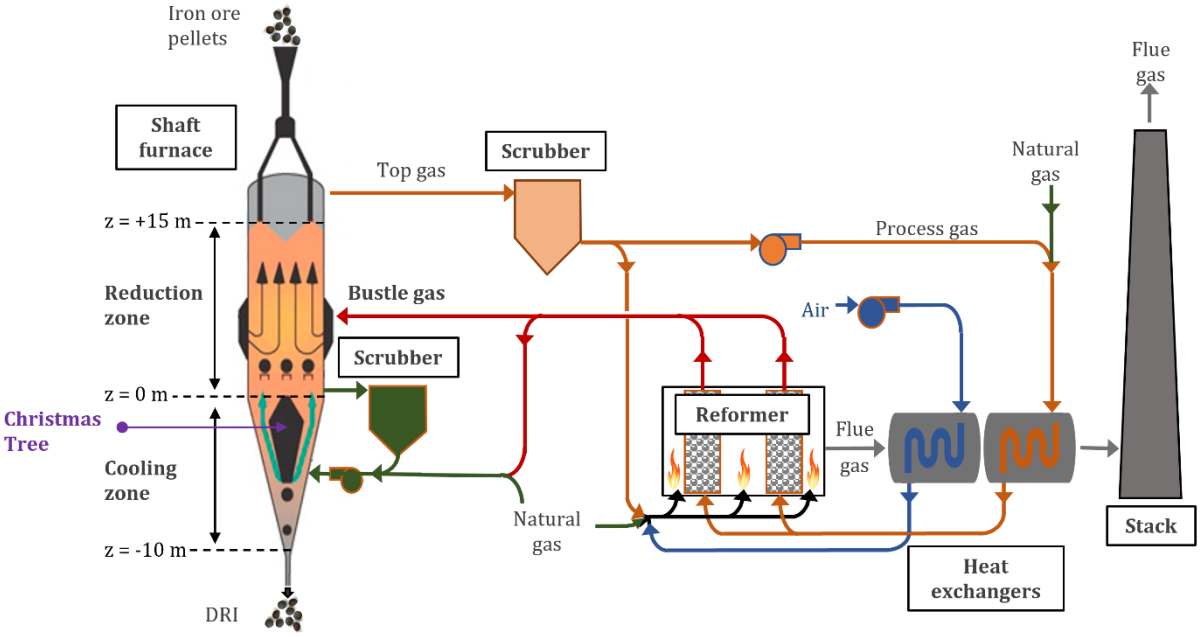

Figure 47: Schematic representation of a NG-DRSF plant [16]. Each process unit is indicated in a text box. The different gas mixtures and their flow in the process units are represented. The reduction and cooling zones refer to the upper and lower sections of the furnace, respectively, and the Christmas tree refers to the solid structure placed at the middle of the cooling zone; it serves as a flow diverter for the pellets and can also act as an additional gas feeder.

In the reduction zone of a DRSF, the temperature must be as high as possible to enhance the overall thermochemical behavior, while it must be kept low enough to avoid sticking of iron pellets, which would disrupt the furnace operation. For these reasons, traditional DRSF are usually operated in the 900-1000°C temperature range. A bustle gas with a proper H_2:CO ratio (3:2 up to 3:1) should be used to ensure great kinetics and sufficient heat supply. The gas demand is itself closely related to this H_2:CO ratio [117]. The target metallization of the DRI for a shaft furnace is 92-96% [118].

In terms of furnace geometry, shaft furnaces present moderate radius and considerable height in order to enhance the homogeneity of temperature and gas distribution in the reduction zone. At the bottom of the furnace, a cooling gas loop enables the introduction of a large quantity of CH_4 that cools down the reduced pellets and favors their carburization. Cooling gas and reduction gas may also be introduced in a so-called "Christmas tree", that is a vertical structure at the bottom of the reduction zone. The latter is usually used as a flow regulator for the solid burden, but is sometimes used as a supplementary gas injection as well. Top gas recycling (TGR) is a common practice in NG-DRSF processes, where part of the off-gas is used in the reformer and another part is used as fuel in the burners (Figure 47). Some features of the two dominant DR technologies, namely MIDREX and HYL-ZR, are given in Table 14.

Most of the research on shaft furnace technology is today devoted to the H_2-DRSF in the framework of CO_2 mitigation. This topic was largely discussed in our paper entitled "Operating Solutions to Improve the Direct Reduction of Iron Ore by Hydrogen in a Shaft Furnace" recently published in *Metals*. This article, referred as Article 3, is reproduced hereafter, in section 2. However, numerous studies in the field of NG-DRSF are still ongoing and they mainly focus on the following aspects of the process:

- fundamental thermochemical considerations. It was shown how the transition from low to high H_2:CO ratios drives the gas demand, and how the presence of CO in the gas preempts from potential heat supply issues at the center of the shaft [23, 117, 119]. It was also shown that blowing oxygen increases the temperature of the gas, which in turns, may compensate for the decrease in the reduction potential of the gas [114, 120];

- advanced shaft modeling. Recent progress in computing power allows for more robustness of Discrete Element Method (DEM) methods for modeling the granular flow of pellets, see e.g. [121, 122] and its coupling with CFD, which stands among the main objectives of the MaxH2DR project. Several articles were recently published on this topic [123, 124]. The modeling of the Christmas tree structure and the assessment of its potential as an additional gas input within the shaft were also conducted. A positive impact of this central gas injection on the gas utilization degree of H_2 and CO was evidenced and quantified [125]. Eventually, a dynamic model that simulates the transition between NG-DRSF and H_2-DRSF was recently presented [126];

- interactions between the shaft reactor and other plant facilities, especially the reforming unit. On this last topic a recent review was conducted by [127]. On a broader scale, a CO_2 optimization of a MIDREX plant based on multicriteria algorithms was conducted using the Aspen Plus software [128, 129].

Table 14: Major features of MIDREX and HYL-ZR processes.

Operational parameters	MIDREX	HYL-ZR
Syngas	Obtained from DMR in a dedicated reformer unit.	Obtained from in-situ SMR.
Associated H2:CO ratio	1:1	3:1
Top gas pressure	1-2 atm	5-8 atm
Size* (reduction zone radius – height)	2.75 m – 25 m	2 m – 17 m
Bustle gas temperature	850-950°C	930-1050°C
DRI carbon content	0.5-3%	2-5%

*Typical size of existing SF.

In the present work, the emphasis was put on the development of the H_2-DRSF model, on the basis of the REDUCTOR model previously developed in our research team. This model was used to study the characteristics of such a furnace and to investigate a set of innovative operating parameters that were presented in Article 3. A bunch of other calculations were also conducted after the submission of this article, to complete the study, and are presented in the following of chapter III.

III.2. The behavior of a pure hydrogen shaft furnace

III.2.1. Article 3: Operating Solutions to Improve the Direct Reduction of Iron Ore by Hydrogen in a Shaft Furnace

Marsigny, A.; Mirgaux, O.; Patisson, F., Operating Solutions to Improve the Direct Reduction of Iron Ore by Hydrogen in a Shaft Furnace. Metals *2025,* 15*, 862. https://doi.org/10.3390/met15080862*

Article 3 – **Abstract**

The production of iron and steel plays a significant role in the anthropogenic carbon footprint, accounting for 7% of global GHG emissions. In the context of CO2 mitigation, the steelmaking industry is looking to potentially replace traditional carbon-based ironmaking processes with hydrogen-based direct reduction of iron ore in shaft furnaces. Before industrialization, detailed modeling and parametric studies were needed to determine the proper operating parameters of this promising technology. The modeling approach selected here was to complement REDUCTOR, a detailed finite-volume model of the shaft furnace, which can simulate the gas and solid flows, heat transfers and reaction kinetics throughout the reactor, with an extension that describes the whole gas circuit of the direct reduction plant, including the top gas recycling set up and the fresh hydrogen production. Innovative strategies (such as the redirection of part of the bustle gas to a cooling inlet, the use of high nitrogen content in the gas, and the introduction of a hot solid burden) were investigated, and their effects on furnace operation (gas utilization degree and total energy consumption) were studied with a constant metallization target of 94%. It has also been demonstrated that complete metallization can be achieved at little expense. These strategies can improve the thermochemical state of the furnace and lead to different energy requirements.

Article 3 – **1. Introduction**

The iron and steel sector accounts for 7% of global CO_2 emissions and 8% of final energy demand [4]. Its sustainability relies on finding a breakthrough decarbonated alternative to the traditional blast furnace (BF), which uses coke to convert iron ore into pig iron before refining the latter in the basic oxygen furnace (BOF). The BF is responsible for 90% of the emissions and the vast majority of the energy needs of the BF-BOF route [16, 33]. The hydrogen direct reduction shaft furnace (H_2-DRSF) process is considered one of the most mature technologies to meet this decarbonization objective; it consumes hydrogen instead of coal and emits water vapor instead of carbon dioxide. Coupled with an electric arc furnace (EAF) for steelmaking, it could replace the usual BF-BOF route with an associated decrease in CO_2 emissions that could reach 97%, assuming carbon-free hydrogen production [130]. This new route is the subject of many topical R&D and industrial projects; see [5, 131] for recent reviews. The present work was carried out within the framework of such a project, namely MaxH2DR, funded by the European Commission.

A DRSF is a silo-like reactor made of a hollow cylinder sitting on top of a conical hopper. It is designed to work in a countercurrent way, meaning that iron oxide pellets fed at the top of the furnace travel downward and react with a hot ascending reducing gas fed at the bottom of the furnace or at the sidewall. DR shafts are currently used in industry in the Midrex and Energiron processes and constitute 5% of global steel production [3]. These processes rely on the use of syngas, a mixture of H_2 and CO obtained from natural gas reforming, as a reducing agent. If the syngas is replaced with pure H_2, one obtains the H_2-DRSF process, which currently exists only at the pilot scale, as with the Swedish Hybrit project [132]. Passing H_2-DRSF from the pilot scale to the industrial scale is an industrial challenge for which very few publications appear. While the

switch from syngas to hydrogen with respect to the reduction reaction has been demonstrated as efficient, the design of the H_2-DRSF process remains to be better specified. The present paper contributes to this topic by studying the influence of some unexplored operating conditions.

In a DRSF, the iron ore pellets are reduced by CO and H_2. The resulting solid product, in the form of porous iron pellets, is called directly reduced iron (DRI) or sometimes sponge iron. It can further be compacted into hot briquetted iron (HBI) for storage and transportation. The reduction from hematite (Fe_2O_3) to iron occurs through intermediate oxides, magnetite (Fe_3O_4) and, above 570 °C, wustite (nonstoichiometric FeO). The reaction equations with H_2 are as follows (with CO, replace H_2 with CO and H_2O with CO_2). In these equations, wustite is written $Fe_{0.95}O$, a composition which corresponds to the wustite/iron equilibrium at 800 °C; the reaction heats are taken from [33].

$$3Fe_2O_{3(s)} + H_{2(g)} = 2Fe_3O_{4(s)} + H_2O_{(g)} \qquad \Delta_r H_{800°C} = -6020\ \text{J mol}^{-1} \qquad (52)$$

$$Fe_2O_{3(s)} + H_{2(g)} = 2Fe_3O_{4(s)} + H_2O_{(g)} \qquad \Delta_r H_{800°C} = -6020\ \text{J mol}^{-1} \qquad (53)$$

$$Fe_{0.95}O_{(s)} + H_{2(g)} = 0.95Fe_{(s)} + H_2O_{(g)} \qquad \Delta_r H_{800°C} = +16{,}410\ \text{J mol}^{-1} \qquad (54)$$

The reduction of iron oxides with H_2 as a whole is endothermic and is operated at high temperatures (800–1000 °C). In a DSRF, the necessary heat is provided by the reducing gas. Consequently, the furnace requires much more gas than the one required for the reduction reactions. To reach a full metallization at 900 °C, Chai et al. [117] indicate a molar ratio of hydrogen to iron of 3.6. This is much higher than the stoichiometric ratio of 1.5 and leads to a relatively low gas utilization degree (GUD) of approximately 0.33:

$$GUD = \left(\frac{x_{H_2O}}{x_{H_2O} + x_{H_2}}\right)_{top} \qquad (55)$$

Since the gas utilization degree is limited and the specific (per unit of solid produced) gas consumption is high in H_2-DRSF, the off-gas contains a massive amount of hydrogen that should be recycled via a top gas recycling setup. A gas loop is also present in natural gas-based DR processes, but it is even more necessary in the hydrogen-based DR process, for which the production of H_2 represents by far the main energy needs of the process—the rest being split between gas heating and compression [133]. Such recycling requires the elimination of H_2O from the off-gas by condensers and the purge of a part of the gas to avoid the accumulation of inert gas in the loop [134].

Numerous mathematical models of the DRSF have been developed to better understand the furnace behavior and help optimize the process. Recent comprehensive reviews of such models are available [23, 26]. Thermodynamic models can predict the theoretical gas demand and relate gas and heat utilization in a DRSF [23, 117, 134]. Other thermodynamics-based models, such as modified Rist models, use graphical tools to determine operating points and perform process control [135]. For the most part, numerical models of the DRSF are based on the kinetics of the reduction of iron ore pellets derived from the three-interface shrinking core model (3-SCM) [70] or the grain model (GM) [77]. Kinetics play a central role in the reduction of iron ore pellets,

especially for the wustite-to-iron reaction, the kinetics of which are often seen as the limiting step of the process. Both 3-SCM and GM rely on the idea that three phenomena can be rate-limiting for reduction: the mass transfer of gas to the surface of the pellet, its diffusion into the pores of the pellet, and the local chemical reaction between the reactant gas and iron oxide. An important feature of these models is their ability to describe reversible kinetics; otherwise, they fail to correctly describe the reduction [26]. To understand the intricate behavior of the countercurrent DRSF operation, numerical one-dimensional (1D) models using computational fluid dynamics (CFD) were developed [25, 133, 136, 137, 138] and validated against Midrex plant data [29, 118, 139]. To further study the issue of heat and reductant gas supply by considering the radial distributions of temperature and species, several models have been adapted in 2D [77, 125, 140, 141, 142, 143, 144, 145]. Such models allow an accurate description of the cooling zone, the conical geometry of which has dramatic consequences for reactor behavior, especially when it is equipped with a so-called Christmas tree [125]. Novel approaches include 3D grids that model gas injections more accurately [146, 147, 148] or use the discrete element method (DEM) for solid flow description [121].

Some interesting conclusions can be drawn from these studies. High and narrow furnaces are preferable since they allow sufficient reduction time and avoid the presence of a cold zone when injecting from the sidewall [15, 18]. Indeed, heat and reductant supply issues appear mainly at the center of the furnace because the reducing gas may not be able to reach this zone. To overcome this difficulty, increasing either the gas flow rate or the gas temperature appears to be a good option [147]. A higher bustle temperature also decreases the gas flow rate necessary for full metallization [136] and improves the degree of metallization and gas utilization [25]. A fraction of the feed gas may also be redirected to a central gas distribution system [144, 145] or to a second lateral injection [140, 149] to improve the distribution of H_2 in the furnace and its overall thermochemical state. A second lateral injection located above the bustle gas injection can be fed with heated off-gas, thus avoiding the need for energy-intensive water [150]. Modifying the solid flow with a Christmas tree-type structure at the center of the furnace is another alternative to avoid the formation of a central “dead zone” [125]. Other solutions considered include the use of microwave heating in non-metallized zones to increase the temperature [151] and the charging of larger pellets at the center of the furnace to improve the permeability of the bed [142]. Small porous pellets are also good solutions for enhancing burden reducibility and strength at the cost of increasing the pressure drop.

In the present paper, we report further numerical simulations of an H2-DRSF associated with its gas circuit. The 2D axisymmetric model REDUCTOR [15, 141] was modified and complemented with a model of the gas loop, as presented in section 2. The results of a representative reference case with a 94% metallization degree are presented in section 3. From this reference case, a parametric study was conducted to investigate the effects of hot charging, gas distribution and N_2 content on the global furnace performances: metallization degree, gas utilization ratio and energy consumption.

Article 3 – **2. Mathematical Model**

Article 3 – **2.1. Model of the H_2-DRSF**

Article 3 – **2.1.1. Principle of the Mathematical Model**

The 2D axisymmetric steady-state model REDUCTOR was adapted to simulate an H_2-DRSF. REDUCTOR describes the solid and gas flows, the heat transfers and the chemical reactions taking place in a DRSF. Both the solid and gas phases are treated as continuous media, and the local mass, energy and momentum balance equations are solved via the finite volume method. The details of this model have been previously extensively presented [15, 18, 77, 141], including a validation against plant data, which relied on a comparison between calculated and measured top gas and DRI characteristics. See [141] for further details. A summary, which includes the new features (gas flow numerical solution), is given below.

The solid burden is modeled as a pseudocontinuous stack of spherical pellets (d_p = 15 mm) with a constant bed porosity ($\epsilon_{bed} = 0.5$). The solid flow is described according to Mullins' model [152]. In this model, the radial velocity is proportional to the radial gradient of the axial velocity (Equation (5)):

$$u_{r,s} = -B\frac{\partial u_{z,s}}{\partial r} \quad (\mathrm{m\ s^{-1}}) \tag{56}$$

The solid heat balance considers convection, conduction, heat exchange with the gas phase; the heat of the reactions is assumed to be entirely attributed to the solid phase (Equation (6)):

$$\begin{gathered} -\rho_b u_{z,s} c_{p,s}\frac{\partial T_s}{\partial z} + \rho_b u_{r,s} c_{p,s}\frac{\partial T_s}{\partial r} = \\ \frac{1}{r}\frac{\partial}{\partial r}\left(r\Gamma_{r,e}\frac{\partial T_s}{\partial r}\right) + \frac{\partial}{\partial z}\left(\Gamma_{z,e}\frac{\partial T_s}{\partial z}\right) + a_b h_T\left(T_g - T_s\right) + \sum_{n=1}^{3} -(r_n \Delta_r H_n) \quad (\mathrm{W\ m^{-3}}) \end{gathered} \tag{57}$$

The gas flow through the packed bed of pellets is described via the Ergun equation [153], which can be combined with the gas continuity equation to solve for the pressure distribution (Equations (7) and (8)):

$$\boldsymbol{u_g} = -\frac{1}{K}\boldsymbol{\nabla P} \quad (\mathrm{m\ s^{-1}}) \tag{58}$$

$$\frac{1}{r}\frac{\partial}{\partial r}\left(r\frac{c_t}{K}\frac{\partial p}{\partial r}\right) + \frac{\partial}{\partial z}\left(\frac{c_t}{K}\frac{\partial p}{\partial z}\right) = 0 \quad (\mathrm{mol\ m^{-3}\ s^{-1}}) \tag{59}$$

The gas heat balance also considers convection, conduction and heat exchange, as well as a specific term related to the evolution of the gas heat capacity during the reaction:

$$\begin{gathered} \rho_g u_{z,s} c_{p,g}\frac{\partial T_s}{\partial z} + \rho_g u_{r,s} c_{p,g}\frac{\partial T_s}{\partial r} = \\ \frac{1}{r}\frac{\partial}{\partial r}\left(r\Gamma_g\frac{\partial T_g}{\partial r}\right) + \frac{\partial}{\partial z}\left(\Gamma_g\frac{\partial T_g}{\partial z}\right) + a_b h\left(T_s - T_g\right) + \sum_i S_i \int_{T_g}^{T_s} c_{p,g,i}\,dT \quad (\mathrm{W\ m^{-3}}) \end{gathered} \tag{60}$$

The pellets react according to a simplified grain model with the law of additive reaction times [43, 47]. This kinetic model assumes that three distinct consecutive phenomena can be rate-limiting for each of the reduction reactions: gas diffusion in the bulk, gas diffusion in the pores of the pellet,

and local chemical reactions. Each of these phenomena influences the reaction rate through a characteristic time τ, which can be expressed as:

$$\tau = \frac{\rho_s \, d_p}{k \, f_m} \quad \text{(s)} \quad \text{with} \quad f_m = c_{H_2} - c_{H_2 eq} \tag{61}$$

where ρ_s is the iron oxide molar density, k is a kinetic factor, and f_m is the driving force of the reaction. For a specific set of gas compositions and temperatures, the instantaneous reaction rate of each reduction reaction is calculated with the law of additive reaction times:

$$v_X = \frac{1}{\tau_{chem} \, f'(X) + \tau_{diff} \, g'(X) + \tau_{ext} \, h'(X)} \quad (\mathrm{s}^{-1}) \tag{62}$$

where f, g, and h are conversion functions related to each phenomenon, and X is the conversion. See Ranzani et al. [77] for more details.

The temperatures and compositions of both phases at the inlets follow Dirichlet boundary conditions. The gas velocity is given at the gas inlet, the gas pressure is given at the top gas outlet, and the gas concentration is calculated according to the ideal gas law. The solid mass flow is given at the top of the furnace. Zero flux conditions are set at the symmetry axis and at the walls, except for the gas inlet.

Article 3 – **2.1.2. Numerical Solution**

The simulation domain is divided into 2000 cells in which the conservation equations are discretized according to the finite-volume method. The standard finite-volume method [154] is used in the upper cylindrical region of the furnace, whereas a deferred correction method [155] is used in the conical region to account for the nonorthogonality of the mesh there. The numerical solution is obtained by solving each equation for each cell via the Gauss–Seidel algorithm. This operation is repeated until the desired convergence for each variable and for mass, momentum and energy balance is obtained. The software is an in-house program (11,000 lines) written in Fortran 95. The pellet kinetic model is a subroutine of the main program. In terms of modeling, the innovations introduced in this article are the operation of a 100% H_2-DRSF, the improvement of boundary conditions for thermal balance, and the integration of a more accurate subalgorithm for solving the gas flow, as explained below.

In this work, we introduced the SIMPLE algorithm [154] into REDUCTOR to improve the resolution of coupled gas pressure–momentum equations; this was accomplished by combining the Ergun equation and the continuity equation. A similar method was recently proposed by Korba et al. [156]. The procedure to solve coupled gas–pressure momentum equations comprises the following steps:

1. An arbitrary pressure field P is given.
2. A preliminary velocity field $\boldsymbol{u}_{\boldsymbol{g}}^{*}$ is derived from P via the Ergun equation.
3. The pressure correction field P' is first set to 0. It is then calculated across the whole computational domain with the combined Ergun-continuity equation.
4. P' is added to P to correct it.
5. The velocity field is corrected with P' via the Ergun equation, and the algorithm returns to step 2.

This update of the code proved to be very efficient since it allowed us to obtain a more accurate mass balance for the gas phase.

Article 3 – **2.2. Model of the Gas Loop**

To describe the gas loop, we retained the top gas recycling setup considered by Shao et al. [133]. The full gas circuit is shown in Figure 48. The off-gas leaving at the top of the furnace is dedusted before it enters a countercurrent heat exchanger. There, energy is recovered to heat the fresh hydrogen produced by electrolysis, which is mixed with recycled gas at the bustle. Water vapor is then removed from the off-gas in a condenser, and the rest of the gas exits the condenser at a temperature of 70 °C. This gas is recycled either to the bustle or in the cooling zone after mixing with fresh H_2 and a compression step. Before injection at the bustle, the bustle gas is heated.

The gas loop model works in a postprocessing framework, meaning that the output results from REDUCTOR are input parameters for the gas loop model. Its main utility is to enable us to complete the energy balance of the process. We assumed that the only relevant energy needs for the whole process are those of water electrolysis, gas heating and gas compression.

H_2 production by electrolysis is supposed to supply the shaft with fresh H_2, and the energy required for this production is calculated considering the need for 18 $MJ/Nm^3_{H_2}$ [133]. The countercurrent heat exchanger was modeled according to the number of transfer units (NTU) method [157] with NTU = 5. Its efficiency was high (0.98). The efficiency of the heater was taken equal to 0.7. The equations and process parameters for the considered units (e.g., the mixer, compressor, heater and electrolysis unit) were taken directly from [133].

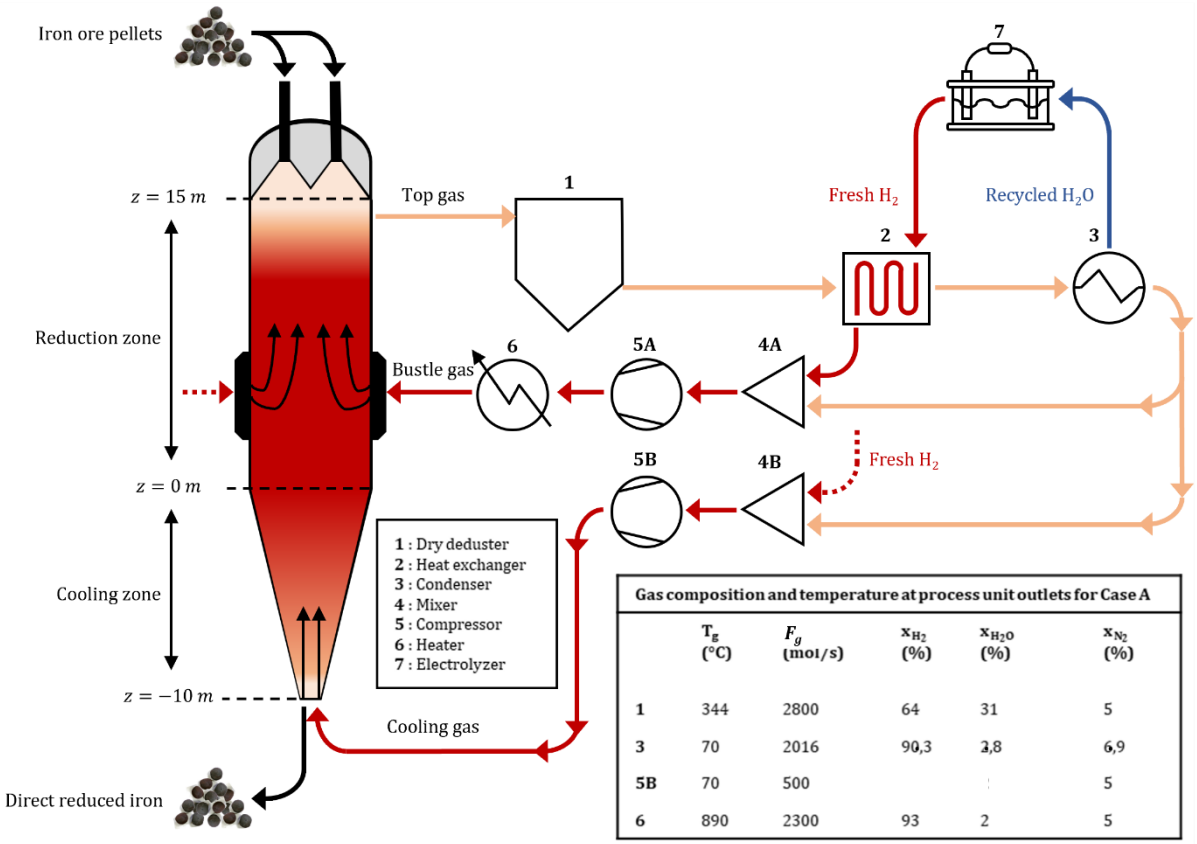

Gas composition and temperature at process unit outlets for Case A

	T_g (°C)	F_g (mol/s)	x_{H_2} (%)	x_{H_2O} (%)	x_{N_2} (%)
1	344	2800	64	31	5
3	70	2016	90,3	3,8	6,9
5B	70	500			5
6	890	2300	93	2	5

Figure 48. Flow chart of the H_2-DRSF plant.

Article 3 – **3. Results and Discussion**

Article 3 – **3.1. Furnace Data and Operating Parameters**

The operating parameters and the geometry of the H_2-DRSF were derived from those of a Midrex DRSF [141]. The shaft furnace is made of a cylindrical upper part that is 15 m long and 2.6 m wide, and a conical lower part that is 10 m long and 1.31 m wide at the solid outlet. The plant delivers approximately 120 t/h of DRI with an average metallization degree close to 94%. The pellets are composed of hematitic ore (96.65 wt-%) and gangue (3.35%, of which CaO 1.39%, SiO_2 0.98%, MgO 0.56%, Al_2O_3 0.42%). The shaft is operated with a high gas flow (2800 mol/s) at relatively low pressures (1.5–2 bar). The reducing gas composition was 93% H_2, 2% H_2O, and 5% N_2 (molar fractions). The same mixture is injected at both inlets, at 890 °C at the bustle and at 70 °C at the bottom. The bustle inlet is located 4.9 m above the bottom of the upper part. The cooling gas both cools the hot DRI and brings fresh hydrogen to the upper part of the furnace. This reference case is labeled case A and is compared with four unlike H_2-DRSF operations detailed below, labeled cases B, C, D and E. The operating parameters for each case are given in Table 15, and the distributions of process variables in the furnace are shown in Figures 50-56. Throughout this paper, the gas fractions are molar fractions, whereas the solid fractions are mass fractions.

Table 15: Operating parameters of cases A, B, C, D and E. The inputs and outputs are given in plain and bold letters, respectively.

Operating Parameters		**Case A**	**Case B**	**Case C**	**Case D**	**Case E**
Bustle gas	F_g (mol/s)	2300	2100	2300	2300	2300
	T (°C)	890	890	950	815	890
	% H_2	93	93	66	93	93
	% H_2O	2	2	2	2	2
	% N_2	5	5	32	5	5
	P (Pa)	**180,400**	**179,600**	**212,400**	**178,900**	**176,700**
Cooling gas	F_g (mol/s)	500	700	500	500	500
	T (°C)	70	70	70	70	70
	% H_2	93	93	66	93	93
	% H_2O	2	2	2	2	2
	% N_2	5	5	32	5	5
	P (Pa)	**181,600**	**181,900**	**215,500**	**180,800**	**178,200**
Solid burden inlet	W (kg/s)	45	45	45	45	43
	T (°C)	20	20	20	1200	20
	% Fe_2O_3	96.65	96.65	96.65	96.65	96.65
	Gangue	3.35	3.35	3.35	3.35	3.35

	Ø (mm)	15	15	15	15	15
	bed porosity	0.5	0.5	0.5	0.5	0.5
Top gas	F_g (mol/s)	2796	2800	2793	2802	2766
	T (°C)	**344**	**341**	**394**	**806**	**353**
	% H_2	**64.1**	**65.1**	**36.1**	**62.9**	**64.6**
	% H_2O	**30.9**	**29.9**	**31.9**	**32.1**	**30.4**
	% N_2	**5**	**5**	**32**	**5**	**5**
	P (Pa)	150,000	150,000	150,000	150,000	150,000
Solid DRI	W (t/h)	117.19	117.22	117.18	116.86	109.88
	T (°C)	**261**	**166**	**402**	**330**	**403**
	% Fe_2O_3	**0**	**0**	**0**	**0**	**0**
	% Fe_3O_4	**0.5**	**2.82**	**0**	**0**	**0**
	% FeO	**7.71**	**5.04**	**8.26**	**7.11**	**0**
	% Fe	**87.16**	**87.51**	**87.11**	**88.24**	**95.15**
	% Gangue	**4.63**	**4.63**	**4.63**	**4.64**	**4.85**
Metallization	%	**93.3**	**93.7**	**93.2**	**94.1**	**100**
Gas utilization degree (GUD)	-	**0.33**	**0.33**	**0.47**	**0.34**	**0.32**
Energy demand	GJ/t_{DRI}	**12.20**	**11.99**	**12.47**	**11.68**	**12.98**

In the next sections, results from the five cases will be discussed successively. To limit the number of figures, in Figures 50-56 the five cases are plotted together in columns. This facilitates the comparison between cases but makes it necessary to consider the same columns from several figures for the interpretation of a given case.

Article 3 – **3.2. Case A—Reference Case Operation**

The results revealing the furnace behavior in case A are illustrated in Figure 49 and the outer left colormaps of Figures 50-56. As shown in Figure 49, the simple geometry leads to near-horizontal pressure drops and almost uniform gas velocity profiles, except at the bustle. In fact, the lowest gas velocities are reached in the furnace center, where hydrogen is not supplied easily. This causes the hydrogen content to decrease there, hindering the reduction of the burden, as shown in Figure 51. This was previously reported by [125]. The solid path follows plug flow behavior, at least until the hopper section (Figure 49). The conical geometry of the solid outlet breaks the flow uniformity and creates a strong gradient of axial mass flux density between the center and the lateral region of this zone; this, in turn, causes the solid to move centripetally with a nonzero radial mass flux density, which is in agreement with Mullins' model.

The gas and solid temperatures are in equilibrium along the entire furnace height, except at the inlets. The solid exits the furnace at an average temperature of 261 °C, indicating that there could be potential for heat recycling by increasing the amount of gas sent to the cooling inlet [145]. Hematite is immediately converted as the burden enters the furnace (Figure 53). The moderate temperature region (500–650°) spanning from 14.5 to 8.5 m leads to a slow reduction in the magnetite in this region; actually, direct reduction of magnetite to iron is not described in the model, and this could induce little variation in the results. Wustite is rapidly converted above the bustle due to highly reducing conditions. After 9 m, complete metallization is reached in the peripheral zone, where the H_2 content and temperature are high (see Figure 51 and Figure 56). The central region, which is hardly supplied with hydrogen and heat, is not metallized, which is in agreement with the findings of Li et al. [142]. Under these operating conditions, a GUD of 0.33 is reached.

For a given metallization degree, a simple oxygen balance gives the necessary flow of fresh hydrogen to reduce the iron ore [133]. With an inlet solid flow rate of 45 kg/s and a metallization degree of 94%, the required flow rate of fresh H_2 is calculated to be 784 mol/s, and the associated energy consumption is 9.73 GJ/t_{DRI}. As shown in Figure 58 (below, section A-3/3.6), the energy required to produce fresh H_2 by electrolysis represents approximately 80% of the total energy consumption of the plant. The same conclusions hold for the other cases.

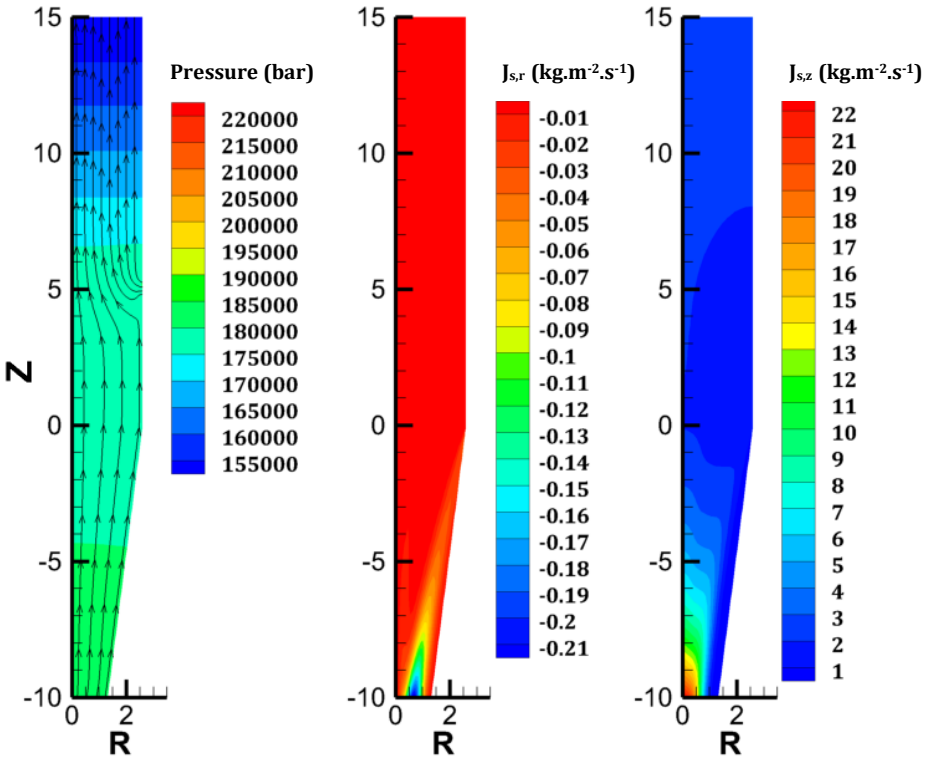

Figure 49. Gas and solid flows in Case A. From left to right: gas streamlines and pressure; radial density of solid mass flux; axial density of solid mass flux.

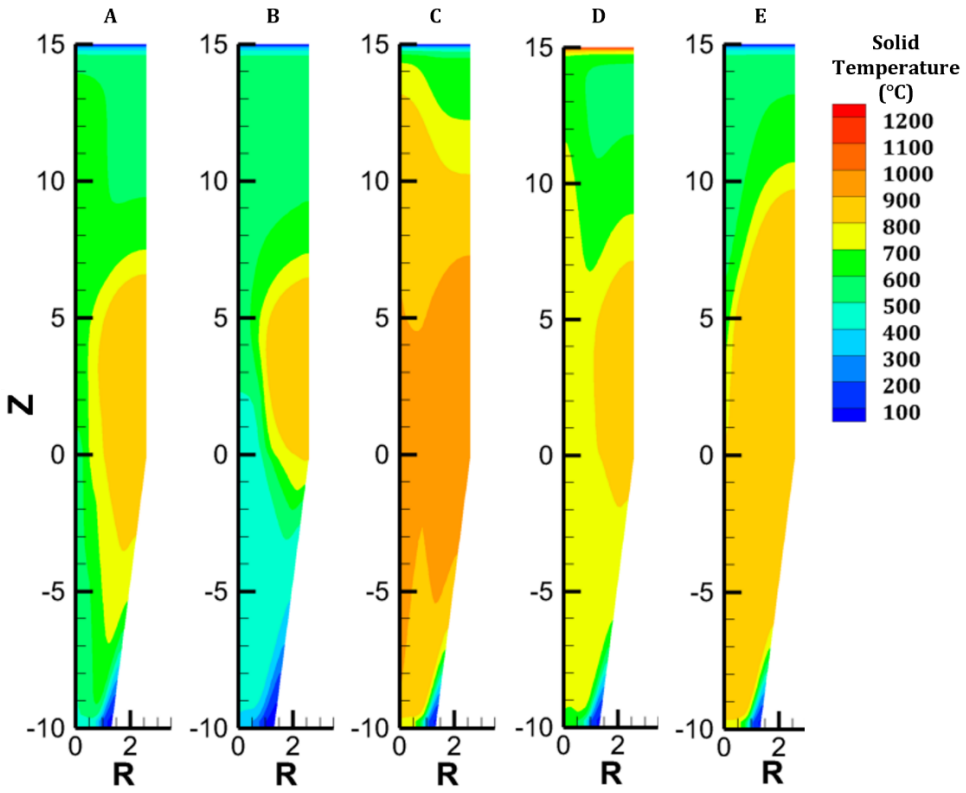

Figure 50. Distribution of the solid temperature in each case.

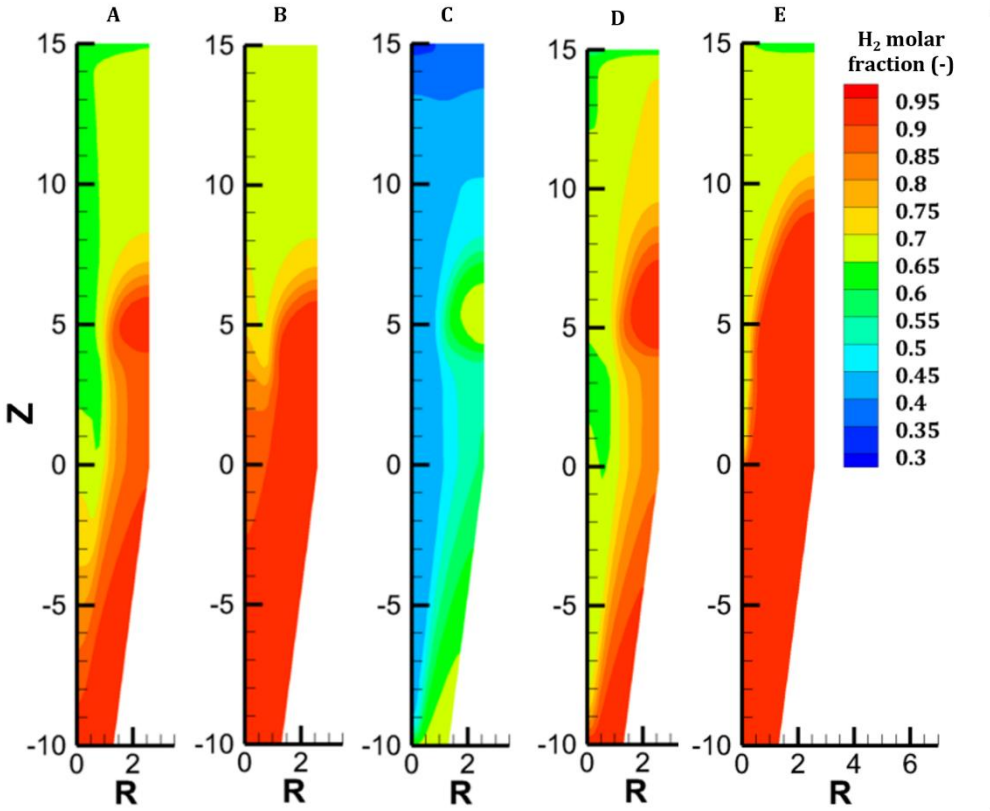

Figure 51. Distribution of H_2 content in each case.

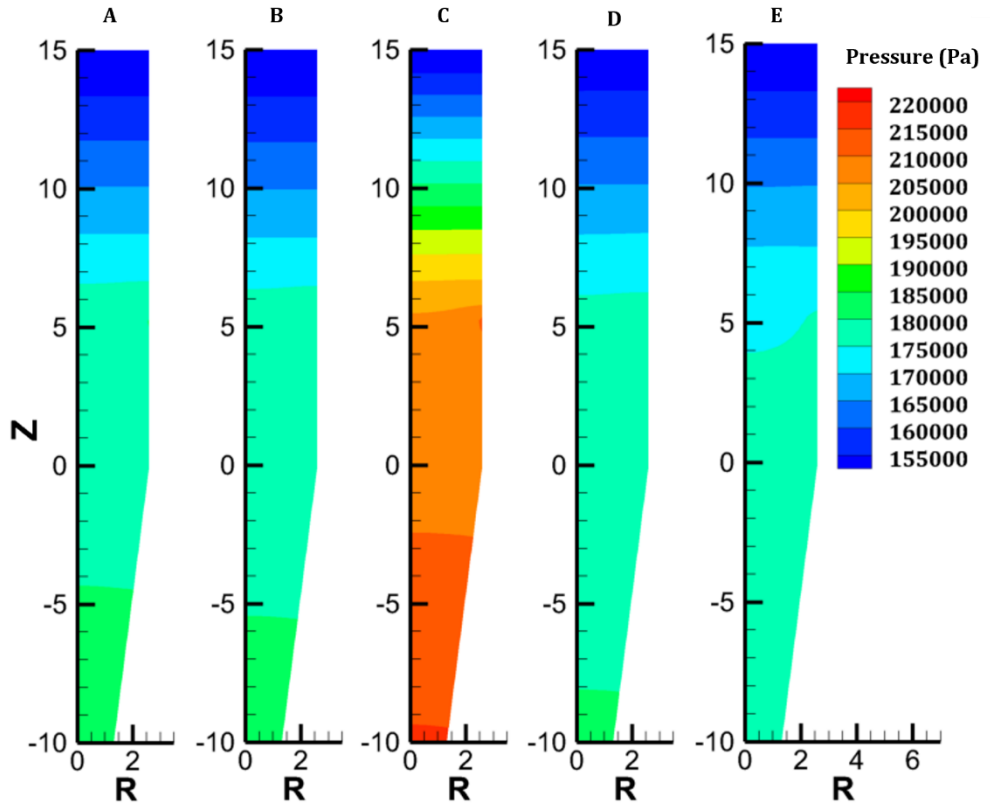

Figure 52. Distribution of gas pressure in each case.

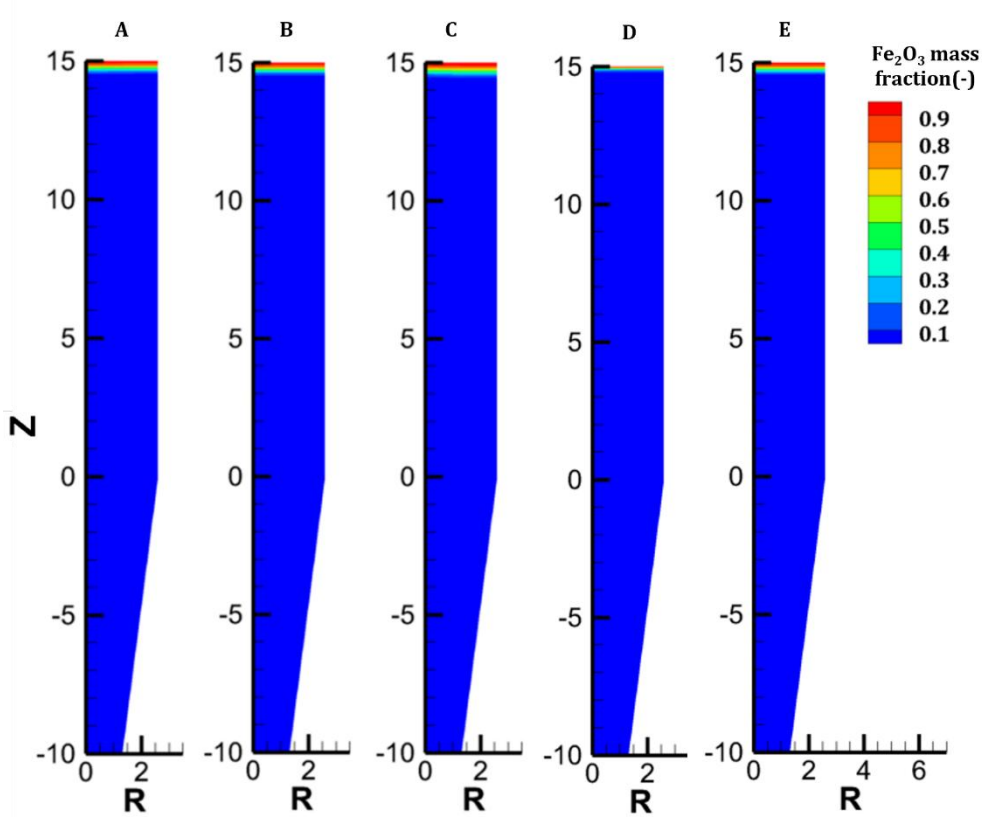

Figure 53. Distribution of the hematite content in each case.

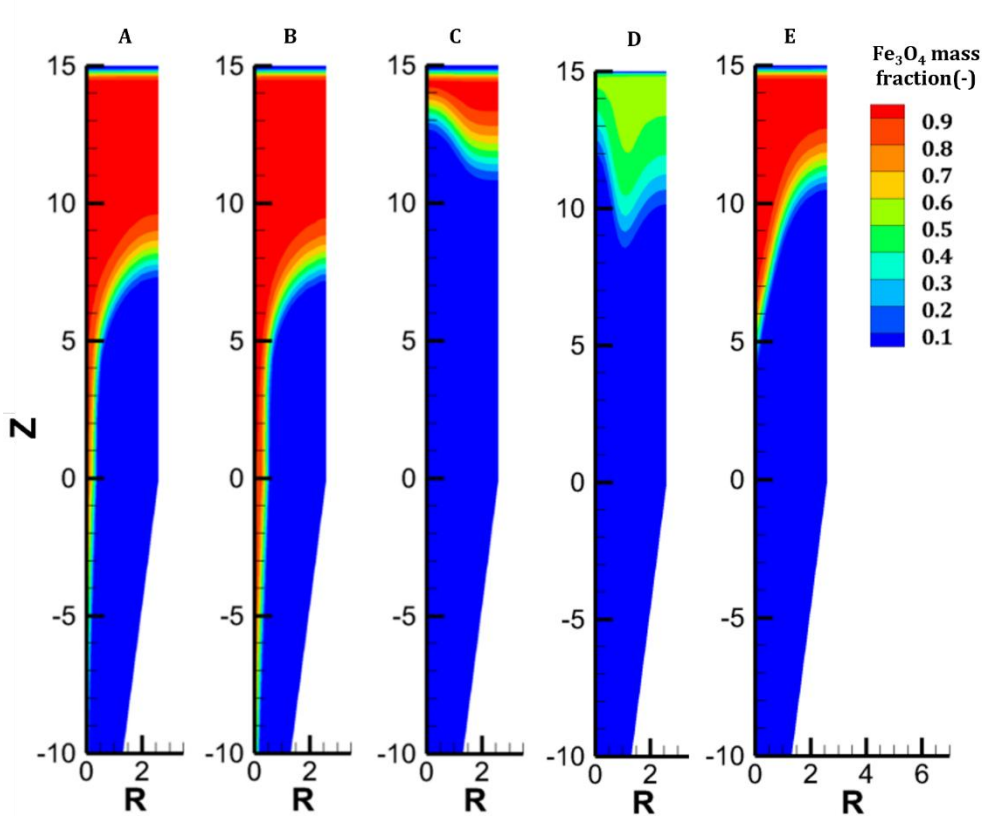

Figure 54. Distribution of the magnetite content in each case.

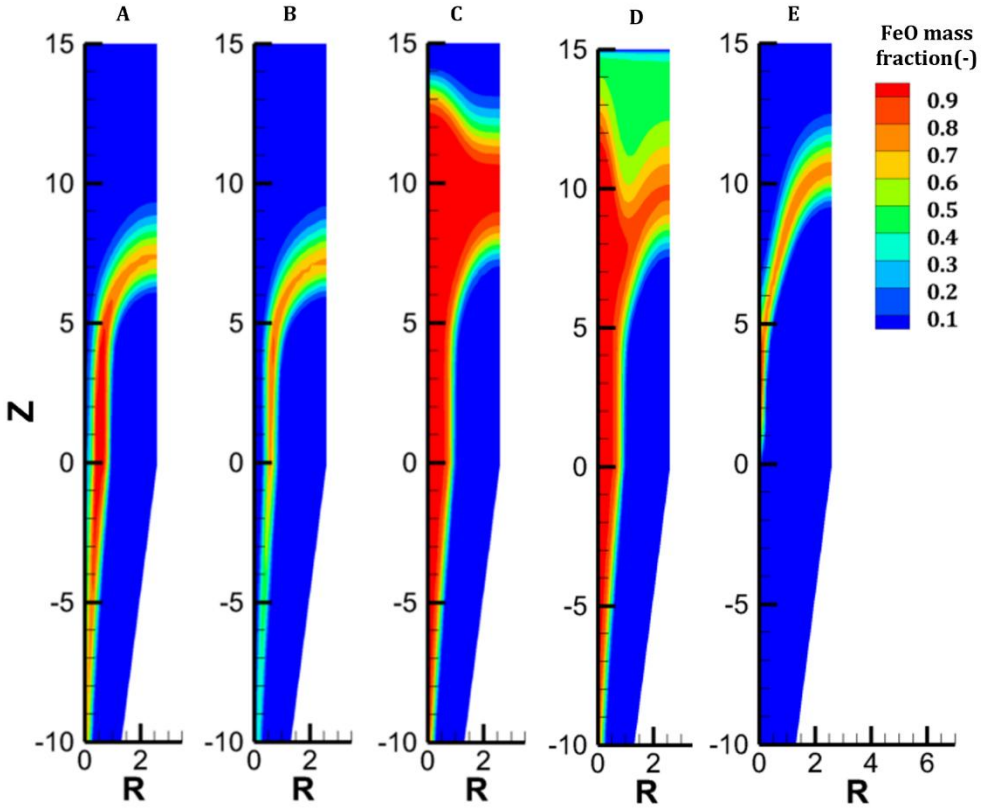

Figure 55. Distribution of the wustite content in each case.

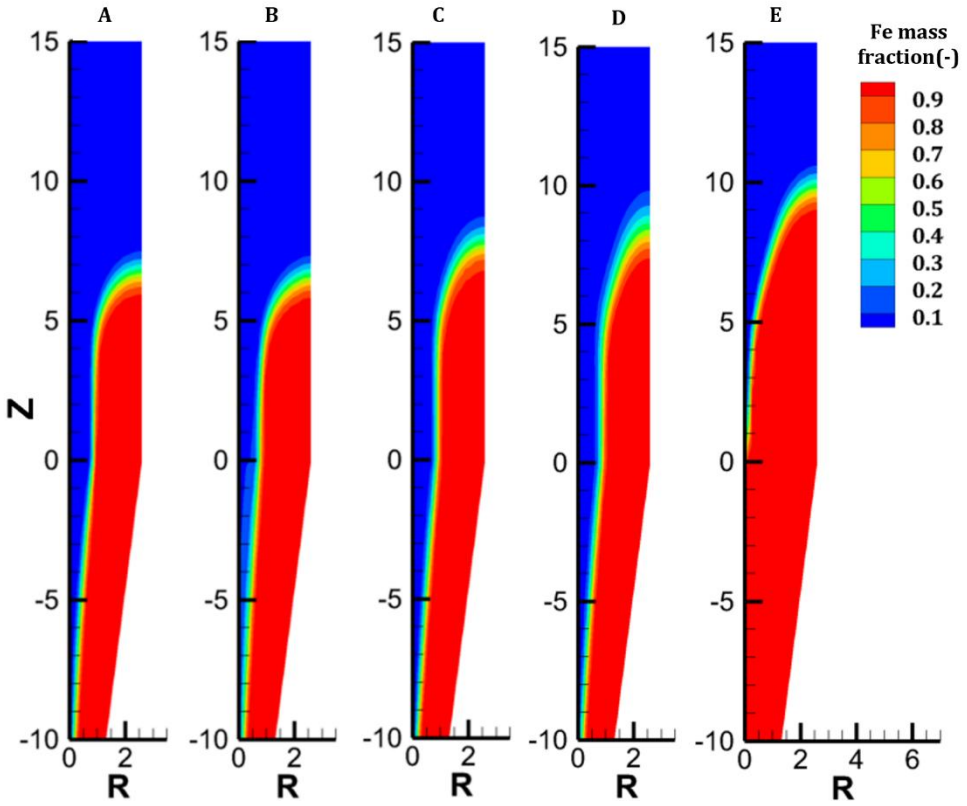

Figure 56. Distribution of the iron content in each case.

Two subcase simulations were performed to quantify the effect of nitrogen dilution. In the first simulation (A1), the nitrogen gas flow rate (140 mol/s) was "removed" from the gas mixture. The total gas flow rate decreased accordingly, from 2800 to 2660 mol/s, while the molar fractions of hydrogen and water vapor were set to 0.98 and 0.02, respectively. This led to degraded metallization (88% vs. 94%). This finding indicates that, to a certain extent, the sensible heat brought by N_2 is more important than its dilution effect, as corroborated by [158]. In the second simulation (A2), hydrogen was partially replaced with nitrogen while keeping the total gas flow rate constant. The gas composition at both the bustle and cooling gas inlets was 88% H_2, 10% N_2 and 2% H_2O. Compared with that of the base case, the metallization decreased (90% vs. 94%). In this case, the gain in sensible heat due to the superior thermal capacity of N_2 was not sufficient to balance the decrease in the driving force due to dilution.

Article 3 – **3.3. Case B—Redirecting Gas from the Bustle to the Cooling Inlet**

In case B, the cooling gas flow rate was increased from 500 mol/s to 700 mol/s while keeping the total gas flow rate constant. The furnace behavior in this case remained quite similar to that in case A. The main differences between the two cases lie in the solid temperature and H_2 content maps (see Figure 50 and Figure 51). On the one hand, a higher cooling gas flow rate better cools the lower region. Owing to this and the lower sensible heat carried at the bustle, the hot zone (T > 700 °C) shrinks. When the global energy consumption decreases, the heat is better valorized. On the other hand, the higher flow of H_2 injected at the bottom homogenizes the H_2 distribution and increases the driving force of the reaction in the furnace center. Overall, this solution remains

almost constant for both the metallization layer and the GUD while decreasing the cost of H_2 heating by 0.2 GJ/t_{DRI} (–1.7%, compared with case A).

To further clarify the influence of the gas flow rate at the cooling inlet, subcase simulations were performed. Figure 57 highlights the effect of the cooling gas flow rate on the burden metallization. The optimum cooling gas flow rate is approximately 600 mol/s (the total gas flow rate is kept constant). This optimum physically represents the balance between high H_2 content and sufficient sensible heat, since increasing the gas flow at the cooling inlet increases the H_2 content at the center of the furnace while decreasing its temperature.

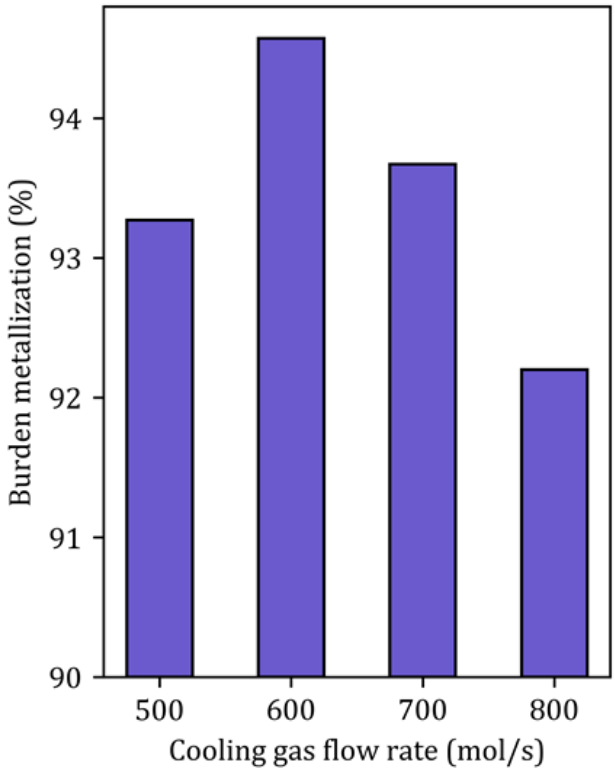

Figure 57. Metallization degree as a function of the cooling gas flow rate in case B.

Article 3 – **3.4. Case C—Bustle Gas Temperature and Nitrogen Content**

Case C addresses the partial replacement of H_2 with N_2 in the feed gas, both at bustle and cooling injections, and with an increased bustle gas temperature. With an N_2 content of 32% and a bustle temperature of 950 °C, the temperature distribution is greatly improved in the shaft, as shown in Figure 50. Despite weak H_2 concentrations in the central part of the furnace, great reduction levels are obtained owing to the high temperature in this zone. Since less heat is consumed to reduce the burden in the lower central part, more heat is available in the upper part, which explains the faster reduction of oxides, particularly magnetite (Figure 54).

Overall, this solution offers a more uniform temperature distribution and an H_2 distribution close to the reference case, as well as a higher GUD of 0.47. However, the higher thermal capacity of N_2 implies greater needs for heating and compression of the gas: both processes account for a total of 2.80 GJ/t_{DRI}, which represents an increase of 0.27 GJ/t_{DRI} (+2.2%) compared with case A.

Article 3 – **3.5. Case D—Introducing the Hot Burden**

We considered the introduction of hot pellets into the shaft. This solution could be attractive if the H_2-DRSF is located close to the pelletization plant. We selected 1200 °C as the maximum hot pellet temperature. The engineering details of hot conveying and charging devices were not investigated in the present parametric study. The sensible heat caused by the heat burden allows us to significantly reduce the temperature of the bustle gas (to 815 °C) while still reaching the DRI metallization target of 94%. In this case, complete conversion of hematite and magnetite is obtained 5 m below the solid inlet. Conversely, the reduction of wustite is not faster than in the previous cases, owing to H_2 starvation in the upper central zone of the furnace. The low wustite-to-iron reduction rate in turn explains the higher temperature observed there, an effect also highlighted in [150]. Overall, introducing hot pellets thus favors the hematite and magnetite reductions but does not lead to better reducing conditions for the most demanding reaction, the wustite-to-iron reduction.

Regarding energy, assuming that the pellets directly come hot from the pelletizing plant and are not heated on purpose, this case decreases the total energy consumption of the process to 11.68 GJ/t_{DRI} (–4.3% compared with case A; see Table 15 and Figure 58). This energy savings is limited by the high temperature of the top gas (806 °C). A large part of the sensible heat of the hot burden is evacuated by the off-gas, and the top gas heat utilization is limited by the necessity to condense its water. This is why this option is relevant only if the pellets are taken right after firing; otherwise, poor heat utilization and an increase in total energy consumption are to be expected, as pinpointed in [133].

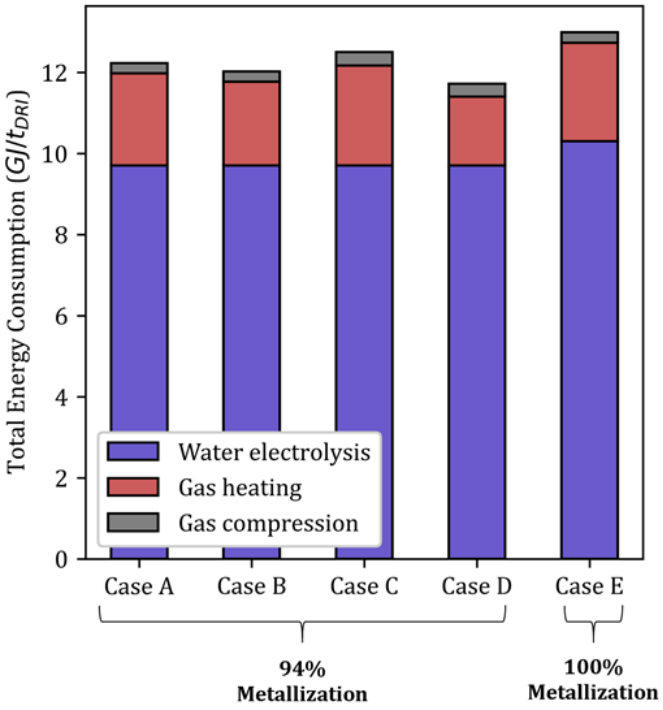

Figure 58. Energy consumption in each case.

Article 3 – **3.6. Case E—H_2-DRSF with 100% DRI Metallization**

The previous cases intentionally targeted a usual average metallization degree of 94%. However, a pure H_2-DRSF can readily lead to 100% metallization. The complete metallization of the burden

requires a sufficient supply of heat and hydrogen to the center of the furnace. This situation can be achieved simply by increasing the gas-to-solid flow rate ratio. We chose here to slightly decrease the burden flow rate from 45 to 43 kg/s at the inlet. Under such operating conditions, the shaft furnace behavior changes, resulting in much lower radial gradients and even 1D behavior in the cooling zone, where the oxides are fully reduced (Figures 50-56). This allows complete metallization with a near-optimized operation.

We thus demonstrated that for H_2-DRSF, only a slow dip in production allows a shift from a conventional metallization (94%) to a full metallization; this increases the molar ratio of hydrogen to iron from 3.26 to 3.4 and slightly lowers the GUD from 0.33 to 0.315. In terms of energy consumption, the hydrogen quantity required to reach full metallization is 780 mol/s; the energy required to produce this hydrogen to reduce 1 ton of DRI is 10.3 GJ/t_{DRI}, and the total energy consumption reaches 12.98 GJ/t_{DRI}. It should now be determined if spending +0.78 GJ/t_{DRI} (+6.4%) is beneficial for the complete metallization that it brings to the EAF operation.

Article 3 – **4. Conclusions**

The iron and steel industry requires breakthrough technologies to mitigate its GHG emissions. The H_2-DRSF seems to be a great candidate for fulfilling this objective. In this work, the finite-volume shaft furnace model REDUCTOR was enhanced and coupled with a gas loop model to perform an innovative parametric study. The influences of gas redirection from the bustle to the cooling inlet, high nitrogen content and temperature, and the introduction of a hot solid burden were compared to those of standard operation of a hypothetical H_2-DRSF; a full metallization case operation was also presented. The main conclusions of this study are as follows.

The redirection of a portion of the gas flow rate from the bustle to the cooling inlet (case B) provides a better distribution of H_2 in the furnace, although it slightly decreases the sensible heat brought by the gas. Overall, this strategy systematically lowers the energy consumption of the process.

The operation of the furnace at high temperature (950 °C) and a high nitrogen content (32%) in the gas mixture (case C) greatly increases the degree of gas utilization at the cost of a high thermal expense. This solution could be interesting if the top gas was not recycled.

The introduction of a hot (1200 °C) solid burden (case D) results in considerable sensible heat in the furnace, which is nevertheless poorly utilized because a large fraction of this heat is evacuated by the top gases. This solution is attractive if the pellets directly come hot from the pelletizing plant and are not heated on purpose; in this case, actual energy savings are to be expected.

The operation of H_2-DRSF for full metallization is readily reached by slightly increasing the gas flow rate or decreasing the production rate. The better supply of heat and hydrogen to the center of the furnace results in quasi 1D behavior in the lower half of the furnace. This complete metallization is obtained at the expense of +0.78 GJ/t_{DRI} (+6.4%).

Overall, these cases show that considerable gains in efficiency are possible while improving the thermochemical state of the furnace. This work provides a set of strategies that could also be applied in most DR plants. Further studies should consider the connections among the pelletizing plant, the DR plant and the EAF. A better description of solid granular flow should also be considered when investigating the influence of pellet size and burden stacking strategies.

Beyond these, after additional studies, the modeling approach presented here could help to answer further topical questions related to hydrogen direct reduction of iron ore, such as the

possible use of lower-grade ores, magnetitic or sideritic ores, and that of ammonia or ammonia–hydrogen mixtures as reactant gases.

III.2.2. The role of kinetics and geometry on a pure hydrogen shaft furnace

III.2.2.1. Modeling choices and objectives

As previously explained, additional simulations were performed after the submission of Article 3. While the simulations presented in the article dealt with innovative solutions for the operation of a pure hydrogen shaft furnace, here, we focused on what is at stake to better operate a pure hydrogen shaft furnace in relatively traditional configurations. To this end, a series of kinetic and geometrical considerations were investigated.

It has to be noted that several improvements were done in the REDUCTOR model for these last calculations. One of the major modifications is the replacement of Dirichlet boundary conditions with Fourier boundary conditions for temperature and chemical species, which allows for chemical reactions and thermal exchanges to take place at boundary cells (Figure 59). This new approach ensures more realistic values of the top gas temperature, for instance, and does not affect the internal behavior of the furnace. Moreover, the bustle gas temperature was changed from 890°C to 900°C in the following simulations, which only brought minor changes on the furnace behavior. Unless explicitly mentioned, the kinetics used in the simulations presented below are the same as those presented in Article 3, recalled in Table 16. The kinetics for CO reduction were taken from [16]. Finally, to keep consistency between the simulations with and without Christmas tree, the height of the cylindrical section of the shaft was set at 15.75 m, while the height of the hopper section was set at 9.25 m. The geometry of the Christmas tree will be presented later (Figure 66, subsection 2.2.5).

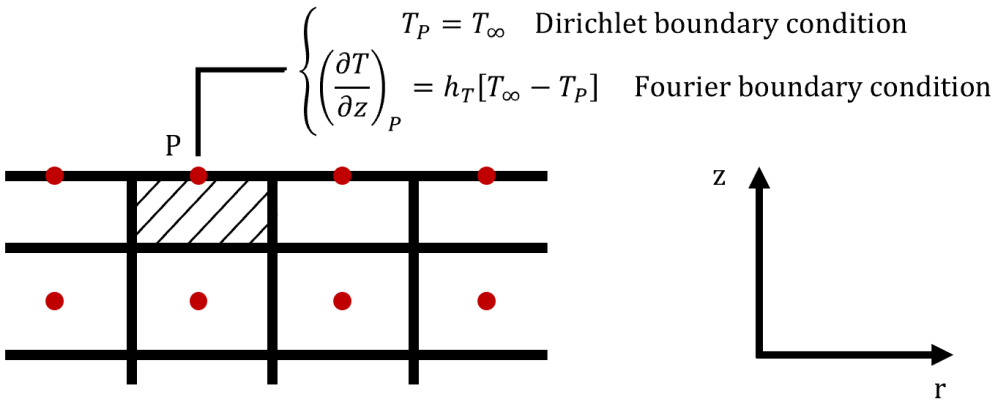

Figure 59: Schematic representation of Dirichlet and Fourier type boundary conditions for the solid temperature at the top of the furnace. The centers and borders of each cell are respectively represented as red dots and black solid lines. T_0 is a constant temperature; T_∞ is the solid temperature at an infinite distance above the boundary, and h_T is a positive heat transfer coefficient.

III.2.2.2. Decreasing the gas-to-solid ratio

As seen in Article 3, the comparison of case A and E showed that a decrease in shaft throughput (inlet solid flowrate lowered from 45 to 43 kg/s) led to an increase in burden metallization (from 93.3% to 100%). Actually, this reasoning also holds true the other way around. In a new

simulation called A3, the solid flowrate was increased up to 50 kg/s, with all other parameters kept constant. A schematic view is shown below, which details the mass and energy flows in this standard geometry (Figure 60).

Table 16: Kinetic parameters used in the simulations for the reduction with H_2 and CO.

H_2 reduction	Hematite → Magnetite	Magnetite → Wustite	Wustite → Iron
Frequency factor	$k_{0,1} = 7.79 \times 10^{-4}\ \text{s}^{-1}$	$k_{0,2} = 1.11 \times 10^{-2}\ \text{s}^{-1}$	$k_{0,3} = 16\ \text{s}^{-1}$
Activation energy	$E_{a,1} = 27000\ \text{J mol}^{-1}$	$E_{a,2} = 55000\ \text{J mol}^{-1}$	$E_{a,3} = 136000\ \text{J mol}^{-1}$
CO Reduction	Hematite → Magnetite	Magnetite → Wustite	Wustite → Iron
Frequency factor	$k_{0,4} = 13\ \text{s}^{-1}$	$k_{0,5} = 5.53 \times 10^{-2}\ \text{s}^{-1}$	$k_{0,6} = 2.27 \times 10^{-3}\ \text{s}^{-1}$
Activation energy	$E_{a,4} = 113859\ \text{J mol}^{-1}$	$E_{a,5} = 73674\ \text{J mol}^{-1}$	$E_{a,6} = 69488\ \text{J mol}^{-1}$

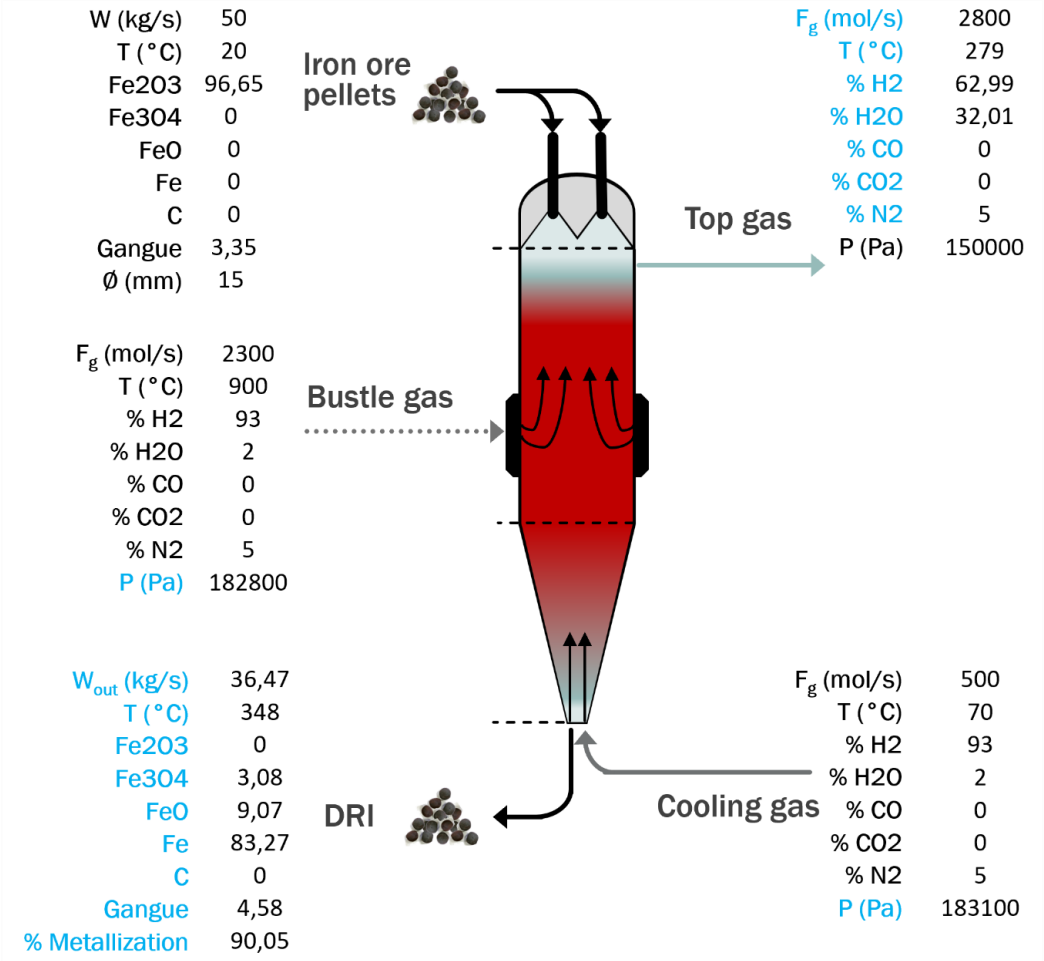

Figure 60: Mass and energy flowchart for the new simulation A3. Output data are highlighted in light blue.

At the center of the furnace, the increased flowrate of solid led to the formation of a cold zone which prevents metallization (see Figure 61a), e)). Conversely, in the cooling zone, the increased solid flowrate reduced the heat exchanges with the cooling gas and prevented from proper cooling at the wall, which explains why the solid temperature hardly decreased until reaching 1 m above the bottom of the furnace. This example illustrates a poor use of heat supply, where the temperature distribution was radially highly inhomogeneous. These features led to a low metallization of 90.05%.

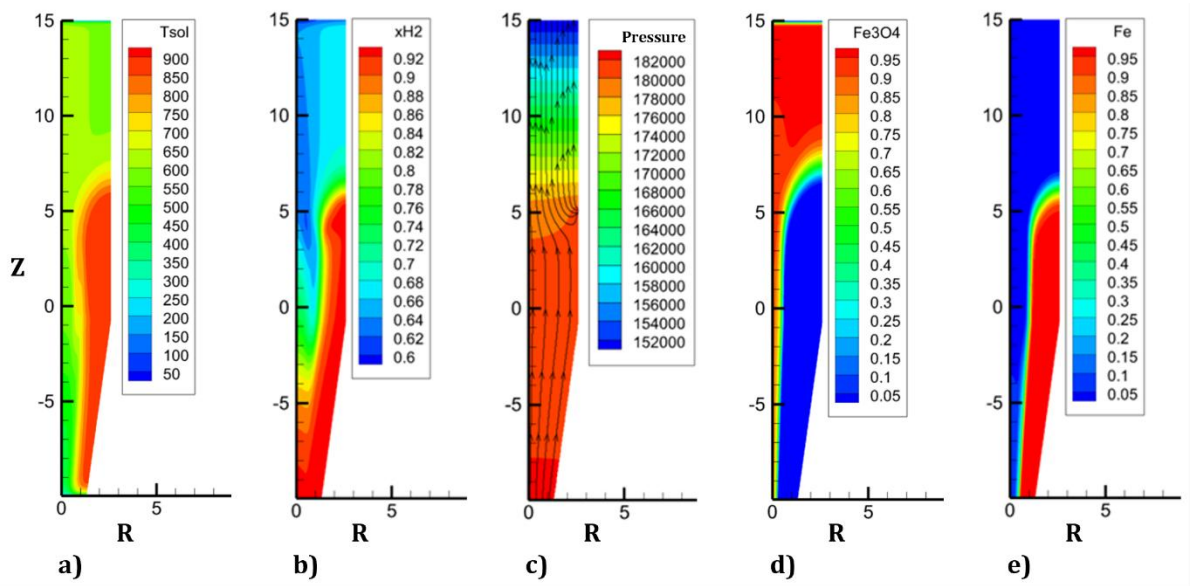

Figure 61: Distribution of process variables for the operation of a high- throughput H_2-DRSF. W = 50 kg/s, M = 90.05%.

III.2.2.3. Updated kinetics

The kinetics of reduction of iron oxides were thoroughly investigated in chapter I, leading to a new set of kinetic parameters, which is reported in Table 17. These parameters were shown to better reproduce the reduction of iron ore pellets in a TGA, especially at temperatures below 700°C, than the previous ones, proposed by [18]. The actual small differences in the resulting rate constants are illustrated in Figure 62.

Table 17: Kinetic triplets used in the DRSF simulations for the reduction of iron oxides with hydrogen.

Costa 2011	This work
$k_{0,1} = 7.79 \times 10^{-4}\ \mathrm{s}^{-1}$ $E_{a,1} = 27233\ \mathrm{J.mol}^{-1}$	$k_{0,1} = 8.89 \times 10^{-4}\ \mathrm{s}^{-1}$ $E_{a,1} = 30584\ \mathrm{J.mol}^{-1}$
$k_{0,2} = 1.11 \times 10^{-2}\ \mathrm{s}^{-1}$ $E_{a,2} = 55000\ \mathrm{J.mol}^{-1}$	$k_{0,2} = 1.65 * 10^{-1}\ \mathrm{s}^{-1}$ $E_{a,2} = 80721\ \mathrm{J.mol}^{-1}$
$k_{0,3} = 16\ \mathrm{s}^{-1}$ $E_{a,3} = 135686\ \mathrm{J.mol}^{-1}$	$k_{0,3} = 2.29\ \mathrm{s}^{-1}$ $E_{a,3} = 115864\ \mathrm{J.mol}^{-1}$

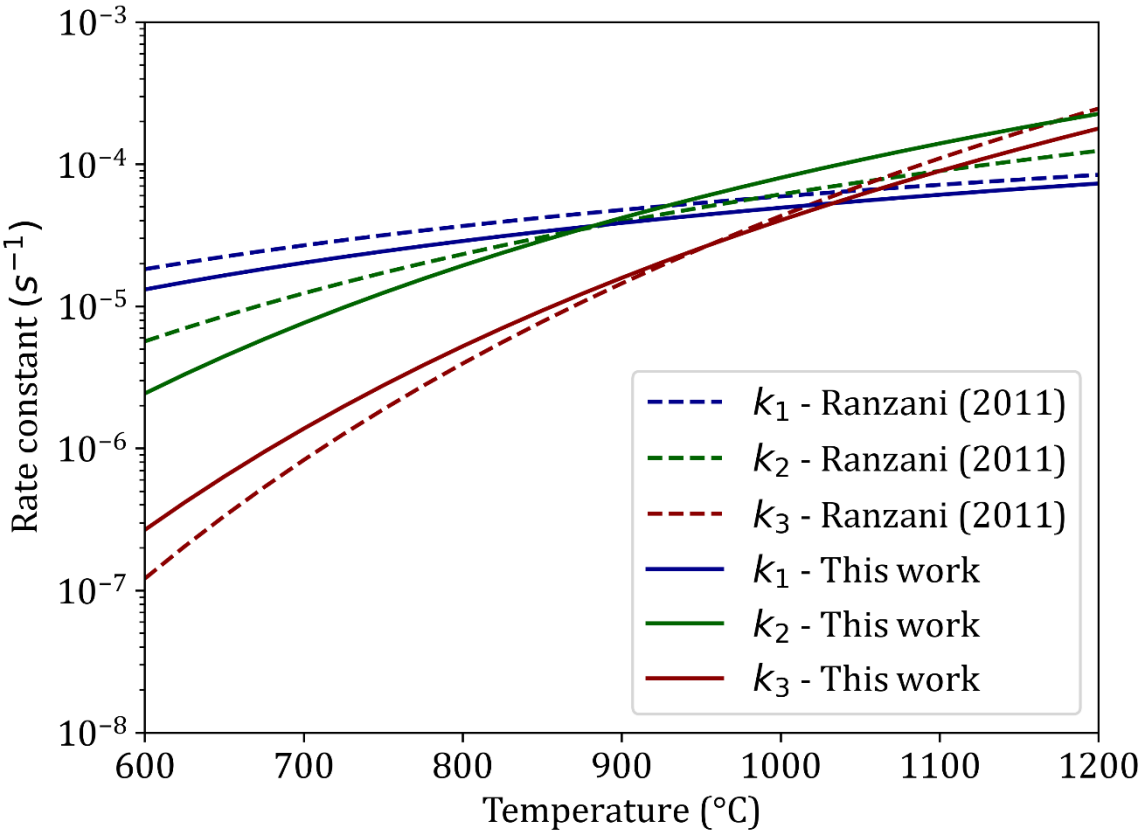

Figure 62: Comparison of the rate constants from Table 17 as a function of temperature.

A new simulation (A3bis) was run with these updated kinetics, keeping values identical values to simulation A3 for all other parameters. The results are presented in Figure 63. Although minor changes can be observed on the solid temperature and hydrogen content maps, no noticeable change was identified. The metallization degree was slightly increased and reached 90.9%, instead of 90.05% in case A3.

This showed that the slight differences in both kinetic triplets are only of minor importance on the behavior of a H_2-DRSF. At the scale of the shaft, it seems that other issues such as heat and reductant supply are of much greater importance.

III.2.2.4. High pressure operation

Some industrial shaft furnaces are operated at “high” pressure (6~7 bar) to improve shaft throughput and minimize the generation of iron ore fines [159]. In the case of pure hydrogen, the theoretical effect of increasing the pressure is to enhance the kinetics of reduction, which should lead to a higher metallization (see chapter I, Article 1). To further investigate the effect of pressure at the scale of the shaft, a simulation was led with an increased top gas pressure and a high solid flowrate (W = 50 kg/s, P = 6bar). The results are presented below (Figure 64 and Figure 65).

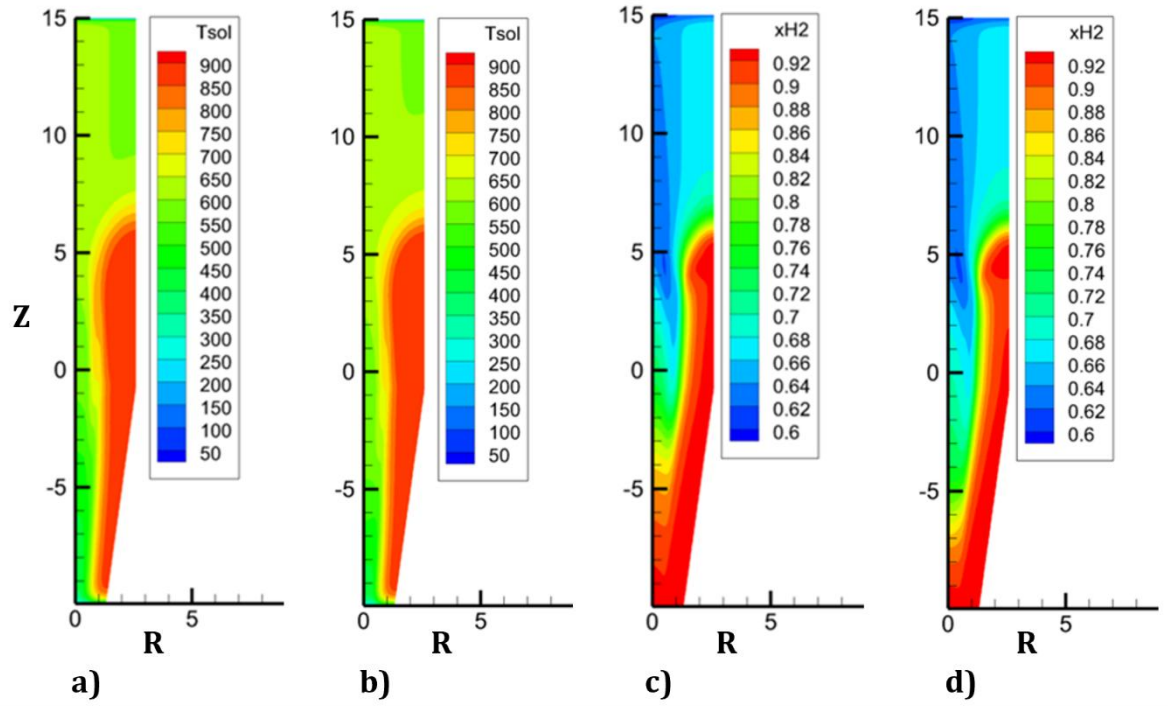

Figure 63: Distribution of temperature and hydrogen content for simulation A3 **a),d)** and A3bis **b),d)**. *W* = 50 kg/s.

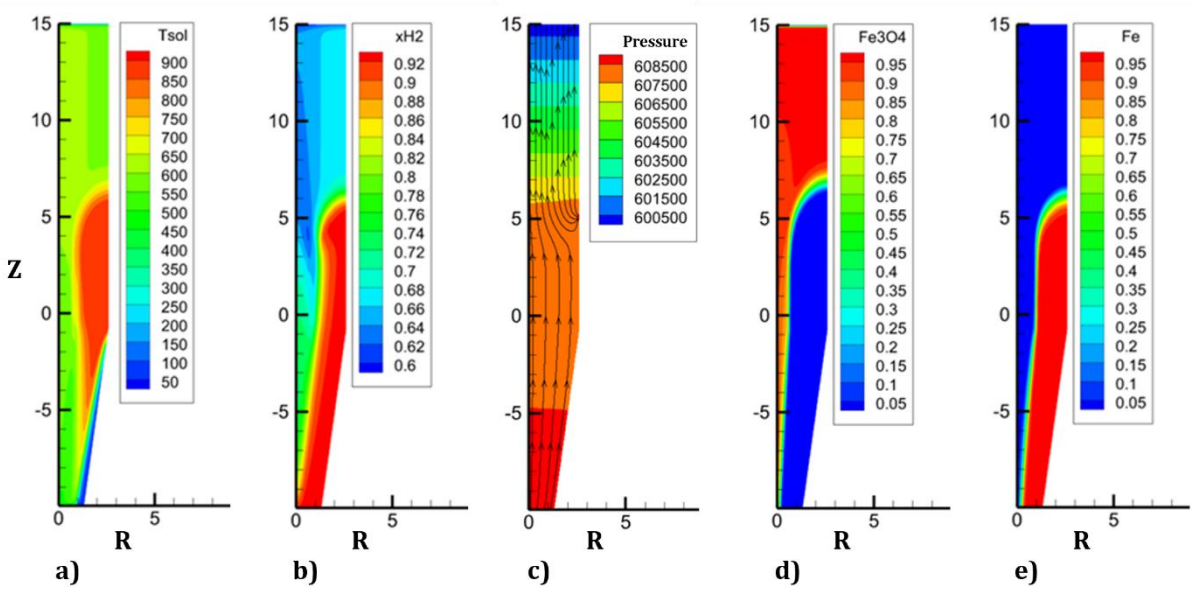

Figure 64: Distribution of process variables for the operation of a high-pressure high- production H_2-DRSF. *W* = 50 kg/s, *P* = 6 bar, *M* = 91.01%.

The increase in the top gas pressure led to a decrease in the pressure drop within the shaft, from 0.32 bar to 0.08 bar, see Figure 61c) and Figure 64c). It also entailed a moderate increase in metallization, from 90% to 91%. As seen in Figure 65, the reaction rates in this simulation were often twice as high as usual reaction rates, which is due to purely kinetic effects related to the increase in pressure. However, this tremendous increase in reaction rates did not result in

significant increase in the metallization, as could have been expected. This leads us to think that, in usual reactor conditions, the kinetics of H_2 reduction are not so significant at the scale of the whole furnace. Even with highly optimized kinetics, the metallization of the DRI and the furnace throughput are still ultimately limited by heat and reductant gas supply.

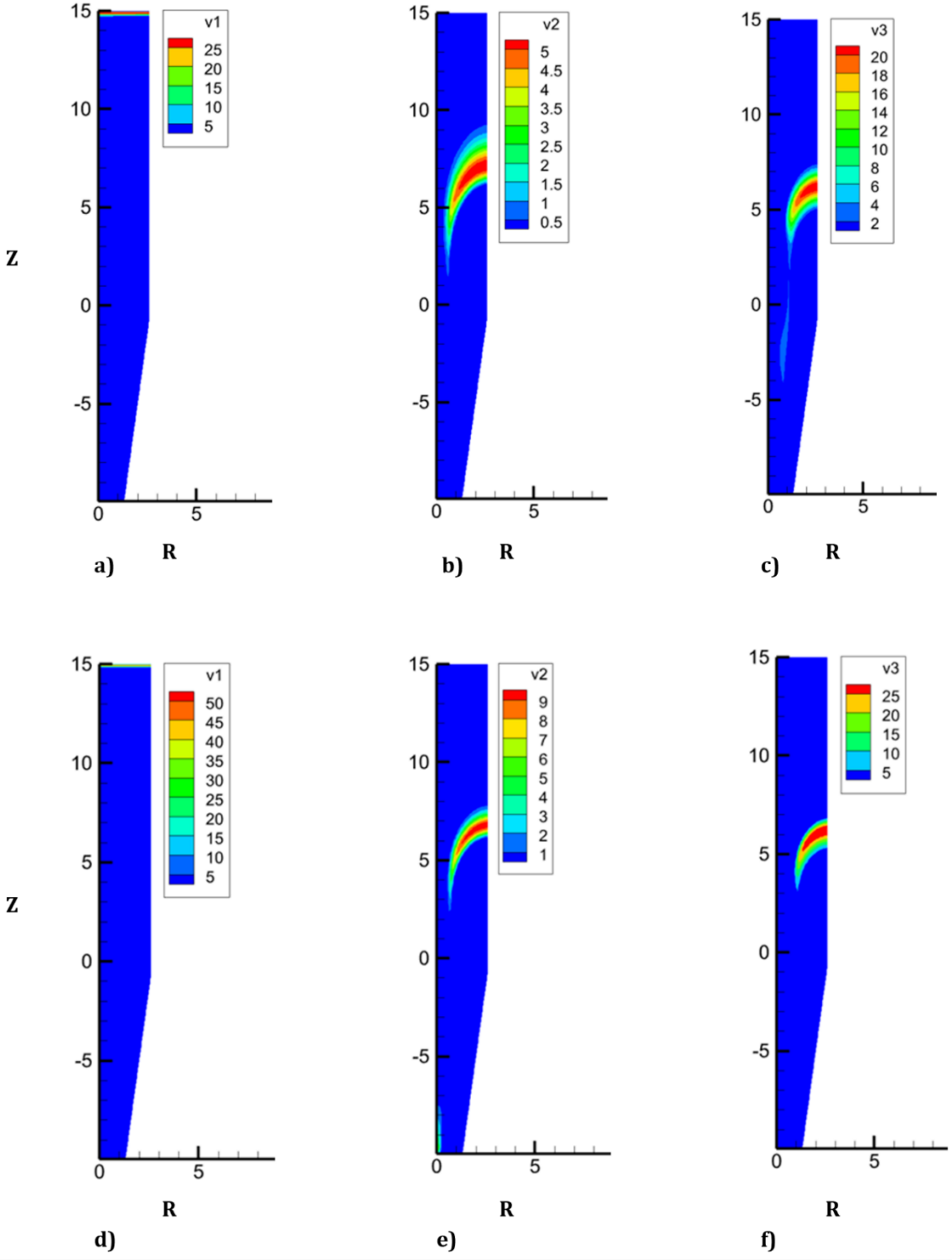

Figure 65: Reaction rates of reduction reactions in a high-production H_2-DRSF with 1.5 bar top gas pressure **a),b),c)** and 6 bar top gas pressure **d),e),f)**.

III.2.2.5. Effect of a Christmas tree type obstacle at the center of the furnace

An important number of MIDREX NG-DRSF are equipped with a so-called "Christmas tree" structure at the center of the furnace. This device, which measures around 5 m in height and which maximum radius can reach half of the furnace radius, is usually placed at the bottom of the reduction zone and extends deep inside the cooling zone. It helps regulate the solid flow and can also be equipped with gas injections, as previously mentioned.

In the present simulation, the mesh of the furnace was modified to account for a Christmas tree, the geometrical characteristics of which are shown in Figure 66. For the sake of simplicity and in the framework of a first attempt to model this configuration, the Mullins model used to describe the solid flow in the cooling zone was replaced here with a simple plug flow. Simulations with more complex solid flow models will be presented in chapter 4.

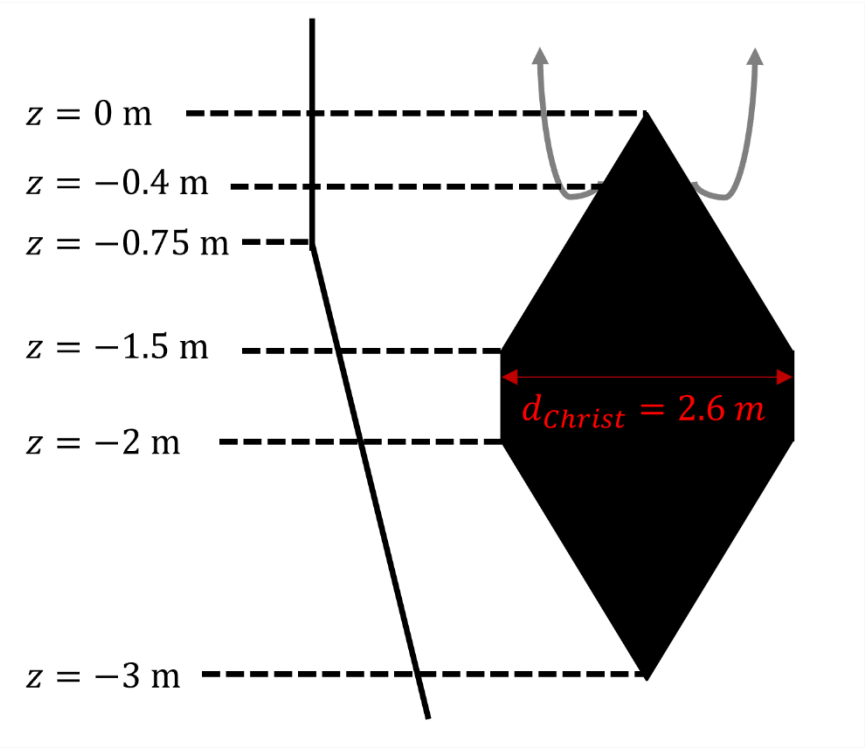

Figure 66: Geometry of the Christmas tree structure used in the simulations. Gas injections are located at – 0.4 m; the top of the hopper section of the furnace is located at – 0.75 m; the diameter of the cylindrical section of the Christmas tree is 2.6 m.

This simulation was run to have first guess of the effects of this obstacle on the distribution of temperature and species within the shaft, see Figure 67. The presence of the obstacle did not result in a significant homogenization of the temperature nor of the species in the cooling zone, as could have been expected. As a consequence, the metallization was only slightly increased with this configuration, and it reached 90.7%. The pressure distribution was hardly modified by this new geometry.

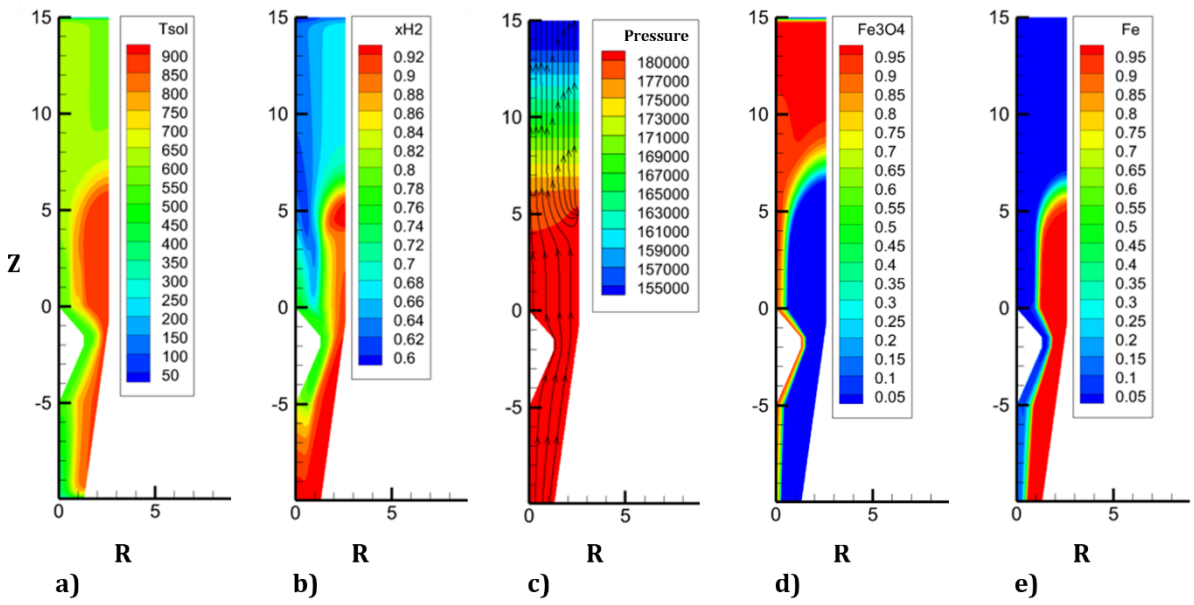

Figure 67: Distribution of process variables for the operation of a shaft furnace equipped with a Christmas tree type obstacle at the furnace center. W = 50 kg/s, M = 90.7%.

III.2.2.6. Effect of a Christmas tree type obstacle at the center of the furnace with an additional gas injection

To test the potential of dual-gas injection with this configuration, a part of the bustle gas (approximately 20%) was redirected towards a new gas injection located on the upper part of the Christmas tree as shown in Figure 68, with the updated mass and energy flows.

This new configuration led to a dramatic modification of the temperature and species distribution inside the furnace, as seen in Figure 69. The hydrogen content of the gas and the temperature were found to be quite low, except at the gas inlets, in comparison to case A3. Such features point out great gas and heat utilization, which directly entailed a considerable increase in metallization, plus 6% in comparison to case A3. It is also to be noticed that in this new configuration, the zone with the lowest metallization degree was not located at the center of the shaft anymore, but rather halfway between the wall and the center of the furnace (Figure 69d). Further calculations may be conducted to find out which optimal partition of the flow rate between bustle and Christmas tree would offer the best metallization.

III.2.2.7. Conclusion

A new series of simulations were carried out to investigate the role of pressure, kinetics, and geometry in a pure hydrogen shaft furnace. It was shown that the impact of great kinetics or high pressure on metallization was limited due to pre-existing heat supply issues: raising the pressure from 1.5 bar to 6 bar only led to a minor improvement in the metallization degree, from 90% to 91%. Moreover, the introduction of a Christmas tree type obstacle at the center of the furnace did not entail any significant homogenization of the temperature nor species distributions and consequently hardly affected the metallization. Conversely, redirecting part of the bustle gas to an additional gas injection located on this Christmas tree made a better heat utilization possible and directly affected the metallization. The redirection of 20% of the gas flowrate from the bustle to the Christmas tree resulted in a surge in the metallization, from 90.7% to 96%.

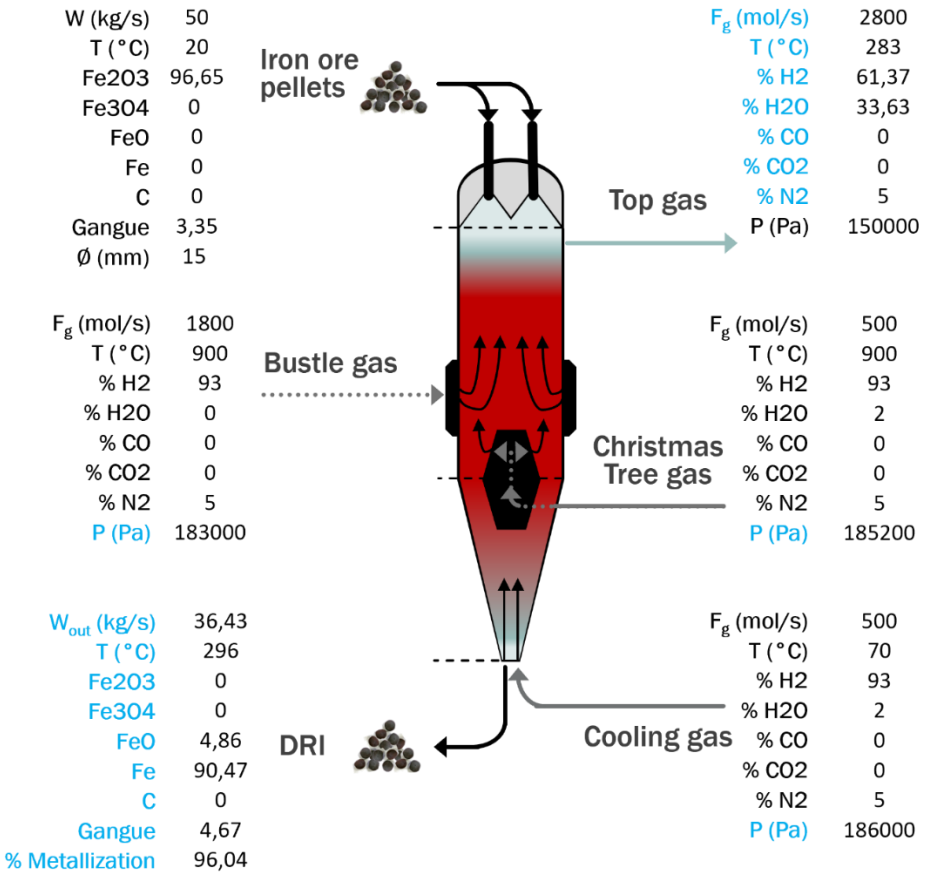

Figure 68: Mass and energy flowchart for a H_2-DRSF with an additional gas injection located on the Christmas tree structure. Output data are highlighted in light blue.

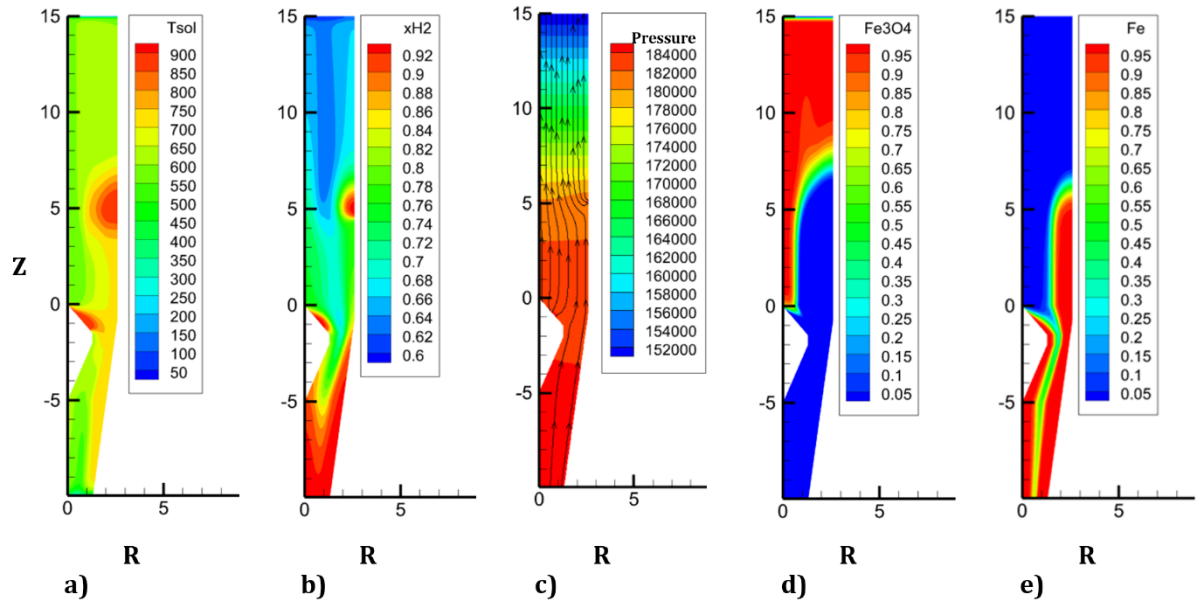

Figure 69: Distribution of process variables for the operation of a shaft furnace equipped with a Christmas tree type obstacle and a gas injection. W = 50 kg/s, M = 96%.

III.3. Hydrogen enrichment of a NG shaft furnace

The reduction of iron ore pellets in a H_2-DRSF results in no direct carbon emissions, which is a huge advantage in comparison to NG-DRSF. However, no industrial DRSF plant has ever run purely on hydrogen yet. To ensure the feasibility of the transition from natural gas to pure hydrogen, the progressive hydrogen enrichment of DRSF is studied in depth in the MaxH2DR project. The reduction of iron ore pellets in gas mixtures made of H_2 and CO were experimentally studied by other members of the project at laboratory scale. The following gas compositions were chosen based on the idea of progressive enrichment: 55% H_2 and 45% CO, 80% H_2 and 20% CO, and 100% H_2 (case A of Article 3).

In this section, we simulated the operation of a NG-DRSF with the abovementioned gas compositions. Due to the impressive heat supply provided by the reduction of a part of the burden with CO, we decided to adjust the throughput in each simulation to keep a constant metallization target close to 94%. Thus, compared with the previous section, all parameters were kept unchanged except for the gas composition and the inlet solid flowrate.

III.3.1. H_2-enrichment of a shaft furnace in the standard geometry

Case 1 - 55% H_2, 45% CO

In a first simulation, the behavior of a furnace running on 55% H_2 and 45% CO with an inlet solid flowrate of 70 kg/s H_2 was investigated. In a NG-DRSF, the introduction of a bustle gas with a H_2:CO ratio close to 1 offers excellent heat supply. Indeed, as seen in Figure 70, the solid temperature was kept at bustle value all along the furnace height, except at the top and bottom inlets. Here, the depletion of both H_2 and CO happened primarily at the center of the furnace, due to a poor penetration of the burden by the gas. At the wall, the reduction of FeO to Fe extended over 3 m in height due to the slow kinetics of CO reduction. Overall, the furnace worked extremely well, as it was able to process 70 kg/s of iron ore with a 93.2% metallization, and as it showed impressive gas utilization degrees (Y_{H_2} = 0.477, Y_{CO} = 0.502).

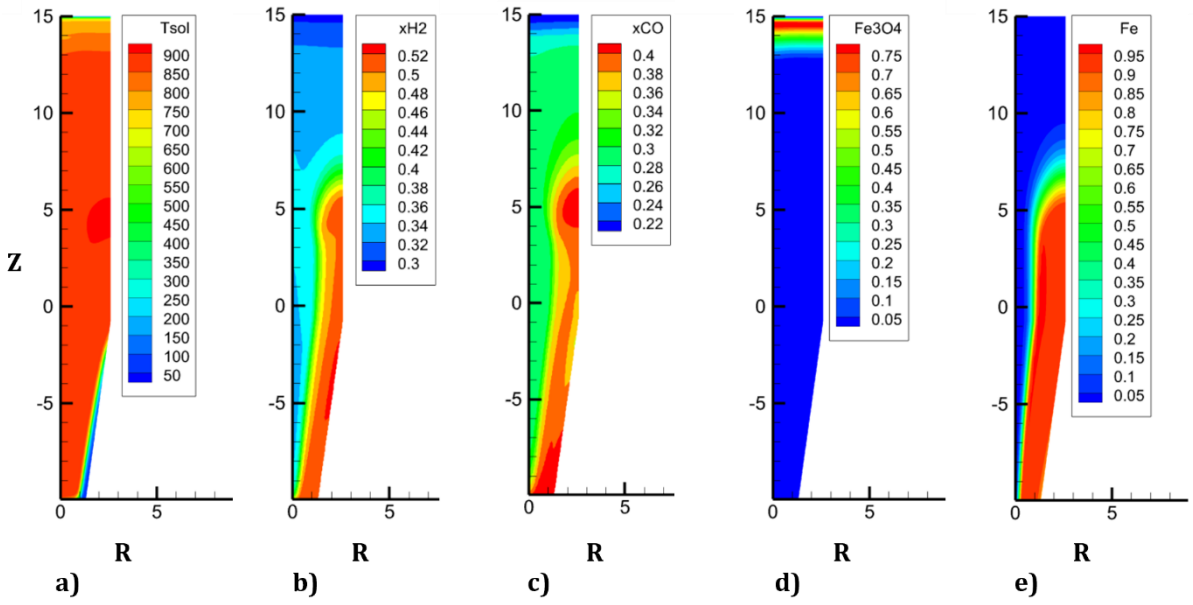

Figure 70: Distribution of process variables for the operation of a shaft furnace running on H_2:CO = 55:45. W = 70 kg/s, M = 93.2%.

Case 2 - 80% H_2, 20% CO

In a second simulation, the gas composition was 80% H_2 and 20% CO while the inlet solid flowrate was set at W = 63 kg/s. The simulated shaft furnace running on this intermediate gas composition showed good thermal and reductant supply, see Figure 71. Here, the magnetite conversion took place on a large portion of the height of the shaft furnace owing to low temperature and low concentration of reductants in this zone. Conversely, at the wall, the higher hydrogen concentration enabled a faster conversion of wustite to iron, which spanned over 2 m in height. Below the bustle, temperature remained radially uniform between +5 m and 0 m. This allowed us a steady reduction of the iron ore burden, which resulted in a high metallization of 94%. It is worth noting that the thermal role of CO at high H_2:CO ratios is much more crucial than at low H_2:CO ratios. Indeed, CO acts as the heat supplier at the center of the furnace – if the heat supply becomes scarce, the reduction reactions with CO will be favored. This is seen in the present simulation, which showed a high CO utilization degree (Y_{CO} = 0.567) and a rather moderate H_2 utilization degree (Y_{H_2} = 0.410) compared with case 1.

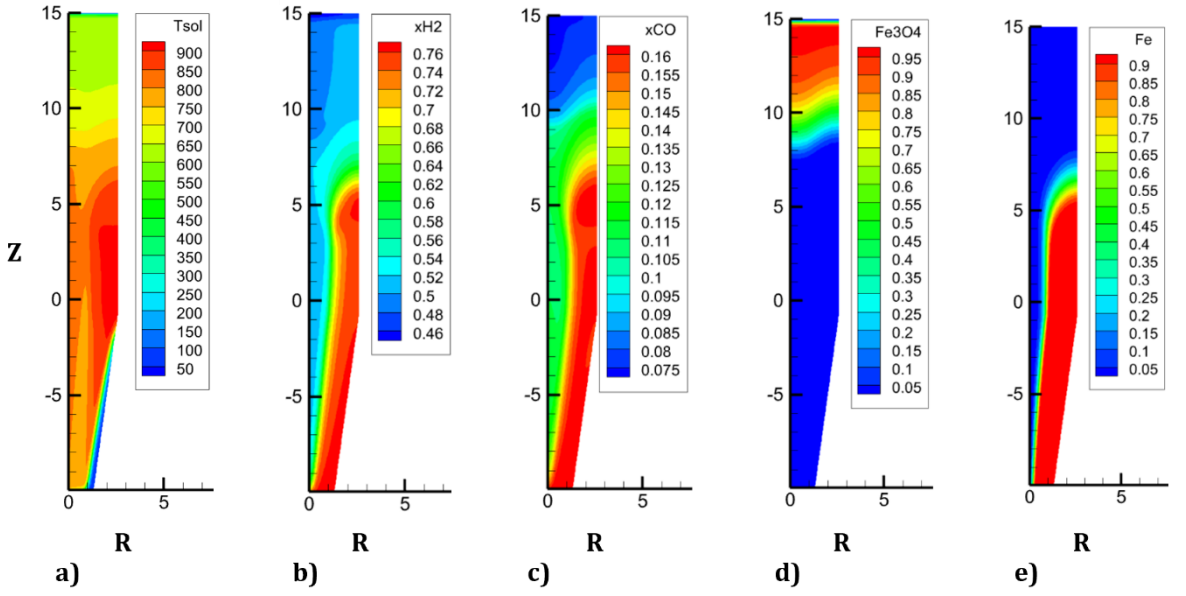

Figure 71: Distribution of process variables for the operation of a shaft furnace running on H_2:CO = 80:20. W = 63 kg/s, M = 94.4%.

Role of CO and H_2 in syngas-based shaft furnaces

As seen in the previous section, the gas utilization degree is a convenient indicator of the role played by each gas in the furnace, and usually its value differs between H_2 and CO. This difference is primarily due to two factors: the better reducing capacities of H_2, and the reaction of CO through the WGSR.

In a NG-DRSF, CO is systematically less used than H_2 during the reduction of the oxides, see Table 18. This is due to the high reaction rate of the reduction with hydrogen. However, a large portion of the available CO reacts through WGSR to produce H_2 (11% in case 1, 17% in case 2). Indeed, the WGSR is favored by low temperature and catalyzed by iron oxides, conditions which were met in both cases at the top of the furnace.

Table 18: Role of CO and H_2 in the reduction of the successive iron oxides in a NG-DRSF.

	Case 1- 55% H_2, 45% CO	*Case 2- 80% H_2, 20% CO*
Part of the hematite reduced by CO (%)	20%	< 1%
Part of the magnetite reduced by CO (%)	32%	12%
Part of the wustite reduced by CO (%)	37%	17%
Part of CO involved in WGSR	11%	17%

In both cases, the carbon deposition was found to be limited. Indeed, carbon deposition only happens in zones where iron and CO are present and at moderate temperatures. These conditions were barely met in these simulations, as the cooling gas flowrate was not large enough to properly cool the iron burden in the hopper section of the furnace.

III.3.2. Benefits of the Christmas tree

As shown in subsection 2.2.6, the introduction of a Christmas tree structure equipped with an additional gas injection offers great benefits for the temperature and gas distributions in a pure hydrogen shaft furnace. In the following simulations, we quantified the benefits of this configuration for a furnace running on the H_2:CO gas mixtures presented above.

As shown in Figure 72, the Christmas tree geometry resulted in efficient distribution of temperature, CO and H_2 in the case where H_2:CO = 55:45. The DRI presented incomplete metallization at the outlet (M = 94.7%), owing to the severe depletion of each reductant gas halfway between the wall and the center of the furnace, albeit the temperature was high everywhere in the furnace.

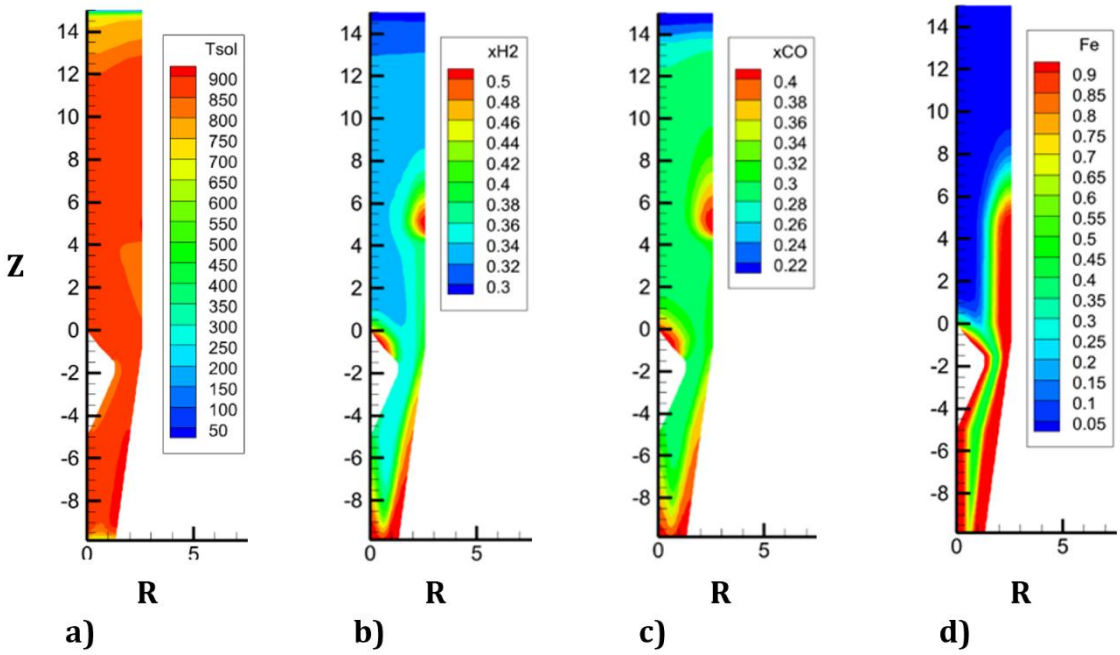

Figure 72: Distribution of process variables for the operation of a shaft furnace equipped with a Christmas tree type obstacle and an additional gas injection. W = 70 kg/s, M = 94.7%, H_2:CO = 55:45.

The same conclusions can be applied to the case where H_2:CO = 80:20, although the metallization was much higher (M = 99.7%), see Figure 73. This is due to a particular efficient distribution of temperature and reductant gases in this case.

In comparison to analogous simulations without Christmas tree, these simulations showed that the depletion of the reductant gases was the main limiting factor for metallization at low H_2:CO ratio (55:45), while the depletion of heat was also of major importance with a high H_2:CO ratio (80:20). Actually, the benefit of the Christmas tree is to offer a better homogenization of the temperature and gas distributions. As a consequence, when the temperature is already uniform without a Christmas tree, which was the case when H_2:CO = 55:45, this benefit is less pronounced. This is explicit when comparing the metallization between cases with or without Christmas tree, see Table 19. When shifting from a geometry to the other, the metallization degree jumped from 90% to 96% in the case of pure H_2; comparatively, the metallization only increased from 93.2% to 94.4% in the case where H_2:CO = 55:45. For the intermediate case where H_2:CO = 80:20, the metallization made a significant increase from 94.4% to 99.7%. From these results we can conclude that the higher the hydrogen content, the better the Christmas tree potential is valorized.

Table 19: Metallization and solid flowrates obtained with different gas mixtures with and without Christmas tree.

	Pure H_2	H_2:CO = 80:20	H_2:CO = 55:45
Without Christmas tree	W = 50 kg/s M = 90%	W = 63 kg/s M = 94.4%	W = 70 kg/s M = 93.2%
With Christmas tree	W = 50 kg/s M = 96%	W = 63 kg/s M = 99.7%	W = 70 kg/s M = 94.7%

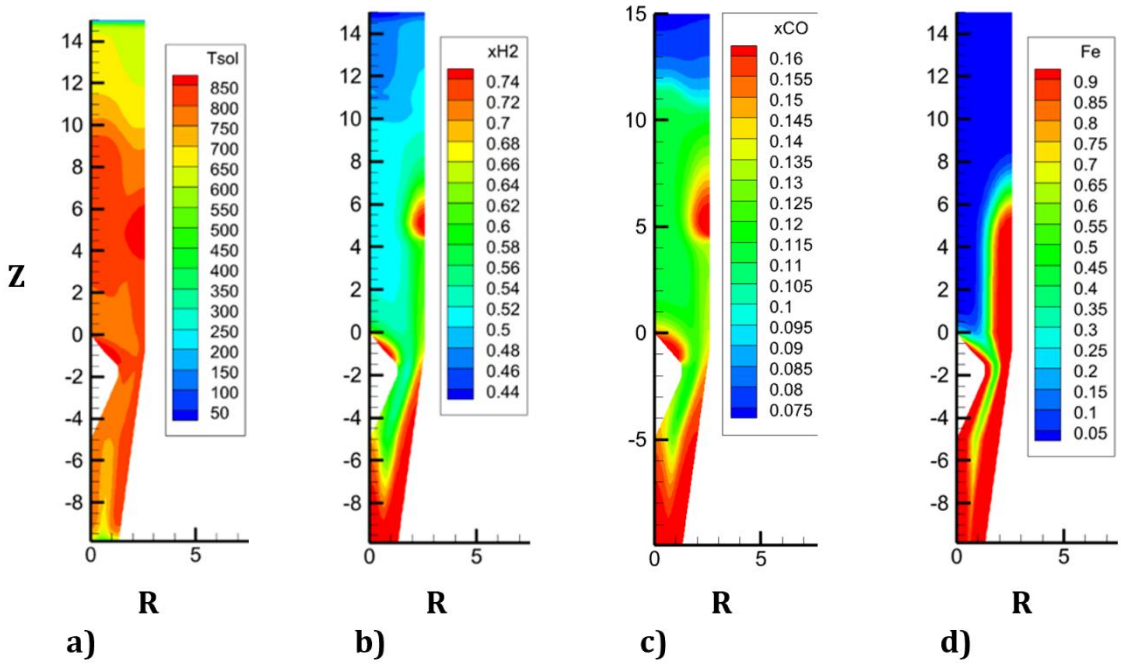

Figure 73: Distribution of process variables for the operation of a shaft furnace equipped with a Christmas tree type obstacle and a gas injection. W = 63 kg/s, M = 99.7%, H_2:CO = 80:20.

III.3.3. Energy demand and CO_2 emissions of H_2- and NG-based shaft furnaces

The energy demand for the operation of a H_2-DRSF was evaluated in Article 3. It was shown that more than 80% of the global energy demand of the furnace was due to the production of green hydrogen through electrolysis. With zero-carbon electricity as the sole energy supply source, the process was shown to virtually emit 0 t_{CO2}/t_{DRI}.

In a NG-DRSF plant, natural gas is used as a reactant in the reforming unit, but it is also used as a fuel in the burners to heat the reforming unit. At the top of the shaft furnace, a portion of the off-gas is recycled, while the rest of the off-gas is used as additional fuel in the burners. Typically, around 65% of the off-gas is recycled in the reforming unit [15, 128]. The flue gas exiting the burners is used to preheat the fuel gas entering the burners, which is the mixture of the off-gas and natural gas.

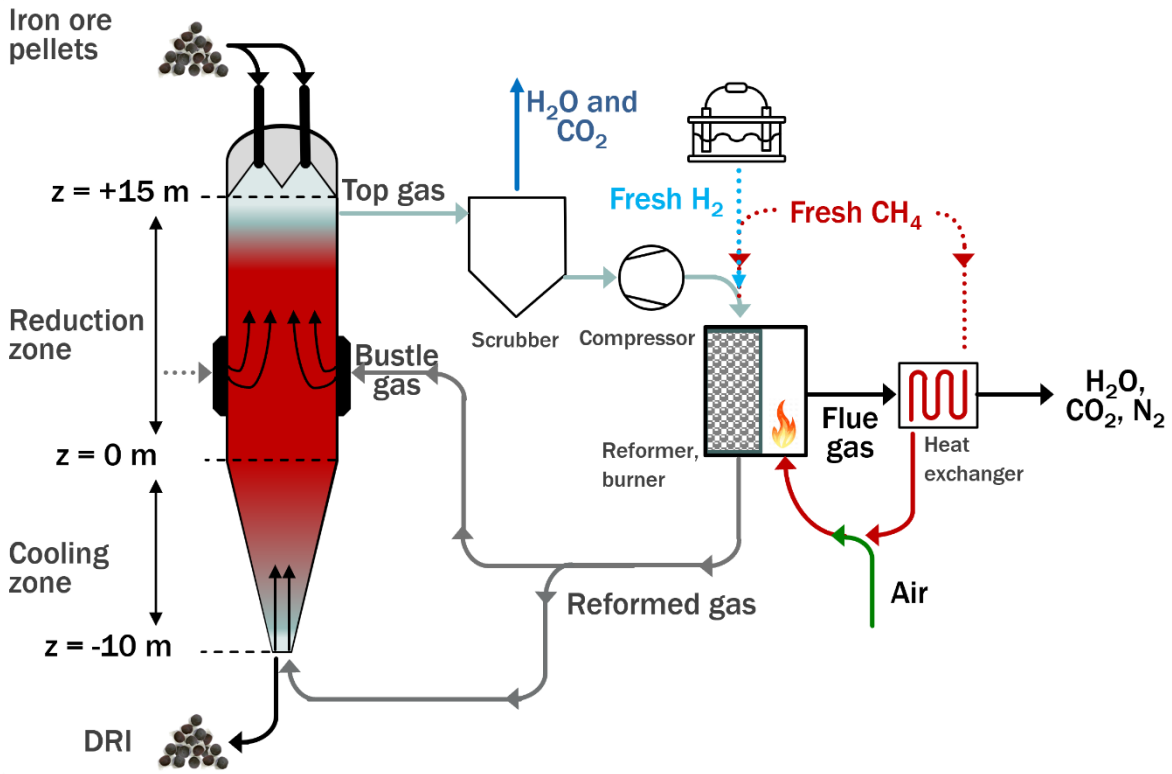

Figure 74: Schematic view of a simplified NG-DRSF plant. For simplification, it is assumed that the part of the CO_2 which is not recycled in the reformer (when considering dry reforming of natural gas) is evacuated in the scrubber.

In the following, a simplified NG-DRSF (without Christmas tree) plant model was developed to evaluate its energy demand and CO_2 emissions. For the sake of simplicity, it was considered that the entirety of the off-gas was recycled in the reforming unit. It was also assumed that methane was processed through dry reforming in case 1 (H_2:CO = 55:45) and steam reforming in case 2 (H_2:CO = 80:20). To reach the targeted gas compositions, it was necessary to add pure H_2, from an electrolysis unit, in the mix. A schematic view of the process is represented in Figure 74, and the modeling assumptions are listed below:

- only portions of CO_2 and H_2O were kept after scrubbing the top gas, as these gases were necessary in the reforming unit. The exit temperature of the scrubber was set to $T_{scrubber} = 53°C$ [29]. The energy demand for compression was given by:

$$dE_{comp} = n * R * T * \ln\left(\frac{P_{comp}}{P}\right) \quad (63)$$

- as explained earlier, two separate quantities of natural gas are needed to run the reforming unit (NG1 and NG2). A first quantity of natural gas (NG1) was used in the reforming unit to replenish the CO content of the gas. A supplementary quantity of pure fresh H_2 (FH_2) was then supplied to reach the targeted bustle composition. Considering the stoichiometry of Reactions 10 and 11, simple molar balance gives:

$$NG1 = n_{bustle}\left(x_{\mathrm{CO},bustle} - x_{\mathrm{CO},top}\right)$$

for steam reforming (64)

$$NG1 = \frac{1}{2} n_{bustle}\left(x_{\mathrm{CO},bustle} - x_{\mathrm{CO},top}\right) \quad (65)$$

for dry reforming

$$FH_2 = n_{bustle}\left(x_{\mathrm{H_2},bustle} - x_{\mathrm{H_2},top}\right) - 3\,NG1 \quad (66)$$

for steam reforming

$$FH_2 = n_{bustle}\left(x_{\mathrm{H_2},bustle} - x_{\mathrm{H_2},top}\right) - 2\,NG1 \quad (67)$$

for dry reforming

- a second quantity of natural gas (NG2) was used as fuel gas for heating and reforming the process gas, which was the mixture of NG1, FH_2 and off-gas. The reforming reactions were assumed to take place at 900°C. The heating of the process gas was assumed to have an efficiency $e_{heating}$=0.7. A small calculation loop was implemented to iteratively calculate NG2, as this quantity appeared in both gas heating and heat exchange equations. Indeed, there was heat exchange when the flue gas exiting the burners was used to preheat the fuel gas entering the burners, see Figure 74. The parameters used to describe the heat exchanger were presented in Article 3 and are not recalled here.

The inlet parameters were chosen similar to case A, case 1 and case 2. The results are presented in Table 20. From this table, we can see that a major increase in throughput, gas utilization degree, and a decrease in energy demand were obtained when using H_2:CO = 80:20 instead of pure H_2. (Note that the global energy demand figures of Cases 2 and 3 should actually be higher than calculated here, since the upstream energy demand associated to the natural gas supply was not included). On the contrary, the transition from H_2:CO = 80:20 to H_2:CO = 55:45 only brought moderate improvements for each of the indicator listed before, at the cost of a 50% increase in the associated CO_2 emissions. Moreover, it should be kept in mind that the addition of a Christmas tree would show even more beneficial figures for the DRSF running on H_2:CO = 80:20, see subsection 3.2.

Table 20: Primary energy demand and process emissions related to each process simulated.

	Case A 100% H_2	Case 2 80% H_2, 20% CO	Case 1 55% H_2, 45% CO
Throughput (kg_{pellet}/s at the top inlet)	45	63	70
Metallization (%)	93.3	94.4	93.2
Global gas utilization degree	0.33	0.44	0.49
Top gas temperature (°C)	344*	272	340
Compression energy (GJ/t_{DRI})	0.25	0.07	0.08
Heating and reforming energy (GJ/t_{DRI})	2.28	2.81	2.78
Electrolysis energy (GJ/t_{DRI})	9.73	0.81	0.73
Global energy demand (GJ/t_{DRI})	12.26	3.69	3.59
Direct carbon emissions (t_{CO2}/t_{DRI})	0	0.29	0.45

(*) In this simulation, the top gas temperature was calculated with the previous boundary conditions, as explained earlier, and its value would be a bit lower with the new boundary conditions.

It is then clear that the transition to a pure hydrogen shaft furnace is technically feasible. Such a furnace could enable a high production at virtually zero carbon emissions. On the short run, a transition to an enriched H_2-DRSF (case 2) could already significantly decrease the carbon emissions of the plant at low cost. On the long run however, only the use of 100% green hydrogen can make the transition to carbon-neutral ironmaking a reality.

III.4. Conclusion

In this chapter, the behavior of a shaft furnace with high hydrogen content was numerically investigated with the finite-volume code REDUCTOR. The results presented in Article 3 showed that the energy consumption of a H_2-DRSF could be decreased by three different solutions: the redirection of a portion of the bustle gas to a cooling gas inlet, the operation at high temperature (950°C) and high nitrogen content (32% vol), and the introduction of hot pellets (1200°C) in the furnace. It was also observed that full metallization was possible with a reasonable increase in the energy consumption (+6.4%). Further results demonstrated the relatively minor importance of pressure on the metallization, which is rather limited by heat supply than by kinetics. Moreover, the injection of a portion of the bustle gas at the center of the furnace enabled an increase in metallization owing to a better distribution of the heat supply.

The exothermic reduction reactions with CO help solving the heat supply issue. In this regard, the operation of a shaft furnace at lower H_2:CO ratios showed increased production and gas utilization degree, though at the cost of increased CO_2 emissions. As the H_2:CO ratio of the gas is lowered, the metallization becomes progressively limited by reductant gas supply rather than heat supply.

As seen in this chapter, the models used to describe the flow of pellets in a shaft furnace are usually fairly simple (plug flow model, kinematic model). While they give reasonable estimates of the discharge flowrate, they are unable to describe the local properties of the solid flow. In the next chapter of this manuscript, a continuum rheology model is presented with the intent to properly describe the flow of pellets in a shaft furnace.

IV. Solid flow patterns in a direct reduction shaft furnace

IV.1. Introduction

The efficient operation of the moving-bed iron ore reduction units (blast furnaces, shaft furnaces) critically depends on the uniform and continuous descent of the burden, often referred to as mass flow (see Figure 75). In a shaft furnace, the mixture of pellets and/or lump ore is subject to heavy mechanical stress caused by gravity, inter-particle friction and confinement between the walls of the furnace. Locally, the pellets can be subject to breaking, degradation or sticking with other pellets. On a larger scale, clusters of pellets may form and clog the outlet, or a channel may develop at the center of the furnace while stagnant zones appear at the walls. Thus, the ability to understand and predict the flow behavior of these materials is essential to ensure safe and continuous operation of the furnaces.

Geometrically, a shaft furnace is a cylinder sitting on top of a conical hopper, sometimes equipped with additional structures inside the furnace (such as a Christmas tree structure). This silo-type geometry led many researchers to draw a parallel between the study of shaft furnaces and the study of the classical silo discharge. The analytical approaches made significant progress during the 20th century. The stress distribution correlations proposed by Janssen, Jenike and others long ago are still used nowadays for the design of industrials silos [160]. In parallel, numerous numerical resolution methods were developed more recently to predict the stress and velocity distributions in all sorts of granular flow geometries, including the granular silo. These methods and the major results that stem from their development are presented in the following paragraphs.

Discrete approaches

A natural approach to handle granular matter is to treat each granule as an individual piece of the system, as it is done in the Discrete Element Methods (DEM). The strength of DEM lies in the simplicity of its formulation and in its enormous potential for engineering application [161]. This extensive method describes the forces and torques acting on each interacting particle in non-cohesive models. Supplementary non-contact forces are also considered in cohesive models, and particularly the wet particle forces. DEM has proven its ability to simulate all sorts of engineering problems, such as the determination of flow patterns, angle of repose, or local granular structure. In gas-solid systems, DEM can be coupled with CFD for the description of the gas phase (CFD-DEM), allowing efficient simulation of industrial reactors.

DEM simulations of the flow of iron ore pellets in a H_2-DRSF rely on the accurate determination of friction parameters. This issue is a major field of research, and is precisely one of the research objectives of the MaxH2DR project, see e.g. [124, 162]. The coupled CFD-DEM simulation of industrial shaft furnaces was recently demonstrated with great success [121, 122]. In the literature, major interest is found for the issue of wall angle and diverter shape, the design of which is studied to optimize the burden descent inside the shaft. The influence of the hopper half angle (noted α in Figure 77 below) on the discharge properties was studied by varying either the height of the hopper or its outlet diameter, in the presence of a flow diversion cone [163]. It was notably shown that for each configuration (i.e., constant height or constant outlet diameter), there exists a critical value of the wall angle above which the flow pattern transitions towards funnel flow, that is a non-uniform flow characterized by the presence of a high velocity channel and low-velocity stagnant zones (Figure 75). In another study, the influence of the shape of the diversion

cone on the flowing properties was studied at constant height and constant outlet diameter [164]. As shown in Figure 76, the standard shaft geometry with no diversion cone (case 1) leads to an important radial gradient of residence time in the hopper section. This results in a highly non-uniform descent of the burden which is not practical for industrial applications. Conversely, it is shown that the presence of a diversion cone with an arbitrary shape is not sufficient to ensure the disappearance of stagnant zones: the lower portion of the diversion cone must be tall enough to ensure that no stagnant zone will form at the center of the furnace, as shown in case 6.

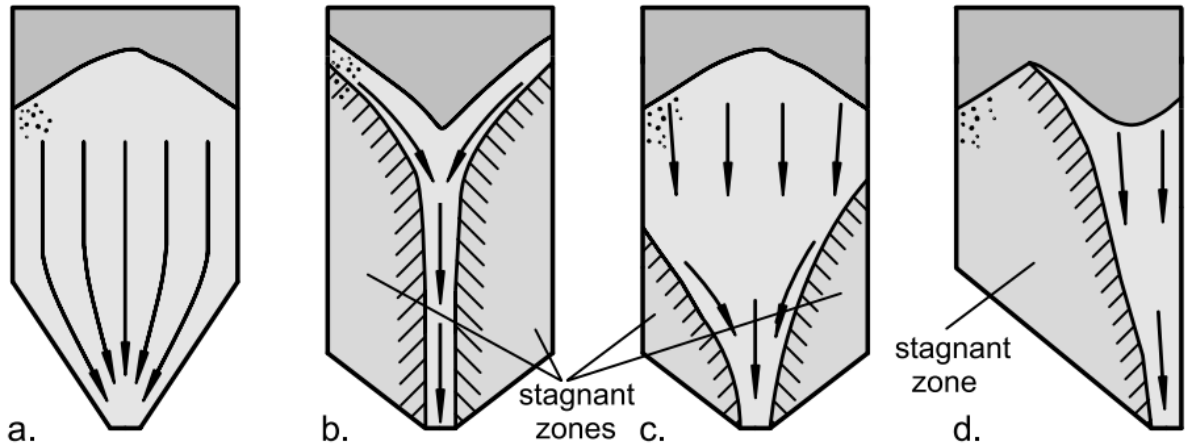

Figure 75: Representation of the different flow profiles observed in a discharging silo: **a.** mass flow; **b.** funnel flow; **c.** mixed flow; **d.** eccentric pipe flow [160].

Compared with continuum methods, DEM is thought to improve the range of situations that can be properly simulated, such as the reduction degradation and clustering phenomena [122]. A clear example of these new capabilities is a recent study on the wear behavior of loose rollers in a shaft furnace [165], where a quantitative estimate of the wear of the rollers was estimated at 0.6 mm per month. However, the calculation needs of these methods are extremely costly and modeling actual engineering systems remains generally infeasible, if not totally impossible [161]. Thus, approximations have to be made in actual studies to speed up the calculations. For instance, in a recent study, the pellet diameter was multiplied by 4, the discharge velocity was largely accelerated and the cylindrical geometry was replaced by a plane geometry slice, 60 cm wide [164]. Likewise, the work presented in [122] only considers a 15° wide radial slice of the cylindrical section of the furnace, thus limiting the ability to have an in-depth study of the flow patterns in such a configuration.

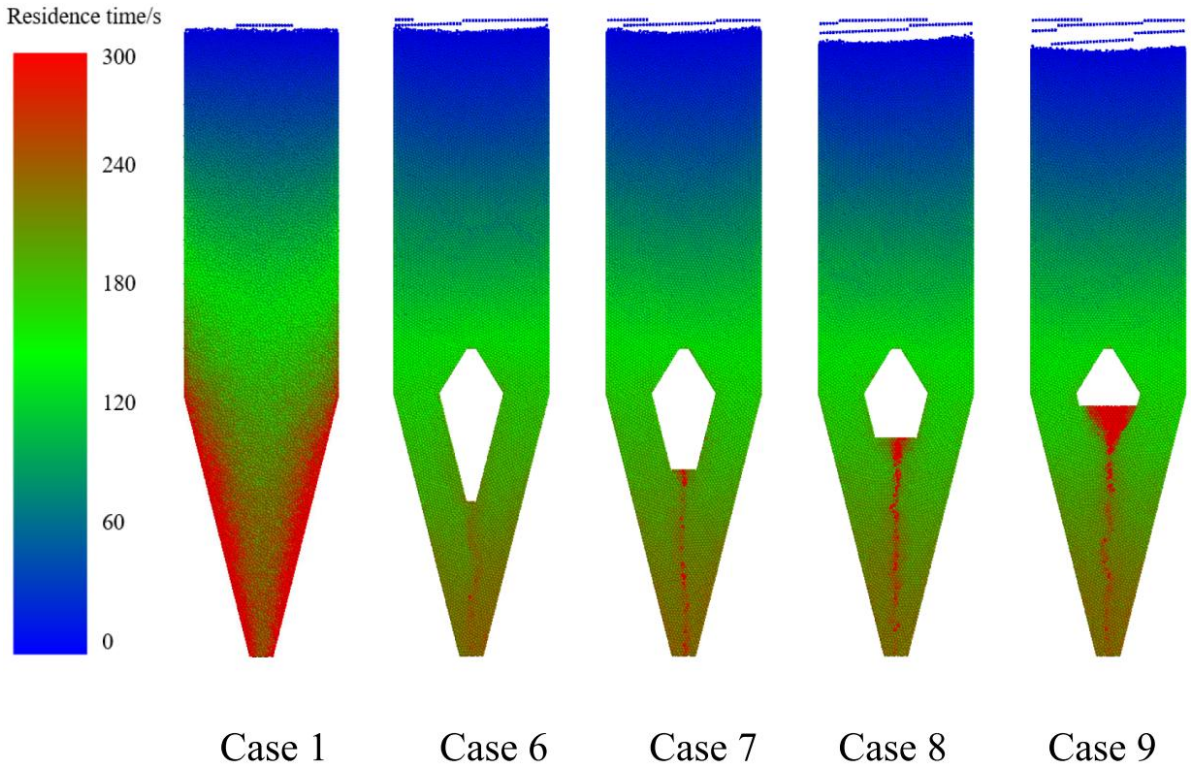

Figure 76: Distribution of particle residence time in a shaft furnace with different types of flow diverter [164]. The residence time is given in s – indeed, the velocities are artificially increased compared with a real shaft furnace to help with the high cost of DEM computation.

Continuum approaches

Another approach to granular materials is to consider the bulk of the solid rather than each individual granule, and to rely on the continuum mechanics framework. Depending on the conditions, the granular flow can either behave as a solid, a liquid, or a gas, so that a general theory of granular matter is hard to establish [166]. Thus, distinct continuum theories were developed for each regime, such as the granular temperature model at extremely low densities [167], the $\mu(I)$ rheological model in dense-flowing regimes (see e.g., Jop et al., 2006)), and the elasto-plastic model for the quasi static regime [168]. Recently, many solid-liquid bridging theories were proposed to "bridge the gap" between elastoplastic methods and modified Navier Stokes methods [166, 169], that is between quasi-static and dense-flowing regimes. Different pressure and shear rate distributions were shown between the two approaches for the flow of granular matter in a flat bottomed silo [170] ; these differences are attributed to intrinsic modeling differences (such as the absence of elasticity in the modified Navier Stokes methods). A model incorporating a solid-fluid bridging theory has proven successful in the simulation of blast furnace operation [171]. It was notably able to capture the different flow regimes (in the plugging and converging zones), as well as the deadman (the stagnant zone at the bottom center of the furnace).

This chapter presents an exploratory investigation of the granular flow dynamics of pellets inside a shaft furnace. A state-of-the-art review for the classical silo discharge and for the flow of granular material is presented, considering the major results in analytical and continuum approaches. Then, a modified model based on the $\mu(I)$ rheology is presented and implemented into the REDUCTOR code, with the intent to replace the plug flow and kinematic models used in previous studies. The first results of this model are then presented and compared with results from previous models, DEM simulations and experiments.

IV.2. State of the art on the continuum modeling of granular flow in moving bed systems

IV.2.1. Analytical aspects of the silo discharge

As mentioned earlier, the flow of granular materials inside a silo is a tough problem due to the complex interactions among the granules, and between the granules and the walls. An overview of the different silo geometries encountered in the industry is presented in Figure 77. For many of these geometries, analytical correlations have been proposed to estimate the distribution of stresses, velocities, as well as the discharge rate. However, these correlations often suffer from discrepancies due to the important number of fitting parameters that they rely on [172]. Even in the case of a simple configuration, like the conical silo, the following problems arise:

- the granular matter is often simplified as a pile of layers with uniform distribution of lateral stresses, which is far from reality;
- the uncertainty associated with surface imperfections on the walls leads to inaccurate estimates of the friction between the wall and the granular material;
- there is a clear discontinuity of stresses between filling and discharging operations which is caused by the opening of the bottom solid outlet.

As a result, the prediction differences between different models are quantitatively less important than errors in the measurements, so that it is difficult to validate one over the others [172]. However, these models can help to get a qualitative idea of the flow regimes, state of stresses, distribution of velocities and discharge rate of the silo.

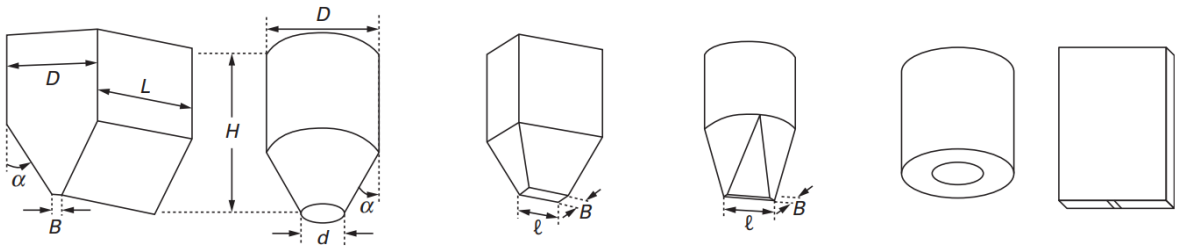

Figure 77: Overview of silo shapes encountered in the industry. From left to right: triangular, conical, pyramidal, Chisel, flat-bottomed and 2D silo geometry [172].

Flow modes in a silo

A priori, there is no certainty that opening the discharge feeder of a silo will result in a steady descent of the granular burden. As mentioned earlier, a number of complications may prevent the bulk of the solid from flowing: arching, interlocking of particles, formation of stagnant zones... However, with appropriate design, the granular matter is expected to flow under two distinct regimes, funnel flow or mass flow, as depicted in Figure 75. These different flow regimes result in different pressure and velocity distributions. Jenike established a mathematical criterion [173] to determine the regions of mass or funnel flow in a conical silo (Figure 78). It was found that the hopper half angle and the wall friction angle were two crucial parameters for determining the flow regime, as an increase in each of them promotes the funnel flow. In many situations, the Jenike criterion for mass flow is found to be quite satisfactory for predicting the flow regime [174].

To ensure a smooth and continuous operation, the industrial shaft furnaces are usually designed to avoid funnel flow. This is achieved by lowering the hopper half angle for the conical geometry.

Another way to maintain a smooth operation of the furnace is to lower the reduction temperature, to avoid sticking and clustering of the pellets. The use of flow helpers such as inverted cones, Christmas tree type structures and appropriate feeders at the discharge end favors a smooth discharge of the granular material [175]. In the following, we will mostly focus on situations of mass flow that enable a uniform descent of the burden. In the upper section of the furnace, this mass flow is equivalent to a plug flow. In the hopper section, the mass flow transitions into a converging flow with the highest axial velocities observed at the center of the furnace.

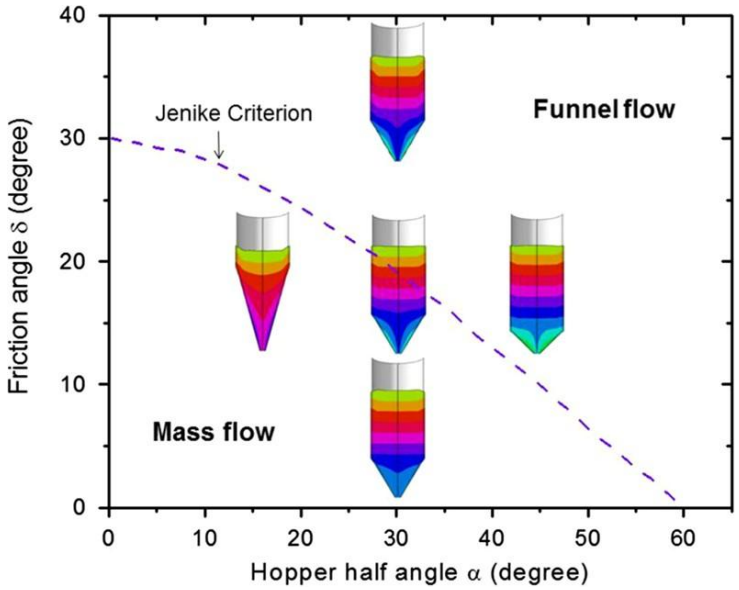

Figure 78: Jenike criterion for mass of funnel flow (dotted line) and FEM simulations of a discharging silo illustrating the different flow regimes [174].

Velocity distribution

In the mass flow regime, the axial velocity distribution in the upper section of the furnace is uniform. In the hopper section however, the flow of granular material cannot be described by the plug flow model. Numerous models have been proposed to calculate a velocity distribution that accounts for the converging hopper geometry. These models are all based on the assumption of radial flow, which states that the material flows towards the apex and that its velocity at a given point *M* is a function of the distance from the apex and the polar angle, see eq. (68) and Figure 79:

$$u_{\mathrm{M}} = -\frac{f(\theta)}{r^n} \tag{68}$$

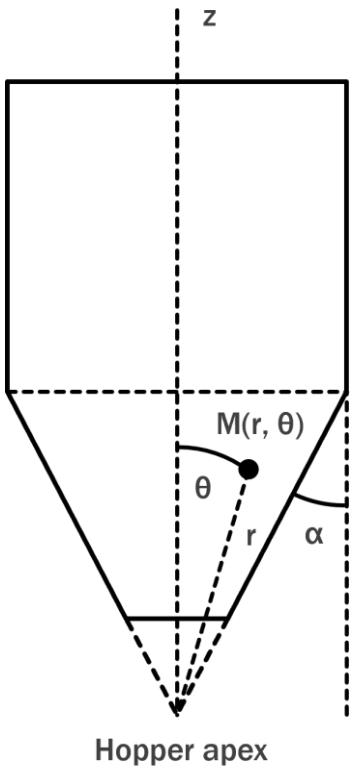

Figure 79: Representation of the conical silo in pseudo-spherical coordinates. Here, the velocity at any point $M(r, \theta)$ is evaluated on the basis of the distance from the apex r and the polar angle θ.

In eq. (68), n is related to the hopper geometry (if it is triangular, conical, etc.). This equation implies that the velocity increases as the solid reaches the outlet, which is what is observed experimentally, and $f(\theta)$ is a fitting function designed to reproduce the experimental velocity distributions. From energetic considerations and assuming a mass flow regime, Brown derived an expression of the velocity that depends purely on the hopper geometry and the discharge flow rate W_{out} (Brown, 1961):

$$f(\theta) = \frac{W_{out} cos(\theta)}{2^{\frac{1}{n}} \pi^{n-1} \int_0^{\alpha} \sqrt{cos(\theta)}\, sin^{n-1}(\theta) d\theta} \tag{69}$$

The resulting velocity distributions obtained from these radial models are more flat than what is observed experimentally [172]. The kinematic models introduced by Nedderman and Mullins have seen better agreement between experiments and predictions [152, 176]. These models are based on the assumption that a particle can only move down in a vacancy created by the descent of another particle right below. A simple mathematical relationship between radial and axial velocities is then derived (here, for a 2-D plane silo):

$$u_{\mathrm{x}} = -\mathrm{B} \frac{\partial u_{\mathrm{z}}}{\partial \mathrm{x}} \tag{70}$$

Multiple studies have shown that a reasonable approximation of B is given by $B = 2d_p$, where d_p is the diameter of the particles. This two dimensional kinematic model was applied to the descent of magnetite ore in a double-outlet shaft furnace, and it was qualitatively able to reproduce the solid flow pattern [177]. More recently, the kinematic model was implemented into REDUCTOR

to describe the converging flow of pellets in the hopper section of the shaft furnace, and the model was validated against industrial data [16].

Stress distribution

The first motivation to determine the stress distribution in a silo is to evaluate the pressure acting on the silo walls and to avoid a rupture of the silo. Moreover, the knowledge of the local stresses on the granular matter allows a finer description of the flow properties, particularly in the continuum mechanics approach. The pressure distribution inside a silo was first proven to be non-isotropic and non-hydrostatic by Janssen [178]. His observation was that part of the pressure induced by gravity was transferred to the walls of the silo. Assuming a uniform stress distribution in the horizontal direction, a balance of the forces acting on a vertical slice of the granular material allows us to derive an expression for the vertical stress acting on a layer at depth z, see eq. (71) (Janssen equation) and Figure 80.

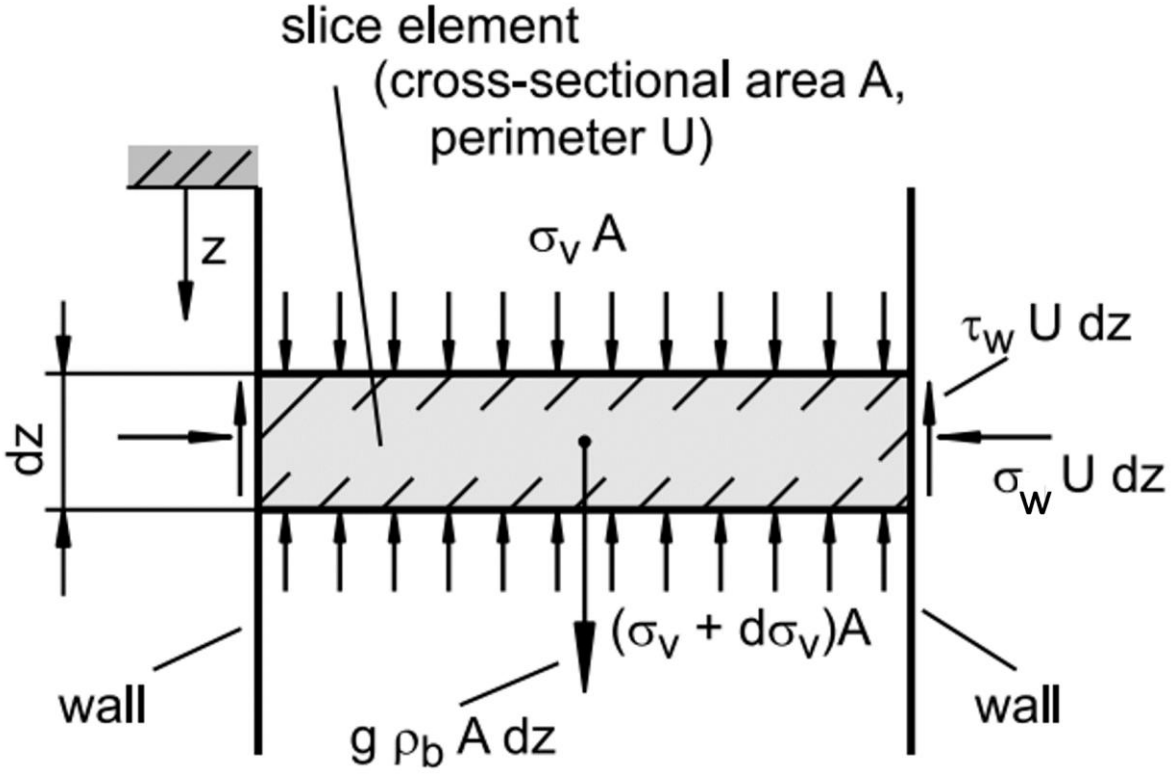

Figure 80: Balance of forces acting on a layer of granular material of surface A in a vertical silo [160]. ρ_b is the bulk density of the material and g is the gravity constant.

$$\sigma_v(z) = P_0\left(1 - exp\left(-\frac{z}{z_0}\right)\right) \tag{71}$$

$$P_0 = \frac{\rho_b g R_h}{2\Phi_w} \tag{72}$$

$$z_0 = \frac{R_h}{2\Phi_w \lambda} \tag{73}$$

Where R_h is the radius (or equivalent hydraulic radius) of the silo, Φ_w is the wall-solid friction angle and λ is the stress transmission coefficient. The latter represents the ratio of the vertical pressure forces that are transferred laterally to the wall. λ is generally derived from the value of

Φ_s, the internal friction angle, and it is evaluated between 0.3 and 0.6. Both the internal friction angle and the wall friction angle can be determined by shearing tests.

Eq. (71) shows that the vertical stress in an infinitely tall silo increases with depth following a negative exponential behavior, then stabilizes at a constant value. An increase in the stress transmission coefficient or the wall friction angle results in a lower z_0, which is the characteristic saturation depth below which the vertical stress remains constant. A linear hydrostatic evolution of pressure is usually retained in the hopper section of the silo [172, 173].

A major issue with these models is that they describe the state of stresses in a silo at rest. Actually, the stresses inside a discharging silo were found to be far superior to those inside a silo at rest [172]. Moreover, the discontinuity which appears at the transition between cylindrical and hopper sections surges during discharge, as shown in Figure 81.

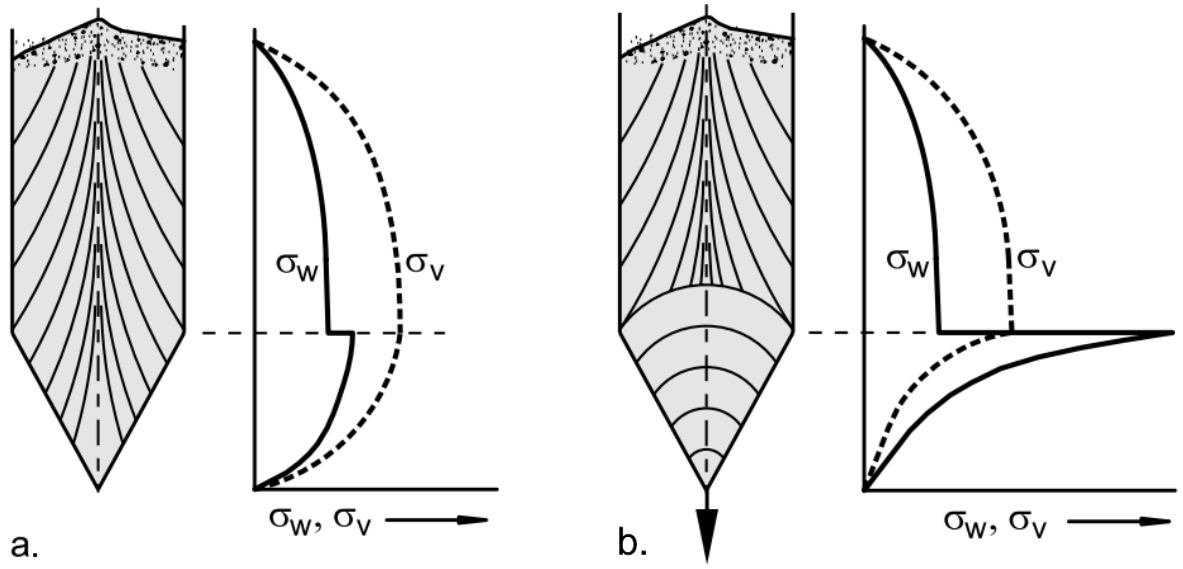

Figure 81: Representation of the typical principal stress distributions in a silo: **a.** at rest; **b.** during discharge [160].

A further work based on the idea of Janssen was presented to evaluate the state of stresses in the hopper section of a discharging silo [168]. The equations that were developed extend the number of fitting parameters but have proven great quantitative correlation with recent experimental measurements and FEM simulation, see Figure 82. Although idealized, these equations help get a qualitative understanding of the pressure distribution inside a silo before and during discharge. If they are sufficiently calibrated, these correlations can prove useful in the development of a FVM model.

Discharge rate

To a certain extent, the classical silo discharge is analogous to the situation in which a Newtonian fluid is discharged from a tank. In the latter case, the discharge velocity is directly derived from the height of the fluid column h through the Torricelli equation:

$$u(t) = \sqrt{2gh(t)} \tag{74}$$

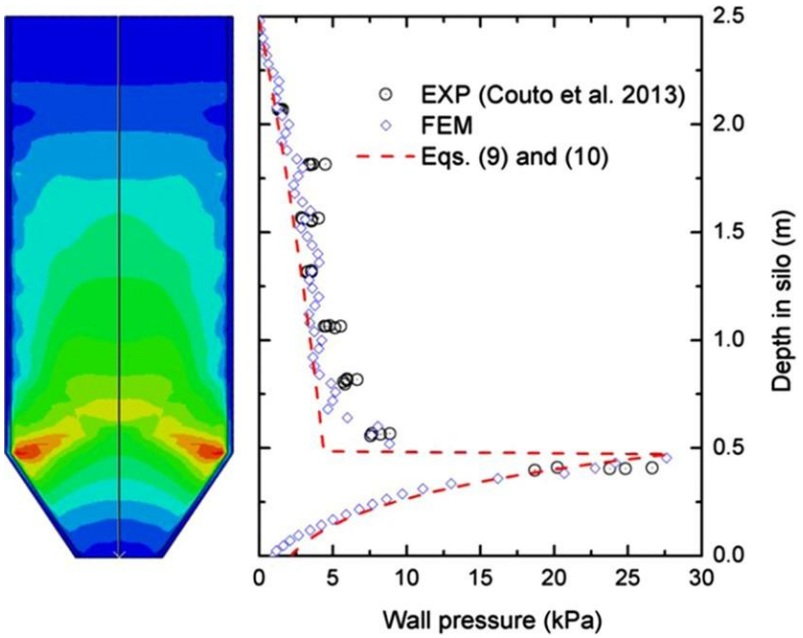

Figure 82: Wall pressure in a cylindrical silo with a conical hopper measured by experiments [179] and compared with calculations through analytical correlations [168] and FEM [174].

However, for coarse-grained bulk solids, experiments have shown no correlation between the height of the solid column and the discharge rate. In a series of experiments, three distinct replica of flat-bottomed silos (see Figure 77) with different outlet sizes D were built, and the discharge flowrate W_{out} was measured after filling at different heights [180]. Fitting of the experimental measurements and dimensional analysis suggested that:

$$W_{out} \propto \rho_b \sqrt{g} D^{2.5} \tag{75}$$

That is, the discharge flowrate of granular materials is highly influenced by the diameter of the outlet, but not by the height of the solid column. Further experiments revealed that in practice, the vertical flow of solid was observed only in an area smaller than the outlet area, the ratio of these areas being proportional to the diameter of the granular material d_p. This led to the famous Beverloo equation [180]:

$$W_{out} = C_B \rho_b \sqrt{g} \left(D - k_B d_p\right)^{2.5} \tag{76}$$

where C_B and k_B are fitting parameters, which were been found to vary in a narrow range: $0.55 < C_B < 0.65$ and $1.5 < k_B < 3$. The validity of this law is completely related to the frictional characteristic of the granular material: it does not work well in simulations where the materials exhibit very low friction [181]. It is also unable to predict the flowrate of materials with a diameter close to the outlet size [182]. In the case of the shaft furnaces, with large outlets and highly frictional materials, this law can constitute a major validation test of a continuum model.

Combined flow of gas and solid in a shaft furnace

A final issue to consider is the influence of the gas flow on the flow of pellets. According to the Geldart diagram shown in Figure 83, industrial iron ore pellets ($d_p > 8$ mm) with a bulk density of 3600 kg/m^3, while the gas density is about 0.3 kg/m^3, belong to the D category, which means that

they are coarse particles hard to fluidize. If the gas injection may influence the flow of pellets at the gas inlets, it is certainly not a major factor influencing the solid flow in the shaft furnace.

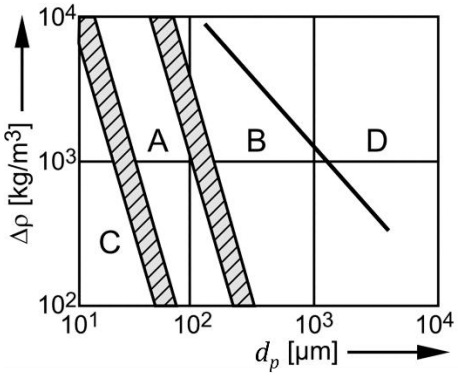

Figure 83: Adapted Geldart diagram [160]. This diagram divides the granular materials in 4 categories according to their diameter d_p and their relative density with the flowing gas, $\Delta\rho = \rho_{solid} - \rho_{gas}$. From A to D, the granular particles become increasingly difficult to fluidize.

IV.2.2. Continuum mechanics approaches

Due to the complex behavior of flowing granular matter, the predictive capacity of the abovementioned analytical models is quite limited. A solution to this issue is to discretize the bulk of the solid and apply the equations used in continuum mechanics. Two concurrent frameworks are found in the literature to describe the flow of granular matter. On the one hand, the elastoplastic approach is derived from soil mechanics and treats the bulk solid as a single entity, with proper elasticity, plastic yield, and flow potential [168]. On the other hand, the hydrodynamic approach approximates the granular material as a non-Newtonian fluid with complex rheology. A major and reasonable assumption of these models is the codirectionality of the stress deviator tensor $\boldsymbol{\tau}$ and the strain rate tensor $\dot{\boldsymbol{\gamma}}$, that is their coaxiality and the equality between the ratio of their principal values [183]. Both of these approaches showed successful for describing steady and unsteady flows in many situations, including the granular silo [170].

IV.2.2.1. Studies based on the hydrodynamic framework

Once the transition of granular material from solid-like state to fluid-state is achieved, the flow can be considered incompressible [169, 184] and the equations of motion rely on simple non-newtonian constitutive equations. The hydrodynamic framework becomes very efficient at describing the fully-developed flow. The equations of motion in steady state are presented in Table 21.

Table 21: Equations of motion in the hydrodynamic framework.

Continuity equation (kg. m^{-3} s^{-1})	
$$\boldsymbol{\nabla} \cdot (\rho_b \boldsymbol{u}) = 0$$	(77)
Momentum equation (kg. m^{-2}. s^{-2})	
$$\boldsymbol{\nabla} \cdot (\rho_b \boldsymbol{u} \otimes \boldsymbol{u}) + \boldsymbol{\nabla} \cdot P = \boldsymbol{\nabla} \cdot \boldsymbol{\tau} + \rho_b \boldsymbol{f_v}$$	(78)
Where $\boldsymbol{f_v}$ is the sum of the body forces, including gravity $\boldsymbol{g}$.	
Shear stress tensor (kg. m^{-1}. s^{-2})	
$$\boldsymbol{\tau} = f(\dot{\boldsymbol{\gamma}})$$	(79)
Strain rate tensor (kg. m^{-1}. s^{-2})	
$$\dot{\boldsymbol{\gamma}} = \left(\frac{\partial u_i}{\partial x_j} + \frac{\partial u_j}{dx_i}\right) \boldsymbol{e_i} \otimes \boldsymbol{e_j}$$	(80)

Newtonian and Bingham fluid approaches

The model of the Newtonian fluid considers direct proportionality between shear stress and strain rate through a constant viscosity η:

$$\boldsymbol{\tau} = \eta \dot{\boldsymbol{\gamma}} \tag{81}$$

In a pioneering study, Chen et al. set up a framework based on a Newtonian fluid to model the unsteady flow of granular solid in moving beds [185]. A first body force was added in the equations of motion to account for the gas-solid interaction through the Ergun equation, while a second body force was added to account for the particular friction at the deadman. This first model was already able to capture the influence of friction at the wall, and it gave satisfying velocity profiles for the descent of packed sand particles (d_p = 1 mm). However, it suffered from severe shortcomings: a strong influence of the boundary conditions, which requires a correct tuning of free-slip and no-slip conditions, and the need to rely on a pre-determined shape of the deadman, which cut the model from most of its predictive potential.

A more convenient approach to determine the stagnant zones in the flow of granular material is to use a Bingham model, based on the following constitutive equations [186]:

$$\begin{cases} \boldsymbol{\tau} = \left(\eta + \dfrac{\tau_0}{\|\dot{\boldsymbol{\gamma}}\|}\right) \dot{\boldsymbol{\gamma}} & \text{if } \dot{\boldsymbol{\gamma}} \neq \boldsymbol{0} \\ \|\boldsymbol{\tau}\| < \tau_0 & \text{if } \dot{\boldsymbol{\gamma}} = \boldsymbol{0} \end{cases} \tag{82}$$

Where $\|\dot{\boldsymbol{\gamma}}\| = \sqrt{\frac{1}{2}\dot{\gamma}_{ij}\dot{\gamma}_{ij}}$ is the second invariant of the strain rate tensor. These equations describe the flow of a viscoplastic material, which flows only if the local stress exceeds a so-called yield stress τ_0 which is characteristic of the material at hand. In all regions where velocity gradients are negligible, the granular material will behave like a solid, which means that it will either move like

a non-deformable solid or not move at all. These are the yielded regions, while regions with sufficient strain rates are called unyielded.

Bingham equations are difficult to implement numerically because of the discontinuity between yielded and unyielded regions, known as the yield surface. To avoid the *a priori* necessary tracking of the yield surfaces, regularization and integration methods are needed [8, 187, 188]. In order to improve the model of the blast furnace discussed earlier [185], the Newtonian fluid was replaced with a Bingham type fluid, see [189]. In their work, they used a popular bi-viscosity method to reduce the Bingham discontinuity, see eq. (83) and Figure 84. Their idea was to linearize the stress-strain relationship in two domains separated by a critical stress τ_c, which is different from the yield stress τ_0.

$$\begin{cases} \tau_c = \dfrac{\eta_c \tau_0}{(\eta_c - \eta)} \\ \tau_{rx} = -\eta_c \dfrac{du}{dr} \quad \text{if } \tau_{rx} < \tau_c \\ \tau_{rx} = \tau_0 - \eta_c \dfrac{du}{dr} \quad \text{if } \tau_{rx} > \tau_c \end{cases} \tag{83}$$

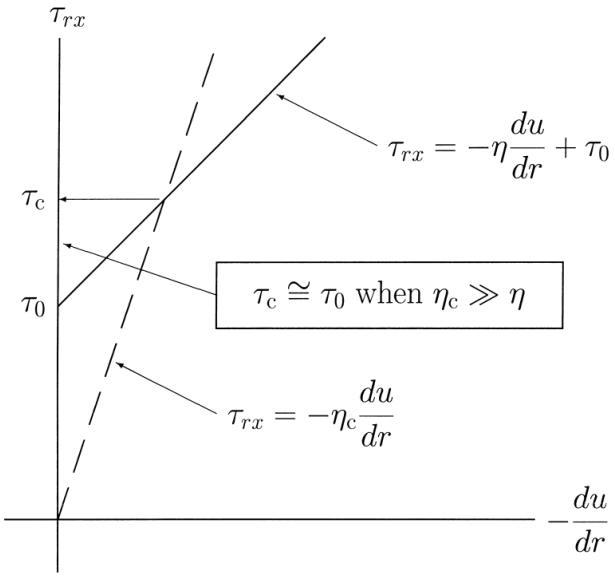

Figure 84: 1D visual representation of the stress-strain rate equation using a bi-viscosity method [189].

Simulations were performed with two different initial conditions: in the first case, the yield stress was independent of the pressure, while in the second case, it was calculated based on a pressure distribution resulting from the Janssen equation, eq. (71). The Bingham model allowed to predict the formation of the deadman with no prior information, which is a clear advantage compared to the Newtonian model. The resulting velocity distribution and the shape of the deadman were found to be in greater agreement with the experiments when the yield stress was derived from the pressure distribution (Figure 85). However, the model was found unable to correctly predict the stress field and the velocity field with a sufficient accuracy.

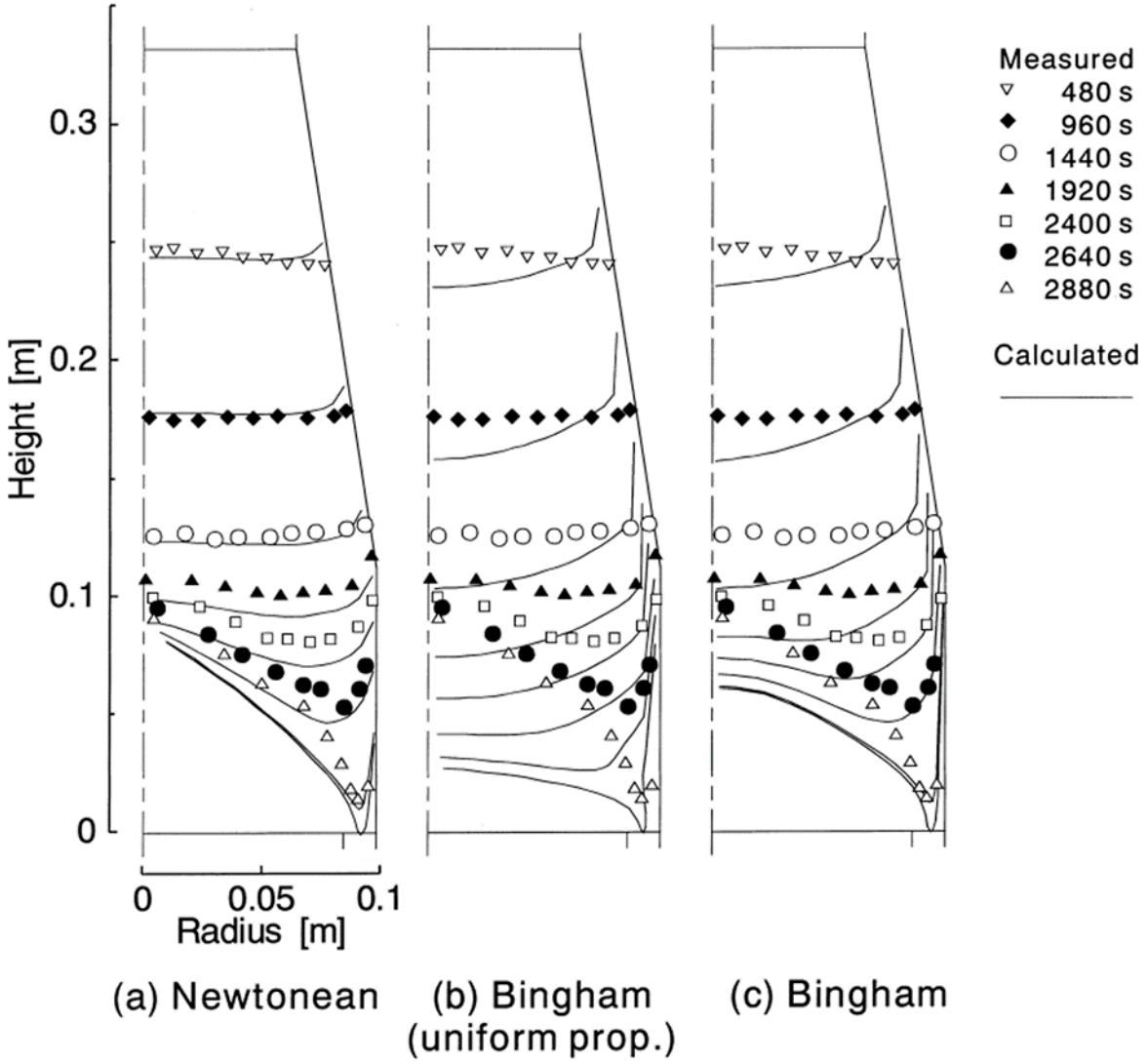

Figure 85: Measured (markers) and simulated (solid line) velocity distributions obtained from the discharge of packed sand in a blast furnace geometry [189]. The Newtonian model offers the best agreement with experiments, as it is derived assuming *a priori* the shape of the deadman.

An extensive 3D method for the flow of fluids obeying a Coulomb rheology (equivalent to the Bingham fluid) was developed in the finite element method (FEM) framework [187]. Their algorithm was validated against two basic fluid mechanics configurations, the lid driven cavity and the flow between two infinite parallel planes. It was also found to properly behave in 3D duct geometries. In their study, they point out the need for multiple regularization schemes that allow better convergence of such a model:

- the variational formulations of the equations of motion are iteratively integrated by a Newton-Raphson algorithm in order to deal with the highly non-linear behavior of the equations;
- the constitutive stress-strain rate law is regularized to avoid divergence:

$$\boldsymbol{\tau} = \left(\eta + \frac{\tau_0}{\|\dot{\boldsymbol{\gamma}}\| + \lambda_r}\right)\dot{\boldsymbol{\gamma}} \tag{84}$$

Where λ_r is a regularization parameter that prevents from divergence, $10^{-8} < \lambda_r < 10^{-4}$. Note that in this formulation, the system of equations is replaced with a single constitutive equation for the stress-strain rate relationship. This way of treating the Bingham fluid was popularized by Papanastasiou, who introduced the concept of continuous viscoplastic equation (CVE). Indeed, the implementation of a Bingham-type fluid can be achieved by transforming the Bingham equations into a single CVE, without the need for a slow integration step [190]. The CVE proposed by Papanastasiou is expressed as [8]:

$$\boldsymbol{\tau} = \left(\eta_0 + \frac{\tau_0\left(1 - \exp(-m_p\|\dot{\boldsymbol{\gamma}}\|\right)}{\|\dot{\boldsymbol{\gamma}}\|}\right)\dot{\boldsymbol{\gamma}} \tag{85}$$

Where m_p is a regularization parameter, called the parameter of stress growth. This parameter expresses how non-Newtonian the fluid is: for m_p = 0, eq. (85) describes a Newtonian fluid. Conversely, as m_p tends towards infinity, the fluid behavior tends toward an ideal Bingham fluid. The CVE presented in eq. (85) is thought to give an appropriate model of a real Bingham fluid, which is somewhere between the Newtonian fluid and the ideal Bingham fluid [8]. A modified method based on this CVE was recently validated against dam-breaks and rotating drum experiments by other partners of the MaxH2DR project [191]. Their results will serve as basis for a future CFD-DEM model for the simulation of hydrogen shaft furnaces.

Rheology approaches

The DEM study of plane shearing by different teams in the early 2000s have shown that in this particular configuration, the granular pressure was isotropic and that the shear stress τ_s was proportional to the pressure through a Coulomb-like friction μ and an inertial parameter I [192]:

$$\tau_s = \mu(I)P \tag{86}$$

$$I = \frac{\dot{\gamma}}{\sqrt{\frac{P}{\rho_p}}}d_p \tag{87}$$

This inertial parameter I can be interpreted as the ratio between two characteristic times: a macroscopic characteristic time representing the time needed for a particle to move forward by a diameter $t_\gamma = \frac{1}{\dot{\gamma}}$, and a microscopic characteristic time representing the local rearrangement of grains under the confining pressure $t_P = d_p\sqrt{\frac{\rho_p}{P}}$, see Figure 86 [192, 193] (d_p is the particle diameter and ρ_p is the particle density). Small values of I indicate that the flow regime is dominated by local rearrangements in the limit of quasi-static flow, while higher values of I indicate a more liquid-like behavior.

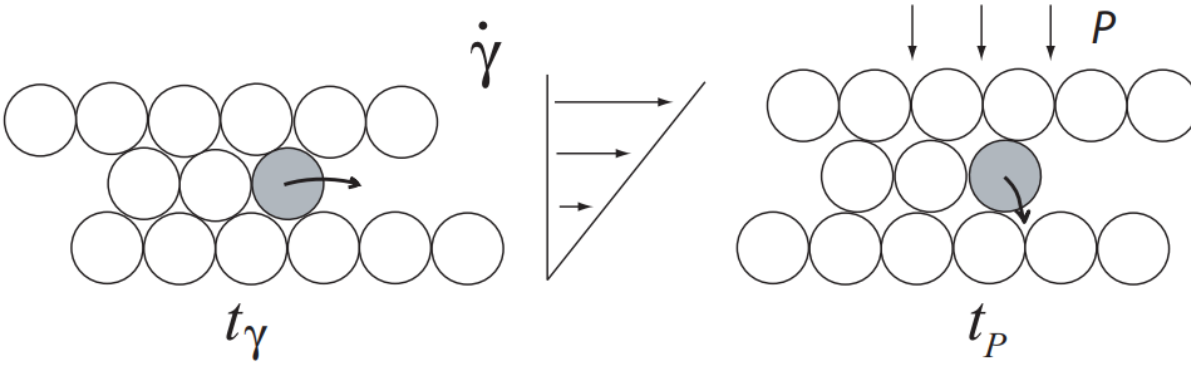

Figure 86: Characteristic times involved in the interpretation of the inertial number I [192].

Although initially designed for specific granular flow configurations, this inertial law showed successful in many configurations, including the granular silo [7, 170, 174, 181]. A simple constitutive law was established between the friction and the inertial number, eq. (88), and it was extended to 3D, eq. (89). This constitutive stress-strain rate relationship relies on a Bingham yield stress, but it also incorporates the local rheology of the granular matter. At the limit of the quasi-static regime, a low strain rate results in a low inertial number and the friction equals the Coulomb friction μ_s. An increase in the strain rate leads to an increase in the friction of the material, ultimately reaching a limit value μ_2 as shown in Figure 87.

$$\mu(I) = \mu_s + \frac{\mu_2 - \mu_s}{\frac{I_0}{I} + 1} \tag{88}$$

$$\boldsymbol{\tau} = \frac{\mu(I)P}{\|\dot{\boldsymbol{\gamma}}\|}\dot{\boldsymbol{\gamma}} \tag{89}$$

In the case of silos, this law proved efficient at capturing the flow properties outside of the quasi-static regime. At sufficiently large values of I, it was shown that the model was able to capture the vertical chute flow between two parallel plates and the results were validated against the analytical solution [9]. A model with a constant friction μ_s is sufficient to numerically retrieve the Beverloo scaling [181], but the presence of the inertial parameter ensures that the scaling law is respected even at particularly high friction $\mu(I) > 0.8$ (Staron et al., 2014). An impressive feature of this model is its ability to quantitatively reproduce the flowing characteristics of many systems with little tuning of the rheological parameters μ_s, μ_2 and I_0 [7, 9, 184]. However, it often fails to correctly capture the transition between liquid and quasi-static regimes, such as the width of shear bands [194] and the hysteretic nature of the transition from a regime to another [166].

IV.2.2.2. Studies based on the elastoplastic framework

The framework of elastic and plastic deformations is traditionally associated with solid mechanics, and it is used to determine the response of solids under load or shear. It has then been progressively adapted to describe the mechanics of soils which flow in the quasi-static regime. The introduction of the flow potential and the critical state theory in the elastoplastic framework made it possible to describe the flow of granular matter in the quasi static regime, see e.g. [195]. In brief, the critical state theory shows that there is an ultimate condition in which plastic shearing can continue indefinitely without changes in volume or effective stresses [195]: the material can flow indefinitely at constant stresses.

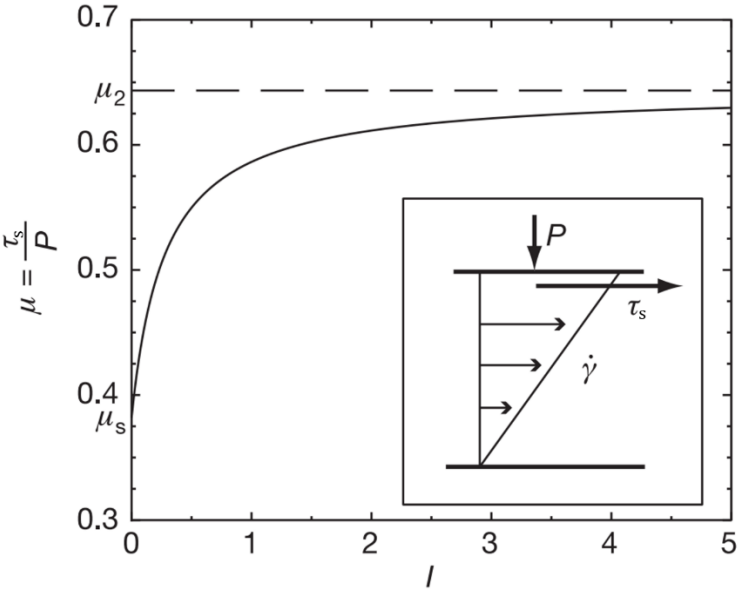

Figure 87: Friction coefficient μ as a function of the inertial parameter I [184].

Compared with the hydrodynamic framework, the yielded region is associated with elastic behavior. Assuming an isotropic elasticity, the stress-strain relationship is derived from Hooke's law:

$$\sigma_{ij} = D_{ijkl}\epsilon_{el} \tag{90}$$

where $\sigma_{ij}, \epsilon_{ij}$ and D_{ijkl} are components of the stress, strain and elasticity tensors, respectively.

As in the hydrodynamic framework, the yield criterion F defines the region in which plastic deformation is occurring. A simple and popular yield criterion is given by the Coulomb equation, which involves the internal friction angle Φ_s:

$$F = q + \mu p = 0 \tag{91}$$

where p and q are respectively the volumetric and deviatoric stress components, and μ is the frictional resistance related to the internal friction angle Φ_s. The elastoplastic theory needs a second function to determine the mechanism of plastic deformations, called the plastic potential G [195]. A simple definition of the plastic flow potential is given by [169]:

$$G = q + \beta_d p + c = 0 \tag{92}$$

where β_d is called the material dilatancy and c is a mathematical free parameter which ensures that the stresses in F and G coincide. The dilatancy accounts for the compaction or dilation behavior of granular matter at the onset of flow, so it is thought to be one of the major parameters that properly separates between the solid and fluid-like behavior of the granular matter [169]. Given these specific constitutive relationships, the stress-strain relationship is calculated in an incremental manner. The specific numerical resolution of the elastoplastic equations is left to the interested reader, see e.g. [170]. Our objective here is only to present this second finite element framework and to compare its efficiency relatively to the hydrodynamic framework.

The discharge of wheat in a conical silo was simulated with a Mohr-Coulomb elastoplastic model, implemented on the commercial software Abaqus [174]. Impressive quantitative agreement with

experimental and analytical models was demonstrated. The simulations were able to reproduce the velocity distribution of associated experiments [196] and to find a realistic value for the coefficient of internal friction Φ_s, for two different values of the wall friction coefficient μ_w = tan(15.6°) and μ_w = tan(28.5°). The calculated wall pressure during discharge proved excellent correlation with the measurements of [179], resulting in a pressure profile more realistic than the analytical one [168]. The results of each approach were shown in Figure 82. The Beverloo scaling was readily recovered in their simulations. In later studies, the operation of a blast furnace was simulated, in which the model was complemented with the $\mu(I)$ rheology [171]. Their model was able to quantitatively reproduce the shape of the deadman and the stagnant zones, and it was also able to describe the segregation of small and large particles during loading at the top of the furnace. In another study, the results of the discharge of a flat-bottomed silo were compared for 4 different models [170]:

- a Bingham fluid with a yield stress called "η_s";
- a non-Newtonian fluid based on the $\mu(I)$ rheology "$\eta_s(I)$";
- an elastoplastic solid with constant friction "μ_s";
- an elastoplastic solid complemented by the $\mu(I)$ rheology "$\mu_s(I)$".

Contour plots of the predicted shear stress inside the silo are shown in Figure 88. It is seen that the shear stress distributions are quite different outside of the flowing zone. This is attributed to the elastic properties of the solid, which are accounted for in the elastoplastic models but not in the hydrodynamic models. Similar conclusions can be drawn regarding the isotropic pressure distributions. However, the discharge rate and the frontiers of the stagnant zones are close for each model studied. One should also note that the hydrodynamic models η_s and $\eta(I)$ are able to predict the flow of granular matter in a funnel flow situation, which they are not supposed to. Same conclusions were drawn elsewhere [7] . This indicates that the $\mu(I)$ rheology has a predicting potential outside of its initially attributed domain.

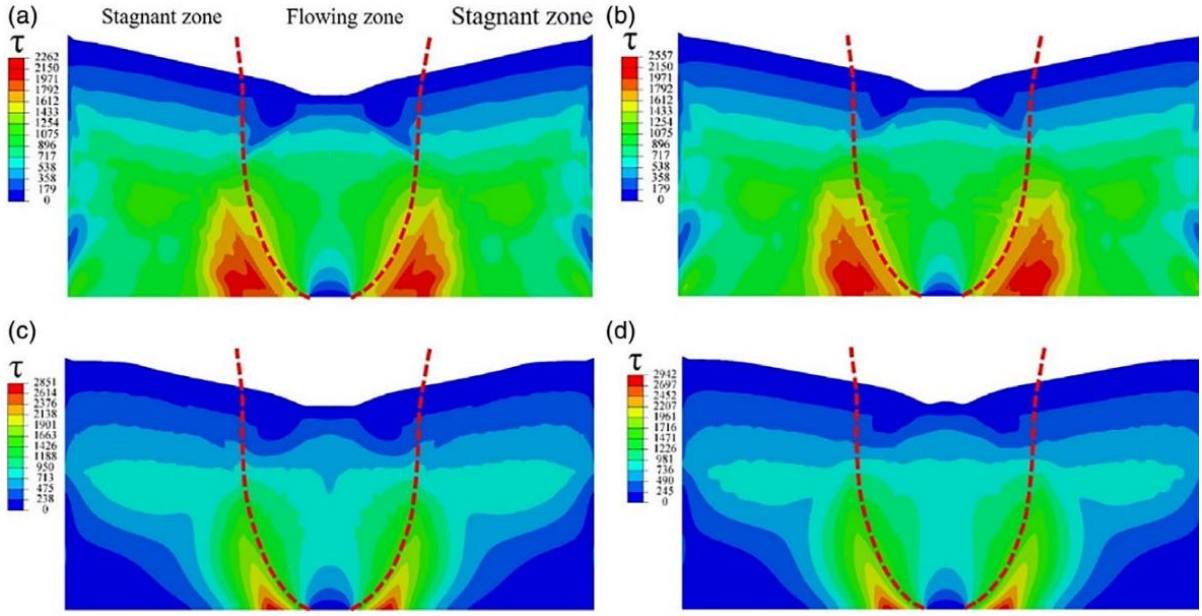

Figure 88: Prediction of shear stress during discharge of a flat-bottomed silos according to each model (a) μ_s , (b) $\mu_s(I)$, (c) η_s , (d) $\eta_s(I)$ [170].

The solid-fluid bridging issue

It can be concluded from the above discussions that the continuum FEM and FVM models still lack of a unified framework able to describe all situations encountered in experimental and industrial situations. Three recent attempts at offering such a unified framework can be found in the literature [166, 169, 183]. With these models, considerable progress is made in tackling non-local effects [183] as well as the hysteresis and dilatancy phenomena, related to the transition from solid to liquid like states [166, 169].

IV.3. A continuum model for the solid flow of pellets in a shaft furnace

In this exploratory work, we set the basis of a FVM viscoplastic model based on the $\mu(I)$ rheology. It is intended to simulate the flow of iron ore pellets in a hydrogen shaft furnace. The implementation strategy is presented, the complete model is detailed and the results of the new model are discussed and compared with previous results and other classical results of the silo discharge problem.

Choice of a model

From the literature review, it is clear that important velocity gradients are expected during the discharge of a shaft furnace [164], which cannot be described by the plug flow model. Meanwhile, both Newtonian and kinematic models are unable to properly describe the flow patterns without prior determination of the stagnant zones [189]. Continuum modeling of the flow in shaft furnaces is however possible with more elaborate models. A first approach considers the pellet burden as a bulk elasto-plastic solid: under specific shear conditions, it flows indefinitely in the critical state theoretical framework, see e.g. [171, 195]. The second approach considers the solid as a non-Newtonian liquid with complex rheology, and is developed in the hydrodynamic framework [184]. The latter $\mu(I)$ model has proven successful in describing the flow of granular matter in a silo [7, 170] and has been retained.

Implementation strategy

In the REDUCTOR code, the solid flow is described either with the plug flow model or the kinematic model, see chapter 3. On the other hand, the gas flow is determined by solving the coupled mass-momentum equations, that is the continuity and the Ergun equation. Since the gas flow is primarily determined by the pressure drop, diffusion and convection terms are absent from the equations. This simplifies the discretization of the equations and it makes the convergence of the algorithm easier. These equations are numerically implemented with a SIMPLE algorithm called S1 through a Gauss-Seidel resolution pattern.

The same numerical architecture can be used to determine the solid flow. To this end, a second SIMPLE algorithm called S2 was developed to solve the coupled mass-momentum equations for the solid phase. In this case, the complete set of equations with diffusion, convection and pressure terms was implemented (see Table 22 below, these equations will be presented in the next subsection). However, the numerical implementation of non-Newtonian models derived from the Bingham theory encounters some difficulties in the resolution due to the high degree of non-linearity of the equations, particularly in the steady-state [9, 187]. To limit this negative outcome, the strategy adopted in this work was to progressively increase the complexity of the model and to test its implementation at each successive step, similarly to the work presented in [185, 189]:

- the SIMPLE algorithm S2 was first tested for a solid flow completely determined by the pressure drop (i.e., $\boldsymbol{u_s} = -\boldsymbol{L}\boldsymbol{\nabla}\boldsymbol{p}$, with L an arbitrary constant);
- the convection and diffusion terms were then added with a constant viscosity, resulting in a Newtonian model, eq. (81);
- the viscosity equation was then modified into a continuous viscoplastic equation (CVE) to describe the solid flow with a Bingham model, eq. (85);
- finally, the constant friction was replaced by the *μ(I)* rheology, eq. (100).

Among the issues we faced in the numerical implementation, one was directly linked to the pressure distribution. It is established that in a silo undergoing discharge, the solid pressure reaches zero at the free surfaces, that is both at the top and at the bottom of the furnace. In the upper section of the shaft furnace, the pressure increases with depth, which opposes the flow of solid: the solid flows under gravity. However, including this gravity term into the general equation was found difficult and systematically led to the divergence of the code. To deal with this issue, it was decided to solve the equations of motion for a modified pressure without the gravity body force. The total pressure is the sum of the pressure stemming from gravity and from the modified pressure, expressed as:

$$p_{tot} = p_{mod} + p_{grav} \tag{93}$$

In this case, the flow is driven by a pressure gradient from top to bottom, which is analogous to the one used to describe the flow of gas, though with the opposite sign. Assuming that the total pressure distribution is correct, the fitting of this pressure gradient should allow us to find the expected solid flowrate. Moreover, an external determination of the static pressure distribution is needed. To this end, it was decided to rely on the analytical equations mentioned in section 4.1) to derive quantitative estimates of the pressure at the wall. A similar approach was followed by [189].

Estimate of the pressure distribution and yield stress in the conical hopper

The Janssen equation is often considered to give a reasonable estimate of the wall pressure in a vertical silo during both filling and discharge operations. Following recommendations from the literature, the lateral transmission coefficient was set at $\lambda = 0.4$ [172]. The radial stress at the vertical wall of the cylindrical section is given by:

$$\sigma_w(z) = \frac{\rho_b g R_h}{2\lambda\Phi_w}\left(1 - \exp\left(\frac{z}{\frac{R_h}{2\Phi_w\lambda}}\right)\right) \tag{94}$$

For the hopper section, the stress state at the wall is derived under the assumption of a passive Rankine state during discharge [168]. With a meticulous choice of friction parameters (Φ_s, Φ_w), these equations have proved to be efficient at giving a quantitative estimate of the wall pressure [174, 179]:

$$\sigma_w(z) = K_1\left\{Q_0\left(\frac{h}{h_0}\right)^{K_2} + \frac{\rho_b g h}{K_2 - 1}\left(1 - \left(\frac{h}{h_0}\right)^{K_2 - 1}\right)\right\} \tag{95}$$

$$2\psi = \phi_w + \sin^{-1}\left(\frac{\sin\phi_w}{\sin\phi_s}\right) \tag{96}$$

$$\begin{cases} K_1 = \dfrac{1 + sin\phi_s cos2\psi}{1 - sin\phi_s\, cos(2\alpha + 2\psi)} \\ K_2 = 2(K_3 - 1) \\ K_3 = K_1\left(\dfrac{\tan\alpha + \tan\phi_w}{\tan\alpha}\right) \end{cases} \tag{97}$$

where Q_0 is the vertical stress at the transition between the upper and the lower sections of the shaft, ρ_b is the bulk density of the solid, ψ is the angle between the wall and the principal stress plane, and h is the height ($h = 0$ refers to the bottom of the hopper, $h = h_0$ refers to the top of the hopper).

This pressure distribution allowed us to derive a distribution of yield stresses. For the sake of simplicity, it was assumed that $p_{grav}(z) = \sigma_w(z)$. The yield stress distribution was readily determined following Terzaghi's theory of yield stress [191]:

$$\tau_0 = p_{grav}\sin\Phi_s \tag{98}$$

The pressure and yield stress distributions obtained with this model are presented in Figure 89. It is seen that they both increase with depth upon reaching a critical depth, after which they stay constant. The maximum value of both pressure and yield stress are reached at the transition between upper and hopper sections of the shaft. This is where yielded stagnant regions are expected to appear.

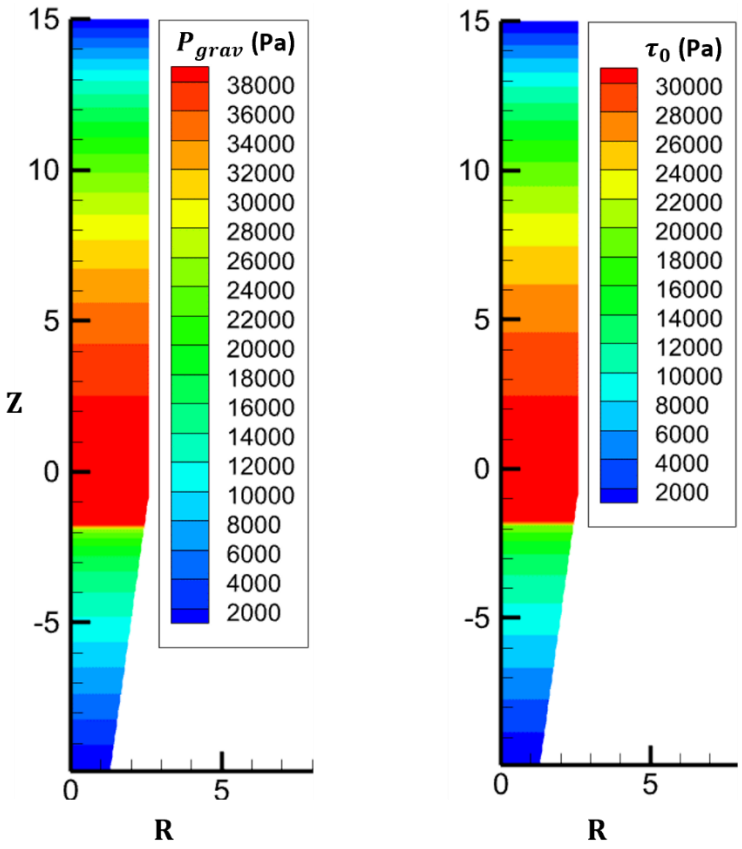

Figure 89: Pressure and yield stress profiles in the shaft furnace. $\rho = 3528\,\mathrm{kg.m^{-3}}, \Phi_s = 52°, \Phi_w = 26.2°,\ \alpha = 7.41°$.

Complete set of equations and boundary conditions

The S2 algorithm solves coupled mass-momentum equations in a procedure analogous to the one described in Article 3. Prior to calculation, the static pressure distribution is calculated and the yield stress distribution is derived. Then, the momentum and continuity equations are iteratively solved to ensure the conservation of both mass and momentum, see eqs. (101) and (102). The complete set of equations is given in Table 22.

The dynamic pressure is specified at the top inlet and at the bottom outlet. The other boundary conditions are given as follows:

- at the center of the furnace: $\frac{\partial P}{dr} = \frac{\partial u_{z,s}}{dr} = \frac{\partial u_{r,s}}{dr} = 0, u_{r,s} = 0$ (symmetry axis)
- at the wall of the furnace: $\frac{\partial P}{dr} = \frac{\partial u_{z,s}}{dr} = \frac{\partial u_{r,s}}{dr} = 0, u_{r,s} = \begin{cases} 0 \text{ in the upper section} \\ -\frac{sin\alpha}{cos\alpha} u_{z,s} \text{ in the lower section} \end{cases}$

Unless explicitly mentioned, no-slip boundary conditions were applied at the wall of the furnace i.e., $u_{r,s} = u_{z,s} = 0$.

Table 22: Equations used in the continuum model.

Static pressure distribution (kg. m^{-1}. s^{-2})	
$$p_{grav}(z) = \sigma_w(z)$$	(99)
Shear stress tensor (kg. m^{-1}. s^{-2})	
$$\boldsymbol{\tau} = \left(\eta_0 + \frac{p_{grav} sin\Phi_s \left(1 - exp\,(-m_p \|\dot{\boldsymbol{\gamma}}\|\right)}{\|\dot{\boldsymbol{\gamma}}\|} + \frac{p_{grav}(\mu_2 - sin\Phi_s)}{\left(\|\dot{\boldsymbol{\gamma}}\| + \lambda_r + \frac{I_0}{d_p}\sqrt{\frac{p_{grav}}{\rho_p}}\right)} \right) \dot{\boldsymbol{\gamma}}$$	(100)
Momentum equation (kg. m^{-2}. s^{-2})	
$$\boldsymbol{\nabla} \cdot (\rho_b \boldsymbol{u} \otimes \boldsymbol{u}) + \boldsymbol{\nabla} \cdot p_{mod} = \boldsymbol{\nabla} \cdot \boldsymbol{\tau}$$	(101)
Continuity equation (kg. m^{-3} s^{-1})	
$$\boldsymbol{\nabla} \cdot (\rho_b \boldsymbol{v}) = 0$$	(102)

Choice of parameters

In the literature, the values of the internal friction angle Φ_s and the wall friction angle Φ_w for iron ore pellets are either unspecified or contradictory [197, 198]. However, considering the similar geometry and materials at hand, we selected the values given by [197]: Φ_w= 26.2° and Φ_s= 52°.

Two rheological parameters were derived from the work of our partners in the MaxH2DR project [191], namely $\eta_0 = 267$ Pa. s and $m_p = 1$ s. They were obtained by fitting the rheological model based on the Bingham Papanastasiou equation (eq. (85)) against experimental and DEM velocity profiles.

The rheological parameter μ_2 was chosen arbitrarily so *that* $\mu_2 > \mu_s, \mu_s = \sin\Phi_s$, and I_0 was taken from [7]. Unless explicitly mentioned, their values were: μ_2 = 0.9 and I_0 = 0.4.

The mesh was made of 120 cells in the axial direction and 20 cells in the radial direction. Simulations have shown that a coarser mesh size slows the convergence, keeping the results almost unchanged.

IV.4. Results of the continuum model

Choice of the boundary conditions at the solid boundaries

The flow of Bingham-type fluids is strongly affected by choosing either free-slip or no-slip boundary conditions, see e.g. [189]. In a first set of simulations, we simulated the flow of iron ore pellets in a shaft furnace with or without a Christmas tree structure at the center of the shaft (the details of each geometry were presented in chapter 3) for both type of boundary conditions. The results are shown in Figure 90. We can see that the maximum axial velocity is very different in each case, and it is much lower in the case of no-slip boundary conditions: the walls play a strong role in slowing and shaping the flow of pellets in the case of no-slip boundary conditions, while they seem to have no influence in the case of free-slip conditions. Quite surprisingly, each configuration predicts a quasi-plug flow behavior in the upper region of the shaft. The no-slip boundary conditions lead to the formation of very low velocity zones at the walls and on the surface of the Christmas tree, which can be considered as stagnant zones.

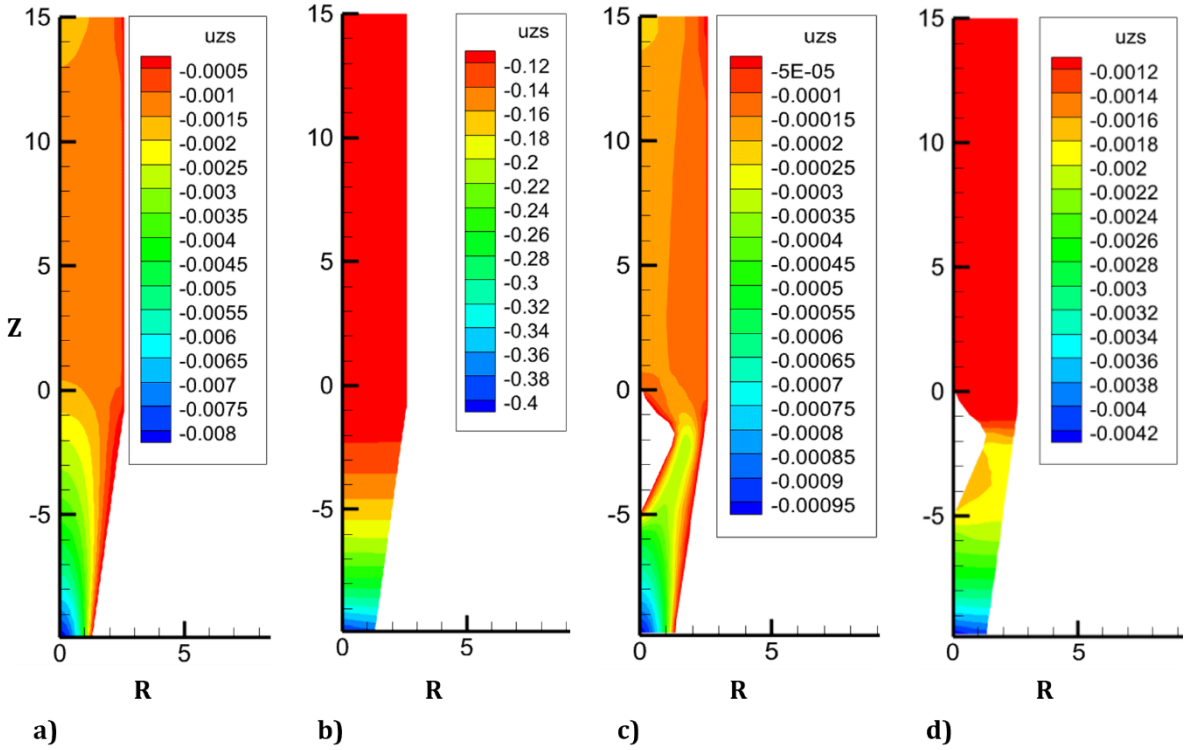

Figure 90: Axial velocity profiles (m s^{-1}) for the descent of pellets in a shaft furnace in both geometries for **a),c)** no-slip**,** and **b),d)** free-slip boundary conditions. $\Delta p_{mod} = 400$ Pa, $\eta_0 = 267$ Pa. s, $m_p = 1$ s, $\Phi_w = 26.2°$, $\Phi_s = 52°$, $\mu_2 = 0.9$, $I_0 = 0.4$, $d_p = 15$ mm, $\lambda_r = 10^{-5}$.

The existence of low-velocity zones at the walls of shaft furnaces in standard geometry was observed in DEM simulations [164] and during experiments, see Figure 91 [26], especially in the hopper section of the shaft. The geometry which includes a Christmas tree structure, was instead numerically proven to promote a uniform flow of the pellets in both sections of the shaft [163, 164].

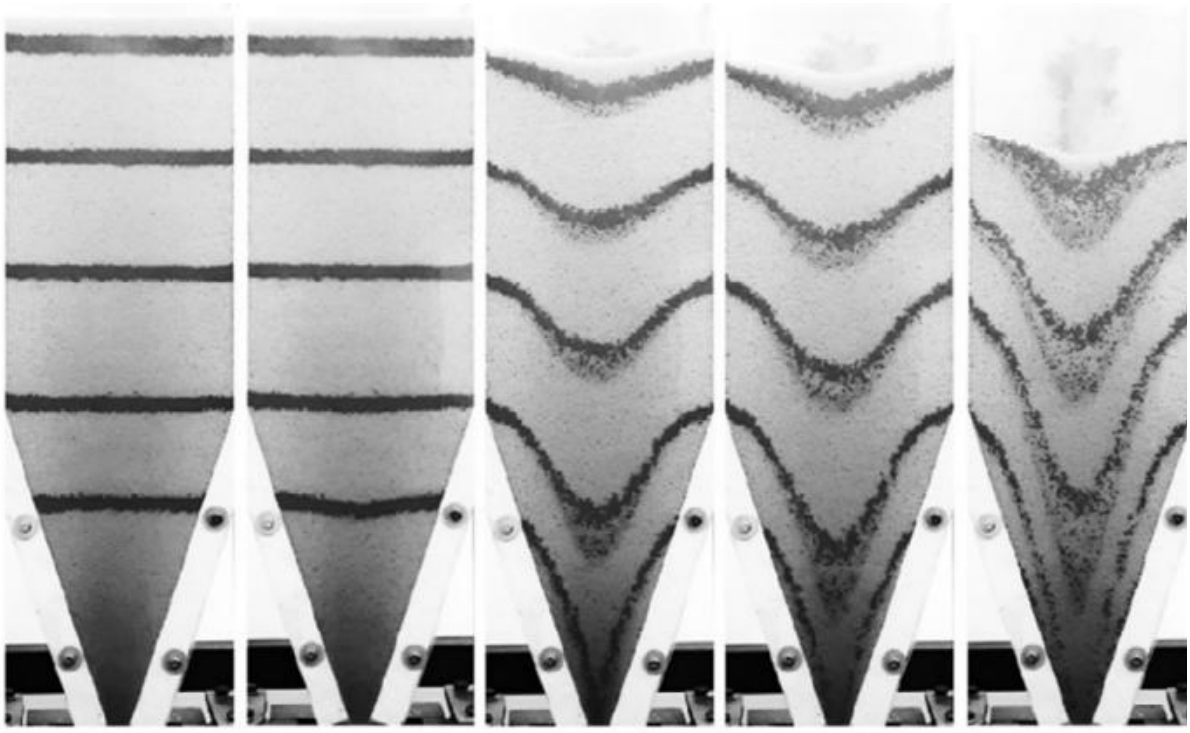

Figure 91: Experimental observation of the flow of granular beads in a lab-scale silo [26]. The upper part of the silo measured 70 cm in height, 22 cm in width and 2 cm in thickness. It was designed to study the flow of glass beads, the diameter of which was 2 mm.

These results suggest that in our model, the no-slip boundary condition seems the better choice in the standard geometry case, whereas the free-slip boundary condition seems better adapted to the Christmas tree geometry case. These choices should lead to more realistic simulations. Actually, this choice of boundary conditions corroborates our previous choice of models: the kinematic model was a good fit for the standard geometry, as it was able to predict the formation of stagnant zones, while the plug flow model was theoretically efficient at predicting the uniform flow of pellets with a Christmas tree.

Comparison with previous models

A comparison of the *μ(I)* rheology with the previous models used in REDUCTOR is shown in Figure 92 and Figure 93. In each case, the modified pressure drop Δp_{mod} was adjusted to reach a flowrate at the outlet similar to industrial operating conditions, see [16]. This was done in isothermal conditions with all chemical reaction rates equal to zero so that only the solid flow properties were calculated.

As seen in Figure 92, each model predicts a plug flow behavior in the upper section of the shaft. In the hopper section, the axial velocity increases as the conical section shrinks. In the standard geometry, the hopper is divided in two distinct zones: a high velocity zone at the center of the shaft and a quasi-stagnant zone at the wall. These zones are limited to the hopper section in the case of the kinematic model, while they extend above the hopper in the case of the *μ(I)* rheology. In the Christmas tree geometry, the plug flow model is mathematically unable to correctly predict the flow of solid in the hopper, since it is calculated along the directions imposed by the mesh. This is why it differs from the rheological model, which predicts a uniform descent of the burden along the height of the furnace, in agreement with the previously mentioned studies.

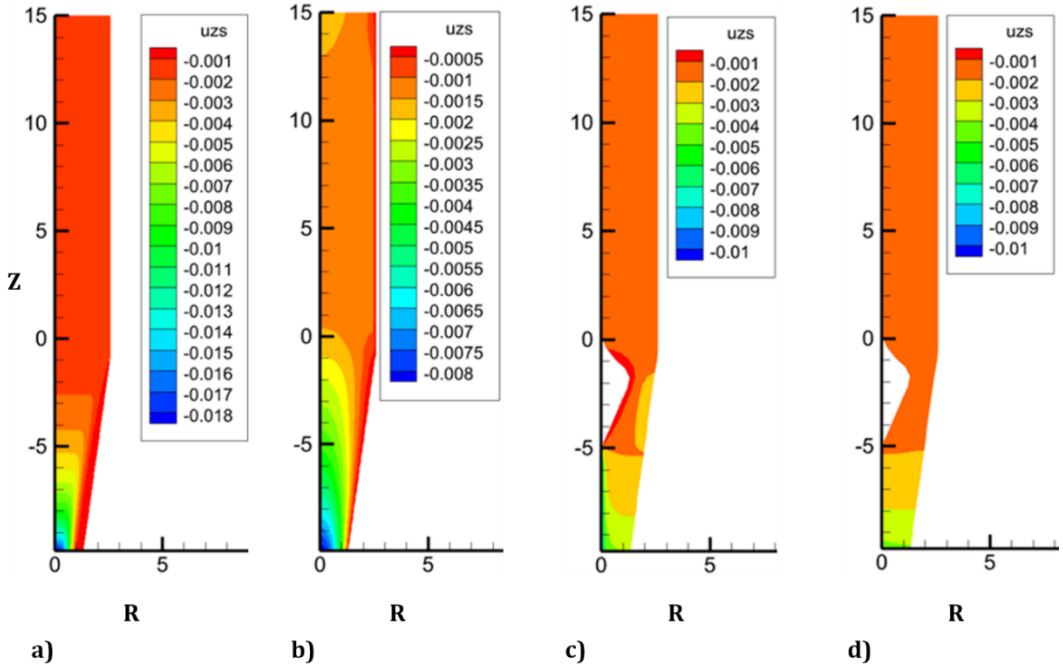

Figure 92: Axial velocity profiles (m s^{-1}) for the descent of pellets in a shaft furnace in both geometries predicted by **a)** the kinematic model, **b),d)** the $\mu(I)$ model and **c)** the plug flow model. $\Delta p_{mod} = 400$ Pa, $\eta_0 = 267$ Pa. s, $m_p = 1$ s, $\Phi_w = 26.2°$, $\Phi_s = 52°$, $\mu_2 = 0.9$, $I_0 = 0.4$, $d_p =$ 15 mm, $\lambda_r = 10^{-5}$.

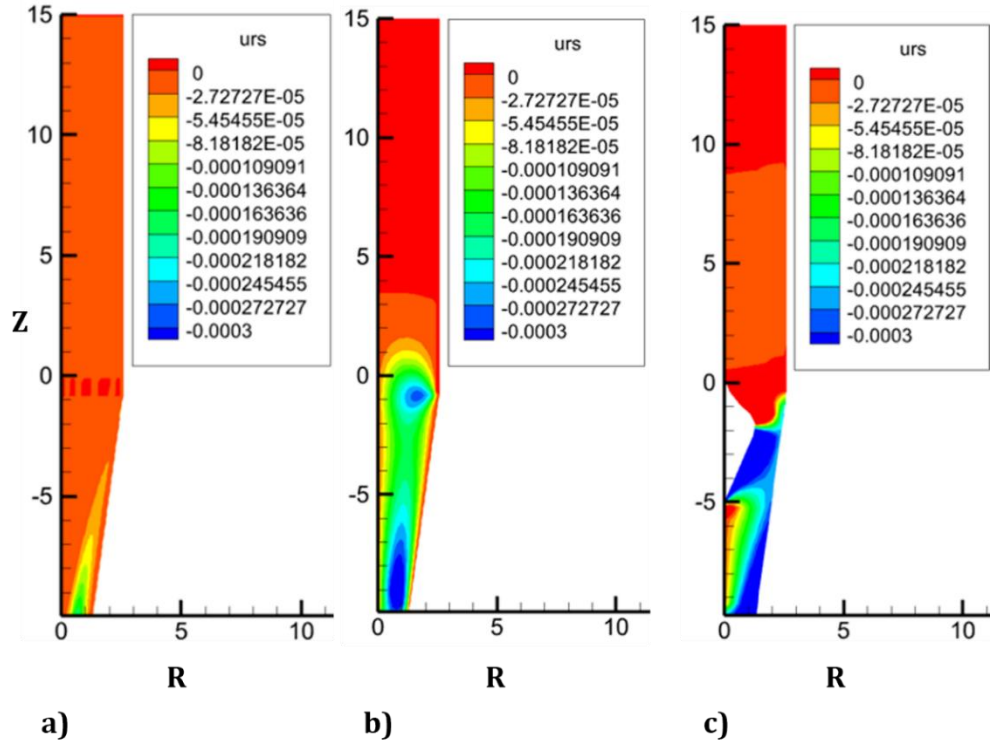

Figure 93: Radial velocity profiles (m s^{-1}) for the descent of pellets in a shaft furnace in both geometries predicted by **a)** the kinematic model and **b),c)** the $\mu(I)$ rheology. $\Delta p_{mod} = 400$ Pa, $\eta_0 =$ 267 Pa. s, $m_p = 1$ s, $\Phi_w = 26.2°$, $\Phi_s = 52°$, $\mu_2 = 0.9$, $I_0 = 0.4$, $d_p =$ 15 mm, $\lambda_r = 10^{-5}$.

The radial velocity distribution is shown for each model (Figure 93) except for the plug flow model where it is zero. In each case, the predicted radial velocity reaches zero in the upper section of the shaft, in agreement with the observed plug flow behavior. In the standard geometry, both models predict low radial velocities at the wall and at the center of the furnace. They also predict the maximum radial velocity to be located halfway between the wall and the center of the furnace, at the bottom of the furnace. However, the radial movement of pellets seen at the transition between the upper section and the hopper section of the shaft for the $\mu(I)$ rheology was not captured at all by the kinematic model. This limits the predicting capability of the latter. With the Christmas tree, the radial velocity follows the geometry: it is positive at the top of the Christmas tree, as the latter diverts the solid flow towards the walls, and it is negative at its bottom as the obstacle progressively vanishes, allowing the pellets to move towards the center of the furnace.

It can be seen from comparison with the previous models that the $\mu(I)$ model allows us to improve the description of the solid flow with a christmas tree. The uniform descent of the pellets in the hopper section of the shaft is correctly captured by the $\mu(I)$ model, which is not the case with the plug flow model. In the standard geometry, a more systematic comparison of experimental and DEM results with our simulations is necessary to test the limits of both kinematic and $\mu(I)$ models. It can however be inferred from the literature that the $\mu(I)$ model should be more flexible to describe the flow in various situations (different values of wall angle, internal friction angle, etc.) than the kinematic model.

Effect of the outlet size on the flowrate

In further simulations, we tested the influence of the outlet size on the discharge flowrate to see if we could recover the Beverloo scaling law, which relates the mass discharge flowrate to the outlet diameter. The results are presented in Figure 94a). As seen from the simulated results, there is a positive correlation between the diameter of the outlet and the mass discharge flowrate. However, it is far from the values predicted by the Beverloo scaling law with usual parameters C_B = 0.58 and k_B = 0 [174]. This is because the Beverloo law is applicable in cases where the burden falls freely upon reaching the outlet. In this regard, it was recently numerically validated [174]. On the contrary, shaft furnaces use discharge systems to limit the discharge flowrate in order to increase the residence time in the shaft and ensure a uniform descent of the burden. These discharge systems rely on screw dischargers, rotors, wiper bars or rotary valves for this purpose, see e.g. [199, 200].

In the simulation corresponding to Figure 94b), the parameters of the Beverloo scaling law were fitted to the simulation results from the $\mu(I)$ model and the best fit was obtained for C_B = 0.00074 and k_B = 0. The fitted value of C_B is far from the usual experimental values, for the reasons explained above. Moreover, the agreement between the simulations and the law with the fitted parameters is not quite satisfying for the range of outlet diameters studied. This indicates that the Beverloo law does not apply in this physical situation. Rather, shaft furnace models should include the simulation of discharge systems to properly describe the solid flow.

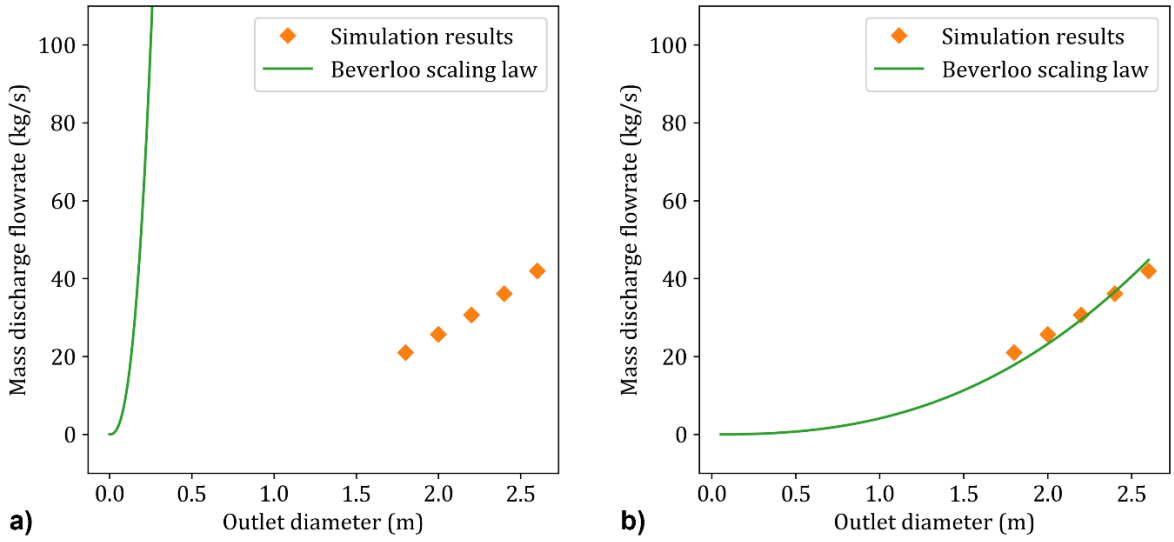

Figure 94: Mass discharge flowrate obtained from the simulation results (orange dots) and from the Beverloo scaling law (green solid line) with **a)** parameters from the literature (C_B = 0.58, k_B = 0) and **b)** parameters obtained from curve-fitting on the simulation results (C_B = 0.00074, k_B = 0). Simulations were led with the usual parameters: $\Delta p_{dyn} = 400\ Pa, \eta_0 = 267\ Pa.s, m_p = 1\ s, \Phi_w = 26.2°, \Phi_s = 52°, \mu_2 = 0.9, I_0 = 0.4, d_p = 15\ mm, \lambda_r = 10^{-5}$. The mass density used in the Beverloo scaling law is $\rho_b = \epsilon_{bed}\rho_p = 1815\ kg.m^{-3}$.

IV.5. Conclusion and outlook

In this chapter, a rheological model was developed to simulate the flow of iron ore pellets in a shaft furnace. The model is based on the popular *μ(I)* rheology, which describes a non-Newtonian fluid with a friction coefficient *μ(I)* that accounts for the inertial properties of the flow. This model should be considered as still under development. To this point, it cannot solve the pressure field on its own, so that it must rely on an external pressure field derived from analytical correlations or experimental measurements. However, under appropriate calibration, it is able to reproduce the flow pattern and stagnant zones observed in experiments and DEM simulations.

The major improvements to bring to this model before it can provide us with accurate predictions are the following:

- a robust algorithm to determine the pressure field. As mentioned earlier, this is a difficult task since the flow of materials with yield introduces high non-linearities that complicate the convergence;
- an experimental validation of the *μ(I)* rheology for conical hoppers equipped with the typical discharge systems that can be found in shaft furnaces, and a thorough determination of the rheological parameters. This would also be useful to determine the boundary conditions in a shaft furnace, which differ from the ones of the classical silo discharge.

In the case where, despite those improvements, the rheological *μ(I)* law was proven unable to properly describe the flow of pellets in a shaft furnace, another framework would then be necessary. A continuum approach would be preferred, since it requires less computational cost than DEM: to this end, the non-local approaches [183] and the solid-fluid bridging theories [166, 169] represent considerable research opportunities. On the short term, the DEM framework can

offer supplementary validation compared to experiments; on the long term, its predicting capabilities should become sufficiently reliable to become the main tool of granular flow modeling, particularly for the industry of direct reduction.

General conclusion and outlook

In the European MaxH2DR project in the framework of which the present work was carried out, the direct reduction of iron ores by a hydrogen-rich gas is studied at multiple scales: from powders to pellets to the shaft furnace and even to the steelmaking plant. The core objective of this project is to identify and bring innovative solutions to the challenges of hydrogen enrichment in the direct reduction shaft furnaces. In this context, UL brought state-of-the-art knowledge in reduction kinetics, gas-solid reactions modeling and finite-volume process modeling. The work presented here put particular emphasis on the modeling of reduction kinetics with hydrogen, relying on a proper characterization of the ores used in reduction experiments. Additionally, the shaft furnace simulator REDUCTOR previously developed in our research group at UL was further improved to gain accuracy and simulate new, unexplored conditions. A continuum model of the flow of pellets within the shaft was also explored. On the basis of these findings, we proposed several leads for the optimized operation of future hydrogen-based shaft furnaces.

The optimization of the reduction processes requires a reliable knowledge of the reduction kinetics. To this end, we used different TGA devices to study the isothermal reduction of hematite pellets by a hydrogen-rich gas. These experiments were realized in a wide range of experimental conditions (varied temperatures, gas dilution, gas flowrates, water contents) and were used to validate a new modified grainy pellet model (MGPM) presented in Article 1. In particular, we showcased the saturation of the gas atmosphere with water vapor at low gas flowrate in TGA devices, and we proposed an accurate modeling of this phenomenon. Additional results were presented in the rest of Chapter I, especially regarding the causes of the kinetic slowdowns observed around 700°C and 950°C, which were clarified, and the dramatic increase in reduction rate at temperatures above 1000°C that was experimentally demonstrated.

Such reduction kinetics are inextricably tied up to the evolution of the pellet structure undergoing reduction process. The latter greatly changes as oxygen is removed, which can in turn considerably affect the kinetics. The physical characterization of several partially reduced pellets enabled us to outline the macroscopic features of the reduction with hydrogen, as presented in Article 2. We showed that the reduction resulted in a dramatic increase in specific surface area and porosity, related to the formation of new pores at the beginning of the reduction. Larger pores are observed with increasing temperature and reduction degree, resulting in the alteration of the iron oxide grains. Above 800°C, these grains disintegrate as wustite is converted to iron, and dense sponge iron is formed. Below 800°C, disintegration of the wustite grains is less frequent and the freshly formed iron is rather porous.

At the scale of the shaft furnace, the hydrogen enrichment of the reducing gas was approached using the in-house REDUCTOR model, which simulates both the reduction and cooling zones of a shaft furnace in a 2D finite-volume framework. This model includes the reduction reactions with CO and H_2 as well as the principal gas-gas and carbon deposition reactions. The operation of a H_2 direct reduction shaft furnace was analyzed in depth in Article 3. In this type of furnace, heat supply is a crucial issue because of the endothermic nature of the reduction with hydrogen. We investigated this issue through an extensive parametric study, in which we considered several innovative solutions. The redirection of a part of the bustle gas to the cooling gas inlet homogenizes the hydrogen supply in the furnace, achieving a higher metallization of the burden with a lesser gas heating expense. In another simulation, we showed that an increase in metallization from 94% to 100% is possible accepting a reasonable increase in the energy consumption (+6.4%). We also studied the influence of the gas pressure and the effect of an

additional injection of reducing gas at the center of the furnace on the metallization of the burden. It was shown that an increase in pressure results in a minor increase in metallization, which is limited by heat supply rather than by the reduction kinetics. The injection of a part of the bustle gas at the center of the furnace greatly improves the supply of heat and reductant gas there, leading to a surge in the metallization degree. Finally, the operation of a shaft furnace with lower H_2:CO ratios proved to be effective in solving the heat supply issue, at the cost of a considerable increase in carbon emissions.

In the last Chapter of this manuscript, we investigated the continuum modeling of the flow of pellets in a shaft furnace with the objective to calculate the solid velocity distribution and to predict the possible formation of stagnant zones within the shaft. We used a specific friction rheology model to describe the flow of pellets in the framework of the Navier Stokes equations. At this stage, the model is able to qualitatively simulate the flow of pellets in a the shaft under different configurations. With a more thorough description of the discharge systems of industrial shaft furnaces, we believe that such a model could give satisfying quantitative results and could then be completely integrated into REDUCTOR.

The direct reduction of iron ores by hydrogen stands as a promising technology for the decarbonization of the steelmaking industry. Further research is however needed to untangle the intricate features of the reduction process and to offer interesting prospects for the direct reduction industry. At the laboratory scale, a few questions still need to be solved. The influence of pellet size on the reduction rate is still not well understood, together with the core-shell evolution of the porous structure and the possible presence of a compact core. Additionally, the dramatic evolution of the porous structure at high temperatures and the resulting swelling and cracking phenomena need to be modeled in order to correctly assess the reduction rate. Both of these subjects heavily depend on the influence of the gangue composition, which need to be thoroughly investigated. To this end, a systematic observation of the porous structure is needed – either with interrupted reduction experiments followed by SEM observations, or with in-situ SEM experiments. The use of X-ray tomography could also be handful, provided that it offers sufficient spatial resolution. In addition, these results could shed light on the microscopic features of the reduction, regarding the formation of pores or the nucleation of the iron phase.

Future work should aim at the validation of the MGPM in non-isothermal and dynamic gas conditions. If the use of carbon-bearing gas was pursued in the industry, the proper determination of the reforming and carburization kinetics would also become a crucial issue. In particular, it would be useful to find conditions which ensure great reduction and carburization of the pellets, avoiding the formation of carbon soot. Finally, using different syngas injections with different H_2:CO ratios may also be of interest for the reduction of pellets in the industry. Regarding the operation of pure hydrogen shaft furnaces, industrial data are still greatly awaited for technology upscaling and model validation. In particular, data related to the flow of pellets are of particular interest in order to design a furnace that would be resilient against sticking and clustering phenomena. The development of continuum and discrete methods could be helpful in this regard. Regarding process optimization, a thorough investigation of the role of lateral and central injections should help to make consistent gains in gas and energy demand for both hydrogen and syngas shaft furnaces.

At a larger scale, emphasis should be set on the use of alternative iron oxide feedstock in shaft furnaces as the high-grade hematite feedstock is becoming scarce. The reduction kinetics of ores made of magnetite, goethite or vanadium-titanomagnetite should be considered, as well as the operation of shaft furnaces fed with these materials.

References

[1] IPCC, « Climate Change 2023: Synthesis Report. Contribution of Working Groups I, II and III to the Sixth Assessment Report of the Intergovernmental Panel on Climate Change ». IPCC, 2023. [En ligne]. Disponible sur: https://www.ipcc.ch/report/ar6/syr/downloads/report/IPCC_AR6_SYR_SPM.pdf

[2] « GHG emissions of all world countries ». Publications Office of the European Union, 2024. [En ligne]. Disponible sur: https://data.europa.eu/doi/10.2760/4002897

[3] J. Somers et others, *Technologies to decarbonise the EU steel industry*. 2022.

[4] « Iron and Steel Technology Roadmap ». IEA, 2020.

[5] M. Shahabuddin, G. Brooks, et M. A. Rhamdhani, « Decarbonisation and hydrogen integration of steel industries: recent development, challenges and technoeconomic analysis », *J. Clean. Prod.*, vol. 395, p. 136391, 2023.

[6] A. Zakeri, K. S. Coley, et L. Tafaghodi, « Microstructural Evolution and Its Effect on Reaction Rate During Reduction of High-Grade Hematite Ore Pellets With Hydrogen », *Journal of Sustainable Metallurgy*, vol. 11, nº 1, p. 278-299, 2025.

[7] L. Staron, P.-Y. Lagrée, et S. Popinet, « Continuum simulation of the discharge of the granular silo: a validation test for the μ (I) visco-plastic flow law », *The European Physical Journal E*, vol. 37, p. 1-12, 2014.

[8] T. Papanastasiou et A. Boudouvis, « Flows of viscoplastic materials: models and computations », *Computers & Structures*, vol. 64, nº 1-4, p. 677-694, 1997.

[9] J. Chauchat et M. Médale, « A three-dimensional numerical model for dense granular flows based on the μ (I) rheology », *Journal of Computational Physics*, vol. 256, p. 696-712, 2014.

[10] « World Steel in Figures ». World Steel Association, 2025.

[11] V. B. Angalakuditi, P. Bhadravathi, R. Gujare, G. Ayyappan, L. R. Singh, et S. S. Baral, « Mineralogical aspects of reducing lump iron ore, pellets, and sinter with hydrogen », *Metall. Mater. Trans. B*, vol. 53, nº 2, p. 1036, 2022.

[12] J. Astier, « Réduction Directe », 2005.

[13] H. Suopajärvi *et al.*, « Use of biomass in integrated steelmaking – Status quo, future needs and comparison to other low-CO2 steel production technologies », *Applied Energy*, vol. 213, p. 384-407, 2018, doi: https://doi.org/10.1016/j.apenergy.2018.01.060.

[14] R. Wang, Y. Zhao, A. Babich, D. Senk, et X. Fan, « Hydrogen direct reduction (H-DR) in steel industry—An overview of challenges and opportunities », *Journal of Cleaner Production*, vol. 329, p. 129797, 2021.

[15] « Direct Reduced Iron Process ». [En ligne]. Disponible sur: https://www.lmmgroupcn.com/direct-reduced-iron-process/.

[16] H. Hamadeh, « Modélisation mathématique détaillée du procédé de réduction directe du minerai de fer », Université de Lorraine, 2017. [En ligne]. Disponible sur: https://theses.hal.science/tel-01740462

[17] D. Wagner, « Etude expérimentale et modélisation de la réduction du minerai de fer par l'hydrogène », PhD Thesis, Institut National Polytechnique de Lorraine-INPL, 2008.

[18] A. Ranzani Da Costa, « La réduction du minerai de fer par l'hydrogène : étude cinétique, phénomène de collage et modélisation », Université de Lorraine, 2011.

[19] « MaxH2DR ». Consulté le: 8 août 2025. [En ligne]. Disponible sur: https://www.estep.eu/clean–steel– partnership/maxh2dr

[20] A. A. El-Geassy, « Gaseous reduction of Fe2O3 compacts at 600 to 1050° C », *J Mater Sci*, vol. 21, nº 11, p. 3889-3900, nov. 1986, doi: 10.1007/BF02431626.

[21] N. Towhidi et J. Szekely, « The influence of carbon deposition on the reduction kinetics of commercial grade hematite pellets with CO, H2, and N2 », *Metall Trans B*, vol. 14, nº 3, p. 359-367, sept. 1983, doi: 10.1007/BF02654354.

[22] H. Zuo, C. Wang, J. Dong, K. Jiao, et R. Xu, « Reduction kinetics of iron oxide pellets with H2 and CO mixtures », *Int J Miner Metall Mater*, vol. 22, nº 7, p. 688-696, juill. 2015, doi: 10.1007/s12613-015-1123-x.
[23] Y. Fei, X. Guan, S. Kuang, A. Yu, et N. Yang, « A Review on the Modeling and Simulation of Shaft Furnace Hydrogen Metallurgy: A Chemical Engineering Perspective », *ACS Eng. Au*, vol. 4, nº 2, p. 145-165, avr. 2024, doi: 10.1021/acsengineeringau.3c00033.
[24] E. Salucci, A. D'Angelo, V. Russo, H. Grénman, et H. Saxén, « Review on the Reduction Kinetics of Iron Oxides with Hydrogen-Rich Gas: Experimental Investigation and Modeling Approaches », *Industrial & Engineering Chemistry Research*, vol. 64, nº 1, p. 1-35, 2024.
[25] R. Takahashi, Y. Takahashi, J. Yagi, et Y. Omori, « Operation and simulation of pressurized shaft furnace for direct reduction. », *ISIJ Int.*, vol. 26, nº 9, p. 765-774, 1986, doi: 10.2355/isijinternational1966.26.765.
[26] A. Zare Ghadi, N. Radfar, M. S. Valipour, et H. Y. Sohn, « A Review on the Modeling of Direct Reduction of Iron Oxides in Gas-Based Shaft Furnaces », *steel research international*, vol. 94, nº 6, p. 2200742, 2023, doi: 10.1002/srin.202200742.
[27] H. Pousette, N. Kojola, et O. Hessling, « Reduction and Carburization Mechanisms for CO + H2 Reduction in Shaft Furnace Conditions », *Metall Mater Trans B*, vol. 55, nº 6, p. 4257-4270, déc. 2024, doi: 10.1007/s11663-024-03235-7.
[28] T. K. S. Kumar, J. Alatalo, H. Ahmed, et B. Björkman, « Effect of Temperature and Gas Mixtures on Cementite Formation During the Carburization of Hydrogen-Reduced DRI », *J. Sustain. Metall.*, vol. 8, nº 4, p. 1450-1464, déc. 2022, doi: 10.1007/s40831-022-00601-0.
[29] K. Alhumaizi, A. Ajbar, et M. Soliman, « Modelling the complex interactions between reformer and reduction furnace in a midrex-based iron plant », *The Canadian Journal of Chemical Engineering*, vol. 90, nº 5, p. 1120-1141, 2012.
[30] M. L. Ali, Q. Fradet, et U. Riedel, « Kinetic mechanism development for the direct reduction of single hematite pellets in H2/CO atmospheres », *steel research international*, vol. 93, nº 12, p. 2200043, 2022.
[31] J. Chipman, « Thermodynamics and phase diagram of the Fe-C system », *Metallurgical Transactions*, vol. 3, nº 1, p. 55-64, janv. 1972, doi: 10.1007/BF02680585.
[32] T. Ramos Ribeiro, J. B. Ferreira Neto, J. G. Rocha Poço, C. Takano, L. Kolbeinsen, et E. Ringdalen, « Steam Reforming of Methane on Sponge Iron: Influence of Gas Composition on Reaction Rate », *ISIJ International*, vol. 61, nº 1, p. 182-189, 2021, doi: 10.2355/isijinternational.ISIJINT-2019-477.
[33] F. Patisson et O. Mirgaux, « Hydrogen Ironmaking: How It Works », *Metals*, vol. 10, nº 7, p. 922, juill. 2020, doi: 10.3390/met10070922.
[34] A. A. El-Geassy et V. Rajakumar, « Gaseous reduction of wustite with H2, CO and H2-CO mixtures », *Transactions of the Iron and Steel Institute of Japan*, vol. 25, nº 6, p. 449-458, 1985.
[35] D. Wang *et al.*, « Innovative evaluation of CO–H2 interaction during gaseous wustite reduction controlled by external gas diffusion », *international journal of hydrogen energy*, vol. 42, nº 20, p. 14047-14057, 2017.
[36] L. Yi, Z. Huang, H. Peng, et T. Jiang, « Action rules of H2 and CO in gas-based direct reduction of iron ore pellets », *J. Cent. South Univ.*, vol. 19, nº 8, p. 2291-2296, août 2012, doi: 10.1007/s11771-012-1274-0.
[37] Z. Shen, S. Sun, J. Xu, Q. Liang, et H. Liu, « Experimental and modeling study on reduction and heat transfer characteristics of single iron ore pellet in H2/CO atmospheres », *ISIJ International*, vol. 63, nº 1, p. 42-53, 2023.
[38] M. Kazemi, M. S. Pour, et D. Sichen, « Experimental and Modeling Study on Reduction of Hematite Pellets by Hydrogen Gas », *Metall Mater Trans B*, vol. 48, nº 2, p. 1114-1122, avr. 2017, doi: 10.1007/s11663-016-0895-3.

[39] A. Zakeri, K. S. Coley, et L. Tafaghodi, « Hydrogen-Based Direct Reduction of Iron Oxides: A Review on the Influence of Impurities », *Sustainability*, vol. 15, nº 17, p. 13047, août 2023, doi: 10.3390/su151713047.
[40] Y. He et P. C. Pistorius, « Laboratory Carburization of Direct-Reduced Iron in CH4-H2-N2 Gas Mixtures, and Comparison with Industrial Samples », *Metall Mater Trans B*, vol. 47, nº 3, p. 1538-1541, juin 2016, doi: 10.1007/s11663-016-0619-8.
[41] P. Münster et H. Grabke, « Kinetics of the Steam Reforming of Methane on Iron as a Catalyst », *Ber. Bunsenges. Phys. Chem.;(Germany, Federal Republic of)*, vol. 84, nº 10, 1980.
[42] T. Ramos Ribeiro, J. B. Ferreira Neto, J. G. Rocha Poço, C. Takano, L. Kolbeinsen, et E. Ringdalen, « Kinetics Analysis of Steam Reforming of Methane on Sponge Iron », *ISIJ International*, vol. 62, nº 3, p. 504-514, 2022, doi: 10.2355/isijinternational.ISIJINT-2021-472.
[43] J. Szekely, J. W. Evans, et H. Y. Sohn, *Gas-solid reactions*. New York: Academic Press, 1976.
[44] W. E. Ranz et W. R. Marshall, « Evaporation from drops », *Chem. Eng. Prog*, nº 48, p. 141-180, 1952.
[45] C. R. Wilke, « A viscosity equation for gas mixtures », *Journal of Chemical physics*, vol. 18, nº 4, p. 517-519, 1950.
[46] M. Tokuda, H. Yoshikoshi, et M. Ohtani, « Kinetics of the Reduction of Iron Ore », *ISIJ Int.*, vol. 13, nº 5, p. 350-363, 1973, doi: 10.2355/isijinternational1966.13.350.
[47] H. Y. Sohn, « The law of additive reaction times in fluid-solid reactions », *Metall Trans B*, vol. 9, nº 1, p. 89-96, mars 1978, doi: 10.1007/BF02822675.
[48] H. Ahn et S. Choi, « A comparison of the shrinking core model and the grain model for the iron ore pellet indurator simulation », *Computers & Chemical Engineering*, vol. 97, p. 13-26, févr. 2017, doi: 10.1016/j.compchemeng.2016.11.005.
[49] P. Metolina, T. R. Ribeiro, et R. Guardani, « Hydrogen-based direct reduction of industrial iron ore pellets: Statistically designed experiments and computational simulation », *Int J Miner Metall Mater*, vol. 29, nº 10, p. 1908-1921, oct. 2022, doi: 10.1007/s12613-022-2487-3.
[50] M. S. Valipour, M. Y. Motamed Hashemi, et Y. Saboohi, « Mathematical modeling of the reaction in an iron ore pellet using a mixture of hydrogen, water vapor, carbon monoxide and carbon dioxide: an isothermal study », *Advanced Powder Technology*, vol. 17, nº 3, p. 277-295, 2006, doi: 10.1163/156855206777213375.
[51] D. Wagner, O. Devisme, F. Patisson, et D. Ablitzer, « A laboratory study of the reduction of iron oxides by hydrogen », 2008.
[52] J. Swisher et E. Turkdogan, « Solubility, permeability, and diffusivity of oxygen in solid iron », *AIME Met Soc Trans*, vol. 239, nº 4, p. 426-431, 1967.
[53] B. Smith RJ, M. Loganathan, et M. S. Shantha, « A review of the water gas shift reaction kinetics », *International Journal of Chemical Reactor Engineering*, vol. 8, nº 1, 2010.
[54] H. Ono-Nakazato, T. Yonezawa, et T. Usui, « Effect of water-gas shift reaction on reduction of iron oxide powder packed bed with H2-CO mixtures », *ISIJ international*, vol. 43, nº 10, p. 1502-1511, 2003.
[55] « MaxH2DR project ». 2025. Consulté le: 8 août 2025. [En ligne]. Disponible sur: https://www.estep.eu/clean–steel–partnership/
[56] M. L. Ali, Q. Fradet, et U. Riedel, « Particle-resolved computational modeling of hydrogen-based direct reduction of iron ore pellets in a fixed bed. Part I: Methodology and validation », *International Journal of Hydrogen Energy*, vol. 87, p. 332-343, oct. 2024, doi: 10.1016/j.ijhydene.2024.09.028.
[57] A. A. Elsherbiny *et al.*, « Parametric study on hematite pellet direct reduction by hydrogen », *Powder Technology*, vol. 435, p. 119434, févr. 2024, doi: 10.1016/j.powtec.2024.119434.
[58] O. Hessling, J. B. Fogelström, N. Kojola, et J. Martinsson, « Influence of Water Content on the Kinetics and Mechanisms of Hydrogen Reduction Using Industrial Iron Ore Pellets at 873

K–1173 K », *ISIJ Int.*, vol. 64, nº 10, p. 1493-1502, 2024, doi: 10.2355/isijinternational.ISIJINT-2023-443.
[59] A. Meshram, J. Govro, R. J. OMalley, S. Sridhar, et Y. Korobeinikov, « Modeling Isothermal Reduction of Iron Ore Pellet Using Finite Element Analysis Method: Experiments & Validation », *Metals*, vol. 12, nº 12, p. 2026, nov. 2022, doi: 10.3390/met12122026.
[60] M. Ohmi et T. Usui, « Improved Theory on the Rate of Reduction of Single Particles and Fixed Beds of Iron Oxide Pellets with Hydrogen », *Transactions of the Iron and Steel Institute of Japan*, vol. 22, nº 1, p. 66-74, 1982, doi: 10.2355/isijinternational1966.22.66.
[61] B. Sadeghi, P. Cavaliere, M. Bayat, N. Ebrahimzadeh Esfahani, A. Laska, et D. Koszelow, « Experimental study and numerical simulation on porosity dependent direct reducibility of high-grade iron oxide pellets in hydrogen », *International Journal of Hydrogen Energy*, vol. 69, p. 586-607, juin 2024, doi: 10.1016/j.ijhydene.2024.05.050.
[62] E. T. Turkdogan et J. V. Vinters, « Gaseous reduction of iron oxides: Part I. Reduction of hematite in hydrogen », *Metall Trans*, vol. 2, nº 11, p. 3175-3188, nov. 1971, doi: 10.1007/BF02814970.
[63] R. G. Olsson et W. M. McKewan, « Diffusion of H2-H2O through porous iron formed by the reduction of iron oxides », *Metall Trans*, vol. 1, nº 6, p. 1507-1512, juin 1970, doi: 10.1007/BF02641993.
[64] Ö. Özgün, I. Dirba, O. Gutfleisch, Y. Ma, et D. Raabe, « Green Ironmaking at Higher H2 Pressure: Reduction Kinetics and Microstructure Formation During Hydrogen-Based Direct Reduction of Hematite Pellets », *J. Sustain. Metall.*, vol. 10, nº 3, p. 1127-1140, sept. 2024, doi: 10.1007/s40831-024-00877-4.
[65] Q. Fradet, M. Kurnatowska, et U. Riedel, « Thermochemical reduction of iron oxide powders with hydrogen: Review of selected thermal analysis studies », *Thermochimica Acta*, vol. 726, p. 179552, août 2023, doi: 10.1016/j.tca.2023.179552.
[66] A. Zhang, B. J. Monaghan, R. J. Longbottom, M. Nusheh, et C. W. Bumby, « Reduction Kinetics of Oxidized New Zealand Ironsand Pellets in H2 at Temperatures up to 1443 K », *Metall Mater Trans B*, vol. 51, nº 2, p. 492-504, avr. 2020, doi: 10.1007/s11663-020-01790-3.
[67] J. O. Edström, « The mechanism of reduction of iron oxides », *J. Iron and Steel Inst.*, nº 175, p. 289-304, 1953.
[68] S.-H. Kim *et al.*, « Influence of microstructure and atomic-scale chemistry on the direct reduction of iron ore with hydrogen at 700°C », *Acta Materialia*, vol. 212, p. 116933, juin 2021, doi: 10.1016/j.actamat.2021.116933.
[69] Y. Ma *et al.*, « Hydrogen-based direct reduction of iron oxide at 700°C: Heterogeneity at pellet and microstructure scales », *Int J Miner Metall Mater*, vol. 29, nº 10, p. 1901-1907, oct. 2022, doi: 10.1007/s12613-022-2440-5.
[70] Q. T. Tsay, W. H. Ray, et J. Szekely, « The modeling of hematite reduction with hydrogen plus carbon monoxide mixtures: Part I. The behavior of single pellets », *AIChE Journal*, vol. 22, nº 6, p. 1064-1072, nov. 1976, doi: 10.1002/aic.690220617.
[71] A. Skaf, L. Tiruta-Barna, et A. Ahmadi, « Assessing the potential of low-temperature ironmaking using pure hydrogen in shaft reactors », *Chemical Engineering Science*, vol. 304, p. 121049, févr. 2025, doi: 10.1016/j.ces.2024.121049.
[72] B. Dussoubs, J. Jourde, F. Patisson, J.-L. Houzelot, et D. Ablitzer, « Modelling of a moving bed furnace for the production of uranium tetrafluoride. Part 2: Application of the model », *Chemical Engineering Science*, vol. 58, nº 12, p. 2629-2642, 2003, doi: https://doi.org/10.1016/S0009-2509(03)00121-0.
[73] « MaxH2DR D1.2. » 2025. Consulté le: 8 août 2025. [En ligne]. Disponible sur: https://www.estep.eu/assets/Projects/MaxH2DR/MaxH2DR_D2_D1.2_Procedures–for–the–determination–of–physical–properties–of–DR–raw–materials–intermediate–and–products.pdf

[74] M. Ohmi, T. Usui, M. Naito, et Y. Minamide, « Experimental Study of the Resistance due to the Rate of Gas Flow on the Hydrogen Reduction of an Iron Oxide Pellet », *ISIJ Int.*, vol. 23, nº 1, p. 81-89, 1983, doi: 10.2355/isijinternational1966.23.81.
[75] H. Kang *et al.*, « Influence of hydrogen flow rate on multistep kinetics of hematite reduction », *International Journal of Hydrogen Energy*, vol. 49, p. 1255-1268, janv. 2024, doi: 10.1016/j.ijhydene.2023.08.295.
[76] O. Hessling, « Some aspects of hydrogen reduction of iron ore », KTH Royal Institute of Technology, 2024.
[77] A. Ranzani Da Costa, D. Wagner, et F. Patisson, « Modelling a new, low CO2 emissions, hydrogen steelmaking process », *Journal of Cleaner Production*, vol. 46, p. 27-35, mai 2013, doi: 10.1016/j.jclepro.2012.07.045.
[78] A. Pineau, N. Kanari, et I. Gaballah, « Kinetics of reduction of iron oxides by H2 », *Thermochimica Acta*, vol. 447, nº 1, p. 89-100, août 2006, doi: 10.1016/j.tca.2005.10.004.
[79] P. Garg, X. Hu, Y. Li, K. Li, S. Nag, et J. Zhang, « Kinetics of Iron Oxide Reduction in H2/H2O Gas Mixture: Global and Stepwise Reduction », *Metall Mater Trans B*, vol. 53, nº 3, p. 1759-1774, juin 2022, doi: 10.1007/s11663-022-02485-7.
[80] D. Spreitzer et J. Schenk, « Reduction of Iron Oxides with Hydrogen—A Review », *steel research int.*, vol. 90, nº 10, p. 1900108, oct. 2019, doi: 10.1002/srin.201900108.
[81] Q. Fradet, M. L. Ali, et U. Riedel, « Development of a Porous Solid Model for the Direct Reduction of Iron Ore Pellets », *steel research international*, vol. 93, nº 12, p. 2200042, 2022, doi: 10.1002/srin.202200042.
[82] R. S. Brodkey et H. C. Hershey, *Transport phenomena: a unified approach*. Brodkey publishing, 2003.
[83] E. Pescott, « Kinetics of the gaseous direct reduction of iron ores in multi-component gas mixtures », *Rapport interne de la société British Steel*, 1976.
[84] C. Scharm *et al.*, « Direct reduction of iron ore pellets by H2 and CO: in-situ investigation of the structural transformation and reduction progression caused by atmosphere and temperature », *Miner. Eng.*, vol. 180, p. 107459, 2022.
[85] M. A. Meyers et T. Tantevee, « Stresses induced in iron-ore pellets by hydrogen reduction », *Metallurgical Transactions B*, vol. 17, p. 217-227, 1986.
[86] E. Turkdogan, R. Olsson, et J. Vinters, « Gaseous reduction of iron oxides: Part II. Pore characteristics of iron reduced from hematite in hydrogen », *Metallurgical Transactions*, vol. 2, nº 11, p. 3189-3196, 1971.
[87] T. Lei *et al.*, « Global iron and steel plant CO2 emissions and carbon-neutrality pathways », *Nature*, vol. 622, p. 514, 2023.
[88] A. Marsigny, J. B. Letz, O. Mirgaux, et F. Patisson, « Kinetics of the reduction of iron ore pellets with hydrogen: a parametric experimental and modeling study », *Metals*, vol. under review.
[89] L. Yi, Z. Huang, T. Jiang, L. Wang, et T. Qi, « Swelling behavior of iron ore pellet reduced by H2–CO mixtures », *Powder Technology*, vol. 269, p. 290-295, 2015.
[90] O. Kovtun, M. Levchenko, E. Oldinski, M. Gräbner, et O. Volkova, « Swelling behavior of iron ore pellets during reduction in H2 and N2/H2 atmospheres at different temperatures », *steel research international*, vol. 94, nº 10, p. 2300140, 2023.
[91] A. Meshram, Y. Korobeinikov, X. Wei, R. J. OMalley, et S. Sridhar, « Quantification of Swelling in Hematite Pellets Reduced Using Hydrogen–Nitrogen Gas Mixture », *steel research international*, vol. 96, nº 5, p. 2400442, 2025.
[92] S. Purohit, M. I. Pownceby, et A. Guiraud, « Sticking and Swelling of Iron Ore Pellets: Mechanisms and Controlling Factors », *Journal of Sustainable Metallurgy*, vol. 11, nº 1, p. 67-87, mars 2025, doi: 10.1007/s40831-024-01000-3.
[93] Y. Korobeinikov *et al.*, « Reduction of Iron-Ore Pellets Using Different Gas Mixtures and Temperatures », *steel research int.*, vol. 94, nº 10, p. 2300066, oct. 2023, doi: 10.1002/srin.202300066.

[94] O. Kovtun, M. Levchenko, M. O. Ilatovskaia, C. G. Aneziris, et O. Volkova, « Results of hydrogen reduction of iron ore pellets at different temperatures », *steel research international*, vol. 96, nº 5, p. 2300707, 2025.
[95] P. Hayes, « Analysis of product morphologies and reaction mechanisms on gaseous reduction of iron oxides », *steel research international*, vol. 82, nº 5, p. 480-493, 2011.
[96] E. Turkdogan et J. Vinters, « Gaseous reduction of iron oxides: Part III. Reduction-oxidation of porous and dense iron oxides and iron », *Metallurgical Transactions*, vol. 3, nº 6, p. 1561-1574, 1972.
[97] M. Moukassi, P. Steinmetz, B. Dupre, et C. Gleitzer, « A study of the mechanism of reduction with hydrogen of pure wustite single crystals », *Metallurgical Transactions B*, vol. 14, nº 1, p. 125-132, 1983.
[98] A. Abdelrahim, M. Iljana, M. Omran, T. Vuolio, H. Bartusch, et T. Fabritius, « Influence of H2-H2O content on the reduction of acid iron ore pellets in a CO-CO2-N2 reducing atmosphere », *ISIJ. Int.*, vol. 60, nº 10, p. 2206, 2020.
[99] L. von Bogdandy et H.-J. Engell, *The reduction of iron ores: scientific basis and technology*. Springer Science & Business Media, 2013.
[100] Y. Pan *et al.*, « Alloying Effects on Iron Oxide Redox Pathways: Insights into Sustainable Hydrogen-Based Reduction », *The Journal of Physical Chemistry Letters*, vol. 16, p. 5506-5514, 2025.
[101] S. Tong, Y. Xu, L. Hong, C. Sun, L. Ai, et J. Chen, « Study on pore structure of iron phase in magnetite pellets reduced by pure hydrogen based on nitrogen adsorption method », *International Journal of Hydrogen Energy*, vol. 114, p. 186-193, 2025.
[102] R. Findorák *et al.*, « Experiments and Simulations on the Low-Temperature Reduction of Iron Ore Oxide Pellets with Hydrogen », *Metals*, vol. 15, nº 3, p. 289, 2025.
[103] D. S. John et P. Hayes, « Microstructural features produced by the reduction of wustite in H2/H2O gas mixtures », *Metallurgical Transactions B*, vol. 13, nº 1, p. 117-124, 1982.
[104] S. E. Moujahid et A. Rist, « The nucleation of iron on dense wustite: a morphological study », *Metallurgical Transactions B*, vol. 19, nº 5, p. 787-802, 1988.
[105] Ö. Özgün, I. Dirba, O. Gutfleisch, Y. Ma, et D. Raabe, « Green ironmaking at higher H2 pressure: reduction kinetics and microstructure formation during hydrogen-based direct reduction of hematite pellets », *Journal of Sustainable Metallurgy*, vol. 10, nº 3, p. 1127-1140, 2024.
[106] E. AA et V. Rajakumar, « Gaseous reduction of wustite with H2, CO and H2-CO mixtures », *Transactions of the Iron and Steel Institute of Japan*, vol. 25, nº 6, p. 449-458, 1985.
[107] D. S. John, S. Matthew, et P. Hayes, « The breakdown of dense iron layers on wustite in CO/CO2 and H2/H2O systems », *Metallurgical Transactions B*, vol. 15, nº 4, p. 701-708, 1984.
[108] S. Matthew, T. Cho, et P. Hayes, « Mechanisms of porous iron growth on wustite and magnetite during gaseous reduction », *Metallurgical transactions B*, vol. 21, nº 4, p. 733-741, 1990.
[109] L. Yi, Z. Huang, T. Jiang, L. Wang, et T. Qi, « Swelling behavior of iron ore pellet reduced by H2–CO mixtures », *Powder Technology*, vol. 269, p. 290-295, 2015, doi: https://doi.org/10.1016/j.powtec.2014.09.018.
[110] J. Feinman, « Kinetics of hydrogen reduction of iron ore in a batch-fluidized bed », *I. & EC. Process Des. Dev.*, vol. 3, nº 3, p. 241-247, 1964.
[111] A. El-Geassy et V. Rajakumar, « Influence of particle size on the gaseous reduction of wustite at 900-1100 C », *Transactions of the Iron and Steel Institute of Japan*, vol. 25, nº 12, p. 1202-1211, 1985.
[112] D. S. John, S. Matthew, et P. Hayes, « Establishment of product morphology during the initial stages of wustite reduction », *Metallurgical Transactions B*, vol. 15, nº 4, p. 709-717, 1984.

[113] Midrex Technologies Inc., « World Direct Reduction Statistics ». 2024. [En ligne]. Disponible sur: https://www.midrex.com/wp-content/uploads/MidrexSTATSBook2024.Final_.pdf
[114] A. Chatterjee, *Sponge iron production by direct reduction of iron oxide*. PHI Learning Pvt. Ltd., 2010.
[115] M. Kou *et al.*, « The effect of operational parameters on the characteristics of gas–solid flow inside the COREX shaft furnace », *Jom*, vol. 67, nº 2, p. 459-466, 2015.
[116] R. Beheshti, « Sustainable Aluminum and Iron Production », PhD Thesis, KTH Royal Institute of Technology, 2017.
[117] X. Chai, Q. Yue, Y. Zhang, et Q. Wang, « Analysis of energy consumption and its influencing factors in hydrogen metallurgy process », *Steel Res. Int.*, vol. 93, nº 7, p. 2100730, 2022.
[118] D. R. Parisi et M. A. Laborde, « Modeling of counter current moving bed gas-solid reactor used in direct reduction of iron ore », *Chem. Eng. J.*, vol. 104, nº 1–3, p. 35, 2004.
[119] Z. Yang *et al.*, « Thermodynamic strategy for hydrogen-based direct reduction shaft furnace to achieve a higher efficiency », *Ironmaking & Steelmaking*, p. 03019233241306335, 2024.
[120] B. Liu, Q. Li, Z. Zou, et A. Yu, « Theoretical Evaluation on Merits of the Processes of Gas-Based Shaft Furnace with Top Gas Recycling », *steel research international*, vol. 87, nº 5, p. 653-661, 2016.
[121] X. Besseron, P. Adhav, et B. Peters, « Parallel multi-physics coupled simulation of a midrex blast furnace », in *Proceedings of the International Conference on High Performance Computing in Asia-Pacific Region Workshops*, 2024, p. 87-98.
[122] T. Iwanaga *et al.*, « Analysis of Heat and Mass Transfer for Hydrogen-enriched Direct Reduction Process Based on DEM-CFD », *ISIJ International*, vol. 65, nº 6, p. 874-883, 2025.
[123] Y. Kaymak et V. Scherer, « Rheology model for simulation of particle flow in moving-bed reactors », présenté à 2nd International Workshop on Reacting Particle-Gas Systems, Magdeburg, 2025.
[124] S. La Manna *et al.*, « First steps in the endeavour to determine particle properties in the direct reduction process of iron ore pellets », in *9th European Coke and Ironmaking Congress (ECIC 2024)*, Curran Associates, Inc, 2024, p. 357-362.
[125] X. Tian *et al.*, « Numerical simulation of the influence of operating parameters on the inner characteristics in a hydrogen-enriched shaft furnace », *International Journal of Hydrogen Energy*, vol. 55, p. 1131-1142, 2024.
[126] J. Immonen et K. M. Powell, « Dynamic modeling of a direct reduced iron shaft furnace to enable pathways towards decarbonized steel production », *Chemical Engineering Science*, vol. 300, p. 120637, 2024.
[127] M. Hosseinzadeh, N. Kasiri, et M. Rezaei, « A comprehensive multiscale review of shaft furnace and reformer in direct reduction of iron oxide », *Minerals Engineering*, vol. 222, p. 109123, 2025, doi: https://doi.org/10.1016/j.mineng.2024.109123.
[128] R. Béchara, H. Hamadeh, O. Mirgaux, et F. Patisson, « Carbon impact mitigation of the iron ore direct reduction process through computer-aided optimization and design changes », *Metals*, vol. 10, nº 3, p. 367, 2020.
[129] R. Béchara, H. Hamadeh, O. Mirgaux, et F. Patisson, « Optimization of the iron ore direct reduction process through multiscale process modeling », *Materials*, vol. 11, nº 7, p. 1094, 2018.
[130] V. Vogl, M. Åhman, et L. J. Nilsson, « Assessment of hydrogen direct reduction for fossil-free steelmaking », *Journal of Cleaner Production*, vol. 203, p. 736-745, 2018, doi: https://doi.org/10.1016/j.jclepro.2018.08.279.
[131] M. Sun, K. Pang, X. Barati, et X. Meng, « Hydrogen-Based Reduction Technologies in Low-Carbon Sustainable Ironmaking and Steelmaking: A Review », *J. Sustain. Metall.*, p. 10-25, 2024.

[132] A. Öhman, E. Karakaya, et F. Urban, « Enabling the transition to a fossil-free steel sector: The conditions for technology transfer for hydrogen-based steelmaking in Europe. », *Energy Res. Soc. Sci*, vol. 84, nº 102384, 2022, [En ligne]. Disponible sur: https://doi.org/10.1016/j.erss.2021.102384
[133] L. Shao, Q. Wang, Y. Qu, H. Saxén, et Z. Zou, « A numerical study on the operation of the H2 shaft furnace with top gas recycling », *Metall. Mater. Trans. B*, vol. 52, nº 1, p. 451, 2021.
[134] L. Shao, J. Xu, H. Saxén, et Z. Zou, « A numerical study on process intensification of hydrogen reduction of iron oxide pellets in a shaft furnace », *Fuel*, vol. 348, nº 128375, 2023, [En ligne]. Disponible sur: https://doi.org/10.1016/j.fuel.2023.128375
[135] T. Quatravaux, J. Barros, P. Gardin, et G. Lucena, « Adaptation of the rist operating diagram as a graphical tool for the direct reduction shaft », *Metals*, vol. 11, nº 12, p. 1953, 2021.
[136] Y. Takenaka, Y. Kimura, K. Narita, et D. Kaneko, « Mathematical model of direct reduction shaft furnace and its application to actual operations of a model plant », *Computers & Chemical Engineering*, vol. 10, nº 1, p. 67-75, janv. 1986, doi: 10.1016/0098-1354(86)85047-5.
[137] Q. T. Tsay, W. H. Ray, et J. Szekely, « The modeling of hematite reduction with hydrogen plus carbon monoxide mixtures: Part II. The direct reduction process in a shaft furnace arrangement », *AIChE J.*, vol. 22, p. 1072-1079, 1976.
[138] T. Y. Omori, « Reduction of iron oxide pellets in moving bed », *Ironmak. Steelmak.*, vol. 3, p. 93-100, 1979.
[139] A. Shams et F. Moazeni, « Modeling and Simulation of the MIDREX Shaft Furnace: Reduction, Transition and Cooling Zones », *JOM*, vol. 67, p. 2681-2689, 2015.
[140] A. Zare Ghadi, M. S. Valipour, et M. Biglari, « CFD simulation of two-phase gas-particle flow in the Midrex shaft furnace: the effect of twin gas injection system on the performance of the reactor », *Int. J. Hydrogen Energy*, vol. 42, nº 1, p. 103, 2017.
[141] H. Hamadeh, O. Mirgaux, et F. Patisson, « Detailed modeling of the direct reduction of iron ore in a shaft furnace », *Materials*, vol. 11, nº 10, p. 1865, 2018.
[142] Z. Li, Z. Qi, L. Zhang, M. Guo, D. Liang, et Q. Dong, « Numerical simulation of H2-intensive shaft furnace direct reduction process », *J. Clean. Prod.*, vol. 409, p. 137059, 2023.
[143] M. S. Valipour et Y. Saboohi, « Numerical investigation of nonisothermal reduction of hematite using Syngas: The shaft scale study », *Model. Simul. Mater. Sci. Eng.*, vol. 15, nº 487, 2007, [En ligne]. Disponible sur: https://doi.org/10.1088/0965-0393/15/5/008
[144] S. Wu, J. Xu, J. Yagi, X. Guo, et L. Zhang, « Prediction of Pre-reduction Shaft Furnace with Top Gas Recycling Technology Aiming to Cut Down CO2 Emission », *ISIJ Int.*, vol. 51, p. 1344-1352, 2011.
[145] L. Shao, H. Yu, et C. Zhao, « Effects of Room-Temperature Center Gas Distributor Injection on the H2 Shaft Furnace Process: A Numerical Study », *Processes*, vol. 12, nº 1666, 2024, [En ligne]. Disponible sur: https://doi.org/10.3390/pr12081666
[146] J. Xu, S. Wu, M. Kou, et K. Du, « Numerical analysis of the characteristics inside pre-reduction shaft furnace and its operation parameters optimization by using a three-dimensional full scale mathematical model », *ISIJ. Int.*, vol. 53, nº 4, p. 576, 2013.
[147] Z. Liu, S. Lu, Y. Wang, J. Zhang, Q. Cheng, et Y. Ma, « Study on optimization of reduction temperature of hydrogen-based shaft furnace—numerical simulation and multi-criteria evaluation », *Int. J. Hydrogen Energy*, vol. 48, nº 42, p. 16132, 2023.
[148] X. Zhang, Z. Luo, et Z. Zou, « Numerical analysis on performance of COREX CGD shaft furnace with top gas recycling », *ISIJ. Int.*, vol. 59, nº 11, p. 1972, 2019.
[149] L. Shao, X. Zhang, C. Zhao, Y. Qu, H. Saxén, et Z. Zou, « Computational analysis of hydrogen reduction of iron oxide pellets in a shaft furnace process », *Renew. Energy*, vol. 179, p. 1537, 2021.
[150] L. Shao, X. Zhang, C. Zhao, Y. Zhai, H. Saxén, et Z. Zou, « A study of options to enhance the operation of a H2 direct reduction shaft furnace using a two-dimensional model »,

International Journal of Hydrogen Energy, vol. 86, p. 124-131, oct. 2024, doi: 10.1016/j.ijhydene.2024.08.390.
[151] S. Yu., L. Shao, Z. Zou, et H. Saxén, « A Numerical Study on the Performance of the H2 Shaft Furnace with Dual-Row Top Gas Recycling », *Processes*, vol. 9, nº 2134, 2021, [En ligne]. Disponible sur: https://doi.org/10.3390/pr9122134
[152] W. Mullins, « Stochastic theory of particle flow under gravity », *Journal of Applied Physics*, vol. 43, nº 2, p. 665-678, 1972.
[153] S. Ergun, « Fluid flow through packed columns. », *Chem. Eng. Prog.*, vol. 48, nº 89, 1952.
[154] S. Patankar, *Numerical heat transfer and fluid flow*. CRC press, 2018.
[155] J. H. Ferziger, M. Perić, et R. L. Street, *Computational Methods for Fluid Dynamics*. Berlin/Heidelberg: Springer, 2019.
[156] D. Korba *et al.*, « A continuum model for heat and mass transfer in moving-bed reactors for thermochemical energy storage », *Appl. Energy*, vol. 313, nº 118842, 2022, [En ligne]. Disponible sur: https://doi.org/10.1016/j.apenergy.2022.118842
[157] R. Karwa, *Heat and Mass Transfer*. Berlin/Heidelberg: Springer, 2020.
[158] S. Yu., L. Shao, et Z. Zou, « Operation enhancement of the H2 shaft furnace: A numerical study on the impact of N2 mixing in feed gas », *Int. J. Chem. React. Eng.*, vol. 22, p. 813-821, 2024.
[159] « Energiron Brochure ». Tenova HYL, 2020.
[160] D. Schulze, *Powders and bulk solids*. Springer, 2021.
[161] W. Ge *et al.*, « Discrete simulation of granular and particle-fluid flows: from fundamental study to engineering application », *Reviews in Chemical Engineering*, vol. 33, nº 6, p. 551-623, 2017.
[162] S. La Manna *et al.*, « Insights from DEM Simulations for Shear Cell Experiments with Wooden Spheres », in *Proceedings of the 11th International Conference on Conveying and Handling of Particulate Solids*, School of Engineering, University of Edinburgh, 2024, p. 41-42.
[163] H. Liao *et al.*, « Influence of Wall Angle of Direct Reduction Shaft Furnace on Particle Flow Pattern by DEM Modeling », *steel research international*, vol. 94, nº 10, p. 2300044, 2023.
[164] X. Tian *et al.*, « Influence of diversion cone structure on inner characteristic in hydrogen-enriched shaft furnace: a DEM study », *Journal of Iron and Steel Research International*, p. 1-12, 2025.
[165] H. Ling, Y. Jin, Z. Huang, Z. Liu, et P. Lin, « Study of Stress and Wear Behavior of Internal Components in Hydrogen-Based Shaft Furnaces Based on the Discrete Element Method (DEM) Model », *Processes*, vol. 13, nº 3, p. 857, 2025.
[166] Q. Zheng, Q. Luo, et A. Yu, « A unified theory for granular matter », *Powder Technology*, vol. 434, p. 119370, 2024.
[167] I. Goldhirsch, « Introduction to granular temperature », *Powder technology*, vol. 182, nº 2, p. 130-136, 2008.
[168] R. M. Nedderman, « Statics and kinematics of granular materials », *(No Title)*, 1992.
[169] J. E. Andrade, Q. Chen, P. H. Le, C. F. Avila, et T. M. Evans, « On the rheology of dilative granular media: bridging solid-and fluid-like behavior », *Journal of the Mechanics and Physics of Solids*, vol. 60, nº 6, p. 1122-1136, 2012.
[170] Q. Luo, Q. Zheng, et A. Yu, « Quantitative comparison of hydrodynamic and elastoplastic approaches for modeling granular flow in silo », *AIChE Journal*, vol. 65, nº 5, p. e16533, 2019.
[171] L. Yang, Q. Zheng, et A. Yu, « Numerical simulation of solid flow and segregation in a blast furnace by coupling granular rheology and transport equation », *Chemical Engineering Science*, vol. 242, p. 116741, 2021.
[172] K. Saleh et M. Leturia, « Stockage et écoulement des solides granulaires dans les silos: Concepts de base et théorie », *Techniques de l'ingénieur*, vol. 2258, 2020.
[173] A. W. Jenike, *Storage and flow of solids*. University of Utah, 1966.

[174] Q. Zheng et A. Yu, « Finite element investigation of the flow and stress patterns in conical hopper during discharge », *Chemical Engineering Science*, vol. 129, p. 49-57, 2015.
[175] J. Ooi, J. F. Chen, et J. Rotter, « Measurement of solids flow patterns in a gypsum silo », *Powder Technology*, vol. 99, nº 3, p. 272-284, 1998.
[176] R. Nedderman et U. Tüzün, « A kinematic model for the flow of granular materials », *Powder Technology*, vol. 22, nº 2, p. 243-253, 1979.
[177] Y. J. Lee, « A scaled model study on the solid flow in a shaft type furnace », *Powder technology*, vol. 102, nº 2, p. 194-201, 1999.
[178] H. Janssen, « Tests on grain pressure silos », *Zeitschrift des Vereines Deutscher Ingenieure*, vol. 39, nº 35, p. 1045, 1895.
[179] A. Couto, A. Ruiz, L. Herráez, J. Moran, et P. Aguado, « Measuring pressures in a slender cylindrical silo for storing maize. Filling, static state and discharge with different material flow rates and comparison with Eurocode 1 part 4 », *Computers and Electronics in Agriculture*, vol. 96, p. 40-56, 2013.
[180] W. A. Beverloo, H. A. Leniger, et J. Van de Velde, « The flow of granular solids through orifices », *Chemical engineering science*, vol. 15, nº 3-4, p. 260-269, 1961.
[181] L. Staron, P.-Y. Lagrée, et S. Popinet, « The granular silo as a continuum plastic flow: The hour-glass vs the clepsydra », *Physics of Fluids*, vol. 24, nº 10, 2012.
[182] S. Zhang, P. Lin, G. Yang, J.-F. Wan, Y. Tian, et L. Yang, « Criteria for Beverloo's scaling law », *Chinese Physics B*, vol. 28, nº 1, p. 018101, 2019.
[183] D. L. Henann et K. Kamrin, « A predictive, size-dependent continuum model for dense granular flows », *Proceedings of the National Academy of Sciences*, vol. 110, nº 17, p. 6730-6735, avr. 2013, doi: 10.1073/pnas.1219153110.
[184] P. Jop, Y. Forterre, et O. Pouliquen, « A constitutive law for dense granular flows », *Nature*, vol. 441, nº 7094, p. 727-730, 2006.
[185] J. Chen, T. Akiyama, H. Nogami, J. Yagi, et H. Takahashi, « Modeling of solid flow in moving beds », *ISIJ international*, vol. 33, nº 6, p. 664-671, 1993.
[186] W. Aboussi, « Theoretical and numerical study of Bingham flows », PhD Thesis, Université Paris-Nord-Paris XIII; Université Mohammed VI Polytechnique …, 2024.
[187] J. Chauchat et M. Médale, « A three-dimensional numerical model for incompressible two-phase flow of a granular bed submitted to a laminar shearing flow », *Computer Methods in Applied Mechanics and Engineering*, vol. 199, nº 9-12, p. 439-449, 2010.
[188] S. Thohura, M. M. Molla, et M. Sarker, « Bingham fluid flow simulation in a lid-driven skewed cavity using the finite-volume method », *International Journal of Computer Mathematics*, vol. 97, nº 6, p. 1212-1233, 2020.
[189] H. Nogami et J. Yagi, « An application of Bingham model to viscous fluid modeling of solid flow in moving bed », *ISIJ international*, vol. 44, nº 11, p. 1826-1834, 2004.
[190] P. Neofytou, « A 3rd order upwind finite volume method for generalised Newtonian fluid flows », *Advances in Engineering Software*, vol. 36, nº 10, p. 664-680, 2005.
[191] Y. Kaymak, « Rheology model for simulation of particle flow in moving-bed reactors », 2025.
[192] P. Jop, « Ecoulements granulaires sur fond meuble », PhD Thesis, Université de Provence-Aix-Marseille I, 2006.
[193] GDR MiDi, « On dense granular flows », *Eur. Phys. J. E*, vol. 14, p. 341-365, 2004, doi: 10.1140/epje/i2003-10153-0.
[194] Y. Forterre et O. Pouliquen, « Flows of dense granular media », *Annu. Rev. Fluid Mech.*, vol. 40, nº 1, p. 1-24, 2008.
[195] D. M. Wood, *Soil behaviour and critical state soil mechanics*. Cambridge university press, 1990.
[196] J. A. S. Cleaver et R. M. Nedderman, « Measurement of velocity profiles in conical hoppers », *Chemical Engineering Science*, vol. 48, nº 21, p. 3703-3712, 1993, doi: https://doi.org/10.1016/0009-2509(93)81027-S.

[197] J. F. Chen, J. M. Rotter, J. Y. Ooi, et Z. Zhong, « Flow pattern measurement in a full scale silo containing iron ore », *Chemical Engineering Science*, vol. 60, nº 11, p. 3029-3041, 2005, doi: https://doi.org/10.1016/j.ces.2004.12.045.
[198] G. Gustafsson, « Mechanical characterization and modelling of iron ore pellets », PhD Thesis, Luleå tekniska universitet, 2012.
[199] D. Beggs et R. M. Escott., « Hot Discharge Direct Reduction Furnace », 4,188,022, 1980
[200] K. Kambara, S. Tanaka, et S. Miyasita, « Discharging device of a shaft furnace having cooling means », 3,913,755, 1975

Abstract

The steel industry accounts for approximately 7% of the global anthropogenic CO_2 emissions, mainly due to the reduction of iron ore in the blast furnace. In the context of the energy transition and carbon neutrality objectives, hydrogen is identified as a key player for the direct reduction of iron ore, partially or totally replacing carbon monoxide. This thesis is part of the European project MaxH2DR, which aims at maximizing hydrogen enrichment in direct reduction shaft furnaces. Our research was structured into four main parts. First, an experimental kinetic study was carried out to characterize the reduction of iron ore pellets by a hydrogen-rich gas mixture. A comprehensive model, based on the Grain Model coupled with the law of additive reaction times**,** was developed to capture the combined effects of diffusion, chemical reaction, and morphological transformations. Second, macroscale characterizations of partially reduced pellets were performed to understand the effect of temperature on the evolution of the pore network during reduction. Third, the kinetic model was implemented in the REDUCTOR code to simulate the operation of a direct reduction shaft furnace under hydrogen-enriched conditions. Several configurations were investigated. The transition from conventional syngas up to pure hydrogen highlights a drastic reduction in CO_2 emissions coupled with increased energy requirements. Finally, a rheological modeling approach was proposed to describe the solid flow of the pellets within the shaft furnace. Preliminary results revealed the impact of geometry on the velocity distributions and the presence of stagnant zones. Overall, this work is expected to contribute to the scientific understanding and multi-physics modeling of hydrogen-based direct reduction, paving the way towards a sustainable steelmaking industry compatible with international climate goals.

Keywords: iron ore, direct reduction, hydrogen, kinetics, shaft furnace, modeling.

Résumé

La sidérurgie est responsable d'environ 7 % des émissions anthropiques mondiales de CO_2, principalement en raison de la réduction du minerai de fer dans les hauts fourneaux. Dans le contexte de la transition énergétique et des objectifs de neutralité carbone, l'hydrogène apparaît comme un acteur clé pour la réduction directe du minerai de fer, en remplacement partiel ou total du monoxyde de carbone. Cette thèse s'inscrit dans le projet européen MaxH2DR**,** dont l'objectif est de maximiser l'enrichissement en hydrogène des fours à cuve de réduction directe. Le travail se décline en quatre volets principaux. Tout d'abord, une étude cinétique expérimentale a permis de caractériser la réduction de boulettes de minerai de fer par des mélanges riches en hydrogène. Un modèle robuste basé sur le modèle des grains couplé à la loi des temps caractéristiques additifs a été développé, qui rend compte des phénomènes de diffusion gazeuse, de réaction chimique et de transformations morphologiques de la boulette. Ensuite, une caractérisation à l'échelle macroscopique de boulettes partiellement réduites a précisé l'influence de la température sur l'évolution du réseau poreux au cours de la réduction. Le modèle cinétique a ensuite été intégré au code REDUCTOR**,** qui a été utilisé pour simuler le fonctionnement d'un four à cuve enrichi en hydrogène. Plusieurs configurations ont été étudiées. Le passage du syngas conventionnel à l'hydrogène pur entraîne une forte réduction des émissions de CO_2 mais une consommation énergétique supérieure. Enfin, un modèle rhéologique a été proposé pour décrire l'écoulement des boulettes dans le four à cuve, révélant l'influence de la géométrie sur la distribution des vitesses ainsi que la présence de zones stagnantes. Ces résultats devraient contribuer à la compréhension fondamentale et à la modélisation multi-physique de la réduction directe à l'hydrogène, ouvrant la voie à une sidérurgie durable et compatible avec les objectifs climatiques internationaux.

Mots clés : minerai de fer, réduction directe, hydrogène, cinétique, four à cuve, modélisation.